

***High-pressure synthesis, structure, and
properties of rare-earth (poly-) nitrides and
carbonitrides***

Doctoral Thesis

submitted to obtain the academic degree of Doctor of Natural Sciences
(Dr. rer. nat.)
of the Bayreuth Graduate School of Mathematical and Natural Sciences
(BayNAT)
of the University of Bayreuth

Andrii Aslandukov

from Kharkiv, Ukraine

Bayreuth, 2024

This doctoral thesis was prepared at the Laboratory of Crystallography (Material Physics and Technology at Extreme Conditions Group) and the Bavarian Research Institute of Experimental Geochemistry and Geophysics (BGI) at the University of Bayreuth from 08/2020 until 07/2024 and was supervised by Prof. Dr. Dr. h. c. Leonid Dubrovinsky and Prof. Dr. Dr. h. c. Natalia Dubrovinskaia.

This is a full reprint of the thesis submitted to obtain the academic degree of Doctor of Natural Sciences (Dr. rer. nat.) and approved by the Bayreuth Graduate School of Mathematical and Natural Sciences (BayNAT) of the University of Bayreuth.

Form of the dissertation: Cumulative dissertation

Date of submission: 27.08.2024

Admission by the executive board: 12.09.2024

Date of defence: 12.02.2025

Acting director: Prof. Dr. Jürgen Köhler

Doctoral committee:

Prof. Dr. Natalia Dubrovinskaia (reviewer)

Prof. Dr. Sander van Smaalen (reviewer)

PD Dr. Catherine McCammon (chairman)

PD Dr. Gerd Steinle-Neumann

(additional reviewer: PD Dr. Alexandra Friedrich)

Table of Contents

Zusammenfassung	5
Summary	8
Acknowledgments	10
1. Introduction.....	12
1.1. High-pressure synthesis.....	12
1.2. <i>In situ</i> characterization of reaction products in LHDACs	13
1.3. High-pressure chemistry of nitrogen.....	14
1.3.1. Nitrogen inorganic compounds at ambient pressure	14
1.3.2. High-pressure behavior of molecular nitrogen.....	15
1.3.3. High-pressure binary X-N compounds	16
1.3.4. High-pressure ternary metal-C-N compounds	18
2. Methods.....	20
2.1. Generation of extreme conditions	20
2.1.1. Pressure generation in DACs	20
2.1.2. Pressure transmitting media	21
2.1.3. Pressure determination	22
2.1.4. Temperature generation in DACs	22
2.2. X-ray diffraction in LHDACs	23
2.2.1. Basic principles	23
2.2.2. XRD experiments in LHDAC: features and limitations	27
2.2.3. Synchrotron SCXRD from multigrain samples in LHDACs: data collection ...	28
2.2.4. Synchrotron SCXRD from multigrain samples in LHDACs: data processing ..	31
2.3. Stability range, equation of state, and recoverability check.....	34
2.4. X-ray Absorption Spectroscopy	35
2.5. Raman spectroscopy.....	36
2.6. Computational approaches	37
3. Thesis synopsis	39
3.1. Methodological development: DAFi program for the analysis of single-crystal X-ray diffraction data from polycrystalline samples	40
3.2. High-pressure synthesis of novel rare-earth di-, oligo- and poly- nitrides.....	41
3.3. High-pressure synthesis of novel rare-earth carbonitrides.....	44
3.4. List of manuscripts and statement of authors' contribution.....	46
4. Bibliography	48

5. Manuscripts of the thesis	58
5.1. Domain Auto Finder (DAFi) program: the analysis of single-crystal X-ray diffraction data from polycrystalline samples	58
5.2. High-pressure yttrium nitride, Y_5N_{14} , featuring three distinct types of nitrogen dimers	68
5.3. Anionic N_{18} macrocycles and a polynitrogen double helix in novel yttrium polynitrides YN_6 and Y_2N_{11} at 100 GPa.....	84
5.4. Stabilization of N_6 and N_8 anionic units and 2D polynitrogen layers in high-pressure scandium polynitrides.....	100
5.5. Stabilization of the CN_3^{5-} anion in recoverable high-pressure $Ln_3O_2(CN_3)$ ($Ln = La, Eu, Gd, Tb, Ho, Yb$) oxoguanidates	129
5.6. Synthesis of $LaCN_3$, $TbCN_3$, $CeCN_5$ and $TbCN_5$ polycarbonitrides at megabar pressures	161
6. List of all author publications	191
(Eidesstattliche) Versicherungen und Erklärungen.....	196

Zusammenfassung

Die Entdeckung der Verkettung von Stickstoffatomen unter hohem Druck hat einen neuen Weg für die Synthese von Polynitrogenverbindungen eröffnet. Theoretische Studien sagen zahlreiche Hochdruck-Polynitride mit exotischen Strukturen voraus, die Oligo- und Polynitrogen-Anionen enthalten und Eigenschaften aufweisen, die auf eine Eignung als Materialien mit hoher Energiedichte schließen lassen.

Diese kumulative Dissertation präsentiert eine experimentelle Untersuchung der Terra incognita der Chemie von Hochdruck-Seltenenerdinitriden und -carbonitriden. Die Hauptziele waren: (1) experimentell zu bestimmen, welche Phasen bei Drücken bis zu 125 GPa gebildet werden, (2) die Regelmäßigkeiten in der Hochdruck-Phasenbildung und der strukturellen Organisation von Seltenenerdinitriden und -carbonitriden zu identifizieren und zu identifizieren und umfassende Muster in der in der Hochdruck-Chemie des Stickstoffs zu finden, (3) die theoretischen Vorhersagen zu überprüfen.

Für die Hochdruck-Hochtemperatur-Synthese wurden Laser-beheizte Diamantstempelzellen (engl. *laser-heated diamond anvil cell*, LHDAC) verwendet, Phasenidentifikation, Strukturlösung und Verfeinerung wurden mittels in-situ Einkristall-Röntgenbeugung (engl. *single-crystal X-ray diffraction*, SCXRD) mit Synchrotronstrahlung durchgeführt. Die Herausforderungen bei der Analyse von mehrphasigen polykristallinen Proben, die in den LHDACs gebildet wurden, wurden mit der Entwicklung der Software DAFi bewältigt. Dieses ermöglicht das Sortieren von SCXRD-Daten einzelner Kristallite in Mehrkornproben ohne vorherige Kenntnisse der Phasenzusammensetzung. Mithilfe von DAFi wurden zunächst binäre Y-N- und Sc-N-Systeme und anschließend komplexere Systeme mit seltenen Erden (La, Ce, Eu, Gd, Tb, Ho, Yb), Stickstoff und Kohlenstoff untersucht. Dichtefunktionaltheorie (DFT) Berechnungen wurden durchgeführt, um die experimentellen Entdeckungen zu bestätigen und zusätzliche Informationen über die strukturellen Merkmale und Eigenschaften der synthetisierten Verbindungen zu gewinnen.

Die Reaktionen zwischen Yttrium und Stickstoff wurden in den LHDACs bei 50 GPa und 100 GPa durchgeführt. Dabei wurden drei neuartige Feststoffe mit ungewöhnlicher Stöchiometrie entdeckt: Y_5N_{14} bei 50 GPa und YN_6 sowie Y_2N_{11} bei 100 GPa. Die Kristallstruktur von Y_5N_{14} enthält drei unterschiedliche Arten von Stickstoffdimeren. Kristallchemische Analysen und DFT-Berechnungen zeigen, dass die Dimere $[N_2]^x$ kristallographisch und chemisch nicht äquivalent sind und unterschiedliche nicht-ganzzahlige Formalladungen (x) besitzen, was Y_5N_{14} von allen bisher bekannten Dinitriden unterscheidet.

Die Kristallstrukturen von YN_6 und Y_2N_{11} weisen eine einzigartige Anordnung von Stickstoffatomen auf – ein bisher unbekannter anionischer N_{18} -Makrozyklus bzw. eine Polynitrogen-Doppelhelix. Die chemischen Reaktionen zwischen Scandium und Stickstoff bei 78-125 GPa und 2500 K in LHDACs führten zur Bildung von vier neuen Verbindungen: Sc_2N_6 , Sc_2N_8 , ScN_5 und Sc_4N_3 . In den Kristallstrukturen der stickstoffreichen Phasen Sc_2N_6 , Sc_2N_8 und ScN_5 bilden kettenförmig verknüpfte Stickstoffatome bisher unbekannte $[\text{N}_6]^{6-}$, und $[\text{N}_8]^{6-}$ Einheiten, die aus kondensierten N_{12} -Ringen bestehen. DFT-Berechnungen zeigen, dass die Feststoffe Sc_2N_6 , Sc_2N_8 und ScN_5 vielversprechende Materialien mit hoher Energiedichte sind. Diese Ergebnisse erweitern die Liste der bekannten kettenförmigen Stickstoffspezies erheblich und zeigen, dass der Grad der Bildung von Stickstoffketten mit dem Druck zunimmt.

Eine Reihe isostruktureller $\text{Ln}_3\text{O}_2(\text{CN}_3)$ ($\text{Ln} = \text{La}, \text{Eu}, \text{Gd}, \text{Tb}, \text{Ho}, \text{Yb}$)-Oxoguanidinate wurde unter Hochdruck-Hochtemperatur-Bedingungen (bei 25 – 54 GPa und 2000 – 3000 K) synthetisiert, deren Kristallstrukturen das $[\text{CN}_3]^{5-}$ Guanidinat-Anion aufweisen. Experimente zur Dekompression haben gezeigt, dass die $\text{Ln}_3\text{O}_2(\text{CN}_3)$ -Verbindungen auch unter Normalbedingungen nachweisbar sind. Bei höheren Drücken wurde eine neue Klasse von Materialien entdeckt, die aus einer aus CN_4 -Einheiten aufgebauten, anionischen 3D-Polycarbonitrid-Gerüststruktur und Metallkationen bestehen. Die ersten Vertreter dieser Polycarbonitride, LaCN_3 , TbCN_3 , CeCN_5 und TbCN_5 , wurden in LHDACs bei Drücken zwischen 90 und 111 GPa synthetisiert. Die Kristallstrukturen dieser Verbindungen bestehen aus dreidimensionalen, anionischen Kohlenstoff-Stickstoff-Netzwerken aus di- oder oligo-Stickstoff-verknüpften CN_4 -Tetraedern, wobei die Kohlenstoff- und Stickstoffatome durch kovalente Einfachbindungen aneinander gebunden sind. Aus der Perspektive der Chemie vervollständigen die neu entdeckten Verbindungen die Reihe der kovalent gebundenen anionischen C-N-Spezies, von den bei Normalbedingungen bestens bekannten Cyaniden $[\text{CN}]^-$ und Carbodiimiden $[\text{NCN}]^{2-}$, bis hin zu den unter Hochdruck gebildeten Guanidinate $[\text{CN}_3]^{5-}$ (25-54 GPa) und Polycarbonitriden $[\text{CN}_4]^{4-\infty}$ (90-111 GPa). Die Stabilisierung des $[\text{CN}_3]^{5-}$ Guanidinat-Anions unter Normalbedingungen eröffnet neue Möglichkeiten für die anorganische und organische Synthesechemie.

Abschließend präsentiert diese Dissertation Ergebnisse zur Synthese von Selten-Erd-(Poly-)Nitriden und -Carbonitriden in LHDACs bei Drücken von 25-125 GPa und Temperaturen bis zu 3000 K. Die Kristallstrukturen wurden mittels Synchrotron-SCXRD gelöst und verfeinert. Das Programm DAFi wurde entwickelt, um SCXRD-Reflexe einzelner Kristallite in Mehrkornproben ohne vorherige Kenntnisse der Phasenzusammensetzung zu sortieren. Diese Software stellt einen Durchbruch in der Strukturuntersuchung von Mehrkornproben dar, sowohl unter Normal-, als auch unter Extrembedingungen. Die SCXRD-

Analyse ergab 17 neuartige Verbindungen, 7 neue Strukturtypen und 6 bisher unbekannte Anionen. Diese systematische experimentelle Studie zeigt, dass: (1) Druck die Bildung homoatomarer Oligo- und Polystickstoff-Anionen begünstigt, wobei der Grad der Stickstoff-Kettenbildung mit steigendem Druck zunimmt; (2) die Vielfalt kettenförmiger Stickstoff-Anionen mit steigendem Druck zunimmt, wobei bei gleichen Drücken unterschiedliche Anionen nebeneinander vorliegen können, (3) die Koordinationszahl von Kohlenstoff in C-N-Anionen mit dem Druck steigt, was zu drastischen Veränderungen in Struktur und Chemie der Carbonitride führt. Unter einer Vielzahl von theoretischen Vorhersagen fanden sich lediglich zwei der 17 experimentell entdeckten neuen Strukturen. Dies unterstreicht den Bedarf an präziseren Methoden zur Vorhersage solcher Verbindungen.

Summary

The discovery of nitrogen catenation under high pressure has opened up a route for the synthesis of polynitrogen compounds. Theoretical studies predict numerous high-pressure polynitrides with exotic structures containing oligo- and polynitrogen anions and properties potentially useful for high-energy-density materials.

This cumulative thesis presents an experimental investigation of the chemistry of the high-pressure rare-earth nitrides and carbonitrides, which hitherto has remained a *terra incognita*. The primary objectives were as follows: (1) to experimentally determine which phases are formed at pressures up to 125 GPa, (2) to identify the regularities in the high-pressure phase formation and structural organization of rare-earth nitrides and carbonitrides, and to find the broader patterns in nitrogen high-pressure chemistry, (3) to examine the theoretical predictions.

The laser-heated diamond anvil cell (LHDAC) technique was used for the high-pressure high-temperature synthesis, and *in situ* synchrotron single-crystal X-ray diffraction (SCXRD) was used for the phase identification, structure solution, and refinement. To overcome the challenges in analyzing SCXRD data from multiphase polycrystalline samples formed in LHDACs, a DAFi program was developed. It enables the sorting of SCXRD data from individual crystallites within multigrain samples without requiring *a priori* knowledge of the sample's phase composition. Using this tool, first binary Y-N and Sc-N systems and then more complex systems containing rare-earth elements (La, Ce, Eu, Gd, Tb, Ho, Yb), nitrogen, and carbon were studied. Density functional theory (DFT) calculations were conducted to corroborate experimental discoveries and provide additional information on the structural features and properties of the synthesized compounds.

The reactions between yttrium and nitrogen were conducted in the LHDACs at 50 GPa and 100 GPa. Three novel solids with unusual stoichiometry: Y_5N_{14} at 50 GPa, and YN_6 along with Y_2N_{11} at 100 GPa were discovered. The crystal structure of Y_5N_{14} contains three distinct types of nitrogen dimers. Crystal chemical analysis and DFT calculations demonstrated that the dimers $[\text{N}_2]^{x-}$ are crystallographically and chemically non-equivalent and possess distinct non-integer formal charges (x) that make Y_5N_{14} unique among known dinitrides. The crystal structures of YN_6 and Y_2N_{11} feature a unique organization of nitrogen atoms—a previously unknown anionic N_{18} macrocycle and a polynitrogen double helix, respectively. The chemical reactions between scandium and nitrogen at 78-125 GPa and 2500 K in LHDACs resulted in the formation of four novel compounds: Sc_2N_6 , Sc_2N_8 , ScN_5 , and Sc_4N_3 . In the crystal structures

of the nitrogen-rich Sc_2N_6 , Sc_2N_8 , and ScN_5 phases nitrogen is catenated forming previously unknown $[\text{N}_6]^{6-}$ and $[\text{N}_8]^{6-}$ units and $\frac{2}{\infty}(\text{N}_5^{3-})$ anionic corrugated 2D-polynitrogen layers consisting of fused N_{12} rings. DFT shows that Sc_2N_6 , Sc_2N_8 , and ScN_5 solids are promising high-energy-density materials. These results significantly extend the list of known catenated nitrogen species and demonstrate that the degree of nitrogen catenation increases with pressure.

A series of isostructural $\text{Ln}_3\text{O}_2(\text{CN}_3)$ ($\text{Ln} = \text{La, Eu, Gd, Tb, Ho, Yb}$) oxoguanidates was synthesized under high-pressure (25-54 GPa) high-temperature (2000-3000 K) conditions. Their crystal structures feature the $[\text{CN}_3]^{5-}$ guanidinate anion. Decompression experiments show that $\text{Ln}_3\text{O}_2(\text{CN}_3)$ compounds are recoverable to ambient conditions. At higher pressures, a new class of materials built of a CN_4 -based 3D polycarbonitride anionic framework comprising metallic cations was discovered. These first polycarbonitrides representatives, LaCN_3 , TbCN_3 , CeCN_5 , and TbCN_5 , were synthesized in LHDACs at pressures between 90 and 111 GPa. The crystal structures of these compounds are built of covalently single-bonded carbon-nitrogen anionic 3D framework consisting of CN_4 tetrahedra connected *via* di- or oligo-nitrogen linkers. From a chemical perspective, these discoveries complete the series of covalently bonded anionic C-N species, from the cyanides $[\text{CN}]^-$ and carbodiimides $[\text{NCN}]^{2-}$ well-known at ambient conditions, to the high-pressure formed guanidates $[\text{CN}_3]^{5-}$ (25-54 GPa) and polycarbonitrides $[\text{CN}_4]^{4-\infty}$ (90-111 GPa). The stabilization of the $[\text{CN}_3]^{5-}$ guanidinate anion at ambient conditions provides new opportunities for inorganic and organic synthetic chemistry.

To conclude, this thesis presents results on the synthesis of rare-earth (poly-) nitrides and carbonitrides in LHDACs at pressures 25-125 GPa and temperatures up to 3000 K. The crystal structures were solved and refined using synchrotron SCXRD. The DAFi program was developed to sort SCXRD reflections from individual crystallites in multiphase polycrystalline samples without knowing their phase composition. This software is a breakthrough in structural studies of multigrain samples under both ambient and extreme conditions. The SCXRD analysis revealed 17 novel compounds, 7 new structure types, and 6 previously unobserved anions. This systematic experimental study demonstrates that: (1) pressure promotes the formation of homoatomic oligo- and polynitrogen anions with a higher degree of nitrogen catenation as pressure increases; (2) the diversity of catenated nitrogen anions increases with rising pressure, and different anions may coexist at the same pressure; (3) the coordination number of carbon in C-N anions increases with pressure, leading to drastic changes in the structure and chemistry of carbonitrides. Despite numerous theoretical predictions, only two out of 17 experimentally observed structures were anticipated by theory which highlights the need for more accurate methods in predicting such compounds.

Acknowledgments

Foremost, I would like to thank my supervisors: Prof. Dr. Leonid Dubrovinsky and Prof. Dr. Natalia Dubrovinskaia. Thank you for your patient guidance while I learned the unfamiliar and challenging field of high-pressure science. Thank you for your support, useful discussions, advice, as well as for your openness to discuss any scientific issues at any time. Thank you for the best working environment and for the freedom in my scientific research. Thank you for your energy, inspiration, and endless optimism, and for keeping a friendly atmosphere in our scientific group. Under your supervision, I enjoyed my four-year PhD journey.

For most of my PhD time, I belonged to the Laboratory of Crystallography. I would like to thank all the members of the Laboratory of Crystallography for a warm and friendly atmosphere for scientific work. Special thanks to Prof. Dr. Sander van Smaalen for helpful discussions on the laboratory seminars and to Dr. Andreas Schönleber for the brilliant lectures in the “Crystallography in Superspace” course. Deep gratitude to Dominique Laniel, who becomes my unspoken mentor and friend, for sharing his expertise, helpful discussions, permanent optimism, and fun beamtimes. Thanks to my office-mates Kerstin Kuspert and Yuqing Yin as well as to Wenju Zhou, Surya Rohith Kotla, Claudio Eisele, and Franz Fischer for your help and friendly working environment. Many thanks to laboratory secretary Denis Kelk-Huth, who helped me with many administrative problems and questions. Additionally, I would like to thank Claudio Eisele for translating the Summary of this thesis into German.

Since physically I have been working on BGI floor, I would like to thank Prof. Hans Keppler, Prof. Tomoo Katsura, and Prof. Dan Frost for providing an excellent environment for collaborative work. I would like to thank the administrative and technical staff of BGI, Anna Dinius, Petra Buchert, Janina Potzel, Dorothea Wiesner, Detlef Krausse, Stefan Übelhack, Heinz Fischer and Ulrike Trenz for their help in corresponding problems. I would like to thank Gerd Steinle-Neumann and Liang Yuan for their help in mastering the DFT calculations. Also, thanks to all the non-mentioned BGI-people for the permanent warm and friendly environment at the institute.

During my PhD, I spent almost half a year participating in experiments at synchrotron facilities I would like to express my appreciation to the staff of the P02.2 beamline at Petra III and of the 13-IDD beamline at APS for the invaluable help during the experiments: Konstantin Glazirin, Hanns-Peter Liermann, Stella Chariton, Vitali Prakapenka. Special thanks to ESRF people, for the help during the experiments as well as for optimism and humor making my stay

in Grenoble incredibly enjoyable: Carlotta Giacobbe, Eleanor Lawrence Bright, Jonathan Wright, Michael Hanfland, Davide Comboni, Tomaz Poreba, Gaston Garbarino, Anna Pakhomova, Mohamed Mezouar, Fabrice Wilhelm, Andrei Rogalev, Xiang Li, Georgios Aprillis, Iliia Kuppenko, Alexander Chumakov, Harald Müller.

I would like to acknowledge my colleagues from different universities for sharing their expertise, fruitful discussions, and productive collaborations: Maxim Bykov, Elena Bykova, James Spender, Akun Liang, Umbertoluca Ranieri, Amanda Ehn, Florian Trybel, and Igor Abrikosov.

I would like to thank my friends from BGI: Saiana Khandarkhaeva, Timofey Fedotenko, Egor Koemets, Iulia Koemets, Artem Chanyshev, Dmitry Bondar, Naira Martyrosyan, Fariia (Lera) Akbar and Alexander Kurnosov. Thank you all for the joyful time we spent together, your kindness and support. Also, I would like to thank my non-BGI friends, who supported me during my PhD journey: Anatolii Arkhipin, Pavel Milkin, Iliia Sadilov, and Efim Kolesnikov.

I am grateful to my first teachers: Larisa Anatolyevna Evdokimenko, Elena Lazarevna Arinkina, Victoria Yulianovna Zenina, Tatyana Ivanovna Voilokova, and Rodion Yurievich Ilyashenko, who instilled in me an interest and love for mathematics and chemistry in my childhood. I am thankful to my teachers from AESC LMSU and Lomonosov Moscow State University for top-quality fundamental natural science education. Special thanks to my first scientific advisor Dr. Valentina V. Utochnikova, who opened up a beautiful world of science for me.

I would like to extend my heartfelt gratitude to my parents, Olha Aslandukova and Nikolai Aslandukov, who have raised me and shaped me into the person I am today. Thank you for your guiding, endless love, and support. Thanks to my brother Matvii Aslandukov, with whom we walk through life shoulder to shoulder despite the physical distance between us. Thank you for your support and willingness to help in any situation.

I would like to express my deepest gratitude to my beloved wife, Alena Aslandukova, for her love and unwavering support. Thank you for your belief in me and for always standing by my side. And thanks to my sunshine, daughter Arina, for reminding me of the beauty and wonder in every moment as well as for your infectious laughter and boundless energy, which have been a constant source of joy and motivation.

1. Introduction

1.1. High-pressure synthesis

The prospects brought forward by the application of the thermodynamic parameter pressure for geoscience, materials science and chemistry are tantalizing. According to the Inorganic Crystal Structure Database (ICSD), more than 97% of all known inorganic compounds have been produced at a single pressure value—ambient pressure—upon which our chemical understanding has been empirically built [ICSD search 01.07.2024]. However, given how radically pressure alters and modifies chemical behavior and the resulting material's properties, it is only natural for high-pressure chemistry to gain traction.

Over the past decades, the high-pressure (GPa scale) high-temperature (up to thousands of kelvin) (HPHT) synthetic chemistry has grown up and drastically changed the established paradigms of chemistry. For example, the synthesis of noble gases compounds (e.g. Na_2He^1), compounds with unusual for ambient chemistry stoichiometries (e.g. NaCl_3 ,² $\text{Fe}_{25}\text{O}_{32}$ ³), superhydrides with enhanced electron transport properties and close-to-room-temperature superconductivity (e.g. LaH_{10}^4), and stabilization of exotic units (e.g. hexazine rings^{5,6}) have been reported.

There are three main approaches to high-pressure synthesis: using autoclaves, large volume presses (LVP), and laser-heated diamond anvil cells (LHDAC). Although the first two methods allow the synthesis of samples up to a few cubic centimeters and millimeters respectively, they cannot compete with LHDACs regarding the accessible pressure-temperature ranges (Fig. 1.1a). Conventional DACs (Fig. 1.1b) operate up to 200 GPa and thousands of degrees, but the simultaneous development of double-stage DACs (ds-DACs) and improvement in laser-heating systems in recent years considerably increased the pressure limit, and recently the possibility of laser heating at 1 TPa was shown.⁷ Thus, it is not surprising that the majority of HPHT syntheses were done using the LHDAC technique.⁸

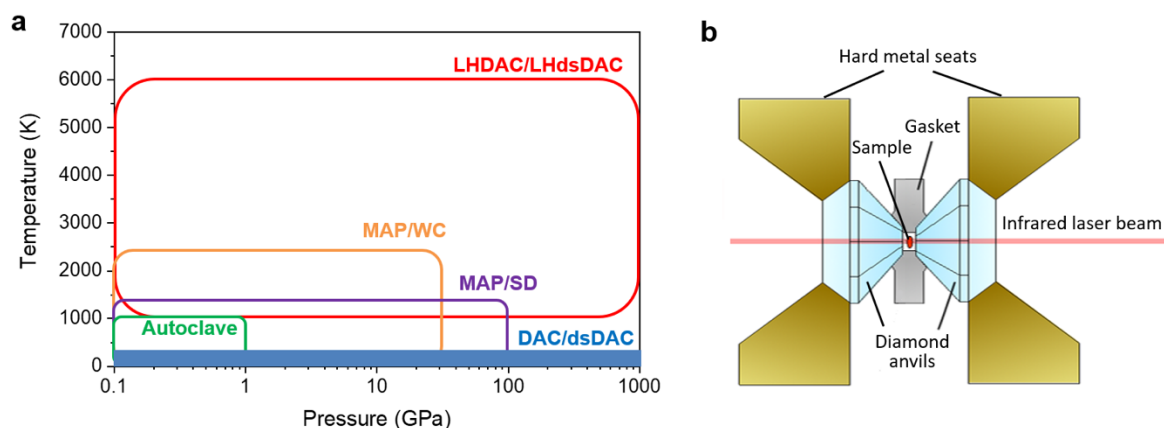


Figure 1.1. (a) Achievable pressures and temperatures of various high-pressure techniques (adapted from Mao et al.⁹). MAP/WC: multi-anvil press with tungsten carbide anvils; MAP/SD: multi-anvil press with sintered diamond anvils; dsDAC: double stage diamond anvil cell; LHDAC/LHdsDAC – laser-heated diamond anvil cell or double stage diamond anvil cell. (b) A principal scheme of a laser-heated DAC.

The LHDAC technique allows very rapid temperature quenching of the reaction products that increases the chance of obtaining kinetically stabilized metastable phases at ambient temperature. The LHDAC provides an ideal reaction chamber and is particularly useful as it allows structural studies of the novel compounds using X-ray diffraction and optical spectroscopy, and allows the recovery of the materials to ambient conditions to be followed *in situ*. This is very important because full pressure release (like in the LVP technique) may lead to a decomposition reaction of synthesized compounds. Without knowledge of phases that exist at high pressure, it is difficult to make a step towards their recovery at ambient conditions and possibly scale up the synthesis using the LVP technique.

1.2. *In situ* characterization of reaction products in LHDACs

After synthesis in LHDACs, one needs to study what has been synthesized under given P-T conditions. DAC environment limits the number of methods that can be applied to study the reaction products *in situ*. Nevertheless, the wide electromagnetic radiation transparency of diamonds still allows the investigation of materials under extreme conditions using various scattering, emission, and absorption methods. The primary *in situ* method for determining which reaction product or products were synthesized is X-ray diffraction. In most cases, this method allows accurate determination of the crystal structure of reaction products. Other complimentary spectroscopy methods such as Raman spectroscopy,¹⁰ luminescence spectroscopy,¹¹ Mössbauer spectroscopy,¹² X-ray absorption spectroscopy,¹³ and solid-state NMR spectroscopy¹⁴ can be also applied *in situ* to give more information about element composition, their valence states and coordination environment.

The laser-heating of the precursors in LHDACs results in chemical reactions, causing the appearance of hundreds of small (micron- or submicron-sized) crystallites (or grains) of one or more often several different phases. When the reaction products are studied *via* X-ray diffraction, each of these crystallites gives its own set of spotty Bragg's reflections. Thus, the diffraction pattern of the sample in LHDACs is complex and represents a superposition of single-crystal diffraction from hundreds of crystallites.

In some simple cases, when the 1D diffraction pattern contains a small number of diffraction lines and they can be easily indexed, the powder X-ray diffraction can be applied with Rietveld refinement: usually, it is the case of only one reaction product with already known crystal structure or known structure type.¹⁵ In some more complex cases, e.g. when one or two unknown phases are observed, powder X-ray diffraction data analysis including Rietveld refinement in combination with *ab initio* structure search sometimes can be successfully used.¹⁶

However, in most cases in LHDACs, the mixture of several novel phases, often having low symmetry crystal structures, is formed. Hence, the powder diffraction pattern is extremely complex with many overlapped lines. In these cases, powder X-ray diffraction data analysis, even with the help of *ab initio* structure search, is not reliable. With a small enough beam, that is available at synchrotron facilities, a powerful method of single-crystal X-ray diffraction can be applied to the multigrain samples. This method — synchrotron single crystal X-ray diffraction from multigrain samples in LHDACs — allows the direct crystal structure determination of reaction products without *a priori* crystallographic information. It was first described in detail in the PhD thesis of Elena Bykova in 2015.¹⁷ This method has many difficulties, the most crucial one is the search and sorting of single crystal X-ray diffraction reflections from different crystallites; hitherto this process has to be performed manually by a scientist. The development of a software solution to resolve this problem is of utmost importance, and it is done within this thesis and presented in Section 5.1.

1.3. High-pressure chemistry of nitrogen

1.3.1. Nitrogen inorganic compounds at ambient pressure

The chemistry of nitrogen at ambient pressure has long been thought to be very limited due to the extreme stability of triple-bonded molecular nitrogen. In inorganic solid-state compounds at ambient pressure, nitrogen does not possess the catenation (with the exception of azides): it is typically present in the form of a nitride anion N^{3-} in ionic compounds, or as distinct N atoms covalently-bonded with non-metal elements.

Nitrides represent an important class of inorganic materials that exhibit outstanding physical and chemical properties. Nitrides of the heavier main group elements are interesting primarily because of their semiconducting properties. UV/blue light emitting diode materials based on Al, Ga, and In nitrides are widely used in industry.^{18–20} Due to strong covalent networks, nitrides of light main group elements often possess high hardness and incompressibility (cubic *c*-BN, *c*-Si₃N₄).²¹ Transition metal nitrides often have exceptional hardness, high melting points, chemical stability, and resistance to oxidation and diffusion of metals. They show high electrical and thermal conductivities.²² Some transition metal nitrides possess different magnetic properties depending on the structural type in which they crystallize (*e.g.* FeN in ZnS²³ or NiAs²⁴ structure types). Some of the transition metal nitrides have a combination of useful properties, *e.g.* δ -NbN is a hard and incompressible superconductor.²⁵ This combination of properties has attracted considerable attention and resulted in numerous technical applications and theoretical investigations. During the last decades, a large number of new ternary nitrides have been discovered with many of them recently gaining increasing attention due to their promising optical and electronic properties.²⁶

1.3.2. High-pressure behavior of molecular nitrogen

In the last two decades, the application of high pressure has broken the established understanding of nitrogen chemistry. Up to 110 GPa molecular nitrogen exhibits an impressive polymorphism, with 11 experimentally observed crystalline allotropes with different arrangements of N₂ molecules.²⁷ Above 110 GPa intramolecular bonds in N₂ are weakened, and heating, breaking the kinetic barrier, leads to the formation of polymeric single-bonded nitrogen atoms networks. Currently, three crystalline polymeric nitrogen allotropes are known: cubic-gauche polymeric nitrogen (cg-N),²⁸ nitrogen with the black phosphorus structure (bp-N),²⁷ and hexagonal layered polymeric nitrogen (hlp-N),²⁹ synthesized at high temperatures and at 110–180 GPa, 124–180 GPa, and 244 GPa, respectively (Fig. 1.2).

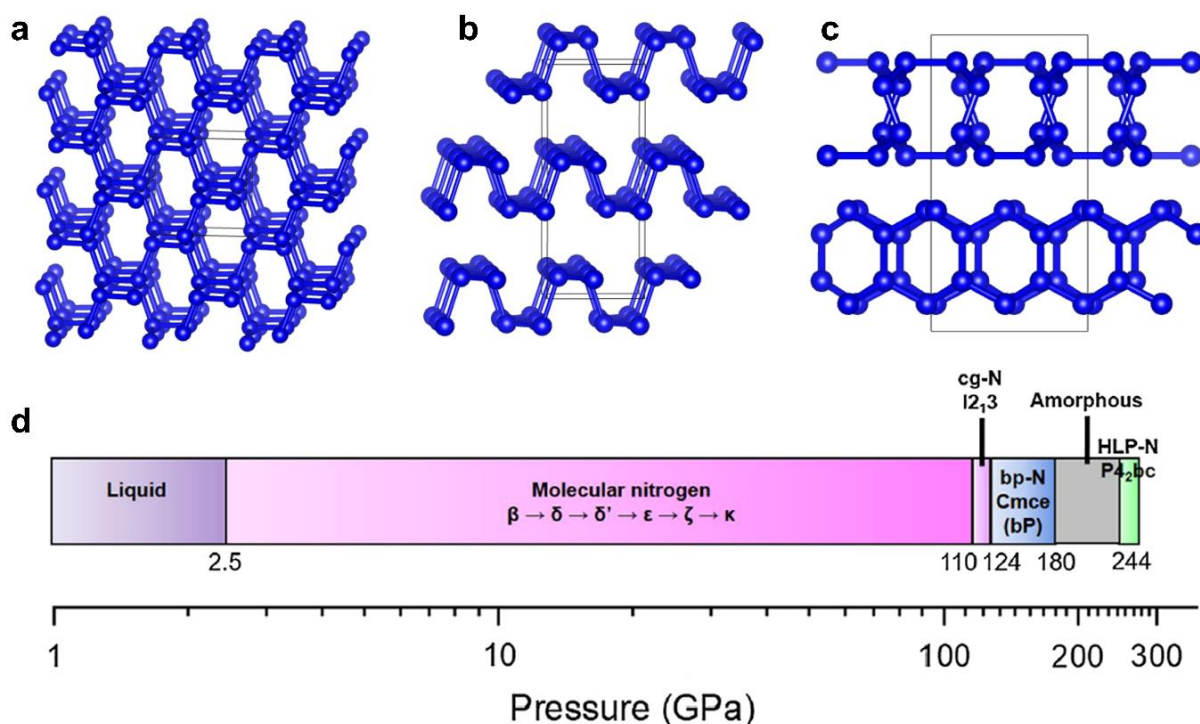


Figure 1.2. The crystal structures of polymeric nitrogen phases: (a) cg-N, (b) bp-N, and (c) hlp-N. (d) The diagram (adapted from²⁷) illustrating the experimentally observed high-pressure nitrogen phases.

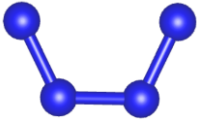
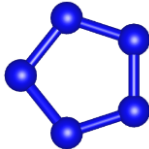
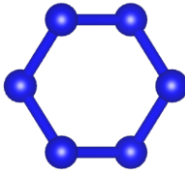
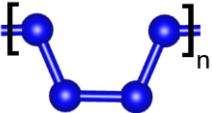
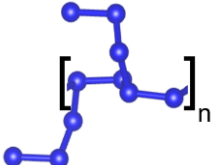
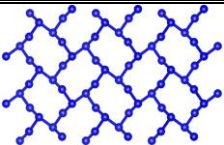
1.3.3. High-pressure binary X-N compounds

The discovery of the polymeric nitrogen allotropes cg-N, bp-N, and hlp-N triggered interest in compounds with covalent N-N bonds, whose subsequent HPHT synthesis opened a new era of nitrogen chemistry, enriched with novel compounds featuring di-, oligo-, and polynitrogen units. Pressure is a useful tool to tune nitrogen reactivity.³⁰ It turned out that nitrogen easily reacts with metals under HPHT conditions and forms various metal-nitrogen compounds featuring charged nitrogen N_2^{x-} dimers^{5,15,31-47} at low-to-mild pressures (10-50 GPa), and polynitrogen units (tetra-nitrogen horseshoe-like N_4^{4-} units,⁴⁸ pentazolate N_5^- rings,^{6,41,49,50} N_6 rings^{5,6,51}), different polymetric nitrogen chains^{48,52-58} and even polynitrogen layers⁵⁷ at mild-to-high pressures (above 50 GPa) (Table 1.1).

Some of the synthesized compounds were found to be recoverable to ambient conditions, indicating that polynitrogen chemistry exists not only under high compression. If so, conventional chemistry routes for the targeted synthesis of compounds with polynitrogen units, first discovered under high pressure, could be found. Indeed, CsN_5 containing N_5^- pentazolate ring was first synthesized under HPHT conditions by laser-heating of CsN_3 in N_2 at 60 GPa.⁵⁰ Although CsN_5 was found non-recoverable to ambient conditions, an approach to producing the pentazolate anion⁵⁹⁻⁶¹ at normal pressure was quickly developed.

The discoveries of unique nitrogen entities not only push the boundaries of fundamental nitrogen chemistry, but reveal high-pressure nitrogen compounds possessing key properties for functional applications. For example, the rhenium nitride pernitride ReN_2 , which is recoverable to ambient conditions, has an extremely low compressibility, high hardness, and metallic conductivity;⁶² a single layer of BeN_4 may become a 2D material with unique electronic properties,⁵⁷ and a variety of polynitrides with high nitrogen content are promising high-energy-density materials.⁶³

Table 1.1. Summary of experimentally observed di- and polynitrogen units and layers prior to this thesis.

N₂ dimers			
	[N ₂] ^{x-} units		
Found in:	Li ₂ N ₂ ⁴⁰ , LiN ₂ ⁴¹ , NaN ₂ ⁴² , CaN ₂ ⁴³ , SrN ₂ ⁴³ , BaN ₂ ⁴³ , Na ₃ (N ₂) ₄ ⁴² , K ₃ (N ₂) ₄ ⁵ , Ca ₃ (N ₂) ₄ ⁴⁴ , Sr ₃ (N ₂) ₄ ⁴⁴ , Ba(N ₂) ₃ ⁴⁴ , TiN ₂ ⁴⁵ , VN ₂ ⁴⁶ , CrN ₂ ⁴⁷ , FeN ₂ ³¹ , CoN ₂ ³¹ , NiN ₂ ^{15,32} , CuN ₂ ³³ , RuN ₂ ³⁴ , RhN ₂ ^{35,36} , PdN ₂ ³⁷ , OsN ₂ ³⁸ , IrN ₂ ^{38,39} , PtN ₂ ³⁹		
isolated polyN units			
	[N ₂] ⁴⁻ units	[N ₅] ⁻ and [N ₅] ²⁻ rings	armchair [N ₆] ⁶⁻ rings and planar [N ₆] ²⁻ and [N ₆] ⁴⁻
Found in:	Mg ₂ N ₄ ⁴⁸	LiN ₅ ⁴¹ , NaN ₅ ⁴⁹ , CsN ₅ ⁵⁰ , Na ₂ N ₅ ⁴⁹ , K ₉ N ₅₆ ⁶	WN ₆ ⁵¹ , K ₂ N ₆ ⁵ , K ₉ N ₅₆ ⁶
polyN chains			
	[N ₄] ²⁻ _∞ Polynitrogen chain		[N ₁₀] ¹⁰⁻ _∞ branched polynitrogen chain
Found in:	tr-BeN ₄ ⁵⁷ , MgN ₄ ⁴⁸ , CoN ₅ ⁵² , FeN ₄ ⁵⁴ , ZnN ₄ ⁵⁸ , ReN ₈ ·xN ₂ ⁵³ , WN ₈ ·N ₂ ⁵⁵ , Os ₅ N ₂₈ ·3N ₂ ⁵⁵ , Hf ₄ N ₂₀ ·N ₂ ⁵⁵ , Hf ₂ N ₁₁ ⁵⁵ ,		TaN ₅ ⁵⁶
polyN layers			
	polynitrogen layers consisting of fused N ₁₀ rings		
Found in:	m-BeN ₄ ⁵⁷		

Nitrogen high-pressure chemistry is not limited to reactions of nitrogen with metals only. The binary nitrogen–non-metals systems have also been studied under HPHT conditions.

For example, novel high-pressure nitrides of non-metal elements of the 14th (c-Si₃N₄,⁶⁴ SiN₂⁶⁵; C₃N₄, CN, and CN₂⁶⁶), 15th (PN₂, P₃N₅,⁶⁷ AsN,⁶⁸ Sb₃N₅⁶⁹), 16th (SN₂⁷⁰), and 18th (Xe(N₂)₂⁷¹) groups of the Periodic system have been reported.

Despite the huge progress in the exploration of X-N systems under high pressure during the last decade, there are still many blind spots (*e.g.* nitrogen-halogen systems, nitrides of 13th group, and rare-earth nitrides) and our knowledge about nitrogen high-pressure chemistry is far from being complete. Numerous computational studies based on *ab initio* crystal structure search predict the stabilization of many exotic X-N compounds under high pressure with unique crystal chemistry and physical properties.^{63,72–77}

Rare-earth nitrides at ambient conditions present as a series of LnN compounds (Ln = Sc, Y, La-Lu) with the rock salt type structure. Under high pressure, their compressional behavior and phase transitions were studied,⁷⁸ however, synthesis of rare-earth di- or polynitrides has never been carried out. Since polynitrides are often considered as high-energy-density materials, where the low molecular weight of the compound is important, polynitrides of scandium and yttrium — the lightest rare-earth elements — would be the most promising for that application. Indeed, there are several theoretical studies,^{79–82} where nitrogen-rich phases with ScN₃, ScN₅, ScN₆, and ScN₇ compositions have been predicted to be stable under 30-110 GPa and may serve as high-energy-density materials. Among Y-N polynitrides, YN₅, YN₈, and YN₁₀ with polynitrogen chains, fused N₁₈ rings, and isolated N₅ rings, respectively, were predicted to be stable near 100 GPa and are all promising prospects as high-energy-density materials.⁸³ Thus exotic Y-N and Sc-N compounds under high pressure with promising physical properties comprised of unique oligo- and poly-nitrogen anions are expected. Sections 5.2-5.4 of this thesis are dedicated to high-pressure studies of Y-N and Sc-N up to megabar pressures.

1.3.4. High-pressure ternary metal-C-N compounds

While the high-pressure chemistry of binary X-N systems has already gained the attention of scientists, the high-pressure chemistry of ternary systems, such as metal-C-N for example, is almost unknown. Inorganic ternary metal-C-N compounds with covalently bonded C-N anions encompass important classes of solids. At ambient conditions, the most investigated classes are cyanides (CN⁻)^{84,85} and carbodiimides (NCN²⁻)^{86–92}, although more complex anions (*i.e.* dicyanamides,^{93,94} tricyanomethanides,⁹⁵ and acetonitriletriide⁹⁶) are known. Inorganic cyanides have applications in gold mining, metal finishing, electroplating⁹⁷ and also can be used as reactants and/or catalysts in organic syntheses.⁹⁸ Inorganic carbodiimides exhibit interesting optical properties, making them useful in optoelectronics and photonics^{86–88} and have a

potential for energy storage and conversion, *e.g.* as electrode materials for lithium-ion batteries, fuel cells, and supercapacitors.^{89–92} While CN^- and CN_2^{2-} anions are well-known, the next members of this anionic series — *i.e.* the CN_3^{5-} anion, a derivative of guanidine, and CN_4^{8-} , a derivative of hypothetical tetraaminomethane — have not been discovered yet, although discussed in the literature.^{99,100}

The carbon coordination number increase can be expected under high pressures. Therefore, the stabilization of the abovementioned CN_3^{5-} and CN_4^{8-} anions or even more complex oligo- and poly-anionic species might be expected at high enough pressures. However, hitherto, high-pressure studies on metal-C-N systems are limited to the investigation of phase transitions in known compounds at relatively low pressures. For example, the polymorphism of KCN, $\text{Zn}(\text{CN})_2$, and $\text{Co}(\text{N}(\text{CN})_2)_2$ compounds was studied up to 2.2, 5.1, and 3.6 GPa, respectively.^{101–103} Thus, the application of mild and high pressures for the synthesis of novel carbonitrides featuring yet unknown structural units is enticing. Sections 5.5 and 5.6 of this thesis are dedicated to high-pressure synthesis of lanthanide carbonitrides at high pressures.

2. Methods

2.1. Generation of extreme conditions

2.1.1. Pressure generation in DACs

Pressure, defined as $P = \frac{F}{A}$, can be increased by either maximizing the force (F) or minimizing the area (A). The former approach is employed in piston-cylinder¹⁰⁴ and multi-anvil apparatuses,¹⁰⁵ using large devices to apply significant force to larger samples (0.1 to 1 cm). In contrast, diamond anvil cells (DACs) use the latter approach, reducing the sample area to around 10-100 μm to achieve high pressure.

The fundamental concept behind pressure generation in the DAC involves compressing the material between the flat tips (culets) of two gem-quality diamond anvils precisely driven against each other. Although various DAC designs have emerged over recent decades, the core idea remains consistent, with different DAC types sharing similar fundamental features. A typical DAC (Fig. 2.1a) comprises a metal body with a pair of seats, diamond anvils precisely positioned on them, and a metallic gasket with a circular hole placed between the anvils.

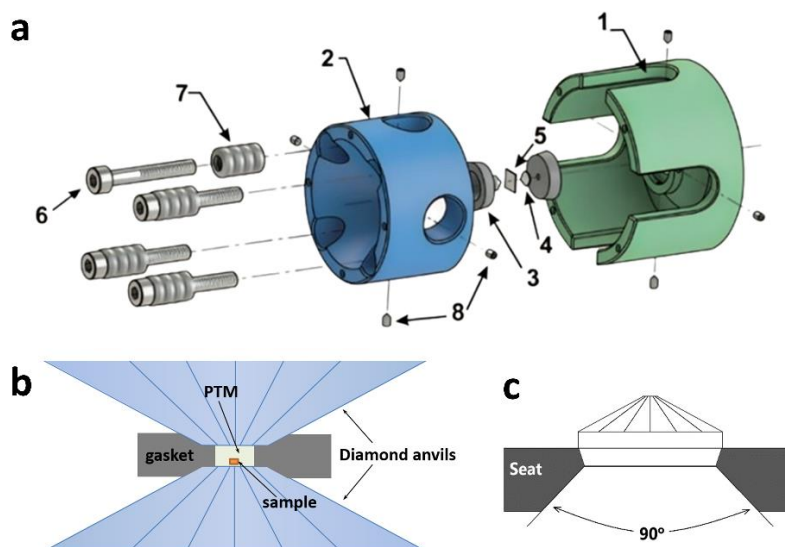


Figure 2.1. (a) BX90-type diamond anvil cell (modified after ¹⁰⁶): (1) outer cylinder part, (2) inner piston part, (3) seats, (4) diamond anvils, (5) metallic gasket, (6) screws for generating loading force, (7) pack of conical spring washers, (8) setscrews for diamond anvils alignment. (b) Schematic diagram of a sample chamber. (c) Boehler-Almax designed diamond anvil and seat for X-ray diffraction experiments.

Seats are typically made of hard materials like tungsten carbide, which transfer external load to the diamond anvils. A metallic gasket with a circular hole is placed between the diamond tips, forming a cylindrical chamber (Fig. 2.1b). This configuration enables the

confinement of the sample position during compression and redistributes uniaxial stress when filled with a (soft) pressure-transmitting medium. Metallic gaskets are usually made from metals or alloys that are chemically inert under ambient conditions. In the studies discussed below, all gaskets were made from rhenium, a 5d transition metal known for its high bulk modulus (over 350 GPa), shear modulus (over 180 GPa), and melting point of 3453 K.^{107,108}

The essential part of DAC is a pair of polished single crystals of diamonds, which serve as the diamond anvils. The size of the diamond anvil culet can range from approximately a millimeter to tens of micrometers, playing a key role in setting the upper limit of attainable pressure. Smaller culets enable the attainment of higher pressures but come with the restriction of the studied sample size.

The combination of the diamond cut's geometry, seat shape, and the aperture of the metallic body can be different and depends on the experiment needed. For single crystal X-ray diffraction experiments involving sample rotation, a large opening of the DAC body, large aperture diamond anvils and seats are essential (Fig. 2.1c). In this thesis, the large aperture BX90-type¹⁰⁶ DACs equipped with Bohler-Almax type diamonds¹⁰⁹ were used. The culet diameters ranged from 80 to 250 μm . Specifically, anvils with 250 μm culet diameters were used for pressures up to 50 GPa, 120 μm culets for pressures up to 100 GPa, and 80 μm culets for pressures above 100 GPa.

2.1.2. Pressure transmitting media

By definition, the DAC is a uniaxial compression device. To achieve hydrostatic or quasi-hydrostatic conditions a pressure-transmitting medium (PTM) is used (Fig. 2.1b). PTM fills the sample chamber, surrounding the sample to ensure hydrostatic or quasi-hydrostatic stress transmission from the diamond anvils. In order to achieve hydrostatic conditions, true fluids—gases or liquids—should be used as PTM. Unfortunately, the solidification of fluids inevitably occurs at some pressure. The solidification pressures of the gases He, Ne, Ar, and N₂, commonly used as PTM, are 12.1 GPa, 4.8 GPa, 1.4 GPa, and 2.4 GPa, respectively, at room temperature.¹¹⁰ Known liquids, including alcohol mixtures and paraffin oil, solidify at ambient temperature under pressures exceeding ~10-15 GPa.^{110,111}

Ideal solid PTM should possess relatively low bulk and shear moduli and, ultimately, low tensile strength. Certain materials, such as solidified gases (He, Ne, Ar, N₂), satisfy these criteria and can be employed. Besides facilitating uniform pressure distribution, PTMs often serve as pressure gauges (e.g., Ne, Ar), or participate as reactants in chemical reactions under extreme conditions (e.g., paraffin oil, O₂, N₂). Gases can be loaded into the DAC sample

chamber using a high-pressure gas loading apparatus¹¹² or cryogenically,¹¹³ while solid and liquid PTMs can be loaded manually under a microscope.

In the present thesis, nitrogen was used as a PTM as well as a chemical precursor. Molecular nitrogen N₂ was loaded using a gas-loading system,¹¹² where the gas was pumped (up to 1.4 kbar) into the vessel with a DAC. Upon releasing the external gas pressure, the DAC was sealed by manually tightening the screws in the piston-driving mechanism.

2.1.3. Pressure determination

Pressure determination in the DAC sample chamber is a crucial aspect of any DAC experiment. There are three well-established pressure scales commonly used for this purpose:

1. **Equation of state (EoS) of a standard material.** A standard material with the well-known EoS is loaded into the sample chamber along with the sample. By measuring the unit cell volume *via* XRD one can compare it to the values reported in the literature. Common EoS standards include metals (Au, Pt) or simple binary compounds (MgO, NaCl, KCl, KBr).^{114–116} Additionally, the PTM (*e.g.* Ne after solidification¹¹⁵) or gasket material (*e.g.* Re¹⁰⁷) can also serve as pressure markers.

2. **Ruby fluorescence scale.** This scale is based on the shift of the R₁ fluorescence line of ruby (Cr-doped α -Al₂O₃) as a function of pressure.¹¹⁷ A ruby piece is loaded into the sample chamber alongside the sample, and the shift in the fluorescence line is used to determine the pressure.

3. **Diamond anvil Raman gauge.** This scale is based on the shift of the high-frequency edge of the Raman band of diamond anvil since it is correlated with the normal stress at the anvils' culet face. The calibration of the diamond Raman edge frequency against the equation of state of Pt up to 310 GPa allows using it for pressure determination.¹¹⁸

In the present thesis, the pressure in the DACs was determined using the Raman signal from the diamond anvils¹¹⁸ and additionally monitored by the X-ray diffraction signal of the Re gasket edge using rhenium's equation of state.¹⁰⁷

2.1.4. Temperature generation in DACs

The transparency of diamonds to a broad range of electromagnetic radiation is a significant advantage in DAC experiments, simplifying sample observation and probing. This allows high-power laser beams to focus on the sample while keeping diamond anvils unharmed¹¹⁹. Laser wavelength selection depends on sample absorption characteristics, with CO₂-based infrared ($\lambda = 10.6 \mu\text{m}$ ¹²⁰) and Nd:YAG near-infrared lasers (NIR, $\lambda \sim 1064 \text{ nm}$ ¹²¹) being

common. NIR lasers are ideal for heating non-transparent materials, while transparent materials are heated by CO₂ infrared lasers.

In the present thesis, a portable double-sided laser-heating setup,¹²² enabling *in situ* temperature determination, was used in the experiments (Fig. 2.2). The temperature during the laser heating was determined by fitting of sample's thermal emission spectra to the grey body approximation of Planck's radiation function in a given wavelength range (570–830 nm).

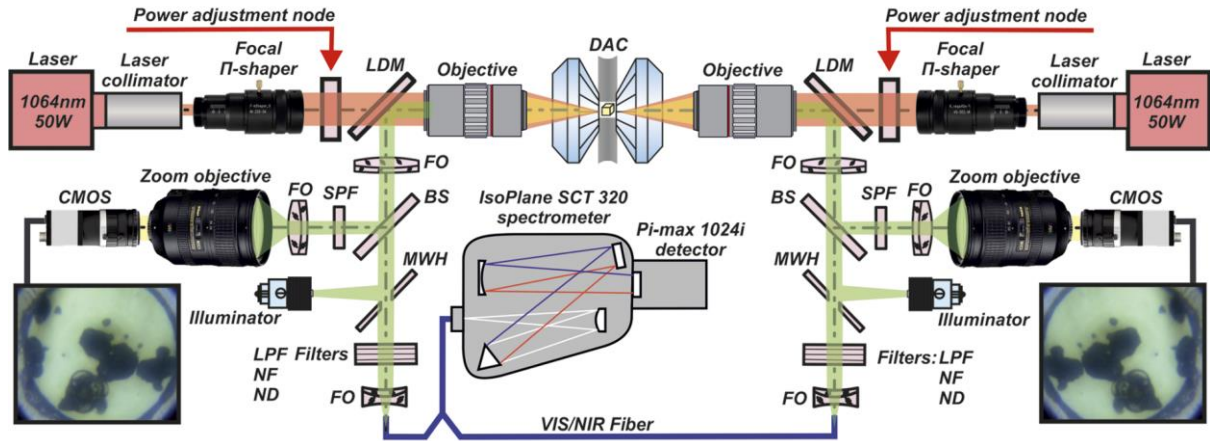


Figure 2.2. Schematic diagram of the double-sided laser heating system for diamond anvil cells. LDMs are the long-pass dichroic mirrors; FOs are the focusing optics; BSs are 50/50 beam splitters; SPFs are the short-pass filters with a cutoff at 800 nm; CMOSs are the cameras for optical observation; MWHs are the mirrors with a hole; LPFs are the long-pass filters with a cut-on wavelength of 550 nm; NFs are the notch filters at 1064 nm; and NDs are neutral density filters. The illustration is reprinted from¹²², with the permission of AIP Publishing.

2.2. X-ray diffraction in LHDACs

2.2.1. Basic principles

X-ray diffraction (XRD) is the phenomenon where X-ray photons undergo elastic scattering by the electrons of atoms. The wavelengths of X-ray photons fall within the angstrom range (0.1 – 100 Å), a scale relevant to the interatomic distances in a solid's crystal structure. Consequently, incident monochromatic X-rays that are in phase, when scattered from a long-range ordered crystal structure, can be constructively or destructively interfered. The condition for constructive interference is described by Bragg's law:

$$2d_{hkl} \cdot \sin(\theta) = n\lambda$$

where d_{hkl} is the spacing between a diffracting family of hkl crystallographic planes, θ is the angle of the incident X-ray, n is an integer number, and λ is the wavelength of the X-ray beam (Fig. 2.3).

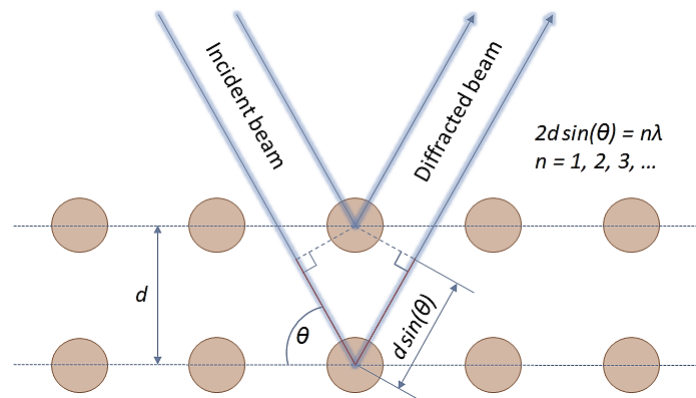


Figure 2.3. Schematic illustration of Bragg’s law. Incident X-rays approach parallel atomic planes in a crystal, and the diffracted X-ray beam scattered from the lower plane traverses an additional path length of $2d \cdot \sin(\theta)$. Constructive interference occurs when this path difference is equal to an integer multiple of the wavelength.

By illuminating the crystalline matter with a monochromatic X-ray beam, one registers a diffraction pattern. When performing XRD experiments, the wavelength of the X-ray beam is known and the diffraction angle is measured. Traditionally, XRD is divided into two main approaches: single-crystal XRD (SCXRD) and powder XRD (PXRD). Typical SCXRD patterns feature diffraction reflections (or Bragg spots) (Fig. 2.4a). As Bragg conditions for a given d -spacing and wavelength are met only at defined θ -angles, the crystal should be irradiated in various orientations with respect to the incident beam to ensure proper measurement of all reflections. PXRD involves working with polycrystalline samples, consisting of randomly oriented fine grains. Since there are thousands or even millions of grains (crystallites) in an irradiated part of a polycrystalline sample, there are always a bunch of grains that fulfill the Bragg equation for each d -spacing. This results in Debye-Scherrer rings in the diffraction pattern (Fig. 2.4b). Both techniques — PXRD and SCXRD — can be performed (1) using lab diffractometers, where X-rays are generated by X-ray tubes, or (2) at synchrotron facilities, where X-rays are produced by the accelerated movement of relativistic electrons. Synchrotron facilities have one significant advantage: the intensity of X-rays is several orders of magnitude higher than those generated by X-ray tubes.

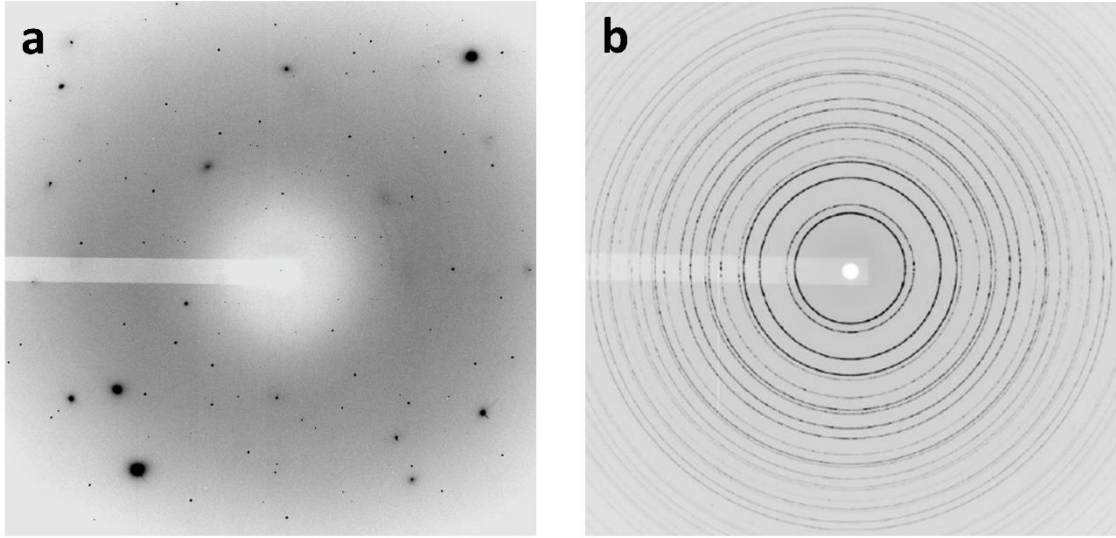


Figure 2.4. XRD patterns collected using a 2D detector produced by (a) a single crystal or (b) a powder.

Based on the positions of the diffraction line (in the case of PXRD) or reflection (in the case of SCXRD) in the diffraction pattern and applying Bragg's law, the corresponding interplanar distances (d -spacings) can be calculated. After indexing, *i.e.* assigning Miller indices (hkl) to each line/reflection in the diffraction pattern, the lattice parameters ($a, b, c, \alpha, \beta, \gamma$) can be determined. The most general formula representing this relationship, applicable to crystals of all symmetries, is:

$$\frac{1}{d_{hkl}^2} = \frac{T_{11}h^2 + T_{22}k^2 + T_{33}l^2 + 2T_{12}hk + 2T_{13}hl + 2T_{23}kl}{V^2}$$

where:

$$T_{11} = b^2c^2\sin^2\alpha$$

$$T_{22} = a^2c^2\sin^2\beta$$

$$T_{33} = a^2b^2\sin^2\gamma$$

$$T_{12} = abc^2(\cos\alpha \cdot \cos\beta - \cos\gamma)$$

$$T_{13} = ab^2c(\cos\alpha \cdot \cos\gamma - \cos\beta)$$

$$T_{23} = a^2bc(\cos\beta \cdot \cos\gamma - \cos\alpha)$$

$$V = abc\sqrt{1 - \cos^2\alpha - \cos^2\beta - \cos^2\gamma + 2\cos\alpha \cdot \cos\beta \cdot \cos\gamma}$$

In the case of a crystal with symmetry higher than triclinic, this formula simplifies. Additionally, by analyzing the systematic absences in the diffraction pattern, the space group (or at least a limited number of possible space groups) can be determined.

While the position of diffraction lines/reflections provides information about the lattice parameters, the intensities of these lines/reflections reveal the electron density distribution within the unit cell. This forms the basis for crystal structure determination, as electron density distribution can be transformed into information about atom types and their positions within the unit cell. SCXRD is the most powerful technique for this purpose, as it allows the extraction of the intensities of each distinct hkl reflection. The intensities of Bragg reflections (I_{hkl}) are proportional to the square of the structure factor (F_{hkl}) amplitude: $I_{hkl} \propto |F_{hkl}|^2$.

The structure factor is the Fourier transform of the electron density, ρ_{xyz} , taken over the whole unit cell, and hence it holds information about the types of atoms and their positions within the unit cell. In the static spherical atom approximation, the structure factor can be represented as:

$$F_{hkl} = \sum_j f_j \cdot \exp[2\pi i \cdot (hx_j + ky_j + lz_j)]$$

where the summing is carried out for the atoms within the unit cell; hkl are Miller indices of a given Bragg reflection; x_j, y_j, z_j are the coordinates of the j^{th} atom and f_j is the scattering factor of the j^{th} atom (tabular value).

In real crystals, atoms undergo thermal motion and may have an occupancy smaller than one. Taking that into account, the structure factor can be written as:

$$F_{hkl} = \sum_j a_j \cdot \exp\left[-8\pi^2 U_j^2 \cdot \left(\frac{\sin(\theta)}{\lambda}\right)^2\right] \cdot f_j \cdot \exp[2\pi i \cdot (hx_j + ky_j + lz_j)]$$

where a_j is the occupancy of the j^{th} atom, while $\{\exp[-8\pi^2 U_j^2 \cdot (\frac{\sin(\theta)}{\lambda})^2]\}$ is a Debye-Waller temperature factor, where U_j is a mean square isotropic displacement of the j^{th} atom, θ is the scattering angle and λ is the X-ray wavelength.

The structure factor is always a complex number which can be represented as $F_{hkl} = |F_{hkl}| \cdot \exp(i\varphi_{hkl})$, where $|F_{hkl}|$ is the amplitude and φ_{hkl} is a phase. Knowing the structure factors, the electron density distribution in the unit cell can be obtained using the inverse Fourier transform. The electron density in an xyz position inside the unit cell (ρ_{xyz}) can be derived *via* the following equation:

$$\rho_{xyz} = \frac{1}{V} \sum_{hkl} F_{hkl} \cdot \exp[-2\pi i \cdot (hx + ky + lz)]$$

where V is the unit cell volume, and the sum is over all the crystal lattice planes characterized by Miller indices.

Measuring the intensities of Bragg reflections in diffraction experiments, the values of $|F_{hkl}|$ structure factor amplitudes can be derived. However, the information about φ_{hkl} phase can not be derived from the experiment. Hence, the direct determination of the φ_{hkl} phase is unfeasible, which is well-known as the “phase problem”.¹²³ Many methods have been developed to overcome the phase problem such as the Patterson syntheses, direct methods, charge-flipping algorithms, dual-space methods and others.^{124,125} Nowadays these methods are implemented as automated procedures in software for crystal structure solution and refinement. Using any of these methods, it becomes possible to establish the distribution of electronic density and complete the initial structural model. At the subsequent stage, the structural model undergoes refinement against the experimental dataset through a least-squares minimization, adjusting parameters such as atomic coordinates, occupancies, and thermal displacement parameters.

2.2.2. XRD experiments in LHDAC: features and limitations

Compared to a routine XRD experiment at ambient conditions, the application of this technique for LHDACs is more complex.

The first bunch of difficulties refers to DAC itself. Firstly, the sample environment gives an additional XRD signal coming from (1) diamond anvils, (2) gasket material, and (3) the solidified pressure-transmitting media. All these parasitic reflections contaminate the signal of interest from a sample. Second, the metallic body of a DAC restricts angles, at which the sample can be irradiated. This problem is not that important in the case of PXRD, but affects a lot the quality of SCXRD data worsening the statistics on the collected data. The third issue is the size of a sample: for the DAC experiments at pressures higher than 40 GPa, the sample size is usually about 10-20 μm , and at megabar pressures and above, sample dimensions do not exceed 3-5 μm . This, of course, imposes strong requirements for (1) the intensity and size of the X-ray beam and (2) the goniometer’s and sample stage motors’ precision as well as reproducibility of movement for aligning the sample to the X-ray beam. Talking about SCXRD, it still can be applied at lab diffractometers to relatively big single crystals at low pressures in DACs. However, for smaller samples at higher pressures, the synchrotron high-brilliance X-ray beam focused down to 1-5 μm in diameter is the only option.

Another difficulty corresponds to laser heating. The laser-heating of the precursors results in chemical reactions, causing the appearance of dozens/hundreds of small (micron- or submicron-sized) crystallites of one or more often several different phases. Each of these crystallites would act as a single crystal and give its own set of spotty Bragg’s reflections. Thus,

the diffraction pattern of the sample in LHDACs (Fig. 2.5) is usually in between the typical XRD patterns produced by a single crystal (Fig. 2.4a) and a powder (Fig. 2.4b).

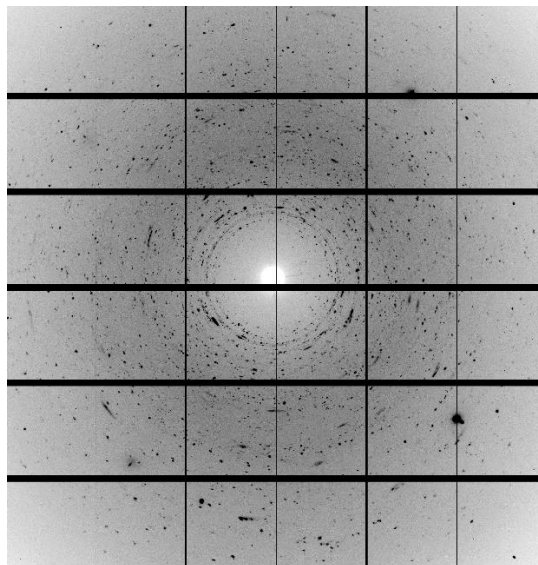


Figure 2.5. 2D XRD pattern collected from a typical multigrain sample in the LHDAC.

Due to the development of 3rd and 4th generation synchrotrons during the last decades, current cutting-edge XRD beamlines provide high-brilliance X-ray beams that can be focused down to nanosize. Taking into account the goniometer's and sample stage motors' precision it is reliably possible to work with X-rays focused down to $0.5 \times 0.5 \mu\text{m}^2$ FWHM. That size becomes commensurate with the size of crystallites (grains or crystalline domains) of polycrystalline samples making it possible to study each micron- to submicron-size grain individually by methods of SCXRD. This method — synchrotron SCXRD from multigrain samples in LHDACs — is the main experimental method used in the studies summarized in this thesis. Below its full methodology — from data collection to crystal structure solution and refinement — is presented.

2.2.3. Synchrotron SCXRD from multigrain samples in LHDACs: data collection

1. Beamline setup and calibration for powder and single-crystal XRD data

In this thesis, the high-pressure X-ray diffraction studies were done at ID11, ID15b, and ID27 beamlines of ESRF (Grenoble, France), P02.2 beamline of DESY (Hamburg, Germany), and 13IDD beamline of APS (Lemont, USA). The principal configuration of all beamlines for XRD high-pressure studies is essentially the same and consists of the following components (Fig. 2.6): (1) X-ray optics which provide a tightly collimated and focused monochromatic X-ray beam, (2) motorized sample stage with at least three x , y , z motors (usually x direction is set as a direction of the X-ray beam) and rotation ω motor, (3) DAC holder, and (4) 2D detector.

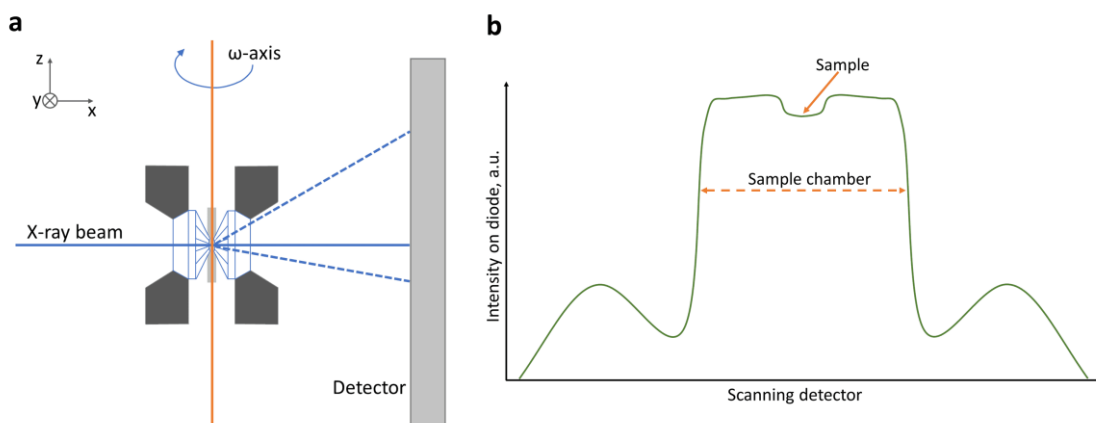


Figure 2.7. A scheme of the XRD experiment in a diamond anvil cell on synchrotron facilities. (a) The experiment geometry (modified after ¹²⁷); (b) an illustration of the absorption profile acquired during the alignment procedure.

The second step — the positioning of the DAC on the rotation axis — is established through triangulation (Fig. 2.8). Normally the ω rotation axis is initially aligned with the primary beam, and therefore only alignment along the x -direction is needed and can be achieved by scanning the sample in a horizontal direction at two different ω positions ($-\omega$ and ω). The correction must be applied using the x -translation motor above the ω -axis with the formula:

$$\Delta x = \frac{d}{\sin(\omega)}$$

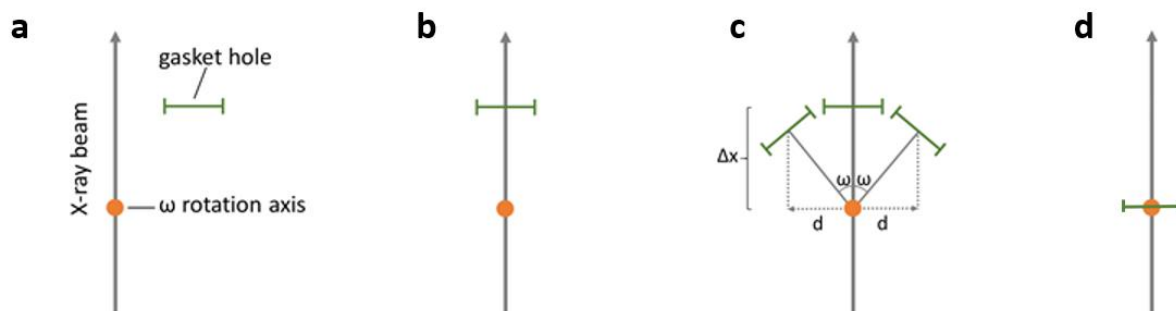


Figure 2.8. A typical process of sample centering shown in the projection along a z -axis (modified after ¹²⁷). (a) Initial state: the gasket hole is away from the X-ray beam and ω -rotation axis. (b) The state after alignment step #1: the center of the sample chamber is under the beam. (c) Alignment procedure of the step #2. (d) The state after alignment step #2: the gasket hole is aligned with the primary beam and with the ω axis.

3. Two-dimensional X-ray mapping of a sample in the DAC

To identify the optimal spots for single-crystal XRD data collection and further obtain information about the distribution of different phases, a 2D map of diffraction still images can be generated. The user sets up a script that moves the sample in small steps along the y - and z -directions. The size of the map is selected to cover the whole area of interest, while the step size along the y - and z -directions is usually selected to be equal to the size of the beam along

corresponding directions. At each step, a still XRD image (without rotation around ω -axis) is collected. Then this set of images can be analyzed in the XDI software¹²⁸, which allows to construct the contrast maps based on the intensity at the specific 2θ angle. Phase analysis can be done in the Dioptas program¹²⁹.

4. SCXRD data collection

The SCXRD is then measured in the selected points. For that DAC is rotated around the vertical goniometer axis ω with the frames being collected within the opening angle of the DAC – usually from $\omega = -36^\circ$ to $\omega = 36^\circ$ with a step of $\Delta\omega = 0.5^\circ$. As a result, one gets a dataset composed of 144 frames, that can be processed in crystallographic packages such as CrysAlis^{Pro}.

2.2.4. Synchrotron SCXRD from multigrain samples in LHDACs: data processing

1. Image conversion and calibration

In this thesis CrysAlis^{Pro} package was used for the single-crystal data processing: peak hunting, indexing, data integration, frame scaling, and absorption correction. First, the images registered by the detector should be converted to the .esperanto CrysAlis^{Pro} format files. Currently, this step is done automatically at each of the used beamlines. Second, before the dataset processing, the calibration file containing instrumental model parameters should be loaded.

2. Peak hunting

After loading a dataset (set of ~144 frames, collected with a step of $\Delta\omega = 0.5^\circ$), we perform a standard peak search procedure as implemented by CrysAlis^{Pro} program. At the end of this procedure, CrysAlis^{Pro} creates a peaktable, containing cartesian coordinates, d-spacing, and preliminary intensity of each found reflection. The peaktable contains the peaks from all crystalline phases, which are present in the collected dataset. These can be reaction products, initial reagents, pressure-transmitting medium, diamonds, gasket material, etc. To visualize the peaktable, we make a reconstruction of the peaktable in the reciprocal space.

3. Unit cell finding

The next step for the user involves identifying the unit cell(s) of the phase(s) of interest. This is the most important and most difficult step in the data analysis. The standard unit cell finding algorithms are not able to find the diffraction peaks from one distinct crystallite out of “big cloud of reflections” originating from many crystallites of phases of interest as well as parasitic diffraction reflections arising from diamonds, the gasket and the PTM. Until

recently, this step was done manually by inspecting all reflections in the reciprocal space viewer. One should have manually noticed a pattern-arranged set of reflections making a reciprocal lattice (Fig. 2.9a). Usually, it was done by finding several rows of equidistant reflections along one direction (Fig. 2.9b). Then CrysAlis^{Pro} unit cell search can index this set of reflections, determining the unit cell parameters and orientation matrix as well as finding other reflections (not found manually) belonging to this lattice (Fig. 2.9c). Of course, such a manual procedure requires (1) a lot of time and (2) enough expertise. Also, manually it is never possible to find all reciprocal lattices, and therefore some phases can be missed during this analysis.

Some progress in simplification of this search was made by Egor Koemets and Maxim Bykov at the University of Bayreuth.¹³⁰ They created a script, that allows to remove some of the parasitic reflections (originating from diamonds, gasket etc.) from the dataset. It is now implemented in CrysAlis^{Pro} as an ‘Advanced filtering’ function. Application of this function helps to clean up the dataset from the “trash” reflections. But still, the manual search for one reciprocal lattice out of dozens or hundreds of reciprocal lattices presented in a multigrain dataset is an extremely challenging task.

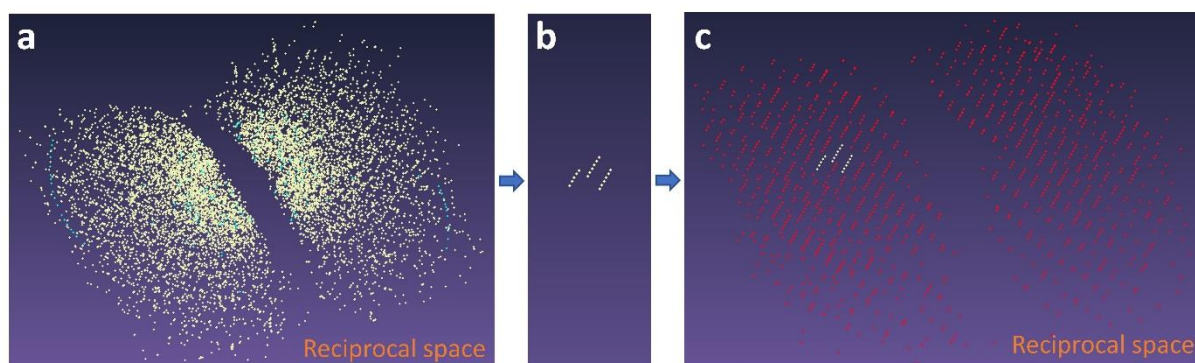


Figure 2.9. Manual search of the reciprocal lattices. (a) SCXRD data from a sample in a LHDAC represented in the reciprocal space (cyan color highlights parasitic reflections filtered by the ‘Advanced filtering’ function). (b) A manual search of several rows of equidistant reflections along one direction. (c) The final reciprocal lattice found by CrysAlis^{Pro}.

In this thesis, the automatization of the manual reciprocal lattice search is achieved using the Domain Auto Finder (DAFi) program, which was developed as part of this work (Fig. 2.10). The latest version of DAFi program (v2.2.1) is compatible with CrysAlis^{Pro} (Rigaku) and APEX4 (Bruker) crystallographic software packages. The next steps 4 and 5 can be applied to each of found domains. Usually, the crystal structures of the best crystallites (that have the highest number of reflections) of every found phase are solved.

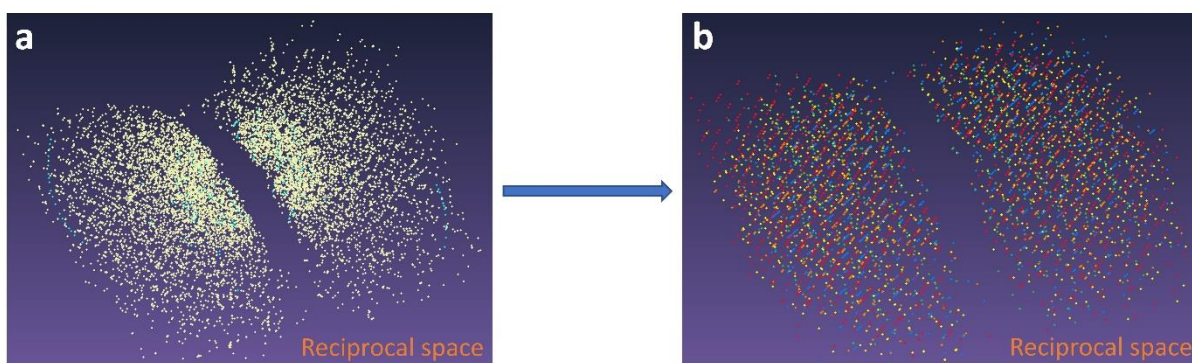


Figure 2.10. Automated search of the reciprocal lattices using the DAFi program. (a) SCXRD data from a sample in a LHDAC represented in the reciprocal space (cyan color highlights parasitic reflections filtered by the ‘Advanced filtering’ function). (b) Five reciprocal lattices found by DAFi (marked with different colors).

4. Data reduction and finalization

Once the single unit cell is found and indexing is done the standard procedure of conventional single-crystal XRD data processing can be applied.

With a given unit cell and orientation matrix (UB-matrix), a procedure of extraction reflection intensities from the images (*data reduction*) can be started. In CrysAlis^{Pro} the data reduction is performed in two stages. In the first step, the program predicts the positions of the reflections based on the UB-matrix, then it analyses partial reflections (whose profile is split over several frames) and reconstructs the reflection shape in the scanning direction. In the second stage, the program extracts reflection intensities based on the reflection shape and the background level. By default after the data reduction the program applies frame scaling, and absorption corrections and searches for a space group by an analysis of systematic absences (*data finalization*).

The user examines the data quality by reviewing the frame scaling curve and confidence values provided by the program:

- $F_{obs}^2/\sigma_{int}(F_{obs}^2)$, that indicates a signal-to-noise ratio,
- $R_{int} = \frac{\sum|F_{obs}^2 - \langle F_{obs}^2 \rangle|}{\sum F_{obs}^2}$, quality of merging intensities of the symmetry-equivalent reflections.

Here F_{obs}^2 is reflection intensity corrected for Lorentz-polarization, $\sigma_{int}(F_{obs}^2)$ is its standard deviation and $\langle F_{obs}^2 \rangle$ is its average value over all measured equivalents. If the integration is of dissatisfied quality, it is possible to rerun the procedure with adjusted parameters that influence the treatment of detector images, involving background correction, masking of reflections, integration range, etc. At this stage, the user can reveal non-optimized parameters of SCXRD data collection, e.g. bad alignment of the grain versus ω rotation axis and too low or too high

acquisition time per frame. In this case, one needs to recollect SCXRD data with better alignment or/and optimized parameters of acquisition.

After data finalization, the software produces several output files (the most important ones: .hkl, .ins, .p4p .cif) containing information about all observed hkl reflections with structural amplitudes F_{hkl}^2 and the standard deviations, wavelength, unit cell parameters, and space group. These files are then used by a separate structure solution program.

5. Structure solution and refinement

The files produced in the previous step (reflection files and instruction files) are subsequently imported into structure solution software. In the current thesis, the JANA2006¹²⁵ and OLEX2¹³¹ are used. In both programs a direct method for crystal-structure determination implemented in SHELXT¹³² was used; the crystal structures were then refined with the ShelXL¹³³ refinement package with the least-squares minimization.

The quality of the refined structural model is defined by agreement between the model and experimental data represented by R-factors:

$$R_1 = \frac{\sum ||F_{obs}| - |F_{calc}||}{\sum |F_{obs}|}$$
$$wR_2 = \left[\frac{\sum w |F_{obs}^2 - F_{calc}^2|}{\sum w F_{obs}^2} \right]^{\frac{1}{2}}$$

where F_{obs} is the observed structure factor amplitude, F_{calc} is the calculated structure factor amplitude based on the model, and w is the weighting factor individually derived for each measured reflection based on its standard deviation. The structural model is of high quality if:

- The R-factors are small (*i.e.* $R_1 < 5\%$ is excellent, $R_1 = 10\%$ is acceptable, $R_1 > 15\%$ indicates serious problems with the data quality or the model solution).
- The data to refined-parameters ratio is high (*i.e.* ratio > 10 is excellent, $10 >$ ratio > 8 is good, $8 >$ ratio > 6 is acceptable if good reasoning is provided, ratio < 6 is unacceptable).
- No major positive or negative electron residual densities exist.
- The model makes sense from the crystallographic and chemical point of view.

2.3. Stability range, equation of state, and recoverability check

Once crystal structures of reaction products in LHDACs are determined, the next important step is to investigate the (meta)stability range of novel compounds and check whether the high-pressure phase can be recovered to ambient conditions or it undergoes a phase

transition or decomposition. This can be done within the DAC decompression. At each pressure point, the XRD experiment can be performed to check the presence of the phase of interest and determine unit cell parameters and crystal structure at a given pressure.

Furthermore, after collecting a set of P-V data points in quasi-hydrostatic conditions, they can be fitted with an equation of state (EoS), which enables the extraction of an important mechanical property of a novel solid: the bulk modulus. The EoS for a system establishes the relationship among thermodynamic variables such as volume (V), pressure (P), and temperature (T) through parameters like bulk modulus and thermal expansion. In this thesis, all equations of state were determined at a constant (ambient) temperature of 293 K. Various types of analytical isothermal EoSes exist.^{134,135} In the present thesis, the Birch-Murnaghan EoS¹³⁵ was used to describe some experimental results in the experiments described below:

$$P = \frac{3K_0}{2} \left[\left(\frac{V_0}{V} \right)^{\frac{7}{3}} - \left(\frac{V_0}{V} \right)^{\frac{5}{3}} \right] \left\{ 1 - \frac{3}{4} (4 - K') \left[\left(\frac{V_0}{V} \right)^{\frac{2}{3}} - 1 \right] \right\}$$

This equation expresses the pressure-volume relationship of matter at constant temperature through the bulk modulus ($K_0 = -V \left(\frac{\partial P}{\partial V} \right)$) and its pressure derivatives, particularly $K' = \frac{\partial K}{\partial P}$. Expressions for the 2nd-order Birch-Murnaghan EoS can be obtained by setting $K' = 4$.

2.4. X-ray Absorption Spectroscopy

X-ray Absorption Spectroscopy (XAS) is a technique based on the interaction of X-ray radiation with matter causing the excitation of the inner-shell electrons. During this process, the photons of specific energies are absorbed depending on the geometric and electronic structure of a sample. The probability of an incident X-ray photon being absorbed increases significantly when its energy is close enough for the transmission of a specific core electron to valence-bound states or to the continuum, resulting in the emission of a photoelectron. This process causes a sharp change in the absorption spectrum, called an absorption edge. The value of energy level (and the absorption edge position) is unique to the element and every electron shell in them. Absorption edges are named based on principal quantum numbers ($n = 1, 2$ and 3 correspond to K-, L- and M-edges, respectively). The XAS spectra are typically divided into two main regions: X-ray absorption near-edge structure (XANES) and extended X-ray absorption fine structure (EXAFS) regions. The XANES operates with a region near the absorption edge, where energy at which a sharp rise in the absorption coefficient of X-rays occurs. The absorption spectrum at the XANES range provides information on the oxidation state of the atom through a well-recognized shift of an edge position. EXAFS operates with a

region of higher energies after the absorption edge. This region is related to the multiple scattering of photoelectrons on the surrounding atoms causing the interference patterns to appear. By applying Fourier transformation to that region and fitting of a model allows obtaining information on the radial distribution function, providing information about the local interatomic distances around the atom-absorber.

The XAS technique can be applied to samples under high pressure in DACs *in situ*, although diamonds absorb a significant fraction of the X-ray radiation (the exact value depends on the diamond's thickness and energy of X-rays) decreasing signal-to-noise ratio in the measured spectrum. Usually, the XANES region still can be accurately studied in DACs, while the EXAFS region often becomes too noisy for reliable analysis.

In the present thesis, the XANES experiments at the La L_{II} edge (~ 5.9 keV) were performed at the beamline ID12 of the ESRF to confirm the +3 oxidation state of lanthanum in $\text{La}_3\text{O}_2(\text{CN}_3)$ compound in a DAC, which is described in Section 5.5.

2.5. Raman spectroscopy

Raman spectroscopy is a spectroscopic technique based on the inelastic scattering of monochromatic optical radiation on the irradiated sample. When light interacts with matter, one of the processes that occurs is scattering. The majority of photons undergo elastic scattering known as Rayleigh scattering, preserving their energy ($E = E_0$). However, a minute fraction ($\sim 10^{-6}$ %) of incident light experiences inelastic scattering, resulting in either a loss (*i.e.*, $E > E_0$, Stokes Raman scattering) or gain (*i.e.*, $E < E_0$, anti-Stokes Raman scattering) of energy. Stokes Raman scattering occurs when the electron cloud absorbs a portion of the incident radiation and falls to an excited vibrational level instead of the ground state. In this case, Stokes Raman scattering possesses lower energy than the incident light. Anti-Stokes Raman scattering transpires when the incident light encounters the electron already populated in an excited vibrational state. The electron is excited to the virtual level and then falls to the ground level with more energy and higher frequency than the incident light. The intensity ratio between Stokes and anti-Stokes scattering relies on the population of vibrational levels described by Boltzmann's distribution. Consequently, at ambient temperature, the Stokes component predominates in the inelastic spectra and is commonly the sole consideration. The frequency of the Raman signals is associated with specific molecular or lattice vibrations, such as symmetric or asymmetric stretching or bending.

It is worth noting, that application of Raman spectroscopy to opaque samples (narrowband semiconductors and metals) has been restricted to a large extent because of the weakness of the Raman signal due largely to the small penetration depth of visible radiation.¹³⁶

In the present thesis, the Raman spectra from the samples in the LHDACs were collected using LabRam systems equipped with a He-Ne (632 nm) laser source. The He-Ne laser operates in continuous mode with a constant power of 50 mW. Raman spectra were collected in the range of 200 – 4000 cm⁻¹ with a resolution of 0.5 cm⁻¹. However, none of the discovered compounds gave a reliable Raman signal, since synthesized compounds are metals themselves, or semiconductors that were synthesized in the mixture with metallic phases. Nevertheless, Raman spectroscopy was still widely used in this thesis for the pressure determination inside the sample chamber using the signal from the diamond anvils.

2.6. Computational approaches

Density functional theory (DFT) is a powerful computational quantum-mechanical modeling method for exploring material properties. The DFT approach is especially valuable for investigating materials under extreme conditions, as experiments under high pressure have limitations in directly measuring the properties of samples in DACs.

DFT is based on two Hohenberg–Kohn theorems.¹³⁷ The first Hohenberg–Kohn theorem demonstrates that the ground-state properties of a many-electron system are uniquely defined by an electron density that relies on only three spatial coordinates. It simplifies the many-body problem of N electrons with 3N spatial coordinates to a problem involving only three spatial coordinates, through the use of functionals of the electron density. The second Hohenberg–Kohn theorem defines an energy functional for the system and proves that the ground-state electron density minimizes this energy functional.

Based on these theorems, Kohn & Sham¹³⁸ proposed an approach to make the complex problem of many-electron systems more manageable. They transformed the intricate problem of interacting electrons into a more tractable one involving non-interacting electrons moving in an effective potential. In Kohn & Sham approach, the Schrödinger equation for each electron can be written as:

$$\left[-\frac{\hbar^2}{2m_i} \nabla_i^2 + V_{\text{eff}}(r) \right] \psi_i(r) = \varepsilon_i \psi_i(r)$$

where the first term is the kinetic energy, V_{eff} is the effective potential, and ε_i is the orbital energy of the corresponding Kohn–Sham orbital ψ_i .

Then the electron density for an N-particle system can be calculated as: $\rho(r) = \sum_i^N |\psi_i(r)|^2$.

The effective potential V_{eff} consists of three components:

$$V_{\text{eff}}(r) = V_{\text{ext}}(r) + \int \frac{\rho(r')}{|r - r'|} dr' + V_{\text{xc}}(\rho(r))$$

where the first term is the external potential due to the nuclei, the second describes the electron-electron interaction, and the third is the exchange-correlation potential.

The exact form of the third term - exchange-correlation functional $V_{\text{xc}}[\rho(r)]$ - is unknown but can be approximated. The most common approximations are (1) the local density approximation (LDA), for which the electronic density is locally approximated as a homogenous electron gas of equal density and (2) the generalized gradient approximation (GGA), where an additional gradient of the electron density is taken into account.¹³⁹ Also, more advanced functionals such as meta-GGA and hybrid functionals exist.^{140,141}

The iterative self-consistent calculations allow finding the ground state and energy of a system. Once the ground state has been found various physical properties can be calculated.

In the present thesis, DFT calculations were used for (1) the validation of crystal structures, obtained from the experiment, (2) the analysis of chemical bonding, (3) the investigation of the stability of synthesized compounds, and (4) the calculation of physical properties, *i.e.* bulk modulus, energy density, and electronic properties. DFT calculations were carried out in Vienna *ab initio* simulation package (VASP)¹⁴². To expand the electronic wave function in plane waves, we used the Projector-Augmented-Wave (PAW) method.¹⁴³ The Perdew–Burke–Ernzerhof (PBE) GGA functional¹⁴⁴ was used for calculating the exchange-correlation energies.

3. Thesis synopsis

This chapter provides a short overview of the results presented in Chapter 5, which have been published in peer-reviewed journals.

Section 5.1 is dedicated to the methodological improvement of single-crystal X-ray diffraction (SCXRD) data processing from multigrain samples, particularly obtained in the laser-heated diamond anvil cells. The developed DAFi program allows the separation of SCXRD from the individual crystallites of multigrain samples. It revolutionizes the state-of-art of multigrain SCXRD data processing. This program is recognized by giant crystallography industry companies such as Rigaku and Bruker as well it is actively used by different scientific groups over the world. The synopsis of Section 5.1 is presented below in Section 3.1.

With this powerful tool in hand, the high-pressure chemistry of nitrogen was studied. First, binary systems — rare-earth elements and nitrogen —, namely Y-N and Sc-N systems. In Sections 5.2 and 5.3 we present the synthesis of Y-N compounds at high temperatures and at 50 GPa and 100 GPa, respectively. In Section 5.4 the synthesis of Sc-N binary compounds in 50-125 GPa pressure range is presented. The synopses of Sections 5.2-5.4 are presented below in Section 3.2.

Then, more complex systems containing rare-earth elements, nitrogen, and carbon were studied. In Section 5.5 the synthesis of a series of isostructural $\text{Ln}_3\text{O}_2(\text{CN}_3)$ ($\text{Ln} = \text{La}, \text{Eu}, \text{Gd}, \text{Tb}, \text{Ho}, \text{Yb}$) oxoguanidates under high-pressure (25-54 GPa) high-temperature (2000-3000 K) conditions is presented. In section 5.6 the synthesis of LaCN_3 , TbCN_3 , CeCN_5 and TbCN_5 polycarbonitrides at ~100 GPa is presented. The synopses of Sections 5.5-5.6 are presented below in Section 3.3.

3.1. Methodological development: DAFi program for the analysis of single-crystal X-ray diffraction data from polycrystalline samples

It has been shown, that single-crystal X-ray diffraction (SCXRD) — a powerful method for determining the structure of crystalline solids — can be applied to multigrain samples. In this technique, each of the illuminated grains (crystallites or single crystal domains in other notations) gives its own set of spotty Bragg’s reflections. The main difficulty in the processing of such single crystal X-ray diffraction data from multigrain samples is the separation of reflections from different crystallites: superposition of numerous reflections originating from a large number of crystallites of the same and/or different (especially unknown) phases usually precludes sorting out the reflections coming from individual crystallites making their automatic indexing impossible. Hitherto this sorting has to be done manually by a scientist, and such a manual procedure is time-consuming and requires enough expertise.

In Section 5.1, we present the Domain Auto Finder (DAFi) program, which allows the separation of SCXRD from the individual crystallites of multigrain samples. The DAFi algorithm is designed for the quick search of subsets of reflections from individual grains in the whole set of SCXRD data. Further indexing of all found subsets can be easily performed using widely accessible crystallographic packages. As the algorithm neither requires *a priori* crystallographic information nor is limited by the number of phases or individual domains, the DAFi is a powerful software to be used for studies of multiphase multigrain materials. The algorithm is validated by testing on X-ray diffraction datasets obtained from real samples: a multi-mineral basalt rock at ambient conditions and products of the chemical reaction of yttrium and nitrogen in a laser-heated diamond anvil cell at 50 GPa (Fig. 3.1).

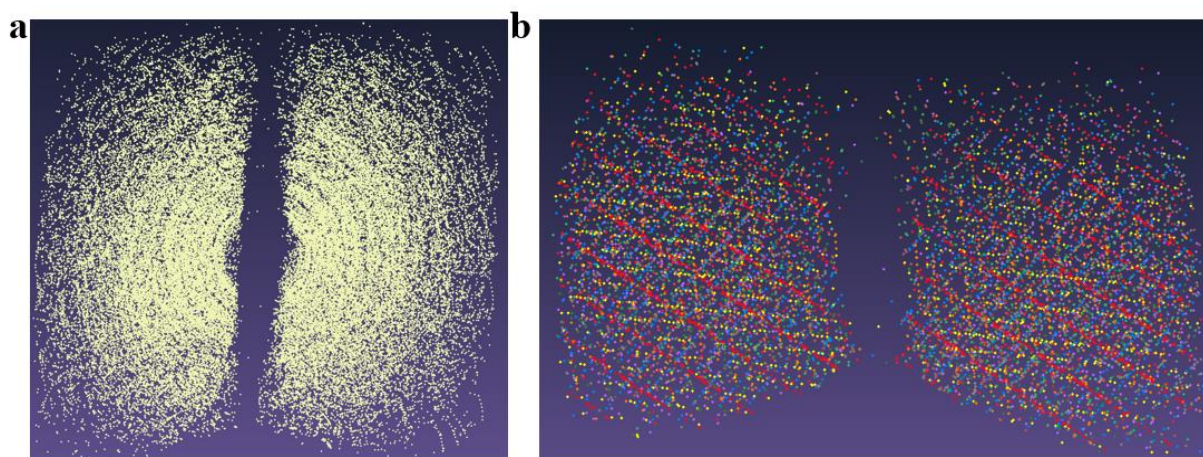


Figure 3.1. Single-crystal X-ray diffraction of laser-heated Y piece embedded in molecular nitrogen in DAC at 50 GPa (from P02.2 beamline of the PETRA III synchrotron) displayed in

the reciprocal space: a) all 68846 reflections, b) first 10 domains (marked with different colors) of reaction product Y_5N_{14} found by DAFi program

The high performance of the DAFi algorithm allows using this program for processing SCXRD data online during experiments at synchrotron facilities. Currently, DAFi is compatible with CrysAlisPro (Rigaku) and APEX4 (Bruker) crystallographic software packages. Moreover, the input and output formats of the DAFi program could be adapted to users' needs and made compatible with other crystallographic software. This breakthrough in the analysis of SCXRD from multigrain samples makes multigrain crystallography accessible to a broad audience and accelerates the accumulation of high-pressure crystal chemistry knowledge.

3.2. High-pressure synthesis of novel rare-earth di-, oligo- and poly-nitrides

As was described in the Introduction Chapter, a significant number of studies on binary metal-nitrogen compounds of alkali, alkaline earth, and transition metal elements under high pressure have been conducted. Although theory predicts exotic high-pressure Sc-N and Y-N compounds with promising physical properties comprised of unique oligo- and poly-nitrogen anions, there is no experimental evidence on such rare-earth di-, oligo- and poly- nitrides formation under high pressure. Here we study Y-N and Sc-N binary systems under high-pressure high-temperature conditions.

The reactions between yttrium and nitrogen were conducted in the laser-heated diamond anvil cells at 50 GPa and 100 GPa (Fig. 3.2). The processing of high-pressure synchrotron single-crystal X-ray diffraction data using the DAFi program enabled the determination of the crystal structures of three novel solids with unusual stoichiometry: Y_5N_{14} at 50 GPa, and YN_6 along with Y_2N_{11} at 100 GPa. The crystal structure of Y_5N_{14} contains three distinct types of nitrogen dimers. Crystal chemical analysis and *ab initio* calculations demonstrated that the dimers $[N_2]^{x-}$ are crystallographically and chemically non-equivalent and possess distinct non-integer formal charges (x) that make Y_5N_{14} unique among known dinitrides. The crystal structures of YN_6 and Y_2N_{11} feature a unique organization of nitrogen atoms—a previously unknown anionic N_{18} macrocycle and a polynitrogen double helix, respectively.

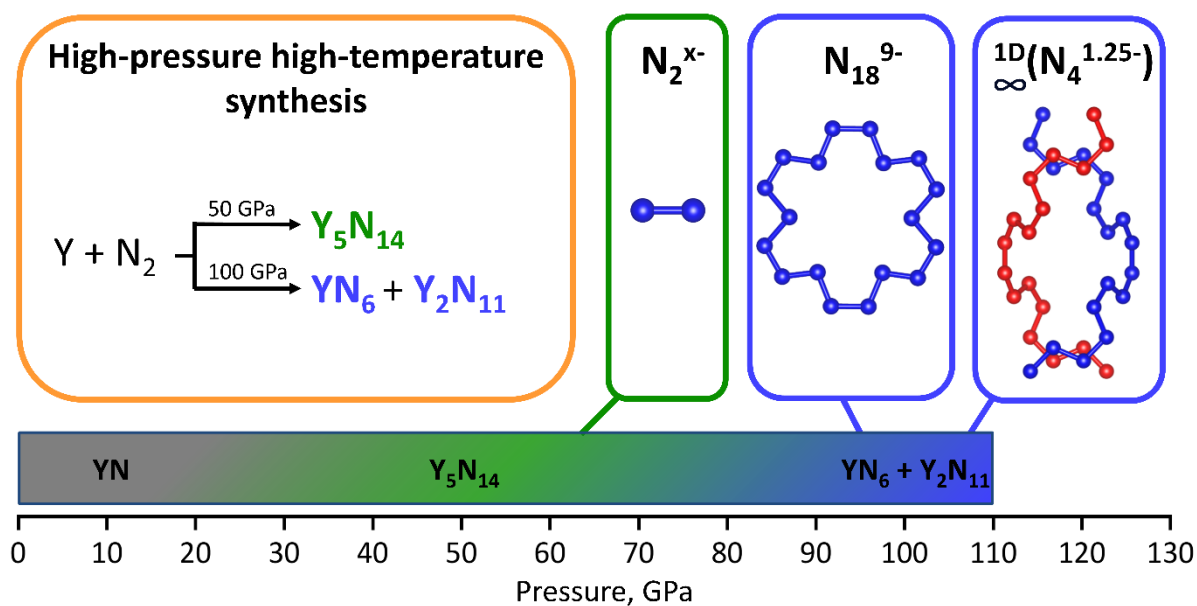


Figure 3.2. Summary of the high-pressure high-temperature induced reactions of Y and N_2 , and structural formulas of di- and poly-nitrogen units found in synthesized di- and poly-nitrides. The color pressure scale at the bottom highlights the synthesis pressures of corresponding di- and poly-nitrides.

Four novel scandium nitrides, Sc_2N_6 , Sc_2N_8 , ScN_5 , and Sc_4N_3 , were synthesized by direct reaction between scandium and nitrogen at 78-125 GPa and 2500 K in laser-heated diamond anvil cells (Fig. 3.3). High-pressure synchrotron single-crystal X-ray diffraction revealed that in the crystal structures of the nitrogen-rich Sc_2N_6 , Sc_2N_8 , and ScN_5 phases nitrogen is catenated forming previously unknown N_6^{6-} and N_8^{6-} units and $\infty(N_5^{3-})$ anionic corrugated 2D-poly-nitrogen layers consisting of fused N_{12} rings. Density functional theory calculations, confirming the dynamical stability of the synthesized compounds, show that Sc_2N_6 and Sc_2N_8 possess an anion-driven metallicity, while ScN_5 is an indirect semiconductor. Sc_2N_6 , Sc_2N_8 , and ScN_5 solids are promising high-energy-density materials with calculated volumetric energy density, detonation velocity, and detonation pressure higher than those of TNT.

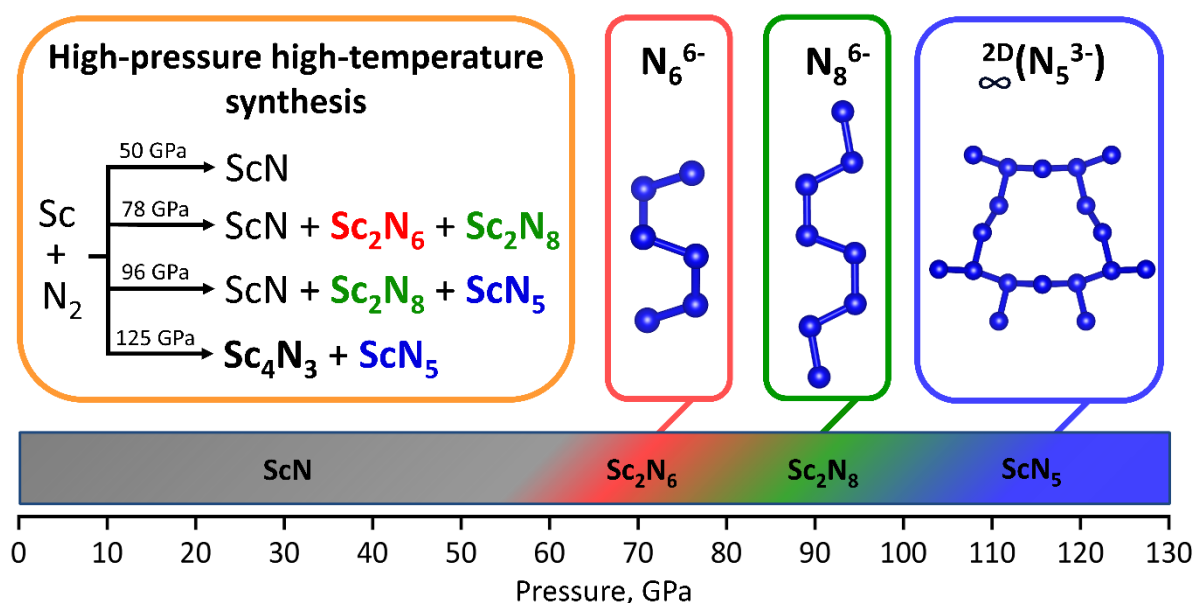


Figure 3.3. Summary of the high-pressure high-temperature induced reactions of Sc and N_2 , and structural formulas of oligo- and poly-nitrogen units found in synthesized polynitrides. The color pressure scale at the bottom highlights the synthesis pressures of corresponding polynitrides.

Presented studies significantly extend the list of known catenated nitrogen species (Table 1.1) by the discovery of previously unknown oligo-nitrogen units – $[\text{N}_6]^{6-}$, $[\text{N}_8]^{6-}$ and $[\text{N}_{18}]^{9-}$ anions as well as the unique second-known type of 2D polynitrogen layer. The degree of nitrogen catenation increases with pressure: dinitrides are synthesized at low pressures (<50 GPa); N_4 , N_6 , and N_8 units are obtained at mild pressures (50-80 GPa), while N_{18} macrocycles, 1D-polynitrogen chains and 2D polynitrogen layers are formed at ~100 GPa. Therefore, these results give an important contribution to our understanding of nitrogen high-pressure chemistry.

3.3. High-pressure synthesis of novel rare-earth carbonitrides

As was shown in the Introduction Chapter, inorganic ternary metal-C-N compounds containing covalently bonded C-N anions represent different classes of solids. Among these, cyanides (CN^-) and carbodiimides (NCN^{2-}) are the most extensively studied and find numerous applications. While the CN^- and CN_2^{2-} anions are well-established, subsequent anions in this series, such as CN_3^{5-} (a fully deprotonated guanidine) and CN_4^{8-} (a derivative of hypothetical tetraaminomethane), have not yet been discovered, though they are discussed in the literature.

Despite numerous attempts to synthesize guanidinate anion by deprotonation of guanidine molecule using strong bases, up to date only partially deprotonated guanidine has been stabilized. In Section 5.5, we report on the successful stabilization of CN_3^{5-} guanidinate anion using not a classic “wet chemistry” approach, but rather a non-conventional route of solid-state synthesis under extreme conditions. A series of isostructural $\text{Ln}_3\text{O}_2(\text{CN}_3)$ ($\text{Ln} = \text{La}, \text{Eu}, \text{Gd}, \text{Tb}, \text{Ho}, \text{Yb}$) oxoguanidates was synthesized under high-pressure (25-54 GPa) high-temperature (2000-3000 K) conditions in laser-heated diamond anvil cells. Decompression experiments show that $\text{Ln}_3\text{O}_2(\text{CN}_3)$ compounds are recoverable to ambient conditions. The synthesis of the CN_3^{5-} guanidinate anion extends the list of carbon-nitrogen inorganic anions and its stabilization at ambient conditions provides new opportunities for inorganic and organic synthetic chemistry.

After the discovery of the CN_3^{5-} anion, synthesized at mild pressures (25-54 GPa) and recoverable to ambient conditions. Knowing that C-N compounds built of CN_4 tetrahedra were obtained at pressures above 70 GPa, stabilization of CN_4^{8-} units or/and the formation of polycarbonitrides built of corner/edge-sharing CN_4 tetrahedra in ternary metal-C-N systems are expected at pressures above 70 GPa. In Section 5.6, we present the high-pressure high-temperature synthesis and characterization of four hitherto unknown lanthanide polycarbonitrides, LaCN_3 , TbCN_3 , CeCN_5 , and TbCN_5 , at megabar pressures. Their crystal structures were solved and refined based on synchrotron single-crystal X-ray diffraction, unveiling an atomic arrangement consisting of previously unobserved anionic single-bonded carbon-nitrogen 3D frameworks consisting of CN_4 tetrahedra connected *via* di- or oligo-nitrogen linkers. Strikingly, despite the theoretical predictions of the high-pressure stabilized CN_4^{8-} orthonitridocarbonate anion, we do not observe its formation. This could suggest that while CN_4 units are indeed the preferred 3D building block, their concatenation is more favorable than having a significant negative charge such as in the CN_4^{8-} anion.

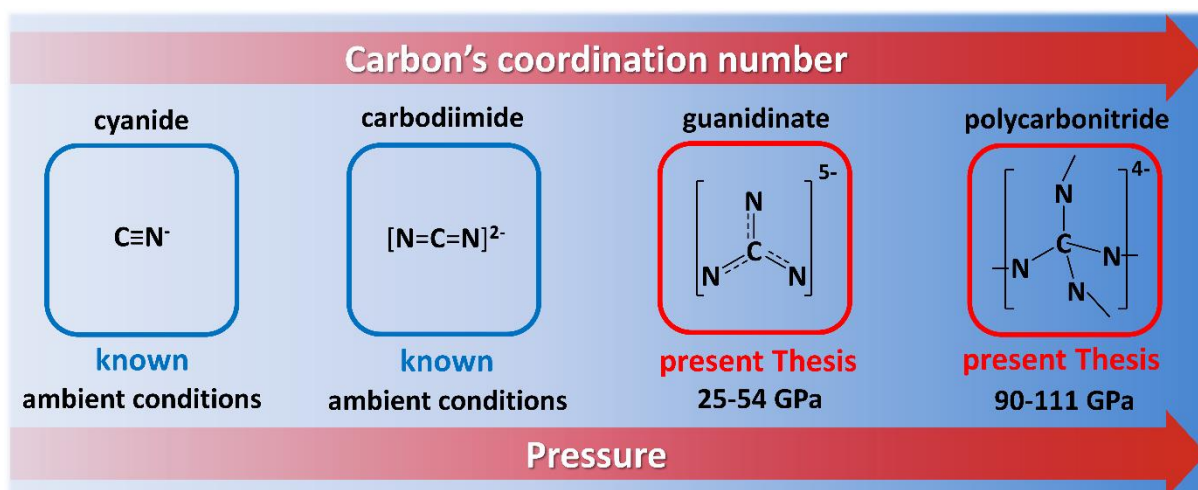


Figure 3.4. Experimentally observed C-N anions. Anions in red frames were first discovered in the present thesis.

Discovered CN_3^{5-} guanidinate anion and CN_4 -based 3D polycarbonitride anionic frameworks complement known covalently bonded C-N anions. The geometry of the C-N anions illustrates well how high pressure stabilizes higher coordination numbers of carbon (Fig. 3.4). In the $^-\text{N}=\text{C}=\text{N}^-$ anion, which is stable at ambient conditions, the C atom is coordinated by two N atoms. At mild pressures (25-54 GPa), CN_3^{5-} anion is formed with the carbon's coordination number of three. At higher pressures (90-111 GPa), we observe tetra-fold coordinated carbon in the crystal structures of LaCN_3 , TbCN_3 , CeCN_5 , and TbCN_5 . Therefore, these results give an important insight into carbonitride high-pressure chemistry.

3.4. List of manuscripts and statement of authors' contribution

1. **A. Aslandukov (AnA)**, M. Aslandukov (MA), N. Dubrovinskaia (ND), L. Dubrovinsky (LD). (2022). Domain Auto Finder (DAFi) program: the analysis of single-crystal X-ray diffraction data from polycrystalline samples, *Journal of Applied Crystallography*, 55(5), 1383-1391. DOI: [10.1107/S1600576722008081](https://doi.org/10.1107/S1600576722008081).

AnA designed the work. MA wrote the program. AnA tested the program. AnA, LD, and ND prepared experimental datasets for program's capabilities demonstration. AnA, MA, LD, and ND prepared the manuscript. The overall A. Aslandukov's contribution is 60%.

2. **A. Aslandukov (AnA)**, A. Aslandukova (AIA), D. Laniel (DL), I. Koemets (IK), T. Fedotenko (TF), L. Yuan (LY), G. Steinle-Neumann (GSN), K. Glazyrin (KG), M. Hanfland (MH), L. Dubrovinsky (LD), N. Dubrovinskaia (ND). (2021). High-pressure yttrium nitride, Y_5N_{14} , featuring three distinct types of nitrogen dimers. *The Journal of Physical Chemistry C*, 125(32), 18077-18084. DOI: [10.1021/acs.jpcc.1c06210](https://doi.org/10.1021/acs.jpcc.1c06210).

AnA, LD, and ND designed the work. AnA prepared samples in DACs. AnA, AIA, DL, IK, TF, KG, and MH performed the synchrotron XRD experiments. AnA processed the synchrotron XRD data. AnA, LY and GSN performed the theoretical calculations. AnA, LD and ND contextualized the data interpretation. AnA, LD, and ND prepared the manuscript with contributions from all co-authors. The overall A. Aslandukov's contribution is 75%.

3. **A. Aslandukov (AnA)**, F. Trybel (FT), A. Aslandukova (AIA), D. Laniel (DL), T. Fedotenko (TF), S. Khandarkhaeva (SK), G. Aprilis (GA), C. Giacobbe (CG), E.L. Bright (ELB), I.A. Abrikosov (IAA), L. Dubrovinsky (LD), N. Dubrovinskaia (ND). (2022). Anionic N_{18} macrocycles and a polynitrogen double helix in novel yttrium polynitrides YN_6 and Y_2N_{11} at 100 GPa. *Angewandte Chemie*, 61(34), e202207469. DOI: [10.1002/anie.202207469](https://doi.org/10.1002/anie.202207469).

AnA, LD, and ND designed the work. AnA prepared samples in DACs. AnA, AIA, DL, TF, SK, GA, CG, and ELB performed the synchrotron XRD experiments. AnA processed the synchrotron XRD data. FT and IAA performed the theoretical calculations. AnA, IAA, LD and ND contextualized the data interpretation. AnA, LD, and ND prepared the manuscript with contributions from all co-authors. The overall A. Aslandukov's contribution is 70%.

4. **A. Aslandukov (AnA)**, A. Aslandukova (AIA), D. Laniel (DL), S. Khandarkhaeva (SK), Y. Yin (YY), F. I. Akbar (FA), S. Chariton (SC), V. Prakapenka (VP), E. L. Bright (ELB), C. Giacobbe (CG), J. Wright (JW), D. Comboni (DC), M. Hanfland (MH), N. Dubrovinskaia (ND), L. Dubrovinsky (LD) (2024). Stabilization of N_6 and N_8 anionic units

and 2D polynitrogen layers in high-pressure scandium polynitrides, *Nature Communications*, 15(1), 2244. DOI: [10.1038/s41467-024-46313-9](https://doi.org/10.1038/s41467-024-46313-9).

AnA, LD, and ND designed the work. AnA prepared samples in DACs. AnA, AIA, DL, SK, YY, FA, SC, VP, ELB, CG, JW, DC, and MH performed the synchrotron XRD experiments. AnA processed the synchrotron XRD data. AnA performed the theoretical calculations. AnA, LD and ND contextualized the data interpretation. AnA, LD, and ND prepared the manuscript with contributions from all co-authors. The overall A. Aslandukov's contribution is 80%.

- 5. A. Aslandukov (AnA)**, P.L. Jurzick (PLJ), M. Bykov (MB), A. Aslandukova (AIA), A. Chanyshv (AC), D. Laniel (DL), Y. Yin (YY), F.I. Akbar (FA), S. Khandarkhaeva (SK), T. Fedotenko (TF), K. Glazirin (KG), S. Chariton (SC), V. Prakapenka (VP), F. Wilhelm (FW), A. Rogalev (AR), D. Comboni (DC), M. Hanfland (MH), N. Dubrovinskaia (ND), L. Dubrovinsky (LD) (2023). Stabilization of the CN_3^{5-} anion in recoverable high-pressure $\text{Ln}_3\text{O}_2(\text{CN}_3)$ ($\text{Ln} = \text{La}, \text{Eu}, \text{Gd}, \text{Tb}, \text{Ho}, \text{Yb}$) oxoguanidates, *Angewandte Chemie*, 135(47), e202311516. DOI: [10.1002/anie.202311516](https://doi.org/10.1002/anie.202311516).

AnA, LD, and ND designed the work. AnA and PLJ prepared samples in DACs. AC performed multi-anvil experiments. AnA, PLJ, MB, AIA, DL, YY, FA, SK, TF, KG, SC, VP, DC, and MH performed the synchrotron XRD experiments. AnA, FW, and AR performed the synchrotron XANES experiments. AnA and PLJ processed the synchrotron XRD data. AnA processed the synchrotron XANES data. AnA performed the theoretical calculations. AnA, LD and ND contextualized the data interpretation. AnA, LD, and ND prepared the manuscript with contributions from all co-authors. The overall A. Aslandukov's contribution is 70%.

- 6. A. Aslandukov (AnA)**, A. Liang (AL), A. Ehn (AE), F. Trybel (FT), Y. Yin (YY), A. Aslandukova (AIA), F. I. Akbar (FA), U. Ranieri (UR), J. Spender (JS), R. T. Howie (RTH), E. L. Bright (ELB), J. Wright (JW), G. Garbarino (GG), M. Mezouar (MM), T. Fedotenko (TF), I. A. Abrikosov (IAA), N. Dubrovinskaia (ND), L. Dubrovinsky (LD), D. Laniel (DL). (2024) Synthesis of LaCN_3 , TbCN_3 , CeCN_5 and TbCN_5 polycarbonitrides at megabar pressures, *Journal of the American Chemical Society*, 146(26), 18161–18171. DOI: [10.1021/jacs.4c06068](https://doi.org/10.1021/jacs.4c06068).

AnA, AL, LD, ND and DL designed the work. AnA and AL prepared samples in DACs. AnA, AL, YY, AIA, FA, UR, JS, RTH, ELB, JW, GG, MM, TF, and DL performed the synchrotron XRD experiments. AnA and AL processed the synchrotron XRD data. AE, FT and IAA performed the theoretical calculations. AnA, AL, DL, IAA, LD and ND contextualized the data interpretation. AnA, AL, DL, LD, and ND prepared the manuscript with contributions from all co-authors. The overall A. Aslandukov's contribution is 50%.

4. Bibliography

1. Dong, X., Oganov, A. R., Goncharov, A. F., Stavrou, E., Lobanov, S., Saleh, G., Qian, G. R., Zhu, Q., Gatti, C., Deringer, V. L., Dronskowski, R., Zhou, X. F., Prakapenka, V. B., Konôpková, Z., Popov, I. A., Boldyrev, A. I. & Wang, H. T. A stable compound of helium and sodium at high pressure. *Nat. Chem.* **9**, 440–445 (2017).
2. Zhang, W., Oganov, A. R., Goncharov, A. F., Zhu, Q., Boulfelfel, S. E., Lyakhov, A. O., Stavrou, E., Somayazulu, M., Prakapenka, V. B. & Konôpková, Z. Unexpected Stable Stoichiometries of Sodium Chlorides. *Science*. **342**, 1502–1505 (2013).
3. Bykova, E., Dubrovinsky, L., Dubrovinskaia, N., Bykov, M., McCammon, C., Ovsyannikov, S. V., Liermann, H. P., Kuppenko, I., Chumakov, A. I., Rüffer, R., Hanfland, M. & Prakapenka, V. Structural complexity of simple Fe₂O₃ at high pressures and temperatures. *Nat. Commun.* **7**, 10661 (2016).
4. Drozdov, A. P., Kong, P. P., Minkov, V. S., Besedin, S. P., Kuzovnikov, M. A., Mozaffari, S., Balicas, L., Balakirev, F. F., Graf, D. E., Prakapenka, V. B., Greenberg, E., Knyazev, D. A., Tkacz, M. & Eremets, M. I. Superconductivity at 250 K in lanthanum hydride under high pressures. *Nature* **569**, 528–531 (2019).
5. Wang, Y., Bykov, M., Chepkasov, I., Samtsevich, A., Bykova, E., Zhang, X., Jiang, S., Greenberg, E., Chariton, S., Prakapenka, V. B., Oganov, A. R. & Goncharov, A. F. Stabilization of hexazine rings in potassium polynitride at high pressure. *Nat. Chem.* **14**, 794–800 (2022).
6. Laniel, D., Trybel, F., Yin, Y., Fedotenko, T., Khandarkhaeva, S., Aslandukov, A., Aprilis, G., Abrikosov, A. I., Bin Masood, T., Giacobbe, C., Bright, E. L., Glazyrin, K., Hanfland, M., Wright, J., Hotz, I., Abrikosov, I. A., Dubrovinsky, L. & Dubrovinskaia, N. Aromatic hexazine [N₆]⁴⁻ anion featured in the complex structure of the high-pressure potassium nitrogen compound K₉N₅₆. *Nat. Chem.* **15**, 641–646 (2023).
7. Dubrovinsky, L., Khandarkhaeva, S., Fedotenko, T., Laniel, D., Bykov, M., Giacobbe, C., Lawrence Bright, E., Sedmak, P., Chariton, S., Prakapenka, V., Ponomareva, A. V., Smirnova, E. A., Belov, M. P., Tasnádi, F., Shulumba, N., Trybel, F., Abrikosov, I. A. & Dubrovinskaia, N. Materials synthesis at terapascal static pressures. *Nature* **605**, 274–278 (2022).
8. Alabdulkarim, M. E., Maxwell, W. D., Thapliyal, V. & Maxwell, J. L. A Comprehensive Review of High-Pressure Laser-Induced Materials Processing, Part I: Laser-Heated Diamond Anvil Cells. *J. Manuf. Mater. Process.* **6**, 111 (2022).
9. Mao, H. K., Chen, B., Chen, J., Li, K., Lin, J. F., Yang, W. & Zheng, H. Recent advances in high-pressure science and technology. *Matter Radiat. Extrem.* **1**, 59–75 (2016).
10. Goncharov, A. F. Raman Spectroscopy at High Pressures. *Int. J. Spectrosc.* **2012**, 617528 (2012).
11. Fu, Z., Wang, K. & Zou, B. Recent advances in organic pressure-responsive luminescent materials. *Chinese Chem. Lett.* **30**, 1883–1894 (2019).
12. Nasu, S. High pressure Mössbauer spectroscopy using a diamond anvil cell. *Hyperfine Interact.* **90**, 59–75 (1994).
13. Shen, G. & Mao, H. K. High-pressure studies with x-rays using diamond anvil cells. *Reports Prog. Phys.* **80**, 016101 (2017).
14. Meier, T., Laniel, D., Pena-Alvarez, M., Trybel, F., Khandarkhaeva, S., Krupp, A.,

- Jacobs, J., Dubrovinskaia, N. & Dubrovinsky, L. Nuclear spin coupling crossover in dense molecular hydrogen. *Nat. Commun.* **11**, 6334 (2020).
15. Niwa, K., Fukui, R., Terabe, T., Kawada, T., Kato, D., Sasaki, T., Soda, K. & Hasegawa, M. High-Pressure Synthesis and Phase Stability of Nickel Pernitride. *Eur. J. Inorg. Chem.* **2019**, 3753–3757 (2019).
 16. Kong, P., Minkov, V. S., Kuzovnikov, M. A., Drozdov, A. P., Besedin, S. P., Mozaffari, S., Balicas, L., Balakirev, F. F., Prakapenka, V. B., Chariton, S., Knyazev, D. A., Greenberg, E. & Eremets, M. I. Superconductivity up to 243 K in the yttrium-hydrogen system under high pressure. *Nat. Commun.* **12**, 5075 (2021).
 17. Bykova, E. Single-crystal X-ray diffraction at extreme conditions in mineral physics and material sciences. PhD thesis, University of Bayreuth. (2015).
 18. Akasaki, I. & Amano, H. Crystal growth and conductivity control of group III nitride semiconductors and their application to short wavelength light emitters. *Japanese J. Appl. Physics, Part 1 Regul. Pap. Short Notes Rev. Pap.* **36**, 5393–5408 (1997).
 19. Akasaki, I. Fascinating journeys into blue light (Nobel Lecture). *Ann. Phys.* **527**, 311–326 (2015).
 20. Ponce, F. A. & Bour, D. P. Nitride-based semiconductors for blue and green light-emitting devices. *Nature* **386**, 351–359 (1997).
 21. Yeung, M. T., Mohammadi, R. & Kaner, R. B. Ultraincompressible, Superhard Materials. *Annu. Rev. Mater. Res.* **46**, 465–485 (2016).
 22. Zhong, Y., Xia, X. H., Shi, F., Zhan, J. Y., Tu, J. P. & Fan, H. J. Transition metal carbides and nitrides in energy storage and conversion. *Adv. Sci.* **3**, 1500286 (2015).
 23. Jouanny, I., Weisbecker, P., Demange, V., Grafouté, M., Peña, O. & Bauer-Grosse, E. Structural characterization of sputtered single-phase γ'' iron nitride coatings. *Thin Solid Films* **518**, 1883–1891 (2010).
 24. Clark, W. P., Steinberg, S., Dronskowski, R., McCammon, C., Kuppenko, I., Bykov, M., Dubrovinsky, L., Akselrud, L. G., Schwarz, U. & Niewa, R. High-Pressure NiAs-Type Modification of FeN. *Angew. Chemie Int. Ed.* **56**, 7302–7306 (2017).
 25. Chen, X. J., Struzhkin, V. V., Wu, Z., Somayazulu, M., Qian, J., Kung, S., Christensen, A. N., Zhao, Y., Cohen, R. E., Mao, H. K. & Hemley, R. J. Hard superconducting nitrides. *Proc. Natl. Acad. Sci. U. S. A.* **102**, 3198–3201 (2005).
 26. Sun, W., Bartel, C. J., Arca, E., Bauers, S. R., Matthews, B., Orvañanos, B., Chen, B. R., Toney, M. F., Schelhas, L. T., Tumas, W., Tate, J., Zakutayev, A., Lany, S., Holder, A. M. & Ceder, G. A map of the inorganic ternary metal nitrides. *Nat. Mater.* **18**, 732–739 (2019).
 27. Laniel, D., Winkler, B., Fedotenko, T., Pakhomova, A., Chariton, S., Milman, V., Prakapenka, V., Dubrovinsky, L. & Dubrovinskaia, N. High-Pressure Polymeric Nitrogen Allotrope with the Black Phosphorus Structure. *Phys. Rev. Lett.* **124**, 216001 (2020).
 28. Eremets, M. I., Gavriluk, A. G., Trojan, I. A., Dzivenko, D. A. & Boehler, R. Single-bonded cubic form of nitrogen. *Nat. Mater.* **3**, 558–563 (2004).
 29. Laniel, D., Geneste, G., Weck, G., Mezouar, M. & Loubeyre, P. Hexagonal Layered Polymeric Nitrogen Phase Synthesized near 250 GPa. *Phys. Rev. Lett.* **122**, 66001 (2019).

30. Kroll, P., Schröter, T. & Peters, M. Prediction of novel phases of tantalum(V) nitride and tungsten(VI) nitride that can be synthesized under high pressure and high temperature. *Angew. Chemie - Int. Ed.* **44**, 4249–4254 (2005).
31. Niwa, K., Terabe, T., Kato, D., Takayama, S., Kato, M., Soda, K. & Hasegawa, M. Highly Coordinated Iron and Cobalt Nitrides Synthesized at High Pressures and High Temperatures. *Inorg. Chem.* **56**, 6410–6418 (2017).
32. Bykov, M., Bykova, E., Ponomareva, A. V., Tasnádi, F., Chariton, S., Prakapenka, V. B., Glazyrin, K., Smith, J. S., Mahmood, M. F., Abrikosov, I. A. & Goncharov, A. F. Realization of an Ideal Cairo Tessellation in Nickel Diazenide NiN₂: High-Pressure Route to Pentagonal 2D Materials. *ACS Nano* **15**, 13539–13546 (2021).
33. Binns, J., Donnelly, M.-E., Peña-Alvarez, M., Wang, M., Gregoryanz, E., Hermann, A., Dalladay-Simpson, P. & Howie, R. T. Direct Reaction between Copper and Nitrogen at High Pressures and Temperatures. *J. Phys. Chem. Lett.* **10**, 1109–1114 (2019).
34. Niwa, K., Suzuki, K., Muto, S., Tatsumi, K., Soda, K., Kikegawa, T. & Hasegawa, M. Discovery of the Last Remaining Binary Platinum-Group Pernitride RuN₂. *Chem. - A Eur. J.* **20**, 13885–13888 (2014).
35. Niwa, K., Terabe, T., Suzuki, K., Shirako, Y. & Hasegawa, M. High-pressure stability and ambient metastability of marcasite-type rhodium pernitride. *J. Appl. Phys.* **119**, 065901 (2016).
36. Bykov, M., Yusenko, K. V., Bykova, E., Pakhomova, A., Kraus, W., Dubrovinskaia, N. & Dubrovinsky, L. Synthesis of Arsenopyrite-Type Rhodium Pernitride RhN₂ from a Single-Source Azide Precursor. *Eur. J. Inorg. Chem.* **2019**, 3667–3671 (2019).
37. Crowhurst, J. C., Goncharov, A. F., Sadigh, B., Zaug, J. M., Aberg, D., Meng, Y. & Prakapenka, V. B. Synthesis and characterization of nitrides of iridium and palladium. *J. Mater. Res.* **23**, 1–5 (2008).
38. Young, A. F., Sanloup, C., Gregoryanz, E., Scandolo, S., Hemley, R. J. & Mao, H. K. Synthesis of novel transition metal nitrides IrN₂ and OsN₂. *Phys. Rev. Lett.* **96**, 155501 (2006).
39. Crowhurst, J. C., Goncharov, A. F., Sadigh, B., Evans, C. L., Morrall, P. G., Ferreira, J. L. & Nelson, A. J. Synthesis and Characterization of the Nitrides of Platinum and Iridium. *Science*. **311**, 1275–1278 (2006).
40. Schneider, S. B., Frankovsky, R. & Schnick, W. High-Pressure Synthesis and Characterization of the Alkali Diazenide Li₂N₂. *Angew. Chemie* **124**, 1909–1911 (2012).
41. Laniel, D., Weck, G. & Loubeyre, P. Direct Reaction of Nitrogen and Lithium up to 75 GPa: Synthesis of the Li₃N, LiN, LiN₂, and LiN₅ Compounds. *Inorg. Chem.* **57**, 10685–10693 (2018).
42. Bykov, M., Tasca, K. R., Batyrev, I. G., Smith, D., Glazyrin, K., Chariton, S., Mahmood, M. & Goncharov, A. F. Dinitrogen as a Universal Electron Acceptor in Solid-State Chemistry: An Example of Uncommon Metallic Compounds Na₃(N₂)₄ and NaN₂. *Inorg. Chem.* **59**, 14819–14826 (2020).
43. Schneider, S. B., Frankovsky, R. & Schnick, W. Synthesis of Alkaline Earth Diazenides M_{AE}N₂ (M_{AE} = Ca, Sr, Ba) by Controlled Thermal Decomposition of Azides under High Pressure. *Inorg. Chem.* **51**, 2366–2373 (2012).
44. Laniel, D., Winkler, B., Fedotenko, T., Aslandukova, A., Aslandukov, A., Vogel, S., Meier, T., Bykov, M., Chariton, S., Glazyrin, K., Milman, V., Prakapenka, V., Schnick,

- W., Dubrovinsky, L. & Dubrovinskaia, N. High-pressure $\text{Na}_3(\text{N}_2)_4$, $\text{Ca}_3(\text{N}_2)_4$, $\text{Sr}_3(\text{N}_2)_4$, and $\text{Ba}(\text{N}_2)_3$ featuring nitrogen dimers with noninteger charges and anion-driven metallicity. *Phys. Rev. Mater.* **6**, 023402 (2022).
45. Bhadram, V. S., Kim, D. Y. & Strobel, T. A. High-Pressure Synthesis and Characterization of Incompressible Titanium Pernitride. *Chem. Mater.* **28**, 1616–1620 (2016).
 46. Asano, S., Niwa, K., Sasaki, T., Gaida, N. A. & Hasegawa, M. High pressure synthesis and the valence state of vanadium ions for the novel transition metal pernitride, CuAl₂-type VN₂. *Dalt. Trans.* **51**, 2656–2659 (2022).
 47. Niwa, K., Yamamoto, T., Sasaki, T. & Hasegawa, M. High-pressure synthesis, crystal growth, and compression behavior of hexagonal CrN₂ having one-dimensionally aligned nitrogen dimer. *Phys. Rev. Mater.* **3**, 53601 (2019).
 48. Laniel, D., Winkler, B., Koemets, E., Fedotenko, T., Bykov, M., Bykova, E., Dubrovinsky, L. & Dubrovinskaia, N. Synthesis of magnesium-nitrogen salts of polynitrogen anions. *Nat. Commun.* **10**, 4515 (2019).
 49. Bykov, M., Bykova, E., Chariton, S., Prakapenka, V. B., Batyrev, I. G., Mahmood, M. F. & Goncharov, A. F. Stabilization of pentazolate anions in the high-pressure compounds Na₂N₅ and NaN₅ and in the sodium pentazolate framework NaN₅·N₂. *Dalt. Trans.* **50**, 7229–7237 (2021).
 50. Steele, B. A., Stavrou, E., Crowhurst, J. C., Zaug, J. M., Prakapenka, V. B. & Oleynik, I. I. High-Pressure Synthesis of a Pentazolate Salt. *Chem. Mater.* **29**, 735–741 (2017).
 51. Salke, N. P., Xia, K., Fu, S., Zhang, Y., Greenberg, E., Prakapenka, V. B., Liu, J., Sun, J. & Lin, J.-F. Tungsten Hexanitride with Single-Bonded Armchairlike Hexazine Structure at High Pressure. *Phys. Rev. Lett.* **126**, 65702 (2021).
 52. Chen, H., Bykov, M., Batyrev, I. G., Brüning, L., Bykova, E., Mahmood, M. F., Chariton, S., Prakapenka, V. B., Fedotenko, T., Liermann, H., Glazyrin, K., Steele, A. & Goncharov, A. F. High-pressure Synthesis of Cobalt Polynitrides: Unveiling Intriguing Crystal Structures and Nitridation Behavior. *Chem. – A Eur. J.* **30**, e202400536 (2024).
 53. Bykov, M., Bykova, E., Koemets, E., Fedotenko, T., Aprilis, G., Glazyrin, K., Liermann, H.-P., Ponomareva, A. V., Tidholm, J., Tasnádi, F., Abrikosov, I. A., Dubrovinskaia, N. & Dubrovinsky, L. High-Pressure Synthesis of a Nitrogen-Rich Inclusion Compound ReN₈·xN₂ with Conjugated Polymeric Nitrogen Chains. *Angew. Chemie Int. Ed.* **57**, 9048–9053 (2018).
 54. Bykov, M., Bykova, E., Aprilis, G., Glazyrin, K., Koemets, E., Chuvashova, I., Kупenko, I., McCammon, C., Mezouar, M., Prakapenka, V., Liermann, H.-P., Tasnádi, F., Ponomareva, A. V., Abrikosov, I. A., Dubrovinskaia, N. & Dubrovinsky, L. Fe-N system at high pressure reveals a compound featuring polymeric nitrogen chains. *Nat. Commun.* **9**, 2756 (2018).
 55. Bykov, M., Chariton, S., Bykova, E., Khandarkhaeva, S., Fedotenko, T., Ponomareva, A. V., Tidholm, J., Tasnádi, F., Abrikosov, I. A., Sedmak, P., Prakapenka, V., Hanfland, M., Liermann, H. P., Mahmood, M., Goncharov, A. F., Dubrovinskaia, N. & Dubrovinsky, L. High-Pressure Synthesis of Metal–Inorganic Frameworks Hf₄N₂₀·N₂, WN₈·N₂, and Os₅N₂₈·3N₂ with Polymeric Nitrogen Linkers. *Angew. Chemie - Int. Ed.* **59**, 10321–10326 (2020).
 56. Bykov, M., Bykova, E., Ponomareva, A. V., Abrikosov, I. A., Chariton, S., Prakapenka, V. B., Mahmood, M. F., Dubrovinsky, L. & Goncharov, A. F. Stabilization of

- Polynitrogen Anions in Tantalum–Nitrogen Compounds at High Pressure. *Angew. Chemie* **133**, 9085–9090 (2021).
57. Bykov, M., Fedotenko, T., Chariton, S., Laniel, D., Glazyrin, K., Hanfland, M., Smith, J. S., Prakapenka, V. B., Mahmood, M. F., Goncharov, A. F., Ponomareva, A. V., Tasnádi, F., Abrikosov, A. I., Bin Masood, T., Hotz, I., Rudenko, A. N., Katsnelson, M. I., Dubrovinskaia, N., Dubrovinsky, L. & Abrikosov, I. A. High-Pressure Synthesis of Dirac Materials: Layered van der Waals Bonded BeN₄ Polymorph. *Phys. Rev. Lett.* **126**, 175501 (2021).
 58. Laniel, D., Aslandukova, A. A., Aslandukov, A. N., Fedotenko, T., Chariton, S., Glazyrin, K., Prakapenka, V. B., Dubrovinsky, L. S. & Dubrovinskaia, N. High-Pressure Synthesis of the β -Zn₃N₂ Nitride and the α -ZnN₄ and β -ZnN₄ Polynitrogen Compounds. *Inorg. Chem.* **60**, 14594–14601 (2021).
 59. Zhang, C., Sun, C., Hu, B., Yu, C. & Lu, M. Synthesis and characterization of the pentazolate anion cyclo-N₅⁻ in (N₅)₆(H₃O)₃(NH₄)₄Cl. *Science*. **355**, 374–376 (2017).
 60. Xu, Y., Wang, Q., Shen, C., Lin, Q., Wang, P. & Lu, M. A series of energetic metal pentazolate hydrates. *Nature* **549**, 78–81 (2017).
 61. Zhang, C., Yang, C., Hu, B., Yu, C., Zheng, Z. & Sun, C. A symmetric Co(N₅)₂(H₂O)₄ 4H₂O high-nitrogen compound formed by cobalt(II) cation trapping of a cyclo-N₅⁻ anion. *Angew. Chemie - Int. Ed.* **56**, 4512–4514 (2017).
 62. Bykov, M., Chariton, S., Fei, H., Fedotenko, T., Aprilis, G., Ponomareva, A. V., Tasnádi, F., Abrikosov, I. A., Merle, B., Feldner, P., Vogel, S., Schnick, W., Prakapenka, V. B., Greenberg, E., Hanfland, M., Pakhomova, A., Liermann, H.-P., Katsura, T., Dubrovinskaia, N. & Dubrovinsky, L. High-pressure synthesis of ultraincompressible hard rhenium nitride pernitride Re₂(N₂)(N)₂ stable at ambient conditions. *Nat. Commun.* **10**, 2994 (2019).
 63. Jiao, F., Zhang, C. & Xie, W. Energy density of high-pressure nitrogen-rich MN_xcompounds. *Phys. Chem. Chem. Phys.* **23**, 7313–7320 (2021).
 64. Zerr, A., Miehe, G., Serghiou, G., Schwarz, M., Kroke, E., Riedel, R., Fueß, H., Kroll, P. & Boehler, R. Synthesis of cubic silicon nitride. *Nature* **400**, 340–342 (1999).
 65. Jurzick, P. L., Krach, G., Brüning, L., Schnick, W. & Bykov, M. Synthesis and crystal structure of silicon pernitride SiN₂ at 140 GPa. *Acta Crystallogr. Sect. E Crystallogr. Commun.* **79**, 923–925 (2023).
 66. Laniel, D., Trybel, F., Aslandukov, A., Khandarkhaeva, S., Fedotenko, T., Yin, Y., Miyajima, N., Tasnádi, F., Ponomareva, A. V., Jena, N., Akbar, F. I., Winkler, B., Néri, A., Chariton, S., Prakapenka, V., Milman, V., Schnick, W., Rudenko, A. N., Katsnelson, M. I., Abrikosov, I. A., Dubrovinsky, L. & Dubrovinskaia, N. Synthesis of Ultra-Incompressible and Recoverable Carbon Nitrides Featuring CN₄ Tetrahedra. *Adv. Mater.* **36**, 2308030 (2024).
 67. Laniel, D., Trybel, F., Néri, A., Yin, Y., Aslandukov, A., Fedotenko, T., Khandarkhaeva, S., Tasnádi, F., Chariton, S., Giacobbe, C., Bright, E. L., Hanfland, M., Prakapenka, V., Schnick, W., Abrikosov, I. A., Dubrovinsky, L. & Dubrovinskaia, N. Revealing Phosphorus Nitrides up to the Megabar Regime: Synthesis of α' -P₃N₅, δ -P₃N₅ and PN₂. *Chem. – A Eur. J.*, **28**, e202201998 (2022).
 68. Ceppatelli, M., Scelta, D., Serrano-ruiz, M., Dziubek, K., Morana, M., Svitlyk, V., Garbarino, G., Pore, T., Mezouar, M., Peruzzini, M. & Bini, R. Forschungsartikel Nitrides Hot Paper Single-Bonded Cubic AsN from High-Pressure and High-

- Temperature Chemical Reactivity of Arsenic and Nitrogen Forschungsartikel. *Angew. Chemie* **134**, e20211419 (2022).
69. Ceppatelli, M., Serrano-Ruiz, M., Morana, M., Dziubek, K., Scelta, D., Garbarino, G., Poręba, T., Mezouar, M., Bini, R. & Peruzzini, M. High-pressure and high-temperature synthesis of crystalline Sb₃N₅. *Angew. Chemie* **136**, e202319278 (2024).
 70. Laniel, D., Bykov, M., Fedotenko, T., Ponomareva, A. V., Abrikosov, I. A., Glazyrin, K., Svitlyk, V., Dubrovinsky, L. & Dubrovinskaia, N. High Pressure Investigation of the S-N₂ System up to the Megabar Range: Synthesis and Characterization of the SN₂ Solid. *Inorg. Chem.* **58**, 9195–9204 (2019).
 71. Laniel, D., Weck, G. & Loubeyre, P. Xe(N₂)₂ compound to 150 GPa: Reluctance to the formation of a xenon nitride. *Phys. Rev. B* **94**, 174109 (2016).
 72. Miao, M., Sun, Y., Zurek, E. & Lin, H. Chemistry under high pressure. *Nat. Rev. Chem.* **4**, 508–527 (2020).
 73. Lin, J., Wang, F., Rui, Q., Li, J., Wang, Q. & Wang, X. A novel square planar N₄²⁻ ring with aromaticity in BeN₄. *Matter Radiat. Extrem.* **7**, 038401 (2022).
 74. Chen, Y., Cai, X., Wang, H., Wang, H. & Wang, H. Novel triadius-like N₄ specie of iron nitride compounds under high pressure. *Sci. Rep.* **8**, 10670 (2018).
 75. Yu, S., Huang, B., Zeng, Q., Oganov, A. R., Zhang, L. & Frapper, G. Emergence of Novel Polynitrogen Molecule-like Species, Covalent Chains, and Layers in Magnesium-Nitrogen Mg_xN_y Phases under High Pressure. *J. Phys. Chem. C* **121**, 11037–11046 (2017).
 76. Liu, L., Wang, D., Zhang, S. & Zhang, H. Pressure-stabilized GdN₆ with an armchair-antiarmchair structure as a high energy density material. *J. Mater. Chem. A* **9**, 16751–16758 (2021).
 77. Liu, Y., Wang, R., Wang, Z., Li, D. & Cui, T. Formation of twelve-fold iodine coordination at high pressure. *Nat. Commun.* **13**, 412 (2022).
 78. Ehrenreich-Petersen, E., Nielsen, M. B. & Bremholm, M. Experimental equation of state of 11 lanthanide nitrides (NdN to LuN) and pressure induced phase transitions in NdN, SmN, EuN, and GdN. *J. Appl. Phys.* **128**, 135902 (2020).
 79. Aslam, M. A. & Ding, Z. J. Prediction of Thermodynamically Stable Compounds of the Sc-N System under High Pressure. *ACS Omega* **3**, 11477–11485 (2018).
 80. Lin, J., Peng, D., Wang, Q., Li, J., Zhu, H. & Wang, X. Stable nitrogen-rich scandium nitrides and their bonding features under ambient conditions. *Phys. Chem. Chem. Phys.* **23**, 6863–6870 (2021).
 81. Wei, S., Liu, Z., Guo, Y., Sun, H., Chang, Q. & Sun, Y. A novel high-pressure phase of ScN₅ with higher stability predicted from first-principles calculations. *J. Phys. Condens. Matter* **33**, 475401 (2021).
 82. Guo, Y., Wei, S., Liu, Z., Sun, H., Yin, G., Chen, S., Yu, Z., Chang, Q. & Sun, Y. Polymerization of nitrogen in two theoretically predicted high-energy compounds ScN₆ and ScN₇ under modest pressure. *New J. Phys.* **24**, 083015 (2022).
 83. Miao, J. Y., Lu, Z. S., Peng, F. & Lu, C. New Members of High-Energy-Density Compounds: YN₅ and YN₈. *Chinese Phys. Lett.* **38**, 066201 (2021).
 84. Chadwick, B. M. & Sharpe, A. G. in *Rev. Inorg. Chem.* **43**, 83–176 (1966).
 85. Schulz, A. & Surkau, J. Main group cyanides: from hydrogen cyanide to cyanido-

- complexes. *Rev. Inorg. Chem.* **43**, 49–188 (2023).
86. Braun, C., Mereacre, L., Hua, W., Stürzer, T., Ponomarev, I., Kroll, P., Slabon, A., Chen, Z., Damour, Y., Rocquefelte, X., Halet, J. & Indris, S. SnCN₂: A Carbodiimide with an Innovative Approach for Energy Storage Systems and Phosphors in Modern LED Technology. *ChemElectroChem* **7**, 4550–4561 (2020).
 87. Kubus, M., Castro, C., Enseling, D. & Jüstel, T. Room temperature red emitting carbodiimide compound Ca(CN₂):Mn²⁺. *Opt. Mater. (Amst)*. **59**, 126–129 (2016).
 88. Liu, Q., Liu, Y., Dai, G., Tian, L., Xu, J., Zhao, G., Zhang, N. & Fang, Y. Size-controllable synthesis of hierarchical copper carbodiimide microcrystals and their pronounced photoelectric response under visible light. *Appl. Surf. Sci.* **357**, 745–749 (2015).
 89. Sougrati, M. T., Darwiche, A., Liu, X., Mahmoud, A., Hermann, R. P., Jouen, S., Monconduit, L., Dronskowski, R. & Stievano, L. Transition-Metal Carbodiimides as Molecular Negative Electrode Materials for Lithium- and Sodium-Ion Batteries with Excellent Cycling Properties. *Angew. Chemie Int. Ed.* **55**, 5090–5095 (2016).
 90. Eguía-Barrio, A., Castillo-Martínez, E., Liu, X., Dronskowski, R., Armand, M. & Rojo, T. Carbodiimides: New materials applied as anode electrodes for sodium and lithium ion batteries. *J. Mater. Chem. A* **4**, 1608–1611 (2016).
 91. Chen, K., Fehse, M., Laurita, A., Arayamparambil, J. J., Sougrati, M. T., Stievano, L. & Dronskowski, R. Quantum-Chemical Study of the FeNCN Conversion-Reaction Mechanism in Lithium- and Sodium-Ion Batteries. *Angew. Chemie - Int. Ed.* **59**, 3718–3723 (2020).
 92. Sougrati, M. T., Arayamparambil, J. J., Liu, X., Mann, M., Slabon, A., Stievano, L. & Dronskowski, R. Carbodiimides as energy materials: which directions for a reasonable future? *Dalt. Trans.* **47**, 10827–10832 (2018).
 93. Jürgens, B., Irran, E. & Schnick, W. Syntheses, vibrational spectroscopy, and crystal structure determination from X-ray powder diffraction data of alkaline earth dicyanamides M[N(CN)₂]₂ with M = Mg, Ca, Sr, and Ba. *J. Solid State Chem.* **157**, 241–249 (2001).
 94. Jürgens, B., Irran, E. & Schnick, W. Synthesis and characterization of the rare-earth dicyanamides Ln[N(CN)₂]₃ with Ln=La, Ce, Pr, Nd, Sm, and Eu. *J. Solid State Chem.* **178**, 72–78 (2005).
 95. Bessler, K. E., Gatto, C. C., de, M. J., Sales, A., Romualdo, L. L. & Ellena, J. A. Pseudohalides of Main Group Metals: The Alkaline Earth Tricyanomethanides - The Crystal Structures of Calcium and Barium Tricyanomethanide. *Main Gr. Met. Chem.* **30**, 135–142 (2007).
 96. Clark, W. P., Köhn, A. & Niewa, R. The Quasi-Binary Acetonitriletriide Sr₃[C₂N]₂. *Angew. Chemie Int. Ed.* **59**, 339–342 (2020).
 97. Dash, R. R., Gaur, A. & Balomajumder, C. Cyanide in industrial wastewaters and its removal: A review on biotreatment. *J. Hazard. Mater.* **163**, 1–11 (2009).
 98. Kieslich, D. & Christoffers, J. Cyanide Anions as Nucleophilic Catalysts in Organic Synthesis. *Synthesis (Stuttg)*. **53**, 3485–3496 (2021).
 99. Luo, D., Qiao, X. & Dronskowski, R. Predicting Nitrogen-Based Families of Compounds: Transition-Metal Guanidates TCN₃ (T=V, Nb, Ta) and Ortho-Nitrido Carbonates T'₂CN₄ (T'=Ti, Zr, Hf). *Angew. Chemie - Int. Ed.* **60**, 486–492 (2021).

100. Gapurenko, O. A., Griбанова, T. N., Minyaev, R. M. & Minkin, V. I. Octacoordinate carbon atom in tetra(metalloamino)methanes CN₄M₄ (M = Be, Mg, Ca): Quantum-chemical investigation. *Russ. J. Org. Chem.* **43**, 685–690 (2007).
101. Decker, D. L., Beyerlein, R. A., Roulton, G. & Worlton, T. G. Neutron diffraction study of KCN III and KCN IV at high pressure. *Phys. Rev. B* **10**, 3584–3593 (1974).
102. Lapidus, S. H., Halder, G. J., Chupas, P. J. & Chapman, K. W. Exploiting High Pressures to Generate Porosity, Polymorphism, And Lattice Expansion in the Nonporous Molecular Framework Zn(CN)₂. *J. Am. Chem. Soc.* **135**, 7621–7628 (2013).
103. Yakovenko, A. A., Chapman, K. W. & Halder, G. J. Pressure-induced structural phase transformation in cobalt(II) dicyanamide. *Acta Crystallogr. Sect. B Struct. Sci. Cryst. Eng. Mater.* **71**, 252–257 (2015).
104. Boyd, F. R. & England, J. L. Apparatus for phase-equilibrium measurements at pressures up to 50 kilobars and temperatures up to 1750°C. *J. Geophys. Res.* **65**, 741–748 (1960).
105. Kawai, N. & Endo, S. The generation of ultrahigh hydrostatic pressures by a split sphere apparatus. *Rev. Sci. Instrum.* **41**, 1178–1181 (1970).
106. Kantor, I., Prakapenka, V., Kantor, A., Dera, P., Kurnosov, A., Sinogeikin, S., Dubrovinskaia, N. & Dubrovinsky, L. BX90: A new diamond anvil cell design for X-ray diffraction and optical measurements. *Rev. Sci. Instrum.* **83**, 125102 (2012).
107. Anzellini, S., Dewaele, A., Occelli, F., Loubeyre, P. & Mezouar, M. Equation of state of rhenium and application for ultra high pressure calibration. *J. Appl. Phys.* **115**, 043511 (2014).
108. Manghnani, M. H., Katahara, K. & Fisher, E. S. Ultrasonic equation of state of rhenium. *Phys. Rev. B* **9**, 1421–1431 (1974).
109. Boehler, R. New diamond cell for single-crystal x-ray diffraction. *Rev. Sci. Instrum.* **77**, 2004–2007 (2006).
110. Klotz, S., Chervin, J.-C., Munsch, P. & Le Marchand, G. Hydrostatic limits of 11 pressure transmitting media. *J. Phys. D. Appl. Phys.* **42**, 075413 (2009).
111. Jayaraman, A. Diamond anvil cell and high-pressure physical investigations. *Rev. Mod. Phys.* **55**, 65–108 (1983).
112. Kurnosov, A., Kantor, I., Boffa-Ballaran, T., Lindhardt, S., Dubrovinsky, L., Kuznetsov, A. & Zehnder, B. H. A novel gas-loading system for mechanically closing of various types of diamond anvil cells. *Rev. Sci. Instrum.* **79**, 045110 (2008).
113. Sekar, M., Kumar, N. R. S., Sahu, P. C., Chandra Shekar, N. V. & Subramanian, N. Cryogenic gas loading in a Mao–Bell-type diamond anvil cell for high pressure-high temperature investigations. *Rev. Sci. Instrum.* **79**, 076103 (2008).
114. Dorfman, S. M., Prakapenka, V. B., Meng, Y. & Duffy, T. S. Intercomparison of pressure standards (Au, Pt, Mo, MgO, NaCl and Ne) to 2.5 Mbar. *J. Geophys. Res. Solid Earth* **117**, 1–15 (2012).
115. Fei, Y., Ricolleau, A., Frank, M., Mibe, K., Shen, G. & Prakapenka, V. Toward an internally consistent pressure scale. *Proc. Natl. Acad. Sci.* **104**, 9182–9186 (2007).
116. Dewaele, A., Belonoshko, A. B., Garbarino, G., Occelli, F., Bouvier, P., Hanfland, M. & Mezouar, M. High-pressure–high-temperature equation of state of KCl and KBr. *Phys. Rev. B* **85**, 214105 (2012).
117. Shen, G., Wang, Y., Dewaele, A., Wu, C., Fratanduono, D. E., Eggert, J., Klotz, S.,

- Dziubek, K. F., Loubeyre, P., Fat'yanov, O. V., Asimow, P. D., Mashimo, T. & Wentzcovitch, R. M. M. Toward an international practical pressure scale: A proposal for an IPPS ruby gauge (IPPS-Ruby2020). *High Press. Res.* **40**, 299–314 (2020).
118. Akahama, Y. & Kawamura, H. Pressure calibration of diamond anvil Raman gauge to 310 GPa. *J. Appl. Phys.* **100**, 043516 (2006).
 119. Bassett, W. A. Diamond anvil cell, 50th birthday. *High Press. Res.* **29**, 163–186 (2009).
 120. Xie, J., Kar, A., Rothenflue, J. A. & Latham, W. P. Temperature-dependent absorptivity and cutting capability of CO₂, Nd:YAG and chemical oxygen–iodine lasers. *J. Laser Appl.* **9**, 77–85 (1997).
 121. Sobhi, R. M., Adawy, N. A. H. & Zaky, I. S. “Comparative study between the efficacy of fractional CO₂ laser, Q-switched Nd:YAG laser (1064 nm), and both types in treatment of keratosis pilaris”. *Lasers Med. Sci.* **35**, 1367–1376 (2020).
 122. Fedotenko, T., Dubrovinsky, L., Aprilis, G., Koemets, E., Snigirev, A., Snigireva, I., Barannikov, A., Ershov, P., Cova, F., Hanfland, M. & Dubrovinskaia, N. Laser heating setup for diamond anvil cells for in situ synchrotron and in house high and ultra-high pressure studies. *Rev. Sci. Instrum.* **90**, 104501 (2019).
 123. Taylor, G. The phase problem. *Acta Crystallogr. Sect. D Biol. Crystallogr.* **59**, 1881–1890 (2003).
 124. Sheldrick, G. M. SHELXT – Integrated space-group and crystal-structure determination. *Acta Crystallogr. Sect. A Found. Adv.* **71**, 3–8 (2015).
 125. Petricek, V., Dušek, M. & Palatinus, L. Crystallographic computing system JANA2006: General features. *Zeitschrift fur Krist.* **229**, 345–352 (2014).
 126. Smith, J. S. & Desgreniers, S. Selected techniques in diamond anvil cell crystallography: centring samples using X-ray transmission and rocking powder samples to improve X-ray diffraction image quality. *J. Synchrotron Radiat.* **16**, 83–96 (2009).
 127. Bykov, M. Structural aspects of pressure- and temperature-induced phase transitions in low-dimensional systems. PhD thesis, University of Bayreuth. (2015).
 128. Hrubciak, R., Smith, J. S. & Shen, G. Multimode scanning X-ray diffraction microscopy for diamond anvil cell experiments. *Rev. Sci. Instrum.* **90**, 025109 (2019).
 129. Prescher, C. & Prakapenka, V. B. DIOPTAS: A program for reduction of two-dimensional X-ray diffraction data and data exploration. *High Press. Res.* **35**, 223–230 (2015).
 130. Koemets, E. The crystal chemistry of iron oxides and oxyhydroxides at extreme conditions: implications for the deep Earth’s oxygen cycle. PhD thesis, University of Bayreuth. (2020).
 131. Dolomanov, O. V., Bourhis, L. J., Gildea, R. J., Howard, J. A. K. & Puschmann, H. OLEX2: A complete structure solution, refinement and analysis program. *J. Appl. Crystallogr.* **42**, 339–341 (2009).
 132. Sheldrick, G. M. SHELXT - Integrated space-group and crystal-structure determination. *Acta Crystallogr. Sect. A Found. Crystallogr.* **71**, 3–8 (2015).
 133. Sheldrick, G. M. Crystal structure refinement with SHELXL. *Acta Crystallogr. Sect. C Struct. Chem.* **71**, 3–8 (2015).
 134. Vinet, P., Ferrante, J., Rose, J. H. & Smith, J. R. Compressibility of solids. *J. Geophys. Res.* **92**, 9319–9325 (1987).

135. Birch, F. Finite elastic strain of cubic crystals. *Phys. Rev.* **71**, 809–824 (1947).
136. Goncharov, A. F. & Struzhkin, V. V. Raman spectroscopy of metals, high-temperature superconductors and related materials under high pressure. *J. Raman Spectrosc.* **34**, 532–548 (2003).
137. Hohenberg, P. & Kohn, W. Inhomogeneous Electron Gas. *Phys. Rev.* **136**, B864–B871 (1964).
138. Kohn, W. & Sham, L. J. Self-Consistent Equations Including Exchange and Correlation Effects. *Phys. Rev.* **140**, A1133–A1138 (1965).
139. Ziesche, P., Kurth, S. & Perdew, J. P. Density functionals from LDA to GGA. *Comput. Mater. Sci.* **11**, 122–127 (1998).
140. Tao, J., Perdew, J. P., Staroverov, V. N. & Scuseria, G. E. Climbing the Density Functional Ladder: Nonempirical Meta-Generalized Gradient Approximation Designed for Molecules and Solids. *Phys. Rev. Lett.* **91**, 146401 (2003).
141. Heyd, J., Scuseria, G. E. & Ernzerhof, M. Hybrid functionals based on a screened Coulomb potential. *J. Chem. Phys.* **118**, 8207–8215 (2003).
142. Kresse, G. & Furthmüller, J. Efficient iterative schemes for ab initio total-energy calculations using a plane-wave basis set. *Phys. Rev. B* **54**, 11169 (1996).
143. Blöchl, P. E. Projector augmented-wave method. *Phys. Rev. B* **50**, 17953–17979 (1994).
144. Perdew, J. P., Burke, K. & Ernzerhof, M. Generalized gradient approximation made simple. *Phys. Rev. Lett.* **77**, 3865–3868 (1996).

5. Manuscripts of the thesis

5.1. Domain Auto Finder (DAFi) program: the analysis of single-crystal X-ray diffraction data from polycrystalline samples

This section contains the following manuscript:

“Domain Auto Finder (DAFi) program: the analysis of single-crystal X-ray diffraction data from polycrystalline samples”

A. Aslandukov, M. Aslandukov, N. Dubrovinskaia, L. Dubrovinsky

Status: published in *Journal of Applied Crystallography*, 55(5), 1383-1391

(2022)

Reproduced under the terms and conditions of the Creative Commons ‘CC BY 4.0’



Domain Auto Finder (DAFi) program: the analysis of single-crystal X-ray diffraction data from polycrystalline samples

Andrey Aslandukov,^{a,b*} Matvii Aslandukov,^c Natalia Dubrovinskaia^{a,d} and Leonid Dubrovinsky^b

Received 1 February 2022
Accepted 12 August 2022

Edited by A. H. Liu, HPSTAR and Harbin Institute of Technology, People's Republic of China

Keywords: single-crystal domain auto finder; DAFi; single-crystal X-ray diffraction; polycrystalline samples; multiphase mixtures.

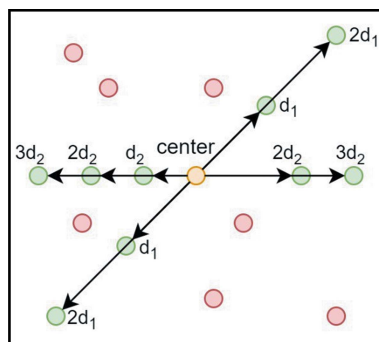
^aMaterial Physics and Technology at Extreme Conditions, Laboratory of Crystallography, University of Bayreuth, Universitaetsstrasse 30, Bayreuth, D-95440, Germany, ^bBayerisches Geoinstitut, University of Bayreuth, Bayreuth, D-95440, Germany, ^cKharkiv National University of Radio Electronics, Nauky Avenue 14, Kharkiv, 61166, Ukraine, and ^dDepartment of Physics, Chemistry and Biology (IFM), Linköping University, Linköping, SE 581 83, Sweden.
*Correspondence e-mail: andrii.aslandukov@uni-bayreuth.de

This paper presents the *Domain Auto Finder (DAFi)* program and its application to the analysis of single-crystal X-ray diffraction (SC-XRD) data from multiphase mixtures of microcrystalline solids and powders. Superposition of numerous reflections originating from a large number of single-crystal domains of the same and/or different (especially unknown) phases usually precludes the sorting of reflections coming from individual domains, making their automatic indexing impossible. The *DAFi* algorithm is designed to quickly find subsets of reflections from individual domains in a whole set of SC-XRD data. Further indexing of all found subsets can be easily performed using widely accessible crystallographic packages. As the algorithm neither requires *a priori* crystallographic information nor is limited by the number of phases or individual domains, *DAFi* is powerful software to be used for studies of multiphase polycrystalline and microcrystalline (powder) materials. The algorithm is validated by testing on X-ray diffraction data sets obtained from real samples: a multi-mineral basalt rock at ambient conditions and products of the chemical reaction of yttrium and nitrogen in a laser-heated diamond anvil cell at 50 GPa. The high performance of the *DAFi* algorithm means it can be used for processing SC-XRD data online during experiments at synchrotron facilities.

1. Introduction

For more than a century, single-crystal X-ray diffraction (SC-XRD) has been a powerful method for determining the structure of crystalline solids. Until very recently it could be applied to single crystals not smaller than dozens of micrometres, but many compounds are only available in a polycrystalline form or as fine powders. State-of-the-art powder X-ray diffraction (XRD) data analysis, including Rietveld refinement in combination with *ab initio* structure search, can help with structure interpretation if sufficiently large crystals are unavailable and their preparation or growth is infeasible. This concerns investigations of natural objects or drugs, *in situ* studies of matter under extreme conditions, or processes in solids involving domain formation or reconstructive phase transitions. However, when it comes to multiphase systems with unknown microcrystalline compounds, the problem of structure solution for individual components becomes even more difficult.

In recent decades, the development of third- and fourth-generation synchrotrons, such as the Advanced Photon Source (in Lemont, USA), PETRA III (in Hamburg, Germany) and the ESRF (in Grenoble, France), with the ESRF-EBS (the



Published under a CC BY 4.0 licence

computer programs

Extremely Brilliant Source, the ESRF's facility upgrade over 2015–2022, which increases the brilliance and coherence of the X-ray beams produced by a factor of 100 compared with present-day light sources; <https://www.esrf.fr/about/upgrade>), has provided users with new opportunities. At the cutting-edge beamlines, such as ID11 at the ESRF, the size of the X-ray beam ($0.5 \times 0.5 \mu\text{m}$ FWHM) is commensurate with the size of crystalline domains of polycrystalline samples or fine powder particles, which makes it possible to study each micrometre- to submicrometre-size grain individually by methods of SC-XRD, considering the sphere of confusion of the diffractometer of only a few hundred nanometres. This approach was devised for and first applied to studying products of chemical reactions and phase transformations in laser-heated diamond anvil cells (DACs); this has led to discoveries of many exotic compounds, revealing their crystal structures *in situ* under high pressure (e.g. Bykova *et al.*, 2016, 2018; Laniel, Winkler, Bykova *et al.*, 2020; Laniel, Winkler, Fedotenko *et al.*, 2020; Bykov *et al.*, 2020, 2021; Aslandukova *et al.*, 2021; Dubrovinskaia & Dubrovinsky, 2018; Ceppatelli *et al.*, 2022).

Still, processing SC-XRD data containing a lot of reflections coming from numerous crystalline grains is a difficult task, especially in the presence of a few different phases in a multicomponent system and/or in the absence of any *a priori* information about their chemical composition and/or basic crystallographic characteristics, such as the unit-cell parameters. The diffraction data collected from samples under high pressure in a DAC are additionally complicated by undesired but unavoidable reflections from diamond anvils, pressure-transmitting media, gasket materials and other factors. Therefore, the development of software which would allow an automatic separation of the reflections originating from an individual crystalline domain, *i.e.* a search for the domain in a

complex pattern of spots in the reciprocal space, is an urgent task aimed at rationalizing SC-XRD data processing and making it routine for inexperienced users.

To date, several programs have been developed for multi-grain indexing. If the unit-cell parameters are known *a priori*, e.g. from powder XRD data, indexing means finding the orientation matrices of the grains in the sample and sorting the reciprocal-space vectors with regard to the grain of origin. Following the presentation of the program *GRAINDEX* (Lauridsen *et al.*, 2001), several alternative approaches have been proposed (Wright, 2006; Ludwig *et al.*, 2009; Moscicki *et al.*, 2009; Schmidt, 2014). The programs *ImageD11* (Wright, 2006) and *GrainSpotter* (Schmidt, 2014) are now incorporated into the *FABLE* (*Fully Automatic BeamLine Experiments*) package (Sørensen *et al.*, 2012). The main limitation of the above-mentioned software is that it is designed to be applied almost exclusively to the analysis of mono-phase materials. Furthermore, the multigrain indexing programs mentioned above all assume that the space group (or at least symmetry) and the unit-cell parameters of phases are known. One straightforward way to generalize the previous approaches is to apply the multigrain indexing algorithms repeatedly, once for each phase (Jimenez-Melero *et al.*, 2011; Sørensen *et al.*, 2012), but this still requires the phases to be identified in advance.

To our knowledge, there have only been a few proposals for dealing with unknown phases, based on a fast Fourier transform approach (Sørensen *et al.*, 2012) or on pattern recognition (Sørensen *et al.*, 2012), or involving a search of reflections and subsequent unit-cell optimization in 3D space (Wejdemann & Poulsen, 2016). Testing of these programs was performed on data sets artificially created by randomly rotating 'grains' with exactly defined unit-cell parameters, and there is no information on how well these programs would

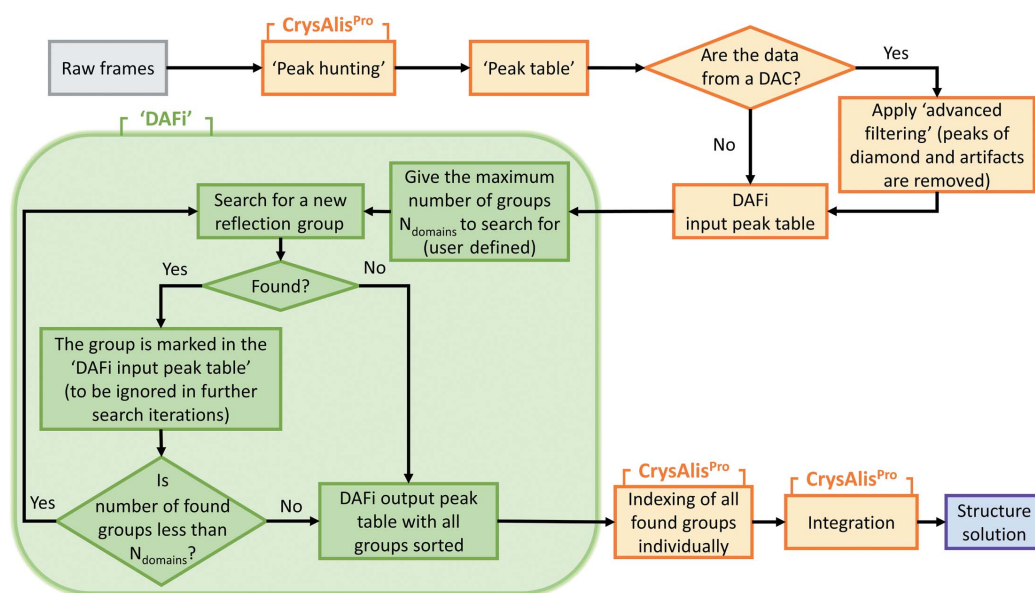


Figure 1

A data flowchart for the analysis of single-crystal XRD data from polycrystalline materials. The *DAFi* program is implemented to sort groups of reflections originating from individual single-crystal domains (see the text for detailed explanations).

work with real data sets where one may need to consider statistical and instrumental errors in the positions of reflections in the reciprocal space, or deal with ‘junk’ reflections characteristic of the XRD data sets originating from high-pressure experiments in DACs. Another important problem is the long program running time; *e.g.* according to Wejdemann & Poulsen (2016), indexing of 500 cementite grains takes 5 days.

In this article, we describe our methodological approach to the analysis of XRD data from polycrystalline materials and present the *DAFi* program which helps to automate the search for individual crystalline domains. A flowchart of the analysis is shown in Fig. 1. The *DAFi* program can be applied at that stage of the analysis when the diffraction from individual crystalline domains should be sorted. The algorithm does not need any *a priori* crystallographic knowledge, and there is no limitation on the phase composition of polycrystalline material and the number of crystalline domains of each phase. The algorithm is implemented with C++ code. Its important advantage is the extremely high speed of data processing. With the number of reflections in the input XRD data set (input peak table) equal to $N_{\text{reflections}}$, the algorithm has $O(N_{\text{reflections}}^2 \log N_{\text{reflections}})$ time complexity on a single-core processor, so that a typical computational time is several minutes. Implemented multithreading capability allows a further decrease of the computational time by dividing by the number of processor cores.

While the *DAFi* program enables the diffraction data of each domain to be separated from those of other domains, the data can be further processed using standard methods of single-crystal X-ray crystallography aimed at structure solution and refinement. The output of the current version of the *DAFi* program is compatible with the *CrysAlis^{Pro}* software, which performs indexing of each found domain individually with just one click. However, there will not be a problem using the *DAFi* output file(s) with other standard indexing algorithms implemented in any available crystallographic programs. The algorithm of the *DAFi* program is described in detail below.

2. Algorithm

2.1. Input and output data

The algorithm requires only a set of coordinates of all reflections in the reciprocal space. Currently, the *DAFi* program reads these coordinates from the `peaktable.tabbin` file generated by the *CrysAlis^{Pro}* software after ‘peak hunting’ (Fig. 1). If the XRD data originate from high-pressure experiments in a DAC, ‘advanced filtering’ (Koemets, 2020) is applied to eliminate the peaks produced by diamonds and the other diffraction artifacts associated with such a type of XRD raw data. After the ‘*DAFi* input peak table’ data processing, the *DAFi* program generates the output file(s), which is the ‘*DAFi* output peak table’ with the subsets of peaks sorted and numbered in the course of the search (see below for details). This means that the *DAFi* program updates the initial *CrysAlis^{Pro}* `peaktable.tabbin` file by marking each reflection with the number of the subset (subset ID) to which it belongs.

2.2. General structure of the algorithm

The ‘peak table’ generated by the *CrysAlis^{Pro}* software presents all diffraction peaks produced by a polycrystalline sample, which are visualized as a set of points in the reciprocal space. The whole set of points is a result of a superposition of numerous ‘subsets’ – the reciprocal-lattice points which belong to individual crystalline domains. Thus, if a subset is identified, then it can be indexed separately using standard crystallographic programs, and the crystal structure of the associated domain can be solved and refined.

Sorting subsets in the whole pattern of points in the reciprocal space is exactly the task of the *DAFi* program. The advantage of the implemented algorithm is that it selects the subsets purely geometrically, considering only a definition of a lattice (no time-consuming indexing is involved). As any 3D lattice is defined by three lattice vectors, the latter define three directions in a 3D space and the distances between the adjacent lattice points in these three directions. Obviously, a lattice can be recognized if considered as rows of equally distant

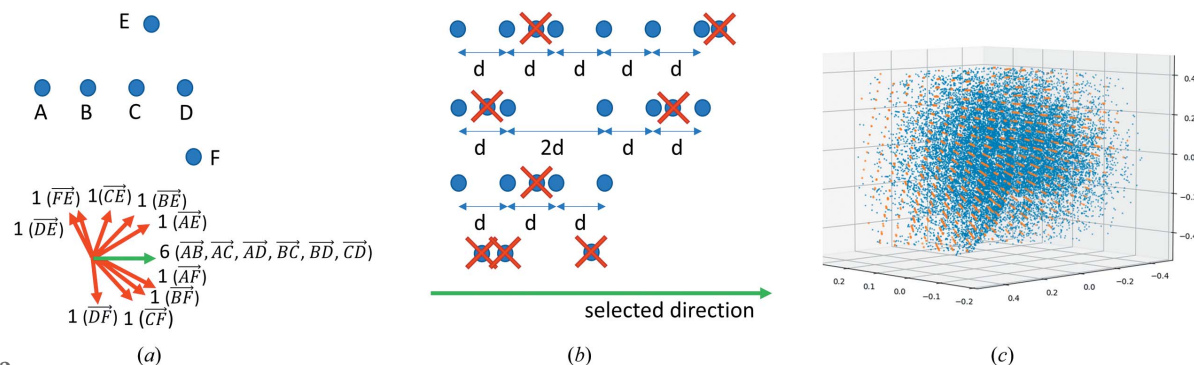


Figure 2 Illustration of the two main stages of the algorithm. (a) First stage: finding a set of possible directions (shown here by arrows) for a given set of reflections (here blue points A through F) and selecting the ‘best’ one(s) to consider at the second stage. Among the ten directions found for the set of points A, B, C, D, E, F, the ‘best’ one (shown by the green arrow) is identified as that corresponding to the largest number of collinear vectors. (b) The second stage: finding the ‘proper’ distance between the reflections (here denoted as ‘d’) in the selected direction. (c) An example of a view of the reciprocal space with the subset of points (orange dots) found in the initial set (blue dots).

points aligned in one direction, so the algorithm relies on finding such rows (*i.e.* a direction vector and a ‘proper’ distance between the adjacent points along the direction vector). This simplifies the search, which is realized iteratively. As soon as one subset of points is found, it is separated from the pool of all points, and only the remaining ones are considered in the next search.

The algorithm consists of two main stages:

(i) Finding a set of possible directions [Fig. 2(a)] and selecting the ‘best’ ones to consider at the second stage.

(ii) Finding the ‘proper’ distance between the reflections for a given direction [Fig. 2(b)] and identifying the nodes of the reciprocal lattice [Fig. 2(c)] generated by the chosen pair (direction, distance).

Combining these two parts we can find the ‘best’ pair (direction, distance), which corresponds to the biggest group of reflections belonging to one single-crystal domain. In Section 2.3 we describe different approaches to finding a set of possible directions, while in Section 2.4 we present an effective way to find the correct group of reflections for the given direction.

For the convenience of further mathematical description of the algorithm, the terms used below are defined as follows:

A *point* is a single diffraction reflection in the reciprocal space. The *points* are denoted as $p_1, p_2, \dots, p_{N_{\text{reflections}}}$ and are represented as radius vectors $\vec{rp}_1, \vec{rp}_2, \dots, \vec{rp}_{N_{\text{reflections}}}$ in a 3D space.

A *row* is a subset of reflections that lie on the same line in the reciprocal space.

A *group* is a subset of reflections in the reciprocal space belonging to a distinct single-crystal domain.

2.3. First stage of the algorithm

Before the main algorithm, *point* normalization is applied:

(i) All radius vectors are shifted by the vector $(-\sum_{i=1}^n \vec{rp}_i)/n$, which shifts the center of the *points*’ system to the coordinate (0, 0, 0).

(ii) The coordinates (x_i, y_i, z_i) of each radius vector are divided by the maximum absolute value of the corresponding coordinate among all radius vectors (*i.e.* $X = \max_{i=1\dots n} |x_i|$, $Y = \max_{i=1\dots n} |y_i|$, $Z = \max_{i=1\dots n} |z_i|$). After that all radius vectors’ coordinates are transformed into $(x_i/X, y_i/Y, z_i/Z)$ and belong to the range $[-1; 1]$.

The shift described in the first step of the normalization procedure aims exclusively to improve the stability of the algorithm during the calculations. Although in practice the shift is very small, the shifting at the very beginning makes the algorithm more stable due to coordinates being transformed into a more uniform distribution. At the same time, the second part of the normalization procedure is important for further calculations [especially for the correct use of allowed absolute and relative errors (epsilon constants) in the second stage].

It is easy to see that the direction vector that determines the *group* will be equal to the direction vector between some two initial *points*. So, the most straightforward approach is to create a set of possible directions as a set of all direction vectors between each pair of initial *points*. However, such a set

has a size of $O(N_{\text{reflections}}^2)$, which is too large for the second stage of the algorithm. In Section 2.3.1 we propose a simple way to select only N_{dirs} ‘best’ directions out of all $O(N_{\text{reflections}}^2)$, where N_{dirs} is any integer constant (naive approach), and in Section 2.3.2 we propose an improved version of such a selection (smart approach). Both naive and smart approaches are implemented in *DAFi* and the user can select which one to use in the configuration file.

2.3.1. Naive approach. Ideally, we would like to select directions along which the second part of the algorithm will produce the largest possible *group*. We do not know in advance which directions are the ‘best’; however, we can see that if a *group* consists of k rows with sizes s_1, s_2, \dots, s_k , then there are exactly $S = \sum_{i=1}^k [s_i(s_i - 1)]/2$ pairs of initial *points* that produce the same direction vector. This allows us to define the ‘best’ direction as the direction with a maximum number of pairs of initial *points* that produce it. However, because the initial *points* are real valued (have non-integer coordinates), all S generated vectors can differ slightly. To compare different real-valued vectors we transform them in two steps.

Before the first step of transforming a vector (x_0, x_1, x_2) , where x_0, x_1, x_2 are the coordinates of the real-valued vector that we are transforming, index $k \in \{0, 1, 2\}$ is found such that $|x_k| = \max\{|x_0|, |x_1|, |x_2|\}$.

In the first step we make a transformation after which opposite vectors are considered to be equal: $(x_0, x_1, x_2) \rightarrow \text{sgn}(x_k) \times (x_0, x_1, x_2)$.

In the second step we transform the obtained vector to an integer-valued triplet: $(x_0, x_1, x_2) \rightarrow \{k, [(x_i + 0.5^{1/2})/\varepsilon_1], [(x_j + 0.5^{1/2})/\varepsilon_1]\}$, where i and j are two indices from $\{0, 1, 2\}$ not equal to k , ε_1 is a constant representing the allowed absolute error, and square brackets denote the integer part of a fractional number.

To illustrate this, let us consider a numerical example. Suppose that we want to transform a direction vector $(-0.36, -0.8, 0.48)$. $x_0 = -0.36, x_1 = -0.8, x_2 = 0.48$. Note that $x_0^2 + x_1^2 + x_2^2 = 1$, because we are working with just a direction. Then the three steps of the transformation will be the following:

- (i) $k = 1$ because $|x_1|$ is maximum among $|x_0|, |x_1|, |x_2|$.
- (ii) $(-0.36, -0.8, 0.48) \rightarrow \text{sgn}(-0.8) \times (-0.36, -0.8, 0.48) = (0.36, 0.8, -0.48)$.
- (iii) $i = 0, j = 2$ because there are only two indices from $\{0, 1, 2\}$ which are not equal to $k = 1$.

Let us also assume that $\varepsilon_1 = 0.01$. Then we get the following integer-valued triplet:

$$\begin{aligned} (0.36, 0.8, -0.48) &\rightarrow \left\{ 1, \left[\frac{x_0 + 0.5^{1/2}}{0.01} \right], \left[\frac{x_2 + 0.5^{1/2}}{0.01} \right] \right\} \\ &= \left\{ 1, \left[\frac{0.36 + 0.5^{1/2}}{0.01} \right], \left[\frac{-0.48 + 0.5^{1/2}}{0.01} \right] \right\} \\ &= \left\{ 1, \left[\frac{1.067}{0.01} \right], \left[\frac{0.2271}{0.01} \right] \right\} = (1, 106, 22). \end{aligned} \tag{1}$$

After such a transformation, each direction is represented as an integer-valued triplet with values in the range $(0 \dots 2, 0 \dots X, 0 \dots X)$, where $X = \lceil (2(0.5)^{1/2})/\varepsilon_1 - 1 \rceil$, so we can calculate a distribution of all directions using an array of size $3X^2$. After distribution calculation, we can find the top N_{dirs} directions in time $O(X^2)$ using a standard selection algorithm for finding the k th-order statistic (Blum *et al.*, 1973). To transform the integer-valued triplet back to the real-valued vector, we can use the following formula:

$$(k, a, b) \rightarrow \overrightarrow{(x_0, x_1, x_2)}, \quad (2)$$

where $x_i = (a + 0.5)\varepsilon_1 - 0.5^{1/2}$, $x_j = (b + 0.5)\varepsilon_1 - 0.5^{1/2}$, $x_k = (1 - x_i^2 - x_j^2)^{1/2}$, and i, j are two indices from $\{0, 1, 2\}$ not equal to k .

This approach is the most straightforward way to select the ‘best’ N_{dirs} directions; however, it has drawbacks. The main one is that this approach does not use information about distances between *points*, which means that even with a large number of *points* lying on the same line, the second part of the algorithm may still not find the *group* if these *points* are located at unequal distances.

2.3.2. Smart approach. Below we present the second approach to select the ‘best’ N_{dirs} directions, which does not have the drawbacks mentioned above. We are still going to select the ‘best’ N_{dirs} directions from some distribution; however, instead of creating a distribution from all $O(N_{\text{reflections}}^2)$ vectors, we will use only some of the more important of them. Namely, let us iterate over the ‘center’ *point* p_c and find all possible *rows* of size at least 4 that go through the *point* p_c and consist of only equidistant *points*. In order to do this, first of all let us group all other $N_{\text{reflections}} - 1$ *points* in *rows* with respect to our center *point* p_c . This can be done by clustering all direction vectors $\overrightarrow{p_c p_k} = \overrightarrow{rp_k} - \overrightarrow{rp_c}$ ($k \neq c$), similarly to the method described in Section 2.3.1. After this, for each *row*, we can independently find the largest subset of *points* where each *point* lies at an equivalent distance from the previous one. To do this, let us find out, for each *point* p_i , at which distances d it will be in the same *row* as a *point* p_c .

Let us denote by D the distance between *points* p_i and p_c . Then we can say that p_i is the k th *point* in a *row* with 0th *point* p_c if the following holds: $|D - kd| \leq d\varepsilon_2$, where ε_2 is some small constant that allows a small absolute error. From this inequality we can obtain that valid distances form the following range: $d \in [D/(k + \varepsilon_2); D/(k - \varepsilon_2)]$. After finding such ranges for all *points* p_i we can find the value of d that belongs to the largest number of ranges using the scanline algorithm (Klee, 1977). If this value is at least 3, then there exists a *row* that contains at least 4 *points* and with high probability belongs to a *group*. Only in such a case will we use the corresponding direction vector in our distribution. Such an approach takes $(N_{\text{reflections}}^2 K_{\text{max}} \log N_{\text{reflections}})$ time, where K_{max} is the maximum *point*’s relative number on the *row* under consideration and $K_{\text{max}} = 5$ works well in practice.

The smart approach catches fewer ‘junk’ reflections (Fig. 3) and, therefore, provides a better distribution of direction vectors to the second stage of the algorithm. However, this approach is a bit slower, because instead of $O(N_{\text{reflections}}^2)$ time, it requires $O(N_{\text{reflections}}^2 K_{\text{max}} \log N_{\text{reflections}})$.

2.4. Second stage of the algorithm

Given a direction vector $\vec{v} = \overrightarrow{(vx_0, vx_1, vx_2)}$, we have to find the ‘best’ distance d between adjacent *points* towards a direction \vec{v} that generates the *group* of maximum size. Let $k = \arg \max |vx_i|$. Then we can project all initial *points* to a plane $x_k = 0$: radius vector $\overrightarrow{rp}(rpx_0, rpx_1, rpx_2)$ of *point* p will be transformed to $\overrightarrow{rp}' = [\overrightarrow{rp} - \vec{v}(rpx_k/vx_k)]$. After such a transformation, all *points* that belong to the same *row* in the direction \vec{v} will be projected to the same *point* on a plane. This allows all different *rows* to be obtained by clustering of all projected *points*. Such clustering can be done in linear time using radix sort (Cormen *et al.*, 2001) and two linear passes that select equal *points* in 2×2 grid squares. After grouping all *points* into *rows*, we can create an array ds of all distances between adjacent *points* in the same *row* and choose d as the most frequent number in the array ds . Because all distances are real numbers, we have to use tolerance ε_3 and choose d

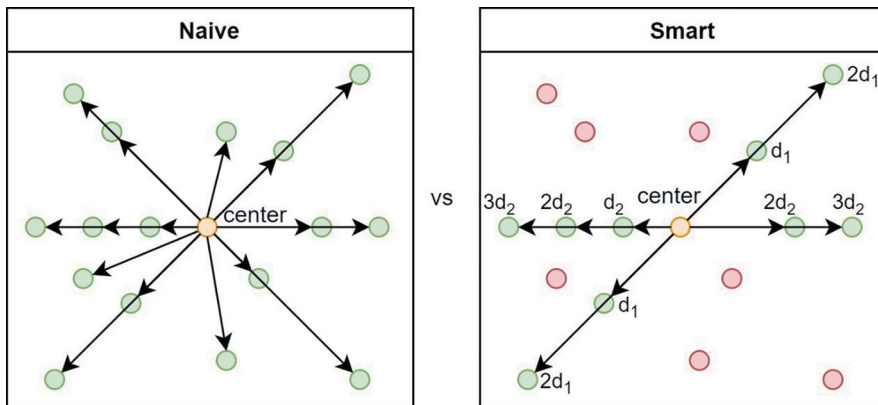


Figure 3 Comparison of naive and smart approaches. The naive approach implies consideration of all directions, while the smart one considers only the directions with *rows* of equidistant *points*.

such that an interval $[d - \varepsilon_3; d + \varepsilon_3]$ contains the most values from the array ds . Such a d can be found in linear time using the two pointers technique for maintaining a sliding window of size $2\varepsilon_3$ after sorting the array ds .

After finding the d value, we can find the exact *group* formed by a pair (\vec{v}, d) as a union of all largest valid subsets of *points* for each independent *row*. In order to find the largest valid subset for a given *row*, we introduce an auxiliary array ‘shifts’, where $shifts_i$ denotes the distance from a *point* p_i to the plane $x_k = 0$ towards the direction \vec{v} . Since the distance between all adjacent *points* in a *group*’s *row* is equal to d , for a valid subset of *points* it holds that all

remainders $\text{shifts}_i \bmod d$ are equal, where mod denotes the modulo operation, *i.e.* $a \bmod b = x$, $0 \leq x < b$, $a - x = Kb$, $K \in \mathbb{Z}$. This allows us to find the largest valid subset as the largest subset of *points* with equal values of $\text{shifts}_i \bmod d$ and pairwise different values of shifts_i/d . It can be found in $O(n \log n)$ time using the two pointers technique for maintaining the set of all values shifts_i/d in a sliding window, where n is the number of *points* in the current *row*. Similarly to Section 2.3.2, the values $\text{shifts}_{i_1} \bmod d$ and $\text{shifts}_{i_2} \bmod d$ are considered equal iff $|\text{shifts}_{i_1} \bmod d - \text{shifts}_{i_2} \bmod d| \leq d\varepsilon_2$. The program has a configuration file that allows one to flexibly adjust all necessary parameters and in particular values ε_1 and ε_2 . Smaller values of tolerance will result in a more precise *group*; however, the found *group* will contain fewer reflections.

The time complexity of this stage can be estimated as $O(N_{\text{reflections}} \log N_{\text{reflections}})$ per direction, so the total time complexity for processing all best N_{dirs} directions found in the previous stage is $O(N_{\text{dirs}} N_{\text{reflections}} \log N_{\text{reflections}})$.

2.5. Speed optimizations

Without any optimizations, the program finds all *groups* one by one, so the total time complexity is

$$O[N_{\text{domains}}(N_{\text{reflections}} \log N_{\text{reflections}})(N_{\text{reflections}} K_{\text{max}} + N_{\text{dirs}})]. \quad (3)$$

There are, however, some implemented optimizations that allow the algorithm to be significantly speeded up:

(i) Both stages of the algorithm allow the use of multi-threading (in the first stage several threads uniformly process $N_{\text{reflections}}$ ‘center’ *points*, and in the second stage several threads uniformly process N_{dirs} different best directions from the first stage).

(ii) The distribution of the ‘best’ directions is calculated only at the beginning of the program and, instead of recalculation from scratch on the following iterations, the distribution is just maintained by subtracting the impact of the removed *points* from the found *group* in time $O(N_{\text{removed}} N_{\text{reflections}})$, where N_{removed} is the number of *points* in the last *group* found.

(iii) In fact, the algorithm finds N_{dirs} different *groups* in one iteration (one for each direction from the first stage), so there is an option to choose not just the largest *group*, but $N_{\text{groups}} > 1$ largest *groups* at once. This is done by firstly selecting the largest *group*, then the largest *group* with *points* not selected in the first *group*, and so on. Such an option allows the algorithm to be speeded up N_{groups} times; however, it may slightly decrease the quality of the search.

When combined, such optimizations allow the algorithm to be speeded up to the time complexity

$$O\left\{ [N_{\text{reflections}}^2 K_{\text{max}} \log N_{\text{reflections}} + (N_{\text{domains}}/N_{\text{groups}}) \times (N_{\text{reflections}}^2 \log N_{\text{reflections}})] / N_{\text{cores}} \right\}, \quad (4)$$

where N_{cores} is the number of processor cores and N_{groups} is the number of *groups* to be found in one iteration. Assuming that

$K_{\text{max}}, N_{\text{cores}}, N_{\text{domains}}$ and N_{groups} are all constants, the total time complexity can be simplified to $O(N_{\text{reflections}}^2 \log N_{\text{reflections}})$.

3. Examples of application

The testing of the *DAFi* program was performed on SC-XRD data sets obtained from real polycrystalline samples: (i) a natural basalt rock and (ii) a piece of yttrium (Y) embedded into molecular nitrogen and laser-heated in a DAC. The results of these tests are described below as examples 1 and 2.

Example 1. Study of a sample of basalt rock from the Rauher Kulm mountain/SC-XRD data collected using an in-house diffractometer. Basalt rock is a natural polycrystalline aggregate of several minerals. A sample of basalt was collected by LD and ND at the Rauher Kulm mountain, which is a paleovolcano located in the Upper Palatinate region of the state of Bavaria, 23 km southeast of Bayreuth (Germany). A small isometric dark-gray grain of the rock (of about 40 μm in diameter) with sub-grains barely distinguishable under an optical microscope ($\times 200$) was mounted on a goniometer head. A single-crystal XRD data set was collected using a diffractometer equipped with a Bruker D8 platform (the three-axis goniometer), an APEX detector and an Ag $K\alpha$ Incoatec I μ S source (beam size of $\sim 50 \mu\text{m}$ FWHM, half-sphere data collection, a collection time of 60 s with a step of 0.3° , 1265 frames). The peak hunting procedure in the *CrysAlis^{Pro}* software found 2928 reflections.

The search for 18 groups of reflections (the number set by the user) in a pool of 2928 reflections took the *DAFi* program 31 s (Fig. 4 and Table 1). Each of the 18 groups found had its own size (the number of reflections included in the group). In the course of further data processing and indexing using *CrysAlis^{Pro}*, some groups were merged, as the *CrysAlis^{Pro}* program recognized them as related to the same single-crystal domain. For example, eight groups (3, 5, 6, 9, 10, 14, 16 and 18) were merged with group 1, whose size increased from 421 (as found by *DAFi*) to 1312 reflections after indexing (see Table 1). Further processing in *CrysAlis^{Pro}* revealed crystallographic parameters of the mineral olivine. The olivine crystallite is mosaic, and its nine slightly misaligned domains were recognized by *DAFi* separately, whereas *CrysAlis^{Pro}*, due to the higher tolerance (0.125 in this particular case), counted the whole crystallite as one domain. Thus, *CrysAlis^{Pro}* revealed the crystallographic data for seven independent

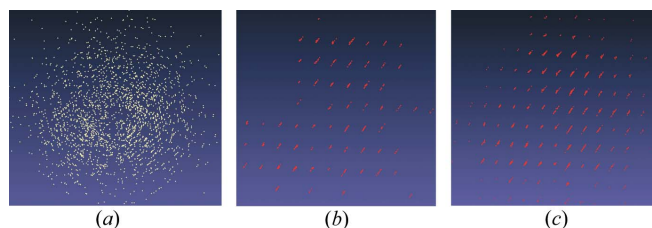


Figure 4 Reciprocal space representing SC-XRD data from a sample of basalt: (a) all reflections; (b) reflections of group 1 as found by the *DAFi* program; (c) reflections of group 1 extended by *CrysAlis^{Pro}* software.

Table 1
Results of the *DAFi* run on the data set collected from a sample of basalt.

Group No.	Size of group found by <i>DAFi</i>	Size of group after indexing in <i>CrysAlis^{Pro}</i> †	Lattice parameters						Minerals
			<i>a</i> (Å)	<i>b</i> (Å)	<i>c</i> (Å)	α (°)	β (°)	γ (°)	
1	421	1312	4.7881 (7)	6.0329 (10)	10.3079 (2)	90	90	90	Olivine
2	197	494	5.2989 (17)	8.911 (3)	9.755 (3)	90	105.47 (3)	90	Phlogopite
3	171	Merged with group 1							
4	137	372	8.425 (3)	8.425 (3)	8.425 (3)	90	90	90	Chromite
5	107	Merged with group 1							
6	57	Merged with group 1							
7	82	Merged with group 2							
8	57	Merged with group 3							
9	38	Merged with group 1							
10	41	Merged with group 1							
11	25	140	8.425 (3)	8.425 (3)	8.425 (3)	90	90	90	Chromite
12	28	Merged with group 3							
13	15	98	5.317 (8)	8.907 (5)	9.723 (9)	90	105.35 (12)	90	Phlogopite
14	16	Merged with group 1							
15	21	86	5.286 (9)	8.970 (17)	9.752 (19)	90	106.0 (2)	90	Phlogopite
16	20	Merged with group 1							
17	20	85	8.398 (6)	8.398 (6)	8.398 (6)	90	90	90	Chromite
18	26	Merged with group 1							

† Indexing performed with a tolerance of 0.125.

single-crystal domains of three different minerals: three domains of phlogopite, three of chromite and one domain of olivine (Table 1).

Example 2. Study of products of the reaction of yttrium and nitrogen in a double-sided laser-heated DAC at 50 GPa. A piece of yttrium was placed in the sample chamber of a BX90-type large X-ray aperture DAC (Kantor *et al.*, 2012) equipped with Boehler–Almax-type diamonds with 250 μm culets. Molecular nitrogen was then loaded into the DAC using a high-pressure gas loading system. The sample was compressed to ~ 50 GPa and laser-heated ($\lambda = 1064$ nm) to 2000 (200) K using the double-sided laser heating system operating at the P02.2 beamline at the PETRA III synchrotron. A single-crystal data set was collected at the same P02.2 beamline ($\lambda = 0.2908$ Å, beam size 1.8×2 μm FWHM, acquisition time 4 s, angular ω step 0.5° , 132 frames). See Aslandukov *et al.* (2021) for more experimental details.

The peak hunting procedure in *CrysAlis^{Pro}* found 68 846 reflections. Since this high-pressure experiment was conducted in a DAC, a lot of undesired reflections from diamonds, the pressure-transmitting medium, the material of the gasket and other artifacts were present in the data set. Therefore, a procedure of ‘advanced filtering’ was applied to remove such reflections before the execution of the *DAFi* program. To realize such a ‘clean-up’, a special script was written by E. Koemets and M. Bykov, and then incorporated into the *CrysAlis^{Pro}* software. After the filtering, 44 312 reflections were left out of 68 846. The size of the *DAFi* input data set (‘*DAFi* input peak table’) was still huge. In such cases, it is more reasonable to search for several strongly diffracting domains of different phases than for all single-crystal domains. A search for ten groups in 44 312 reflections took the *DAFi* program 5 min 25 s.

The results of the search are shown in Fig. 5 and Table 2. It appeared that all ten groups of reflections belong to the same

phase. Each group was indexed independently in *CrysAlis^{Pro}* [see Table 2 and Figs. 5(b) and 5(c) as an example], and the crystal structure of the phase (identified as Y_5N_{14}) was solved

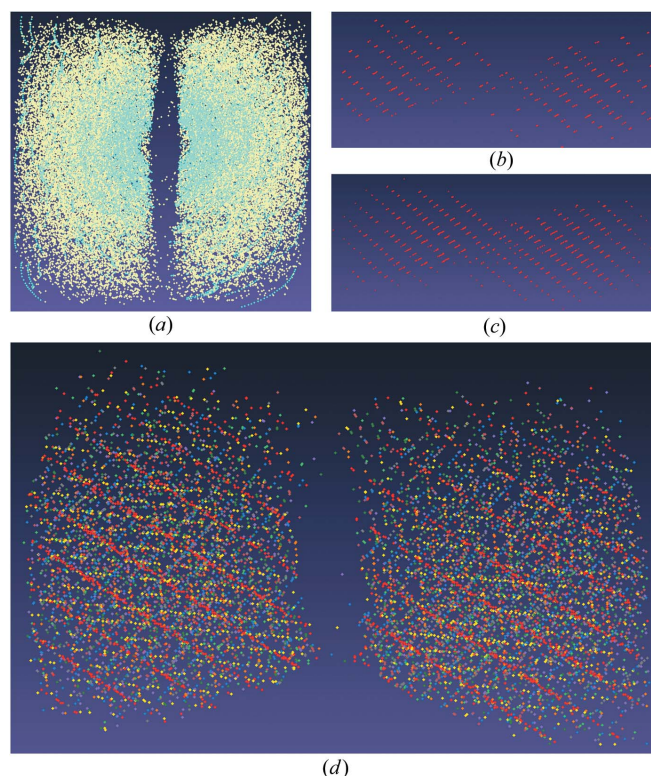


Figure 5
Reciprocal space representing SC-XRD data from a sample of $\text{Y}+\text{N}_2$ in a DAC: (a) all reflections (cyan reflections are those filtered after applying ‘advanced filtering’); (b) reflections of group 1 belonging to the first Y_5N_{14} domain found by the *DAFi* program; (c) reflections of group 1 belonging to the Y_5N_{14} domain extended by *CrysAlis^{Pro}*; (d) reflections of ten groups (1 through 10) belonging to ten Y_5N_{14} domains marked by ten different colors.

Table 2

Results of the *DAFi* run on the data set collected from a sample of $Y+N_2$ in a DAC at 50 GPa.

Group No.	Size of group found by <i>DAFi</i>	Size of group after indexing in <i>CrysAlis^{Pro}</i> †	Lattice parameters						Phase
			<i>a</i> (Å)	<i>b</i> (Å)	<i>c</i> (Å)	α (°)	β (°)	γ (°)	
1	617	1286	8.4595 (3)	8.4595 (3)	4.7032 (5)	90	90	90	Y_5N_{14}
2	590	1044	8.4788 (6)	8.4788 (6)	4.6883 (3)	90	90	90	Y_5N_{14}
3	499	954	8.4527 (8)	8.4527 (8)	4.7034 (11)	90	90	90	Y_5N_{14}
4	485	997	8.4459 (5)	8.4459 (5)	4.7182 (7)	90	90	90	Y_5N_{14}
5	531	1199	8.4538 (4)	8.4538 (4)	4.711 (2)	90	90	90	Y_5N_{14}
6	483	1095	8.4737 (5)	8.4737 (5)	4.6922 (4)	90	90	90	Y_5N_{14}
7	478	1011	8.4710 (5)	8.4710 (5)	4.6977 (4)	90	90	90	Y_5N_{14}
8	375	984	8.4690 (5)	8.4690 (5)	4.7047 (19)	90	90	90	Y_5N_{14}
9	361	823	8.4606 (5)	8.4606 (5)	4.7065 (3)	90	90	90	Y_5N_{14}
10	308	935	8.4677 (9)	8.4677 (9)	4.699 (3)	90	90	90	Y_5N_{14}

† Indexing performed with a tolerance of 0.05.

and refined for each of its single-crystal domains (Aslandukov *et al.*, 2021) (e.g. for domain 6, the integration led to $R_{int} = 6.47\%$; based on 597 independent reflections, the structure of Y_5N_{14} was solved and refined to $R_1 = 4.88\%$). Note that the unusual stoichiometry of the Y_5N_{14} phase was not known initially and was determined as a result of the crystal structure solution and refinement using the standard crystallographic software *OLEX2* (Dolomanov *et al.*, 2009), considering that the elements present in the system were known. In the example of Y_5N_{14} , only a piece of yttrium and nitrogen were loaded into the DAC, thus limiting the set of possible elements (Y, N) in the new compound. Other possible elements (for example, C from the diamond anvils, Re from the gasket or other impurities in the initial sample) would have to be taken into consideration in the case of unsatisfactory structure refinement (which was not the case for Y_5N_{14}).

The *DAFi* program could have been run to find more domains. However, this would have made sense only if there were other phases in the sample. In this particular case, a quick check of the powder diffraction pattern generated for the whole data set showed no extra reflections apart from the found phase; therefore there was no reason to continue the search.

4. Summary

Existing indexing algorithms for single-crystal data analysis implemented in available crystallographic programs have no proven record of application to SC-XRD data processing from a multiphase mixture of microcrystalline samples. Superposition of numerous reflections originating from a large number of single-crystal domains of the same and/or different (especially unknown) phases precludes the sorting of reflections coming from individual domains, making their automatic indexing impossible. The *DAFi* algorithm presented in this work is designed for a quick search for subsets of reflections from individual domains in a whole set of SC-XRD data from a seemingly polycrystalline sample. Further indexing of all found subsets can be easily performed in one click using widely accessible crystallographic packages such as *CrysAlis^{Pro}*. The fact that the algorithm presented above neither

requires *a priori* crystallographic information nor is limited by the number of the various phases and their individual domains makes *DAFi* a powerful software tool to be used for studies of multiphase polycrystalline and microcrystalline (powder) materials. It has been shown to be especially valuable for the analysis of single-crystal diffraction data from products of chemical reactions being realized in laser-heated DACs. Such data are always very complex due to (i) the presence of undesired reflections from diamond anvils and gaskets, and other technical and diffraction artifacts (e.g. ‘bad’ or ‘saturated’ detector pixels, or reflections from the body of the DAC itself), and (ii) the limited opening angle of DACs, which shadows a part of the Ewald sphere. To our knowledge, there are no existing software tools capable of finding the domains of unknown phases in such a complicated XRD data set as in example 2. The *DAFi* program tackles the task within a few minutes and finds several strongly diffracting domains, so that their XRD patterns can be indexed, the data integrated, and the crystal structures solved and refined. The high performance of the proposed algorithm allows the use of this program for online processing of the XRD data directly during experiments at synchrotron facilities.

The *DAFi* program is not designed to be effective with non-merohedral twins, where a large fraction of reflections are overlapped, while some of them overlap only partially or do not overlap. Once *DAFi* finds the reflection group, the program removes it from consideration for the next iterations. If reflections do not overlap, *DAFi* finds two separate reflection groups which can be processed afterwards by the user. If reflections overlap partially, *DAFi* finds two separate reflection groups; however, the first group would contain all reflections of the first crystal in a twin, while the second group would contain only non-overlapped reflections of the second one. If a large number of reflections overlap, the second group most likely will not be found.

The current version of the *DAFi* program does not find all reflections belonging to a particular single-crystal domain, as the algorithm searches for rows of at least three reflections along a certain direction, so that single reflections or those which are only two in a row are overlooked. Also, several groups of reflections can be found to belong to the same

domain, as in the 3D reciprocal space the algorithm searches for rows of reflections in only one direction. These technical peculiarities of the program are not crucial for further data processing, as the input and output format of the *DAFi* program are compatible with the *CrysAlis^{Pro}* software. Moreover, the input and output formats of the *DAFi* program could be adapted to users' needs and made to be compatible with other crystallographic software.

5. Distribution

The *DAFi* program and its documentation can be downloaded from <https://github.com/AsMaNick/Domain-Auto-Finder/>.

Acknowledgements

The authors thank D. Laniel for testing the program, reporting bugs and giving useful hints for further improvement. Open access funding enabled and organized by Projekt DEAL.

Funding information

ND and LD thank the Federal Ministry of Education and Research, Germany (BMBF, grant No. 05K19WC1), and the Deutsche Forschungsgemeinschaft (DFG projects DU 954-11/1, DU 393-9/2, DU 393-13/1) for financial support. ND also thanks the Swedish Government Strategic Research Area in Materials Science on Functional Materials at Linköping University (Faculty Grant SFO-Mat-LiU No. 2009 00971).

References

- Aslandukov, A., Aslandukova, A., Laniel, D., Koemets, I., Fedotenko, T., Yuan, L., Steinle-Neumann, G., Glazyrin, K., Hanfland, M., Dubrovinsky, L. & Dubrovinskaia, N. (2021). *J. Phys. Chem. C*, **125**, 18077–18084.
- Aslandukova, A., Aslandukov, A., Yuan, L., Laniel, D., Khandarkhaeva, S., Fedotenko, T., Steinle-Neumann, G., Glazyrin, K., Dubrovinskaia, N. & Dubrovinsky, L. (2021). *Phys. Rev. Lett.* **127**, 135501.
- Blum, M., Floyd, R. W., Pratt, V., Rivest, R. L. & Tarjan, R. E. (1973). *J. Comput. Syst. Sci.* **7**, 448–461.
- Bykov, M., Chariton, S., Bykova, E., Khandarkhaeva, S., Fedotenko, T., Ponomareva, A. V., Tidholm, J., Tasnádi, F., Abrikosov, I. A., Sedmak, P., Prakapenka, V., Hanfland, M., Liermann, H. P., Mahmood, M., Goncharov, A. F., Dubrovinskaia, N. & Dubrovinsky, L. (2020). *Angew. Chem. Int. Ed.* **59**, 10321–10326.
- Bykov, M., Fedotenko, T., Chariton, S., Laniel, D., Glazyrin, K., Hanfland, M., Smith, J. S., Prakapenka, V. B., Mahmood, M. F., Goncharov, A. F., Ponomareva, A. V., Tasnádi, F., Abrikosov, A. I., Bin Masood, T., Hotz, I., Rudenko, A. N., Katsnelson, M. I., Dubrovinskaia, N., Dubrovinsky, L. & Abrikosov, I. A. (2021). *Phys. Rev. Lett.* **126**, 175501.
- Bykova, E., Bykov, M., Černok, A., Tidholm, J., Simak, S. I., Hellman, O., Belov, M. P., Abrikosov, I. A., Liermann, H.-P., Hanfland, M., Prakapenka, V. B., Prescher, C., Dubrovinskaia, N. & Dubrovinsky, L. (2018). *Nat. Commun.* **9**, 4789.
- Bykova, E., Dubrovinsky, L., Dubrovinskaia, N., Bykov, M., McCammon, C., Ovsyannikov, S. V., Liermann, H. P., Kupenko, I., Chumakov, A. I., Ruffer, R., Hanfland, M. & Prakapenka, V. (2016). *Nat. Commun.* **7**, 10661.
- Ceppatelli, M., Scelta, D., Serrano-Ruiz, M., Dziubek, K., Morana, M., Svitlyk, V., Garbarino, G., Poręba, T., Mezouar, M., Peruzzini, M. & Bini, R. (2022). *Angew. Chem.* **134**, e20211419.
- Cormen, T. H., Leiserson, C. E., Rivest, R. L. & Stein, C. (2001). *Introduction to Algorithms*, Section 8.3, pp. 170–173. Cambridge: MIT Press/McGraw-Hill.
- Dolomanov, O. V., Bourhis, L. J., Gildea, R. J., Howard, J. A. K. & Puschmann, H. (2009). *J. Appl. Cryst.* **42**, 339–341.
- Dubrovinskaia, N. & Dubrovinsky, L. (2018). *Phys. Scr.* **93**, 062501.
- Jimenez-Melero, E., van Dijk, N. H., Zhao, L., Sietsma, J., Wright, J. P. & van der Zwaag, S. (2011). *Mater. Sci. Eng. A*, **528**, 6407–6416.
- Kantor, I., Prakapenka, V., Kantor, A., Dera, P., Kurnosov, A., Sinogeikin, S., Dubrovinskaia, N. & Dubrovinsky, L. (2012). *Rev. Sci. Instrum.* **83**, 125102.
- Klee, V. (1977). *Am. Math. Mon.* **84**, 284–285.
- Koemets, E. (2020). Dissertation, University of Bayreuth, Germany.
- Laniel, D., Winkler, B., Bykova, E., Fedotenko, T., Chariton, S., Milman, V., Bykov, M., Prakapenka, V., Dubrovinsky, L. & Dubrovinskaia, N. (2020). *Phys. Rev. B*, **102**, 134109.
- Laniel, D., Winkler, B., Fedotenko, T., Pakhomova, A., Chariton, S., Milman, V., Prakapenka, V., Dubrovinsky, L. & Dubrovinskaia, N. (2020). *Phys. Rev. Lett.* **124**, 216001.
- Lauridsen, E. M., Schmidt, S., Suter, R. M. & Poulsen, H. F. (2001). *J. Appl. Cryst.* **34**, 744–750.
- Ludwig, W., Reischig, P., King, A., Herbig, M., Lauridsen, E. M., Johnson, G., Marrow, T. J. & Buffière, J. Y. (2009). *Rev. Sci. Instrum.* **80**, 033905.
- Moscicki, M., Kenesei, P., Wright, J., Pinto, H., Lippmann, T., Borbély, A. & Pyzalla, A. R. (2009). *Mater. Sci. Eng. A*, **524**, 64–68.
- Schmidt, S. (2014). *J. Appl. Cryst.* **47**, 276–284.
- Sørensen, H. O., Schmidt, S., Wright, J. P., Vaughan, G. B. M., Techert, S., Garman, E. F., Oddershede, J., Davaasambuu, J., Paithankar, K. S., Gundlach, C. & Poulsen, H. F. (2012). *Z. Kristallogr.* **227**, 63–78.
- Wejdemann, C. & Poulsen, H. F. (2016). *J. Appl. Cryst.* **49**, 616–621.
- Wright, J. P. (2006). *ImageD11*, <https://github.com/FABLE-3DXRD/ImageD11/>.

5.2. High-pressure yttrium nitride, Y_5N_{14} , featuring three distinct types of nitrogen dimers

This section contains the following manuscript and the related supplementary material:

“High-pressure yttrium nitride, Y_5N_{14} , featuring three distinct types of nitrogen dimers”

A. Aslandukov, A. Aslandukova, D. Laniel, I. Koemets, T. Fedotenko, L. Yuan, G. Steinle-Neumann, K. Glazyrin, M. Hanfland, L. Dubrovinsky, N. Dubrovinskaia.

Status: published in *The Journal of Physical Chemistry C*, 125(32), 18077-18084.

(2021)

Reprinted with permission from ACS Publications

High-Pressure Yttrium Nitride, Y_5N_{14} , Featuring Three Distinct Types of Nitrogen Dimers

Andrey Aslandukov,* Alena Aslandukova, Dominique Laniel, Iuliia Koemets, Timofey Fedotenko, Liang Yuan, Gerd Steinle-Neumann, Konstantin Glazyrin, Michael Hanfland, Leonid Dubrovinsky, and Natalia Dubrovinskaia

Cite This: *J. Phys. Chem. C* 2021, 125, 18077–18084

Read Online

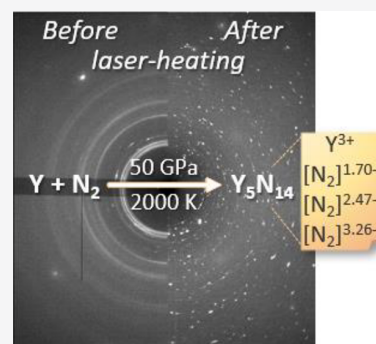
ACCESS |

Metrics & More

Article Recommendations

Supporting Information

ABSTRACT: Yttrium nitride, Y_5N_{14} , was synthesized by direct reaction between yttrium and nitrogen at ~ 50 GPa and ~ 2000 K in a laser-heated diamond anvil cell. High-pressure single-crystal X-ray diffraction revealed that the crystal structure of Y_5N_{14} (space group $P4/mbm$) contains three distinct types of nitrogen dimers. Crystal chemical analysis and *ab initio* calculations demonstrated that the dimers $[N_2]^{x-}$ are crystallographically and chemically nonequivalent and possess distinct noninteger formal charges (x) that make Y_5N_{14} unique among known compounds. Theoretical computations showed that Y_5N_{14} has an anion-driven metallicity, with the filled part of its conduction band formed by nitrogen p-states. The compressibility of Y_5N_{14} , determined on decompression down to ~ 10 GPa, was found to be uncommonly high for dinitrides containing +3 cations (the bulk modulus $K_0 = 137(6)$ GPa).



INTRODUCTION

Nitrides of metals often possess technologically relevant properties, e.g., superior chemical stability, high electrical conductivity, unique electronic structure, large bulk moduli, and high hardness.^{1–3} While at ambient pressure nitrogen is typically present in nitrides in the form of N^{3-} anion, over the past 20 years it has been shown that high pressure opens new possibilities for the synthesis of dinitrides with $[N_2]^{x-}$ units.^{4–13} Usually, dinitrides have a MN_2 composition, in which the metal atoms (M) possess their common oxidation state, while the dinitrogen anion formally accommodates from 1 to 4 electrons. Thus, four charge states of nitrogen dimers have been established:

- (1) $[N_2]^-$ in $M^I N_2$ ($M = Li, Na$);^{4,5}
- (2) $[N_2]^{2-}$ in $M^{II} N_2$ ($M = Ca, Ba, Sr, Ni, Pd$);^{6–8}
- (3) $[N_2]^{3-}$ in $M^{III} N_2$ ($M = Cr, Fe, Co, La, Ru, Rh$);^{9–13}
- (4) $[N_2]^{4-}$ in $M^{IV} N_2$ ($M = Ti, Pt, Ir, Os$).^{14–17}

The charge transferred from the metal to the nitrogen dimers significantly affects the properties of the materials; e.g., the bulk moduli (K_0) of dinitrides decrease as follows: $K_0(M^{IV}N_2) > K_0(M^{III}N_2) > K_0(M^{II}N_2) > K_0(M^I N_2)$.¹⁸

Recently, uncommon compounds such as $Na_3(N_2)_4$,^{5,19} $K_3(N_2)_4$,²⁰ $Ca_3(N_2)_4$,¹⁹ $Sr_3(N_2)_4$,¹⁹ and $Ba(N_2)_3$,¹⁹ containing $[N_2]^{x-}$ units with noninteger formal charges (x) were reported. The discovery of these phases not only indicates the possibility of a more complex organization of N_2 units but also gives impetus to a paradigm shift in consideration of the electron distribution in structures.¹⁹ Still, the uniformity of the $[N_2]^{x-}$

units in a distinct dinitride remains unchallenged: in each of all known phases featuring nitrogen dimers, there is only one kind of $[N_2]^{x-}$ species, with a given N–N bond length and charge.

Despite a significant number of studies on binary metal–nitrogen compounds of alkali, alkaline earth, and transition metal elements under high pressure,^{4–17,19–21} dinitrides of rare-earth elements (with the exception of LaN_2)^{11,21} have not been investigated yet. That would be of interest, as even known rare-earth nitrides possess a wealth of interesting electronic and magnetic properties at ambient conditions and, therefore, may have potential applications in electronics, spintronics, and magnetic refrigeration.²² Unlike typical transition metals, rare-earth elements in compounds exhibit usually the same oxidation state of +3, thus enabling control of this very important variable and generalization of the results of the analysis of experimental observations.

Prior to this work, only one binary yttrium–nitrogen compound was known: cubic yttrium nitride YN with the rock salt structure. Still, *ab initio* calculations predict stable phases at high pressures with YN^{23} and YN_2 ²⁴ stoichiometry. Here, we report the results of the synthesis and character-

Received: July 12, 2021

Revised: July 23, 2021

Published: August 10, 2021



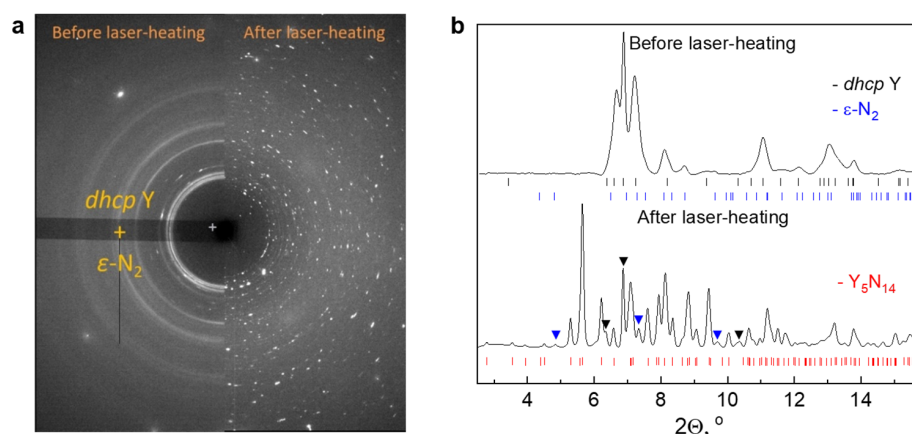


Figure 1. (a) 2D XRD patterns and (b) integrated powder XRD patterns of the sample before (at 47(1) GPa) and after (at 49(1) GPa) laser heating. The black and blue triangle symbols identify reflections of *dhcp* Y and ϵ -N₂, respectively.

ization of a previously unknown high-pressure yttrium nitride, Y₅N₁₄, containing three distinct [N₂]^{x-} species that break down the previously observed uniformity of nitrogen dimers in one compound.

EXPERIMENTAL METHODS

Sample Preparation. The BX90-type large X-ray aperture diamond anvil cell (DAC)²⁵ equipped with 250 μ m culet diameter Boehler–Almax-type diamonds²⁶ was used for the experiments. The sample chamber was formed by preindenting of a rhenium gasket to \sim 25 μ m thickness and drilling a hole of \sim 105 μ m in diameter in the center of the indentation. A piece of yttrium (99.9%, Sigma-Aldrich) was placed in a sample chamber, and molecular nitrogen was loaded using a high-pressure gas loading system (1300 bar).²⁷ The sample was compressed to \sim 50 GPa and laser-heated ($\lambda = 1064$ nm) up to 2000(200) K using the double-sided laser-heating system of the P02.2 beamline (PETRA III). The temperature during laser heating was determined by a blackbody radiation fit. The sample pressure was determined using the equation of state of pure N₂,²⁸ and cross-verified with the diamond anvils' Raman edge.²⁹

X-ray Diffraction. XRD measurements were performed at beamline P02.2 of the PETRA III synchrotron with the X-ray beam ($\lambda = 0.2908$ Å) focused to 1.8×2 μ m² by a Kirkpatrick–Baez mirror system, and the XRD patterns were collected on a PerkinElmer 1621 XRD flat-panel detector. XRD measurements upon sample decompression were performed at the ID15B beamline (ESRF) with an X-ray beam ($\lambda = 0.4103$ Å) focused to a size of 8×8 μ m², and the XRD patterns were collected on an Eiger2X CdTe 9 M hybrid photon-counting pixel detector. Powder diffraction images were collected during the continuous rotation of the DAC around the vertical ω axis in a range $\pm 20^\circ$ with an acquisition time of 40 and 4 s at the P02.2 and ID15B beamlines, respectively. The powder XRD images were integrated into powder patterns with the Dioptas software.³⁰ Powder patterns were analyzed with the Le Bail fitting technique using the TOPAS 5.0 software. For single-crystal XRD measurements, the sample was rotated around the vertical ω axis in the range of $\pm 35^\circ$. The XRD images were collected with an angular step of $\Delta\omega = 0.5^\circ$ and an exposure time of 4 s/frame at the P02.2 beamline and 0.2–0.4 s/frame at the ID15B beamline. The CrysAlis^{Pro} software package was used for the analysis of the single-crystal XRD data (indexing,

data integration, frame scaling, and absorption correction). To calibrate the instrumental model in the CrysAlis^{Pro} software, i.e., the sample-to-detector distance, detector's origin, offsets of the goniometer angles, and rotation of both the X-ray beam and detector around the instrument axis, a single crystal of orthoenstatite [(Mg_{1.93}Fe_{0.06})(Si_{1.93}Al_{0.06})O₆, *Pbca* space group, $a = 8.8117(2)$ Å, $b = 5.18320(10)$ Å, and $c = 18.2391(3)$ Å] was used. Using the Jana2006 software package, the structure was solved with the ShelXT structure solution program³¹ using intrinsic phasing and refined with the ShelXL³² refinement package using least-squares minimization. Crystal structure visualization was made with the VESTA software.³³ The equation of state of the synthesized material was obtained by fitting the pressure–volume data using the EoSFit7-GUI.³⁴

Raman Spectroscopy. Raman spectra were measured using the LabRam spectrometer equipped with a $\times 50$ Olympus objective. Sample excitation was accomplished using a continuous He–Ne laser (excitation wavelength is 632.8 nm) with a focused laser spot of about 2 μ m in diameter.

Ab Initio Calculations. Density functional theory (DFT) based calculations were performed with the plane-wave approach and periodic boundary conditions using the Vienna *ab initio* simulation package (VASP).^{35,36} We use the projector-augmented-wave (PAW) method³⁷ and atomic files (with valence configurations of 4s²4p⁶5s²4d¹ for Y and 2s²2p³ for N) provided in the VASP potential database³⁸ and approximate exchange and correlation by the generalized gradient approximation.³⁹ The planewave energy cutoff was chosen as 600 eV and Kohn–Sham eigenvalues computed on a Monkhorst–Pack⁴⁰ k-point grid of $4 \times 4 \times 6$ in the Brillouin zone. All structures were relaxed until the energy difference for the electronic self-consistent calculation was smaller than 10^{-8} eV/cell and the Hellman–Feynman forces became less than 2×10^{-3} eV/Å. The resulting charge densities were evaluated in terms of electronic band structure and the electron localization function. Simulations were performed for 11 unit cell volumes each for Y₅N₁₄, ϵ -N₂, YN, and three phases of YN₂,²⁴ covering the pressure range between 0 and 100 GPa, found with constant pressure simulations with 10 GPa distances. Using energy, pressure, and volume values from the simulations, the enthalpy difference between Y₅N₁₄ and assemblies of other Y-nitrides plus ϵ -N₂ was calculated to determine the (static) stability of Y-nitrides as a function of pressure. Lattice

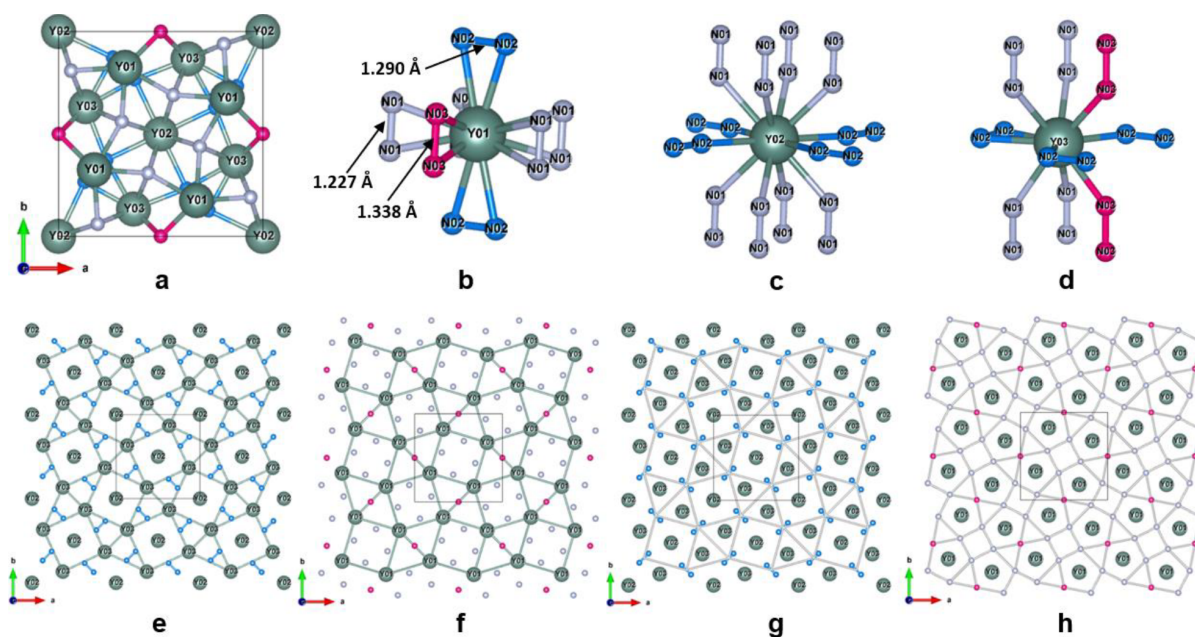


Figure 2. Crystal structure of Y_5N_{14} . All Y atoms are greenish; N01 atoms are gray; N02 atoms are blue; and N03 atoms are pink; gray thin lines outline the unit cell. (a) A projection of the structure on the ab plane. The coordination environment of (b) Y01, (c) Y02, and (d) Y03 atoms. Representation of the crystal structure as a set of 2D networks alternating along the c -direction: (e) the network formed by Y03, Y02, and N02–N02 dimers (blue dumbbells), all laying in the same plane; Y02 atoms are located in the centers of squares formed by the Y03 net with the $3^2.4.3.4$ vertex symbol; (f) the net formed by Y01 atoms; the N01 and N03 are seen in the projection, as only the middle points of the dumbbells are located in the same plane with the Y01 atoms; (g) 2D net drawn through the centers of N02–N02 dimers; and (h) 2D net drawn through the centers of N01–N01 and N03–N03 dimers.

dynamics calculations for the Y_5N_{14} phase were carried out using the finite displacement method as implemented in the PHONOPY code⁴¹ with a $2 \times 2 \times 2$ supercell of the Y_5N_{14} phase on a $2 \times 2 \times 3$ q -point mesh for two unit cell volumes, corresponding to 0 and 50 GPa.

RESULTS AND DISCUSSION

A diamond anvil cell containing a sample composed of a piece of yttrium embedded in molecular nitrogen was compressed to 47(1) GPa. Synchrotron X-ray diffraction data obtained before sample laser heating showed the expected yttrium powder with the *dhcp* structure (space group $P6_3/mmc$, $a = 3.0173(7)$ Å, $c = 9.716(3)$ Å) and ϵ -N₂ (space group $R\bar{3}c$, $a = 6.934(2)$ Å, $c = 9.786(4)$ Å), the stable polymorphs of yttrium⁴² and nitrogen⁴³ at this pressure. After laser heating to 2000(200) K, pressure increased to 49(1) GPa, and new diffraction lines characteristic of a new phase were observed (Figure 1). High-quality single-crystal X-ray diffraction data were collected from the sample and revealed the formation of a novel yttrium nitride for which the crystal structure could be determined (Figure 2).

The new yttrium nitride crystallizes in the tetragonal structure (space group $P4/mbm$, #127) with the lattice parameters of $a = 8.4510(16)$ Å and $c = 4.7316(9)$ Å at 49(1) GPa (see Table S1 and the CIF for the full crystallographic data) and adopts an unusual stoichiometry, Y_5N_{14} . The structure of Y_5N_{14} (Figure 2a) is composed of yttrium and nitrogen atoms, each occupying three crystallographically distinct positions. All nitrogen atoms form dimers but, strikingly, of three different types: four N01–N01, two N02–N02, and one N03–N03, per Y_5N_{14} formula unit, with

the lengths of 1.227(8) Å, 1.290(11) Å, and 1.338(15) Å at 49(1) GPa, respectively (Figure 2b).

The yttrium–nitrogen distances in the Y_5N_{14} structure at 49(1) GPa vary from 2.193(3) Å to 2.487(6) Å. The coordination environments of all three yttrium atoms in Y_5N_{14} are markedly different. The Y01 atom possesses the largest coordination number, CN = 14, which is achieved due to seven N₂ units (four N01–N01, two N02–N02, and one N03–N03) in a side-on manner (Figure 2b). The Y02 atoms have a CN = 12 and display distorted cuboctahedron coordination with 12 end-on N₂ dimers (Figure 2c), and the Y03 atoms are 10-fold coordinated (CN = 10) by eight end-on N₂ units and one side-on N₂ unit (Figure 2d). The orientation of the dimers is found to influence the length of the Y–N contact; e.g., Y03–N02 distances are 2.354(6) Å and 2.320(6) Å for N02–N02 dumbbells in end-on and side-on configurations (Figure 2d), respectively.

While the structural type of Y_5N_{14} is unique, the framework of yttrium atoms resembles the structure of U_3Si_2 ,⁴⁴ if the difference in elements in the latter is ignored. As a whole, the Y_5N_{14} structure can be described as the stacking along the c -axis of two 2D nets built of crystallographically different yttrium atoms, Y03 (Figure 2e) and Y01 (Figure 2f). The nets have the same $3^2.4.3.4$ vertex symbol⁴⁵ and are separated on $1/2c$. The Y02 atoms are located in the centers of the square tiles in the Y03 net, whereas the N02–N02 dumbbells bridge the sides of the triangle tiles (Figure 2e). Considering the centers of the N02–N02 dumbbells as the nodes of a separate net, the latter appears to have the same vertex symbol $3^2.4.3.4$ like the Y03 net (Figure 2g). There are no other atoms except Y01 in the plane of the Y1 net (Figure 2f). As the N01–N01 and N03–N03 dumbbells are aligned along the c -axis, they are

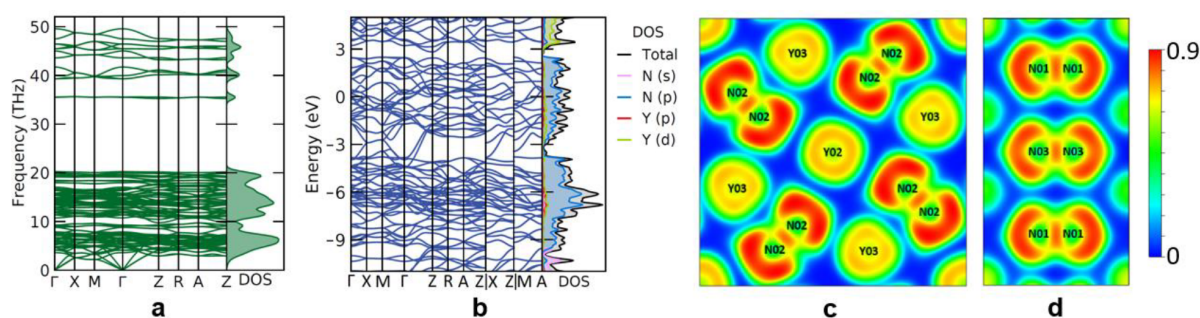


Figure 3. Results of DFT-based calculations for Y_5N_{14} at 50 GPa. (a) Phonon dispersion curves along high-symmetry directions in the Brillouin zone and phonon density of states and (b) electron density of states; the Fermi energy level was set to 0 eV. The electron localization function calculated in (c) the (001) plane and (d) a selected plane containing both N01–N01 and N03–N03 dimers.

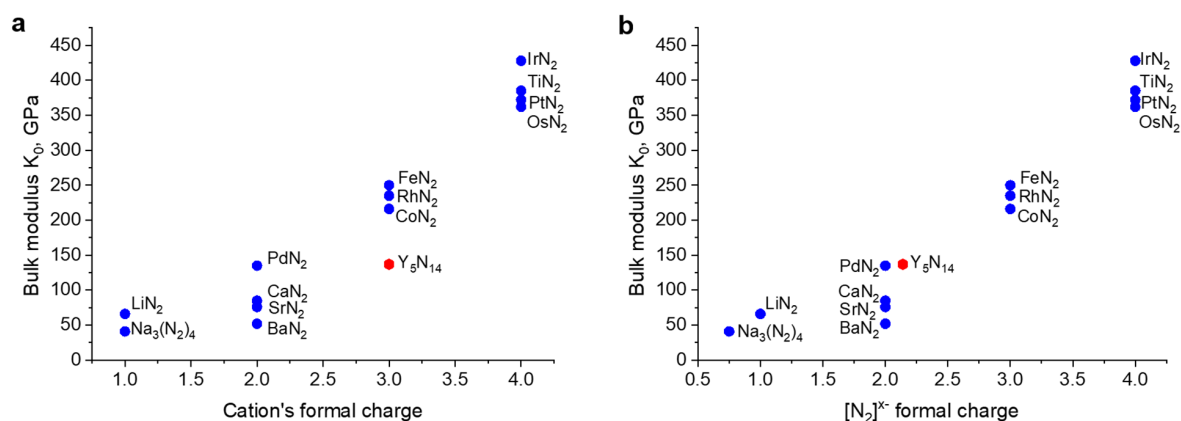


Figure 4. Bulk modulus of binary dinitrides, including the novel Y_5N_{14} , as a function of the formal charge of the (a) cations and (b) $[N_2]^{x-}$ units. The values of bulk moduli are taken from $K_0(Na_3(N_2)_4) = 41$ GPa,³ $K_0(LiN_2) = 63$ GPa,⁴⁶ $K_0(BaN_2) = 46$ GPa,⁴⁷ $K_0(SrN_2) = 77$ GPa,⁴⁷ $K_0(PdN_2) = 135$ GPa,⁸ $K_0(CoN_2) = 216$ GPa,¹⁰ $K_0(RhN_2) = 235$ GPa,¹³ $K_0(FeN_2) = 250$ GPa,¹⁸ $K_0(OsN_2) = 362$ GPa,⁴⁸ $K_0(PtN_2) = 372$ GPa,¹⁷ $K_0(TiN_2) = 385$ GPa,¹⁴ and $K_0(IrN_2) = 428$ GPa.¹⁶

seen in the projection in Figure 2f, but only their middle points are located in the same plane with the Y1 atoms, forming their own plain 2D net (Figure 2h) with two types of vertexes: 3.5.4.5 (related to N01 atoms) and 3.5.3.5 (related to N03 atoms) (Figure 2h).

Density functional theory (DFT) based calculations using the Vienna *ab initio* simulation package³⁵ show that relaxed structural parameters for Y_5N_{14} (Table S2) closely reproduce the corresponding experimental values at 49(1) GPa. The calculations agree well with the experimental determination that the structure of Y_5N_{14} contains three different kinds of N–N dimers (Table S2): the calculated N–N distances are 1.232 Å, 1.267 Å, and 1.320 Å for N01–N01, N02–N02, and N03–N03 dimers at 50 GPa, respectively. Phonon dispersion relations calculated in the harmonic approximation show that the Y_5N_{14} phase is dynamically stable at 50 GPa (Figure 3a) but unstable at ambient pressure (Figure S1). To estimate the thermodynamic stability of Y_5N_{14} , we compared its static enthalpy to that of the well-known YN in the rock salt structure and the predicted YN_2 structures²⁴ in the 0–100 GPa pressure range (Figure S2). We found out that in the 20–100 GPa pressure range Y_5N_{14} is thermodynamically more favorable than YN and the three previously reported YN_2 structures. Below 20 GPa, Y_5N_{14} is not thermodynamically stable, and the assembly of YN plus N_2 is favored.

The computed electron density of states (DOS) shows that, at 50 GPa, Y_5N_{14} is a metal (Figure 3b). The metallic nature of Y_5N_{14} may explain the absence of a Raman signal from this phase (Figure S3). Remarkably, the electronic DOS at the Fermi level comes almost exclusively from the nitrogen p-states, with a negligible contribution from yttrium states. A similar observation has recently been reported for dinitrides of alkali and alkaline earth metals,^{5,19} and the corresponding compounds attributed to an anion-driven metallicity.¹⁹ One of the chemical bonding features of this class of compounds is a predominately ionic bonding between cations and N–N units and a covalent bonding between nitrogen atoms forming dimers.¹⁹ Indeed, for Y_5N_{14} , the calculated electron localization function at 50 GPa demonstrates a strong covalent bonding between nitrogen atoms (Figure 3c,d). At the same time, there is no obvious sign of covalent bonding between nitrogen and yttrium atoms, and there is no sign of electron localization between atoms, as expected for electrides.

After the synthesis of Y_5N_{14} at 49(1) GPa, the sample was decompressed in a few pressure steps down to 1 bar. The X-ray diffraction reflections of the Y_5N_{14} phase can be traced down to ~10 GPa (Figure S4). Further decompression to 2 GPa resulted in the disappearance of the Y_5N_{14} diffraction reflections and the formation of a Y (*hcp* structure, space group $P6_3/mmc$, $a = 3.5866(2)$ Å, $c = 5.6663(8)$ Å) and YN

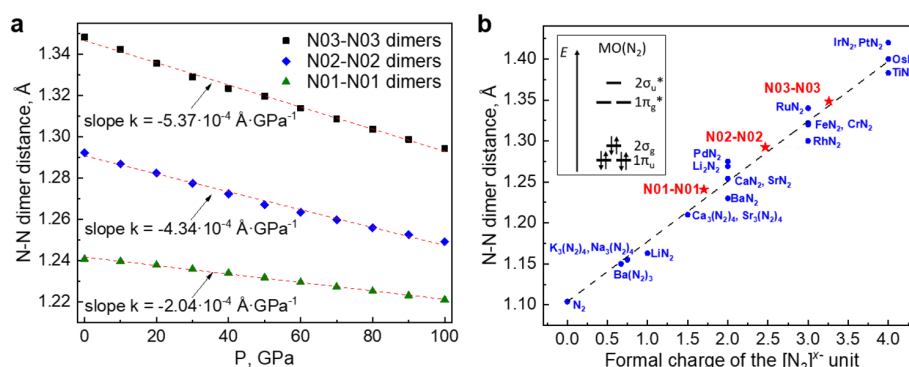


Figure 5. Characteristic bond lengths of N–N dimers. (a) Nitrogen–nitrogen bond lengths extracted from the DFT-relaxed structure of Y_5N_{14} as a function of pressure. (b) Calculated $d(\text{N–N})$ distances for 20 binary compounds containing $[\text{N}_2]^{x-}$ units (circle symbols) and for Y_5N_{14} (star symbols). All distances were computed at 1 bar, except for LiN_2 (20 GPa). The linear correlation between the N–N bond lengths (BL) and the formal charge (FC) of $[\text{N}_2]^{x-}$ dimers is expressed as $\text{BL} = 0.074(1) \text{ \AA FC} + 1.104 \text{ \AA}$ and is drawn as a dashed line. Inset: Qualitative molecular orbital diagram of N_2 . Panel b adapted from with permission from ref 19.

Table 1. Nitrogen–Nitrogen Bond Length and Charge States of N_2 Units in Y_5N_{14} Structure Determined by Various Approaches

dimer	bond length			charge state of N_2 dimer			
	exptl	calcd		CHARDI	DDEC6	bond length analysis	
		at 49(1) GPa	at 50 GPa			at 1 bar	only integer
N01–N01	1.227(8) Å	1.232 Å	1.241 Å	–1.96	–0.96	–2	–1.70
N02–N02	1.290(11) Å	1.267 Å	1.292 Å	–2.34	–1.22	–2	–2.47
N03–N03	1.338(15) Å	1.320 Å	1.348 Å	–2.50	–1.36	–3	–3.26

(rock salt structure, space group $Fm\bar{3}m$, $a = 4.8638(9) \text{ \AA}$) powder mixture (Figure S4).

The lattice parameters of Y_5N_{14} (Table S3) were extracted from the single-crystal X-ray diffraction data collected between 10 and 49 GPa. The c/a ratio (~ 1.79) was found not to change, within the accuracy of the measurements, in the whole studied pressure range—underlining the isotropic response of Y_5N_{14} to pressure. The quality of the structural data collected on decompression was sufficient to accurately locate the position of yttrium atoms, but uncertainties in the position of the nitrogen atoms do not allow us to precisely evaluate changes in the intramolecular N–N bond lengths with pressure. Still, the N03–N03 bond is found to be systematically longer than N01–N01 and N02–N02 at all pressures (Table S3).

Fitting of the Y_5N_{14} experimental pressure–volume data with the second-order Birch–Murnaghan equation of state gives the bulk modulus $K_0 = 137(6) \text{ GPa}$ ($V_0 = 423(2) \text{ \AA}^3$) (Figure S5) that agrees with the bulk modulus $K_0 = 139.8(4) \text{ GPa}$ obtained as a result of fitting the energy–volume points of Y_5N_{14} DFT-relaxed structures in the pressure range of 0–100 GPa, also using the second order Birch–Murnaghan equation of state ($V_0 = 424.37 \text{ \AA}^3$ was fixed) (Figure S5). The obtained bulk modulus is significantly lower than expected for dinitrides stabilized by +3 cations. Indeed, Figure 4 shows a trend of bulk moduli of different dinitrides as a function of formal charges of cations and $[\text{N}_2]^{x-}$ units. The bulk modulus of Y_5N_{14} is off-trend, if the cation's charge (i.e., 3+) is considered, but it is on-trend if instead the formal charge of the $[\text{N}_2]^{x-}$ dimers is considered—using, for Y_5N_{14} , the average $[\text{N}_2]^{x-}$ dumbbell's formal charge, ~ 2 . This suggests that the charge state of the nitrogen dimers, rather than the oxidation state of the metal,

could be used to estimate the compressibility of binary solids containing $[\text{N}_2]^{x-}$ units.

The calculated intramolecular N–N distances in the relaxed structures are found to decrease with increasing pressure. The rigidity of the nitrogen–nitrogen bond, which correlates with the slope of the pressure–bond length dependence (Figure 5a), increases from the longest bond in N03–N03 dimers to the shortest in the N01–N01 dimer. The different behavior on compression of each type of $[\text{N}_2]^{x-}$ dimers emphasizes the correlation of the bond rigidity with the charge state of the N–N dimers.

Both crystal-chemical analysis and *ab initio* calculations show three different types of nitrogen dimers in the Y_5N_{14} structure with distinct nitrogen–nitrogen bond lengths and compressibility. The multiplicity of the N–N bond and the charge states of the $[\text{N}_2]$ units are usually considered using a nitrogen molecular orbital diagram (Figure 5b, inset). If the bonding orbitals $1\pi_u$ and $2\sigma_g$ are filled up with six electrons, neutral N_2 species are formed with a triple bond. Further electrons on the $1\pi_g^*$ antibonding molecular orbitals result in the formation of charged $[\text{N}_2]^{x-}$ ($x = 1, 2, 3, 4$), a reduction of the bonding multiplicity, and the elongation of the N–N bond. By now it is well established that in nitrogen dimers the bond length correlates with its multiplicity and the formal charge of $[\text{N}_2]^{x-}$: N–N distances of 1.16–1.20 Å,⁴⁹ 1.23–1.29 Å,^{6,7} 1.30–1.34 Å,^{50–52} and 1.38–1.42 Å^{14,50} are typically observed in the charged dinitrides $[\text{N}_2]^-$, $[\text{N}_2]^{2-}$, $[\text{N}_2]^{3-}$, and $[\text{N}_2]^{4-}$, respectively, at ambient pressure and barely change upon compression of a few dozen of GPa.⁵

First considering that only an integer number of electrons can be located on the $1\pi_g^*$ antibonding orbitals, at the synthesis pressure of 49(1) GPa it would be reasonable to assign the shortest intramolecular bonds of 1.227(8) Å and

1.290(11) Å to the double-bonded $[\text{N}=\text{N}]^{2-}$ dimers and that of 1.338(15) Å to the $[\text{N} \equiv \text{N}]^{3-}$ dimers, with a bond multiplicity of 1.5. In total, there would be six $[\text{N}=\text{N}]^{2-}$ dimers and one $[\text{N} \equiv \text{N}]^{3-}$ dimer per Y_5N_{14} formula unit, corresponding to the typical Y^{3+} oxidation state for all yttrium atoms. The yttrium nitride chemical formula could then be written as $\text{Y}^{3+}_5[\text{N}_2]^{2-}_6[\text{N}_2]^{3-}$. However, with this integer-charge hypothesis, all six $[\text{N}_2]^{2-}$ dimers (i.e., N01–N01 and N02–N02 dumbbells) should be identical and behave equally upon compression. This strongly contradicts the crystal chemistry analysis and theoretical calculations—thus forcing us to rule out this interpretation.

A second interpretation, in line with recent results,¹⁹ is suggested from charge analysis using the CHARDI method⁵³ and DFT-based DDEC6 method⁵⁴ (Table S4). These computations unambiguously point out that the charges of the three distinct N–N dimers differ significantly—correlating with the nitrogen–nitrogen bond lengths (Table 1)—and can thus not be described by integer values. The Y_5N_{14} phase has to instead be considered as containing three noninteger charged nitrogen dimers. Figure 5b shows the dependence of the N–N bond length as a function of the formal charge of $[\text{N}_2]^{x-}$ for many different compounds computed at ambient pressure. Based on this plot and the parameters of its linear fit,¹⁹ the charges of the nitrogen dimers in Y_5N_{14} were calculated using the least-squares method (Table 1), using the +3 oxidation state of Y as a constraint on total charge. The chemical formula of the Y_5N_{14} compound calculated in this fashion can be written as $\text{Y}^{3+}_5[\text{N}_2]^{1.70-}_4[\text{N}_2]^{2.47-}_2[\text{N}_2]^{3.26-}$, at ambient pressure. The noninteger charges of the N_2^{x-} dimers are due to the delocalization of the electrons in the conduction band and also provide an explanation for the metallicity of Y_5N_{14} adding further credibility to the recently proposed model of compounds with anion-driven metallicity.¹⁹ The presence of the structurally and chemically distinct $[\text{N}_2]^{x-}$ units with noninteger formal charges in Y_5N_{14} —a unique case despite the plethora of known binary nitrogen compounds bearing them—explains all of our experimental and theoretical observations on the different bond lengths and compressibility of the N–N dumbbells. Similar nitrides are expected to be found in lanthanides, transition metals, and may represent a wide class of inorganic and even metal–organic compounds.

CONCLUSIONS

In this study, we reported that a reaction between yttrium and molecular nitrogen under laser heating at ~2000 K at ~50 GPa yields a novel compound, Y_5N_{14} . High-pressure single-crystal X-ray diffraction revealed that the crystal structure of Y_5N_{14} contains three distinct types of nitrogen dimers. Upon decompression at ambient temperature, Y_5N_{14} was observed down to ~10 GPa. Its compressibility (the bulk modulus $K_0 = 137(6)$ GPa) is uncommonly high for dinitrides containing +3 cations, but it is on-trend if the average formal charge of the $[\text{N}_2]^{x-}$ dimers is considered.

Ab initio calculations reproduced well the crystal structure, and the experimentally determined properties of Y_5N_{14} showed the dynamical stability at 50 GPa and disclosed that Y_5N_{14} has an anion-driven metallicity, with the filled part of its conduction band formed by nitrogen p-states.

Both crystal-chemical analyses and *ab initio* calculations showed three different types of nitrogen dimers in the Y_5N_{14} structure with distinct nitrogen–nitrogen bond lengths,

compressibility, and charge state, which cannot be described with integer formal charges. The noninteger charges of N_2^{x-} dimers are due to the delocalization of the electrons in the conduction band and also explain the metallicity of Y_5N_{14} . Thus, Y_5N_{14} is the first example of the presence of three different types of charged nitrogen dimers in the same structure, which indicates more complex chemical processes of dense dinitride formation under high pressure and opens up a new class of inorganic compounds.

ASSOCIATED CONTENT

Supporting Information

The Supporting Information is available free of charge at <https://pubs.acs.org/doi/10.1021/acs.jpcc.1c06210>.

Details of structure refinement, DFT-relaxed structure parameters, phonon dispersion curves for Y_5N_{14} at 1 bar, calculated static enthalpy as a function of pressure, Raman spectra, powder XRD patterns of the sample upon decompression, equation of state of Y_5N_{14} , and charge analysis (PDF)

AUTHOR INFORMATION

Corresponding Author

Andrey Aslandukov – Material Physics and Technology at Extreme Conditions, Laboratory of Crystallography, University of Bayreuth, 95440 Bayreuth, Germany;
orcid.org/0000-0003-0988-6066;
Email: andrii.aslandukov@uni-bayreuth.de

Authors

Alena Aslandukova – Bavarian Research Institute of Experimental Geochemistry and Geophysics (BGI), University of Bayreuth, 95440 Bayreuth, Germany

Dominique Laniel – Material Physics and Technology at Extreme Conditions, Laboratory of Crystallography, University of Bayreuth, 95440 Bayreuth, Germany;
orcid.org/0000-0002-6889-9820

Iuliia Koemets – Bavarian Research Institute of Experimental Geochemistry and Geophysics (BGI), University of Bayreuth, 95440 Bayreuth, Germany

Timofey Fedotenko – Material Physics and Technology at Extreme Conditions, Laboratory of Crystallography, University of Bayreuth, 95440 Bayreuth, Germany

Liang Yuan – Bavarian Research Institute of Experimental Geochemistry and Geophysics (BGI), University of Bayreuth, 95440 Bayreuth, Germany

Gerd Steinle-Neumann – Bavarian Research Institute of Experimental Geochemistry and Geophysics (BGI), University of Bayreuth, 95440 Bayreuth, Germany

Konstantin Glazyrin – Photon Science, Deutsches Elektronen-Synchrotron, 22607 Hamburg, Germany

Michael Hanfland – European Synchrotron Radiation Facility, BP 220, 38043 Cedex Grenoble, France

Leonid Dubrovinsky – Bavarian Research Institute of Experimental Geochemistry and Geophysics (BGI), University of Bayreuth, 95440 Bayreuth, Germany

Natalia Dubrovinskaia – Material Physics and Technology at Extreme Conditions, Laboratory of Crystallography, University of Bayreuth, 95440 Bayreuth, Germany;
Department of Physics, Chemistry and Biology (IFM), Linköping University, SE-581 83 Linköping, Sweden

Complete contact information is available at:

<https://pubs.acs.org/10.1021/acs.jpcc.1c06210>

Notes

The authors declare no competing financial interest.

ACKNOWLEDGMENTS

The authors acknowledge the Deutsches Elektronen-Synchrotron (DESY, PETRA III) and the European Synchrotron Radiation Facility (ESRF) for provision of beamtime at the P02.2 and ID15b beamlines, respectively. Computations were performed at the Leibniz Supercomputing Center of the Bavarian Academy of Sciences and the Humanities and the research center for scientific computing at the University of Bayreuth. D.L. thanks the Alexander von Humboldt Foundation for financial support. G.S.N. thanks the Deutsche Forschungsgemeinschaft (DFG project STE1105-13/2) for financial support. N.D. and L.D. thank the Federal Ministry of Education and Research, Germany (BMBF, grant no. 05K19WC1), and the Deutsche Forschungsgemeinschaft (DFG projects DU 954-11/1, DU 393-9/2, DU 393-13/1) for financial support. N.D. also thanks the Swedish Government Strategic Research Area in Materials Science on Functional Materials at Linköping University (Faculty Grant SFO-Mat-LiU No. 2009 00971).

REFERENCES

- (1) Wang, H.; Li, J.; Li, K.; Lin, Y.; Chen, J.; Gao, L.; Nicolosi, V.; Xiao, X.; Lee, J. M. Transition Metal Nitrides for Electrochemical Energy Applications. *Chem. Soc. Rev.* **2021**, *50* (2), 1354–1390.
- (2) Jiang, H. X.; Lin, J. Y. Nitride MicroLEDs and beyond - a Decade Progress Review. *Opt. Express* **2013**, *21* (S3), 475–484.
- (3) Yeung, M. T.; Mohammadi, R.; Kaner, R. B. Ultrahard Compressible, Superhard Materials. *Annu. Rev. Mater. Res.* **2016**, *46*, 465–485.
- (4) Laniel, D.; Weck, G.; Gaiffe, G.; Garbarino, G.; Loubeyre, P. High-Pressure Synthesized Lithium Pentazolate Compound Metastable under Ambient Conditions. *J. Phys. Chem. Lett.* **2018**, *9*, 1600–1604.
- (5) Bykov, M.; Tasca, K. R.; Batyrev, I. G.; Smith, D.; Glazyrin, K.; Chariton, S.; Mahmood, M.; Goncharov, A. F. Dinitrogen as a Universal Electron Acceptor in Solid-State Chemistry: An Example of Uncommon Metallic Compounds $\text{Na}_3(\text{N}_2)_4$ and NaN_2 . *Inorg. Chem.* **2020**, *59* (20), 14819–14826.
- (6) Schneider, S. B.; Frankovsky, R.; Schnick, W. Synthesis of Alkaline Earth Diazenides MAEN_2 (MAE = Ca, Sr, Ba) by Controlled Thermal Decomposition of Azides under High Pressure. *Inorg. Chem.* **2012**, *51* (4), 2366–2373.
- (7) Niwa, K.; Fukui, R.; Terabe, T.; Kawada, T.; Kato, D.; Sasaki, T.; Soda, K.; Hasegawa, M. High-Pressure Synthesis and Phase Stability of Nickel Pernitride. *Eur. J. Inorg. Chem.* **2019**, *2019* (33), 3753–3757.
- (8) Chen, W.; Tse, J. S.; Jiang, J. Z. Stability, Elastic and Electronic Properties of Palladium Nitride. *J. Phys.: Condens. Matter* **2010**, *22* (1), 015404.
- (9) Niwa, K.; Yamamoto, T.; Sasaki, T.; Hasegawa, M. High-Pressure Synthesis, Crystal Growth, and Compression Behavior of Hexagonal CrN_2 Having One-Dimensionally Aligned Nitrogen Dimer. *Phys. Rev. Mater.* **2019**, *3* (5), 53601.
- (10) Niwa, K.; Terabe, T.; Kato, D.; Takayama, S.; Kato, M.; Soda, K.; Hasegawa, M. Highly Coordinated Iron and Cobalt Nitrides Synthesized at High Pressures and High Temperatures. *Inorg. Chem.* **2017**, *56* (11), 6410–6418.
- (11) Wessel, M.; Dronskowski, R. Nature of N-N Bonding within High-Pressure Noble-Metal Pernitrides and the Prediction of Lanthanum Pernitride. *J. Am. Chem. Soc.* **2010**, *132* (7), 2421–2429.
- (12) Niwa, K.; Suzuki, K.; Muto, S.; Tatsumi, K.; Soda, K.; Kikegawa, T.; Hasegawa, M. Discovery of the Last Remaining Binary Platinum-Group Pernitride RuN_2 . *Chem. - Eur. J.* **2014**, *20* (43), 13885–13888.
- (13) Niwa, K.; Dzivenko, D.; Suzuki, K.; Riedel, R.; Troyan, I.; Eremets, M.; Hasegawa, M. High Pressure Synthesis of Marcasite-Type Rhodium Pernitride. *Inorg. Chem.* **2014**, *53* (2), 697–699.
- (14) Bhadram, V. S.; Kim, D. Y.; Strobel, T. A. High-Pressure Synthesis and Characterization of Incompressible Titanium Pernitride. *Chem. Mater.* **2016**, *28* (6), 1616–1620.
- (15) Bykov, M.; Chariton, S.; Fei, H.; Fedotenko, T.; Aprilis, G.; Ponomareva, A. V.; Tasnádi, F.; Abrikosov, I. A.; Merle, B.; Feldner, P.; et al. High-Pressure Synthesis of Ultrahard Incompressible Hard Rhenium Nitride Pernitride $\text{Re}_2(\text{N}_2)(\text{N})_2$ Stable at Ambient Conditions. *Nat. Commun.* **2019**, *10* (1), 6–13.
- (16) Young, A. F.; Sanloup, C.; Gregoryanz, E.; Scandolo, S.; Hemley, R. J.; Mao, H. K. Synthesis of Novel Transition Metal Nitrides IrN_2 and OsN_2 . *Phys. Rev. Lett.* **2006**, *96* (15), 1–4.
- (17) Crowhurst, J. C.; Goncharov, A. F.; Sadigh, B.; Evans, C. L.; Morrall, P. G.; Ferreira, J. L.; Nelson, A. J. Synthesis and Characterization of the Nitrides of Platinum and Iridium. *Science* **2006**, *311* (5765), 1275–1278.
- (18) Bykov, M.; Bykova, E.; Aprilis, G.; Glazyrin, K.; Koemets, E.; Chuvashova, I.; Kuppenko, I.; McCammon, C.; Mezouar, M.; Prakapenka, V.; et al. Fe-N System at High Pressure Reveals a Compound Featuring Polymeric Nitrogen Chains. *Nat. Commun.* **2018**, *9* (1), 2756.
- (19) Laniel, D.; Winkler, B.; Fedotenko, T.; Aslandukova, A.; Aslandukov, A.; Vogel, S.; Meier, T.; Bykov, M.; Chariton, S.; Glazyrin, K.; et al. High-Pressure $\text{Na}_3(\text{N}_2)_4$, $\text{Ca}_3(\text{N}_2)_4$, $\text{Sr}_3(\text{N}_2)_4$, and $\text{Ba}(\text{N}_2)_3$ Featuring Nitrogen Dimers with Non-Integer Charges and Anion-Driven Metallicity. *arXiv:2105.11288v1 [cond-mat.mtrl-sci]* **2021**.
- (20) Wang, Y.; Bykov, M.; Bykova, E.; Zhang, X.; Jiang, S.; Greenberg, E.; Chariton, S.; Prakapenka, V. B.; Goncharov, A. F. Stabilization of Hexazine Rings in Potassium Polynitride at High Pressure. *arXiv:2010.15995 [cond-mat.mtrl-sci]*, **2020**.
- (21) Tschauner, O.; Luo, S. N.; Chen, Y. J.; McDowell, A.; Knight, J.; Clark, S. M. Shock Synthesis of Lanthanum-III-Pernitride. *High Pressure Res.* **2013**, *33* (1), 202–207.
- (22) Natali, F.; Ruck, B. J.; Plank, N. O. V.; Trodahl, H. J.; Granville, S.; Meyer, C.; Lambrecht, W. R. L. Rare-Earth Mononitrides. *Prog. Mater. Sci.* **2013**, *58* (8), 1316–1360.
- (23) Zerroug, S.; Ali Sahraoui, F.; Bouarissa, N. Ab Initio Calculations of Yttrium Nitride: Structural and Electronic Properties. *Appl. Phys. A: Mater. Sci. Process.* **2009**, *97* (2), 345–350.
- (24) Menescardi, F.; Ehrenreich-Petersen, E.; Ceresoli, D. High-Pressure Computational Search of Trivalent Lanthanide Dinitrides. *J. Phys. Chem. C* **2021**, *125* (1), 161–167.
- (25) Kantor, I.; Prakapenka, V.; Kantor, A.; Dera, P.; Kurnosov, A.; Sinogeikin, S.; Dubrovinskaia, N.; Dubrovinsky, L. BX90: A New Diamond Anvil Cell Design for X-Ray Diffraction and Optical Measurements. *Rev. Sci. Instrum.* **2012**, *83* (12), 125102.
- (26) Boehler, R. New Diamond Cell for Single-Crystal x-Ray Diffraction. *Rev. Sci. Instrum.* **2006**, *77* (11), 115103.
- (27) Kurnosov, A.; Kantor, I.; Boffa-Ballaran, T.; Lindhardt, S.; Dubrovinsky, L.; Kuznetsov, A.; Zehnder, B. H. A Novel Gas-Loading System for Mechanically Closing of Various Types of Diamond Anvil Cells. *Rev. Sci. Instrum.* **2008**, *79* (4), 045110.
- (28) Olijnyk, H. High Pressure X-Ray Diffraction Studies on Solid N_2 up to 43.9 GPa. *J. Chem. Phys.* **1990**, *93* (12), 8968–8972.
- (29) Akahama, Y.; Kawamura, H. Pressure Calibration of Diamond Anvil Raman Gauge to 310 GPa. *J. Appl. Phys.* **2006**, *100* (4), 043516.
- (30) Prescher, C.; Prakapenka, V. B. DIOPTAS: A Program for Reduction of Two-Dimensional X-Ray Diffraction Data and Data Exploration. *High Pressure Res.* **2015**, *35* (3), 223–230.
- (31) Petricek, V.; Dušek, M.; Palatinus, L. Crystallographic Computing System JANA2006: General Features. *Z. Kristallogr. - Cryst. Mater.* **2014**, *229* (5), 345–352.
- (32) Sheldrick, G. M. Crystal Structure Refinement with SHELXL. *Acta Crystallogr., Sect. C: Struct. Chem.* **2015**, *71* (1), 3–8.

- (33) Momma, K.; Izumi, F. VESTA 3 for Three-Dimensional Visualization of Crystal, Volumetric and Morphology Data. *J. Appl. Crystallogr.* **2011**, *44* (6), 1272–1276.
- (34) Gonzalez-Platas, J.; Alvaro, M.; Nestola, F.; Angel, R. EosFit7-GUI: A New Graphical User Interface for Equation of State Calculations, Analyses and Teaching. *J. Appl. Crystallogr.* **2016**, *49* (4), 1377–1382.
- (35) Kresse, G.; Furthmüller, J. Efficiency of Ab-Initio Total Energy Calculations for Metals and Semiconductors Using a Plane-Wave Basis Set. *Comput. Mater. Sci.* **1996**, *6* (1), 15–50.
- (36) Kresse, G.; Furthmüller, J. Bayesian Optimization for Calibrating and Selecting Hybrid-Density Functional Models. *Phys. Rev. B: Condens. Matter Mater. Phys.* **1996**, *54* (16), 11169.
- (37) Blöchl, P. E. Projector Augmented-Wave Method. *Phys. Rev. B: Condens. Matter Mater. Phys.* **1994**, *50* (24), 17953–17979.
- (38) Kresse, G.; Joubert, D. From Ultrasoft Pseudopotentials to the Projector Augmented-Wave Method. *Phys. Rev. B: Condens. Matter Mater. Phys.* **1999**, *59* (3), 1758–1775.
- (39) Perdew, J. P.; Burke, K.; Ernzerhof, M. Generalized Gradient Approximation Made Simple. *Phys. Rev. Lett.* **1996**, *77* (18), 3865–3868.
- (40) Monkhorst, H. J.; Pack, J. D. Special Points for Brillouin-Zone Integrations. *Phys. Rev. B* **1976**, *13* (12), 5188.
- (41) Togo, A.; Oba, F.; Tanaka, I. First-Principles Calculations of the Ferroelastic Transition between Rutile-Type and CaCl₂-Type SiO₂ at High Pressures. *Phys. Rev. B: Condens. Matter Mater. Phys.* **2008**, *78* (13), 134106.
- (42) Pace, E. J.; Finnegan, S. E.; Storm, C. V.; Stevenson, M.; McMahan, M. I.; MacLeod, S. G.; Plekhanov, E.; Bonini, N.; Weber, C. Structural Phase Transitions in Yttrium up to 183 GPa. *Phys. Rev. B: Condens. Matter Mater. Phys.* **2020**, *102* (9), 1–8.
- (43) Gregoryanz, E.; Goncharov, A. F.; Sanloup, C.; Somayazulu, M.; Mao, H. K.; Hemley, R. J. High P-T Transformations of Nitrogen to 170 GPa. *J. Chem. Phys.* **2007**, *126* (18), 184505.
- (44) Zachariasen, W. H. Crystal Chemical Studies of the 5 f -Series of Elements. VIII. Crystal Structure Studies of Uranium Silicides and of CeSi₃, NpSi₃, and PuSi₂. *Acta Crystallogr.* **1949**, *2* (2), 94–99.
- (45) Blatov, V. A.; O'Keeffe, M.; Proserpio, D. M. Vertex-, Face-, Point-, Schläfli-, and Delaney-Symbols in Nets, Polyhedra and Tilings: Recommended Terminology. *CrystEngComm* **2010**, *12* (1), 44–48.
- (46) Laniel, D.; Weck, G.; Loubeyre, P. Direct Reaction of Nitrogen and Lithium up to 75 GPa: Synthesis of the Li₃N, LiN, LiN₂, and LiN₅ Compounds. *Inorg. Chem.* **2018**, *57* (17), 10685–10693.
- (47) Wessel, M.; Dronskowski, R. A First-Principles Study on the Existence and Structures of the Lighter Alkaline-Earth Pernitrides. *J. Comput. Chem.* **2010**, *32* (2), 1613–1617.
- (48) Chen, Z. W.; Guo, X. J.; Liu, Z. Y.; Ma, M. Z.; Jing, Q.; Li, G.; Zhang, X. Y.; Li, L. X.; Wang, Q.; Tian, Y. J.; Liu, R. P. Crystal Structure and Physical Properties of OsN₂ and PtN₂ in the Marcasite Phase. *Phys. Rev. B: Condens. Matter Mater. Phys.* **2007**, *75* (5), 1–4.
- (49) Binns, J.; Donnelly, M.-E.; Peña-Alvarez, M.; Wang, M.; Gregoryanz, E.; Hermann, A.; Dalladay-Simpson, P.; Howie, R. T. Direct Reaction between Copper and Nitrogen at High Pressures and Temperatures. *J. Phys. Chem. Lett.* **2019**, *10* (5), 1109–1114.
- (50) Yu, R.; Zhan, Q.; De Jonghe, L. C. Crystal Structures of and Displacive Transitions in OsN₂, IrN₂, RuN₂, and RhN₂. *Angew. Chem., Int. Ed.* **2007**, *46* (7), 1136–1140.
- (51) Zhao, Z.; Bao, K.; Tian, F.; Duan, D.; Liu, B.; Cui, T. Potentially Superhard Hcp CrN₂ Compound Studied at High Pressure. *Phys. Rev. B: Condens. Matter Mater. Phys.* **2016**, *93* (21), 214104.
- (52) Wang, Z.; Li, Y.; Li, H.; Harran, I.; Jia, M.; Wang, H.; Chen, Y.; Wang, H.; Wu, N. Prediction and Characterization of the Marcasite Phase of Iron Pernitride under High Pressure. *J. Alloys Compd.* **2017**, *702*, 132–137.
- (53) Nespolo, M. Charge Distribution as a Tool to Investigate Structural Details. IV. A New Route to Heteroligand Polyhedra. *Acta Crystallogr., Sect. B: Struct. Sci., Cryst. Eng. Mater.* **2016**, *72* (1), 51–66.
- (54) Manz, T. A.; Limas, N. G. Introducing DDEC6 Atomic Population Analysis: Part 1. Charge Partitioning Theory and Methodology. *RSC Adv.* **2016**, *6* (53), 47771–47801.

Supporting information

High-Pressure Yttrium Nitride, Y_5N_{14} , Featuring Three Distinct Types of Nitrogen Dimers

Andrey Aslandukov,^{1} Alena Aslandukova,² Dominique Laniel,¹ Iuliia Koemets,² Timofey Fedotenko,¹ Liang Yuan,² Gerd Steinle-Neumann,² Konstantin Glazyrin,³ Michael Hanfland,⁴ Leonid Dubrovinsky,² Natalia Dubrovinskaia,^{1,5}*

¹ Material Physics and Technology at Extreme Conditions, Laboratory of Crystallography, University of Bayreuth, 95440 Bayreuth, Germany

² Bavarian Research Institute of Experimental Geochemistry and Geophysics (BGI), University of Bayreuth, Univesitaetsstrasse 30, 95440 Bayreuth, Germany

³ Photon Science, Deutsches Elektronen-Synchrotron, Notkestrasse 85, 22607 Hamburg, Germany

⁴ European Synchrotron Radiation Facility, BP 220, 38043 Grenoble Cedex, France

⁵ Department of Physics, Chemistry and Biology (IFM), Linköping University, SE-581 83 Linköping, Sweden

Table S1. Structure refinement details of Y₅N₁₄ at 49.1 GPa. The full crystallographic dataset was deposited to the CCDC under the deposition number 2085508.

Chemical formula	Y ₅ N ₁₄			
Temperature (K)	293			
Pressure (GPa)	49.1			
Crystal data				
Mr	640.6			
ρ (g/cm ³)	6.296			
Crystal system, space group	tetragonal, <i>P4/mbm</i>			
a (Å)	8.4510(16)			
c (Å)	4.7316(9)			
V (Å ³)	337.93(14)			
Z	2			
Radiation type	X-ray, $\lambda = 0.2908$ Å			
μ (mm ⁻¹)	3.968			
Data collection				
No. of measured, independent and observed [I > 3 σ (I)] reflections	1554/586/439			
R _{int}	5.05%			
(sin θ / λ) _{max} (Å ⁻¹)	1.056			
Refinement				
R[F ² > 3 σ (F ²)], wR(F ²), GOF	0.0348, 0.0788, 1.08			
data/parameters ratio	586/30			
$\Delta\rho_{\max}$, $\Delta\rho_{\min}$ (e Å ⁻³)	2.40, -2.47			
Atomic positions				
Atom	Wyckoff site	Fractional atomic coordinates		
		x	y	z
Y01	4g	0.67473(6)	0.17473(6)	0.5
Y02	2a	0	0	0
Y03	4h	0.13326(6)	0.63326(6)	0
N01	16l	0.1909(4)	0.0609(4)	0.3703(8)
N02	8i	0.1263(6)	0.2658(6)	0
N03	4f	0	0.5	0.3586(15)

Table S2. Experimentally determined crystallographic data for the Y_5N_{14} phase at 49(1) GPa in comparison with the corresponding DFT-relaxed structure

	Experimental				Calculations			
Pressure (GPa)	$P_{\text{exp}} = 49(1)$ GPa				$P_{\text{theor}} = 50$ GPa			
Space group	$P4/mbm$				$P4/mbm$			
a (Å)	8.4510(16)				8.4813			
c (Å)	4.7316(9)				4.6978			
V (Å ³)	337.93(14)				337.93 (fixed)			
Fractional atomic coordinates (x y z)	Y01	0.6747	0.1747	0.5	Y01	0.6749	0.1749	0.5
	Y02	0	0	0	Y02	0	0	0
	Y03	0.1333	0.6334	0	Y03	0.1338	0.6338	0
	N01	0.1909	0.0609	0.3703	N01	0.1907	0.0601	0.3689
	N02	0.1263	0.2658	0	N02	0.1269	0.2674	0
	N03	0	0.5	0.3586	N03	0	0.5	0.3595
N-N distances (Å)	N01-N01	1.227(8)			N01-N01	1.232		
	N02-N02	1.290(11)			N02-N02	1.267		
	N03-N03	1.338(15)			N03-N03	1.320		

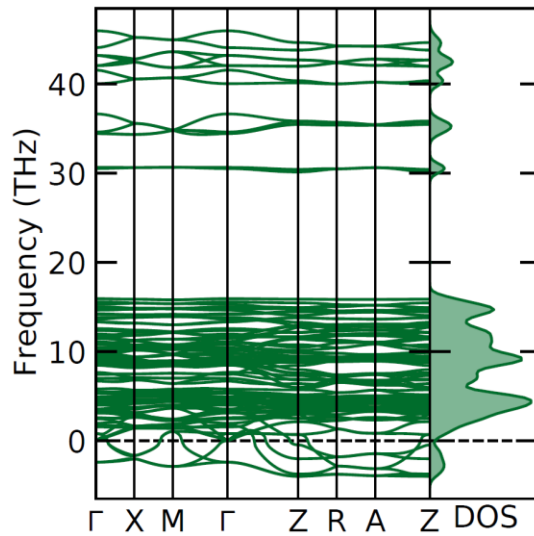


Figure S1. Phonon dispersion curves for Y_5N_{14} along the high symmetry directions in the Brillouin zone and the phonon density of state at ambient pressure. Imaginary frequencies indicate the dynamic instability of the compound.

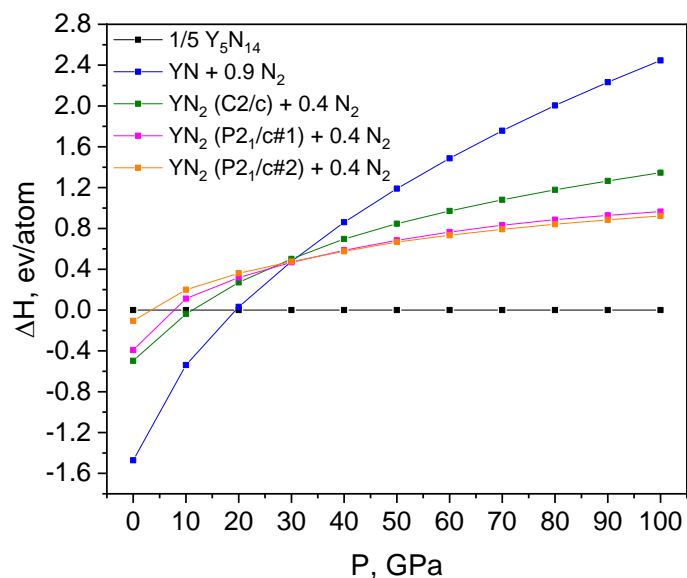


Figure S2. Calculated static enthalpy as a function of pressure of YN (rocksalt structure) plus 0.9 N₂ (ϵ -N₂ structure) and YN₂ (three predicted polymorphs¹) plus 0.4 N₂ (ϵ -N₂ structure) relative to Y₅N₁₄. Following the approach of Menescardi *et al.*,¹ the ϵ -N₂ polymorph was used to model solid nitrogen over the whole pressure range as it is reported to be the most stable polymorph between 16 and 62 GPa.²

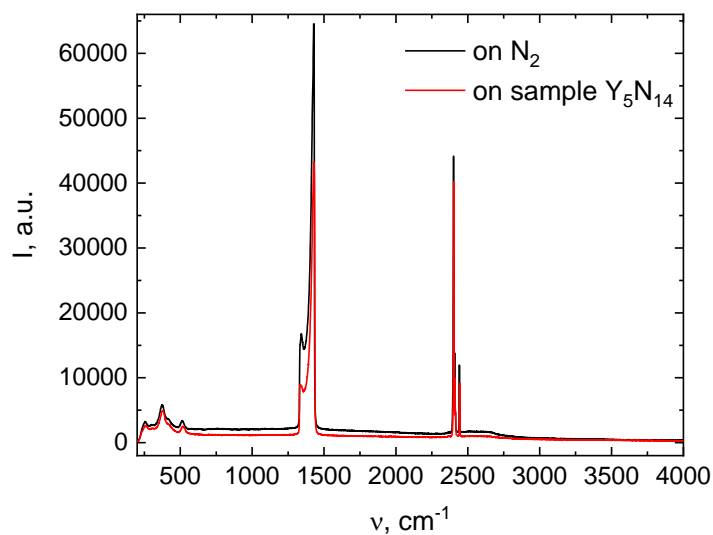


Figure S3. Raman spectra collected on the sample chamber of DAC at 49(1) GPa after laser heating. Signals from a region of the sample chamber with nitrogen only (black) shows the Raman spectrum of ϵ -N₂, for a region containing Y₅N₁₄ (red) the signal does not differ significantly.

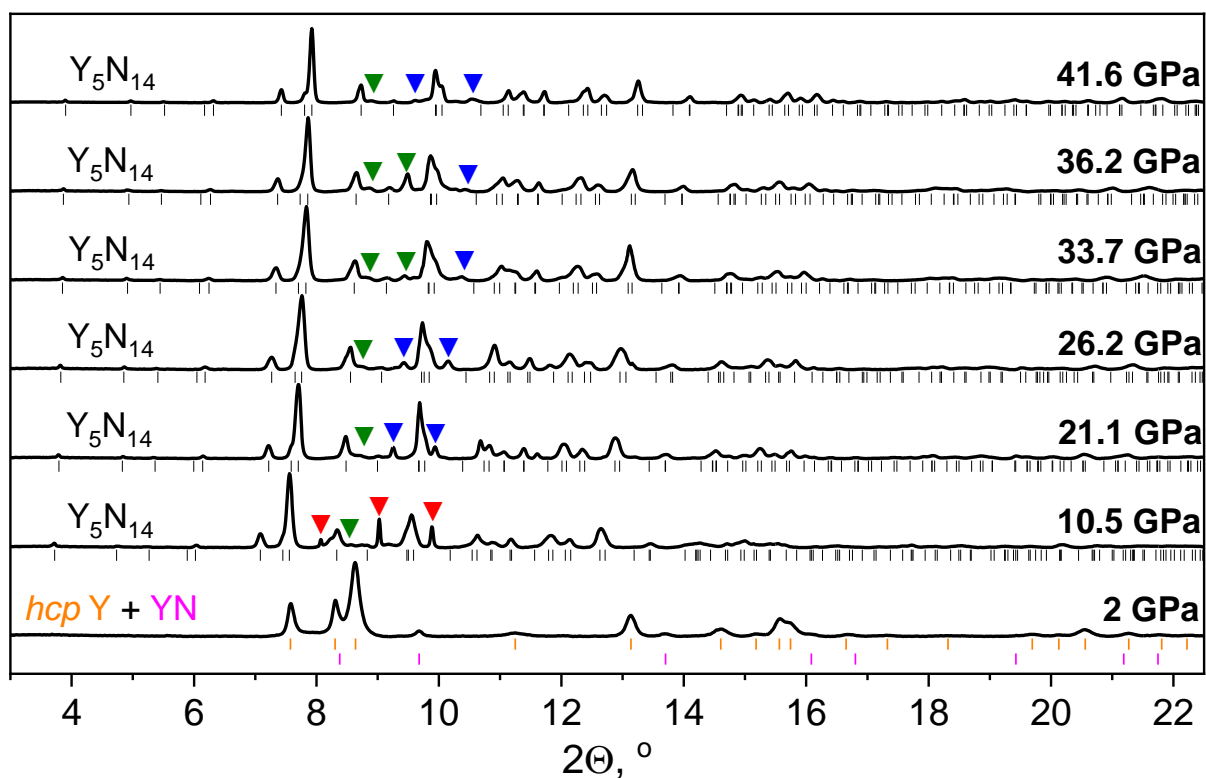


Figure S4. Background-subtracted X-Ray diffraction profiles from the sample collected on decompression. Black tick marks are the position of the reflections belonging to Y_5N_{14} phase; the \blacktriangledown , \blacktriangledown and \blacktriangledown symbols identify *dhcp* Y, ϵ - N_2 and δ - N_2 phases, respectively. The orange and magenta tick marks represent the position of the reflections corresponding to *hcp* Y and *fcc* YN phases at 2 GPa, respectively.

Table S3. Structure refinement details of Y₅N₁₄ from measurements upon decompression.

Pressure (GPa)	49.1	41.6	33.7	26.2	21.1	10.5	
ρ (g/cm ³)	6.296	6.196	6.019	5.824	5.701	5.386	
Space group	<i>P4/mbm</i>	<i>P4/mbm</i>	<i>P4/mbm</i>	<i>P4/mbm</i>	<i>P4/mbm</i>	<i>P4/mbm</i>	
a (Å)	8.4510(16)	8.5189(15)	8.6091(16)	8.6787(16)	8.752(2)	8.9197(16)	
c (Å)	4.7316(9)	4.7316(5)	4.7692(9)	4.8500(9)	4.8718(9)	4.9649(9)	
a/c ratio	1.79	1.80	1.80	1.79	1.80	1.80	
V (Å ³)	337.93(14)	343.38(18)	353.48(11)	365.30(12)	373.21(12)	395.01(12)	
Z	2	2	2	2	2	2	
No. of measured, independent, observed [I>3 σ (I)] reflections	1554 586 439	819 317 219	917 349 239	887 366 262	1030 280 177	1124 337 175	
R _{int}	5.05%	7.38%	4.46%	9.79%	6.66%	9.06%	
R[F > 3 σ (F)], wR(F), GOF	0.0348 0.0788 1.08	0.1137 0.1296 1.93	0.0479 0.0486 1.83	0.1056 0.1202 1.98	0.0369 0.0358 1.19	0.0595 0.0742 1.32	
data/parameters ratio	586/30	317/30	349/30	366/30	308/30	337/30	
Atoms fractional coordinates							
Y01	x	0.67473(6)	0.6743(2)	0.6731(1)	0.6735(2)	0.6726(1)	0.6717(2)
	y	0.17473(6)	0.1743(2)	0.1731(1)	0.1735(2)	0.1726(1)	0.1717(2)
	z	0.5	0.5	0.5	0.5	0.5	0.5
Y02	x	0	0	0	0	0	0
	y	0	0	0	0	0	0
	z	0	0	0	0	0	0
Y03	x	0.13326(6)	0.1340(2)	0.1333(1)	0.1339(2)	0.1338(1)	0.1335(2)
	y	0.63326(6)	0.6340(2)	0.6333(1)	0.6339(2)	0.6338(1)	0.6335(2)
	z	0	0	0	0	0	0
N01	x	0.1909(4)	0.1896(18)	0.1906(8)	0.1917(13)	0.1954(7)	0.1962(12)
	y	0.0609(4)	0.0610(18)	0.0601(8)	0.0597(14)	0.0617(7)	0.0662(11)
	z	0.3703(8)	0.381(3)	0.3727(14)	0.374(2)	0.3770(13)	0.375(2)
N02	x	0.1263(6)	0.112(4)	0.1266(12)	0.128(3)	0.1261(11)	0.134(2)
	y	0.2658(6)	0.286(4)	0.2662(12)	0.267(2)	0.2698(11)	0.270(2)
	z	0	0	0	0	0	0
N03	x	0	0	0	0	0	0
	y	0.5	0.5	0.5	0.5	0.5	0.5
	z	0.3586(15)	0.353(4)	0.358(2)	0.361(4)	0.361(2)	0.361(4)
N-N distances							
N01-N01	1.227(8)	1.13(3)	1.214(14)	1.22(2)	1.200(13)	1.25(2)	
N02-N02	1.290(11)	1.23(7)	1.31(3)	1.29(5)	1.290(2)	1.21(4)	
N03-N03	1.338(15)	1.39(4)	1.35(2)	1.35(4)	1.34(2)	1.37(4)	

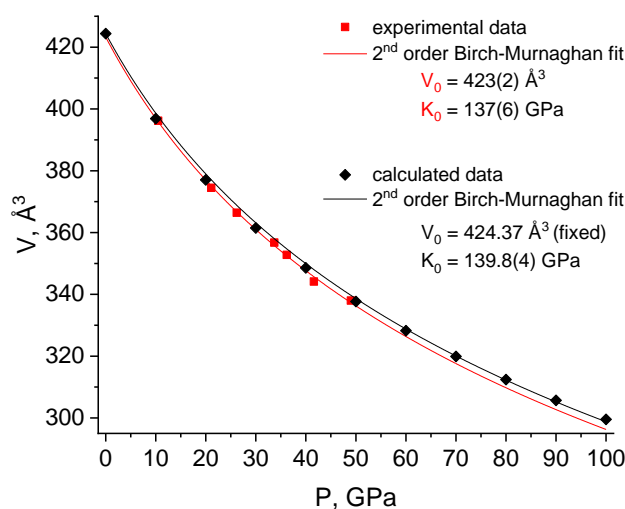


Figure S5. Experimental (red points) pressure dependence of the Y_5N_{14} unit cell volume and the fit of the experimental P-V data (red curve) using the 2nd order Birch-Murnaghan equation of state. Errors in experimental data are within the symbol size. As well as pressure points calculated by Hellmann-Feynman stresses (black points) and the fit of calculated E-V data (black curve) using the 2nd order Birch-Murnaghan equation of state. Calculated E-V data also can be fitted using a 3rd order Birch-Murnaghan equation of state, yielding $K_0=131(2)$ GPa, $K_0'=4.46(3)$ and $V_0=424.6(4)$ Å³.

Table S4. Results of charge analysis

Atom	Charge	
	CHARDI	DDEC6
Y01	+2.97	+1.37
Y02	+2.92	+1.62
Y03	+3.07	+1.61
N01	-0.98	-0.48
N02	-1.17	-0.61
N03	-1.25	-0.67

References

- (1) Menescardi, F.; Ehrenreich-Petersen, E.; Ceresoli, D. High-Pressure Computational Search of Trivalent Lanthanide Dinitrides. *J. Phys. Chem. C* **2021**, *125* (1), 161–167.
- (2) Gregoryanz, E.; Goncharov, A. F.; Sanloup, C.; Somayazulu, M.; Mao, H. K.; Hemley, R. J. High P-T Transformations of Nitrogen to 170 GPa. *J. Chem. Phys.* **2007**, *126* (18), 184505.

5.3. Anionic N₁₈ macrocycles and a polynitrogen double helix in novel yttrium polynitrides YN₆ and Y₂N₁₁ at 100 GPa

This section contains the following manuscript and the related supplementary material:

“Anionic N₁₈ macrocycles and a polynitrogen double helix in novel yttrium polynitrides YN₆ and Y₂N₁₁ at 100 GPa”

A. Aslandukov, F. Trybel, A. Aslandukova, D. Laniel, T. Fedotenko, S. Khandarkhaeva, G. Aprilis, C. Giacobbe, E.L. Bright, I.A. Abrikosov, L. Dubrovinsky, N. Dubrovinskaia.

Status: published in *Angewandte Chemie*, 61(34), e202207469

(2022)

Reproduced under the terms and conditions of the Creative Commons ‘CC BY 4.0’

VIP Polynitrides Very Important Paper

How to cite: *Angew. Chem. Int. Ed.* **2022**, *61*, e202207469

International Edition: doi.org/10.1002/anie.202207469

German Edition: doi.org/10.1002/ange.202207469

Anionic N₁₈ Macrocycles and a Polynitrogen Double Helix in Novel Yttrium Polynitrides YN₆ and Y₂N₁₁ at 100 GPa

Andrey Aslandukov,* Florian Trybel, Alena Aslandukova, Dominique Laniel, Timofey Fedotenko, Saiana Khandarkhaeva, Georgios Aprilis, Carlotta Giacobbe, Eleanor Lawrence Bright, Igor A. Abrikosov, Leonid Dubrovinsky, and Natalia Dubrovinskaia

Abstract: Two novel yttrium nitrides, YN₆ and Y₂N₁₁, were synthesized by direct reaction between yttrium and nitrogen at 100 GPa and 3000 K in a laser-heated diamond anvil cell. High-pressure synchrotron single-crystal X-ray diffraction revealed that the crystal structures of YN₆ and Y₂N₁₁ feature a unique organization of nitrogen atoms—a previously unknown anionic N₁₈ macrocycle and a polynitrogen double helix, respectively. Density functional theory calculations, confirming the dynamical stability of the YN₆ and Y₂N₁₁ compounds, show an anion-driven metallicity, explaining the unusual bond orders in the polynitrogen units. As the charge state of the polynitrogen double helix in Y₂N₁₁ is different from that previously found in Hf₂N₁₁ and because N₁₈ macrocycles have never been predicted or observed, their discovery significantly extends the chemistry of polynitrides.

The chemistry of nitrogen has long been thought to be very limited due to triple-bonded molecular nitrogen's extreme stability. As a result, in inorganic solid-state compounds at ambient pressure, nitrogen is typically present in the form of a nitride anion N³⁻ and does not form catenated polyanions (with the exception of azides). However, over the past 20 years, it has been shown that at high pressure nitrogen's chemistry significantly changes. For example, charged nitrogen N₂^{x-} dimers,^[1–16] tetranitrogen N₄⁴⁻ units,^[17] pentazolate N₅⁻ rings,^[18–20] hexazine N₆ rings,^[21–23] and different polynitrogen chains^[17,24–29] have been synthesized, and an even greater variety of nitrogen species is expected to form under high-pressure conditions according to theoretical calculations.^[30–37] Such a diversity of nitrogen species can suggest that the scale of nitrogen chemistry under high pressure may be close to the scale of the rich carbon chemistry at ambient pressure. In addition to the discoveries of unique nitrogen entities that push the boundaries of fundamental nitrogen chemistry, nitrides synthesized under high pressure often possess key properties for functional applications, e.g. ReN₂, which is recoverable to ambient conditions,^[4] has an extremely high hardness, a single layer of BeN₄ is a 2D material with unique electronic properties,^[29] and a variety of nitrides with high nitrogen content are promising for applications as high energy density materials.^[38] Recently, YN₅, YN₈, and YN₁₀ with polynitrogen chains, fused N₁₈ rings and isolated N₅ rings, respectively, were predicted to be stable near 100 GPa and are all promising prospects as high energy density materials.^[37]

Whereas a significant number of studies on binary metal-nitrogen compounds of alkali, alkaline earth, and transition metal elements under high pressure have been conducted,^[1–7,9–29] the high-pressure chemistry and physical properties of rare earth metal nitrides are almost unknown. Until recently, in the yttrium-nitrogen system, only one binary Y–N compound was known: cubic yttrium nitride YN with the rock salt structure.^[39] In 2021 our group demonstrated that even at moderate compression (≈50 GPa) yttrium and nitrogen form a novel compound, Y₅N₁₄, with a new structural type.^[8] In the Y₅N₁₄ structure, all nitrogen atoms form [N₂]^{x-} dimers but, strikingly, there are three crystallographically distinct nitrogen dimers with different N–N bond lengths and charge states *x*, indicating the

[*] A. Aslandukov, Dr. D. Laniel, S. Khandarkhaeva, Prof. N. Dubrovinskaia
 Material Physics and Technology at Extreme Conditions, Laboratory of Crystallography, University of Bayreuth
 Universitätsstrasse 30, 95440 Bayreuth (Germany)
 E-mail: andrii.aslandukov@uni-bayreuth.de

A. Aslandukov, A. Aslandukova, Prof. L. Dubrovinsky
 Bayerisches Geoinstitut, University of Bayreuth
 Universitätsstrasse 30, 95440 Bayreuth (Germany)

Dr. F. Trybel, Prof. I. A. Abrikosov, Prof. N. Dubrovinskaia
 Department of Physics, Chemistry and Biology (IFM), Linköping University
 58183 Linköping (Sweden)

Dr. D. Laniel
 Centre for Science at Extreme Conditions and School of Physics and Astronomy, University of Edinburgh
 Edinburgh EH9 3FD (UK)

Dr. T. Fedotenko
 Photon Science, Deutsches Elektronen-Synchrotron
 Notkestrasse 85, 22607 Hamburg (Germany)

Dr. G. Aprilis, Dr. C. Giacobbe, Dr. E. Lawrence Bright
 European Synchrotron Radiation Facility
 BP 220, 38043 Grenoble Cedex (France)

© 2022 The Authors. Angewandte Chemie International Edition published by Wiley-VCH GmbH. This is an open access article under the terms of the Creative Commons Attribution License, which permits use, distribution and reproduction in any medium, provided the original work is properly cited.

complexity of chemical processes leading to the formation of dense rare earth metal nitrides under high pressure.

In this study, we present the synthesis and characterization of two novel never predicted yttrium nitrides YN_6 and Y_2N_{11} at 100 GPa, demonstrating a unique organization of nitrogen atoms in their structures, forming anionic N_{18} macrocycles and a polynitrogen double helix.

A diamond anvil cell, containing a sample composed of two pieces of yttrium embedded into molecular nitrogen, was compressed to 100(1) GPa and laser-heated to 3000 (200) K (see Figure 1a and Supporting Information for details). The precise 2D X-ray diffraction map, collected with a step of 0.5 μm at ID11 ESRF beamline from the bigger piece of yttrium after heating, revealed the crystallization of novel phases and allowed to pinpoint the location of crystallites most appropriate for single-crystal X-ray diffraction measurements (Figure 1b). High-quality synchrotron single-crystal X-ray diffraction (SCXRD) data were then collected from the sample (Figure 1c). The subsequent crystal structure solution and refinement revealed the formation of two novel yttrium nitrides with chemical formulas of YN_6 and Y_2N_{11} . The refinement against SCXRD data resulted in very good reliability factors (R-factors, see Tables S1, S2). For cross-validation of the structural models, we performed density functional theory (DFT) based calculations (see Supporting Information for details). We carried out variable cell structural relaxations for both compounds and found that the relaxed structural parameters closely reproduce the corresponding experimental values (Table S3). The distribution of the YN_6 and Y_2N_{11} phases shown in the 2D X-ray diffraction map (Figure 1b) demonstrates that the heated area consists of many tiny crystallites and there is no obvious chemical gradient in the distribution. The formation of a mixture of phases with different chemical compositions and structures is a very common phenomenon at high-pressure synthesis in a laser-heated diamond anvil cell mainly attributed to the temperature gradient during laser heating.

The structure of YN_6 (Figure 2) has the monoclinic space group $C2/m$ (#12) with two Y and five N atoms on crystallographically distinct positions (see Table S1 and the CIF for the full crystallographic data^[40]). Nitrogen atoms form isolated, almost planar N_{18} macrocycles aligned in the (4 0 -1) planes (Figure 2b). The Y1 atoms are located in the centers of the N_{18} macrocycles, while the Y2 atoms occupy the space between the stacking planes (Figure 2a). Thus, Y1 atoms are twelve-fold coordinated (coordination number $\text{CN}=12$) by six nearest nitrogen atoms of the N_{18} ring itself and by three nitrogen atoms of the previous and next rings in the stack (Figure 2c). The equatorial coordination of Y1 is very similar to the coordination of the rare-earth metals in complexes with hexaaza-18-membered macrocyclic ligands.^[41–43] Y2 atoms are thirteen-fold coordinated ($\text{CN}=13$) by N atoms of the six surrounding rings (Figure 2d). Both Y1 and Y2 atoms are located in the ac plane forming a 2D tiling which can be described by two types of parallelograms (Figure S1). The nets of Y atoms are alternating in the b -direction.

Although 2D polynitrogen layers composed of fused N_{18} rings were predicted for YN_8 ^[37] and K_2N_{16} ,^[44] the isolated anionic N_{18} rings observed in YN_6 have never been reported from experiments or calculations. Hypothetically, a non-charged N_{18} ring would be an aromatic planar ring with 18 electrons in the conjugated π -system with the N–N bond order of 1.5. However, in the case of the YN_6 compound, assuming +3 charge of yttrium atoms, the π -system of each N_{18} ring should accommodate additional 9 electrons at the π^* orbitals, which results in 27 electrons in the π -system, losing aromaticity and thereby decreasing the average N–N bond order to 1.25 and consequently increasing of the N–N bond length. Moreover, the N_{18} rings in YN_6 are non-planar (the biggest torsion angle is $6.2(6)^\circ$), not satisfying the aromaticity condition. The N–N distances ($d_{\text{N-N}}$) in the N_{18} macrocycle obtained from the SCXRD data are not equal and vary from 1.270(5) Å to 1.364(7) Å with the average $d_{\text{N-N}}=1.306(9)$ Å, in good agreement with the values

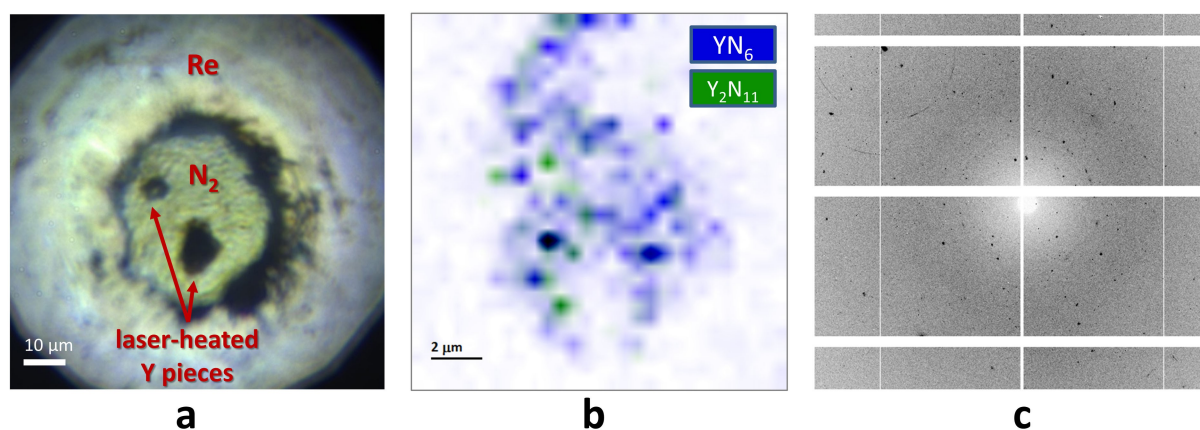


Figure 1. Experimental details. a) Microphotograph of the sample chamber. b) 2D X-ray diffraction map showing the distribution of the two yttrium nitrides phases within the heated sample. The color intensity is proportional to the intensity of the following reflections: the (2 0 0), (0 2 0), and (1 1 -2) of YN_6 for the blue regions; the (1 0 1), (2 -1 0), and (2 -1 4) of Y_2N_{11} for the green regions. c) Example of an X-ray diffraction pattern collected from the laser-heated sample at 100 GPa.

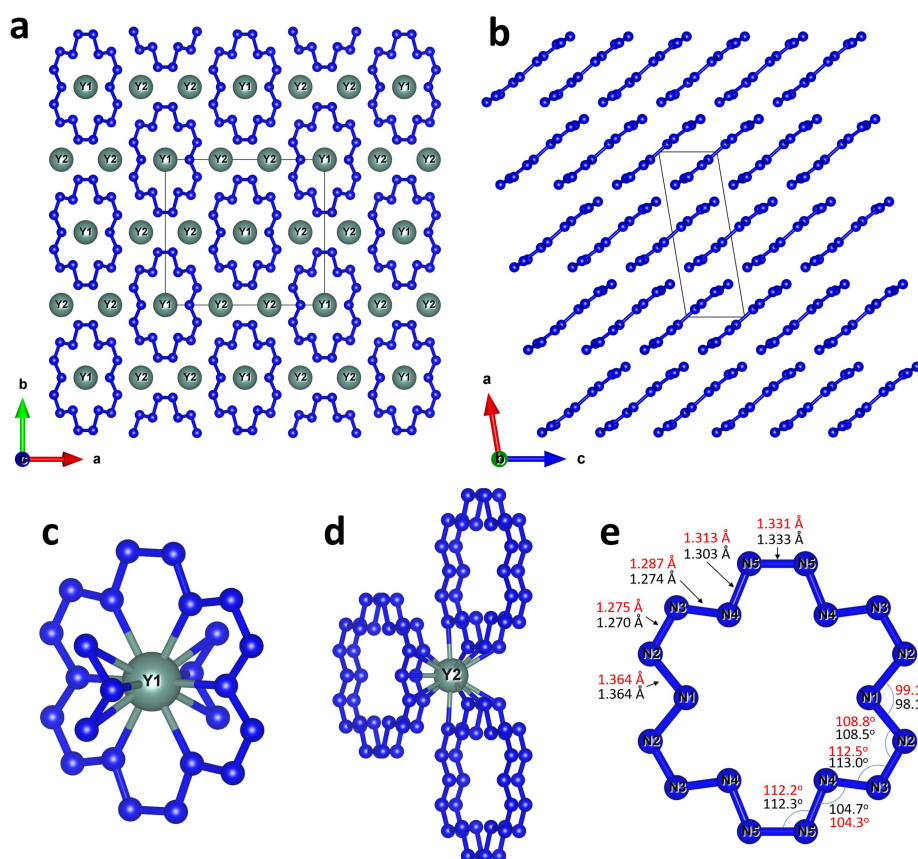


Figure 2. Crystal structure of YN₆. All Y atoms are greenish, N atoms are blue; grey thin lines outline the unit cell. a) A view of the crystal structure along the *c*-axis. b) A view of the crystal structure along the *b*-axis; yttrium atoms are omitted. c) The coordination environment of the Y1 and d) Y2 atoms. e) A view of a N₁₈ macrocycle; values of bond lengths and angles obtained from the experiment are shown in black, while those obtained from the DFT calculations are shown in red.

obtained from the DFT-relaxed structure (Figure 2e). The analysis of N–N bond lengths suggests that N1–N2 and N5–N5 are single bonds (single N–N bonds vary from 1.30 to 1.44 Å at ≈ 100 GPa^[24,27,29,45]), N2–N3 and N3–N4 have a bond order of 1.5 (the length of N–N bonds with the multiplicity of 1.5 is known to be in the range of 1.24 to 1.30 Å at ≈ 100 GPa^[25]), while the multiplicity of the N4–N5 bond should be in between of 1 and 1.5. If one assumes the bond order of 1.125 for the N4–N5 bond, the average bond order in the [N₁₈]⁹⁻ ring is of 1.25, which corresponds to 27 electrons in the π -system and a total 9- charge. Non-integer charges and bond orders were previously reported in metallic nitrides under high pressure.^[2,7,8,26]

Although 18-membered cycles are not common, they are known for a number of organic compounds. As an example, one can mention 18-crown-6 ether, whose molecule is non-planar as all ring-forming atoms are sp³-hybridized. A closer analog to the N₁₈ rings we observed in YN₆ would be an unsaturated cyclooctadecanonaene C₁₈H₁₈ ([18]annulene). The [18]annulene C₁₈H₁₈ is a fully planar aromatic compound, and until now the most nitrogen-substituted known derivative is hexaaza[18]annulene C₁₂N₆H₁₂.^[46] The existence of [N₁₈]⁹⁻ anionic macrocycle allows us to assume that high-pressure could provide a route to the synthesis of N₁₈

aromatic molecule–full nitrogen substituted [18]annulene derivative.

The Y₂N₁₁ compound, also synthesized at 100(1) GPa, crystallizes in the structure with the hexagonal space group *P*6₂22 (#180), in which there are one Y and four N distinct atomic positions (see Table S2 and the CIF for the full crystallographic data^[40]). Notably, the introduction of a racemic twinning law during the final structure refinement against SCXRD data leads to a slight decrease in the R₁ factor, therefore, Y₂N₁₁ with the space group *P*6₂22 coexists with its enantiomorph Y₂N₁₁ with the space group *P*6₄22 (#181). The structure of Y₂N₁₁ (Figure 3) is built of Y atoms (CN=10) coordinated by discrete nitrogen atoms, N₂ dumbbells, and polynitrogen chains (Figure 3c). Each discrete nitrogen atom is surrounded by four yttrium atoms forming regular tetrahedra NY₄, which are connected through vertexes, forming a motif similar to the SiO₄ tetrahedral motif in β -quartz^[47] (Figure 3a,b). Like SiO₄ groups in the structure of β -quartz, the NY₄ tetrahedra in Y₂N₁₁ form channels along the *c*-axis (Figure 3a), which are occupied by nitrogen dumbbells with their centers on the 6₂ axis (Figure 3a). The dumbbells themselves are also in a tetrahedral coordination environment of Y atoms (Figure 3d). Two polymeric nitrogen chains are running along the channels in

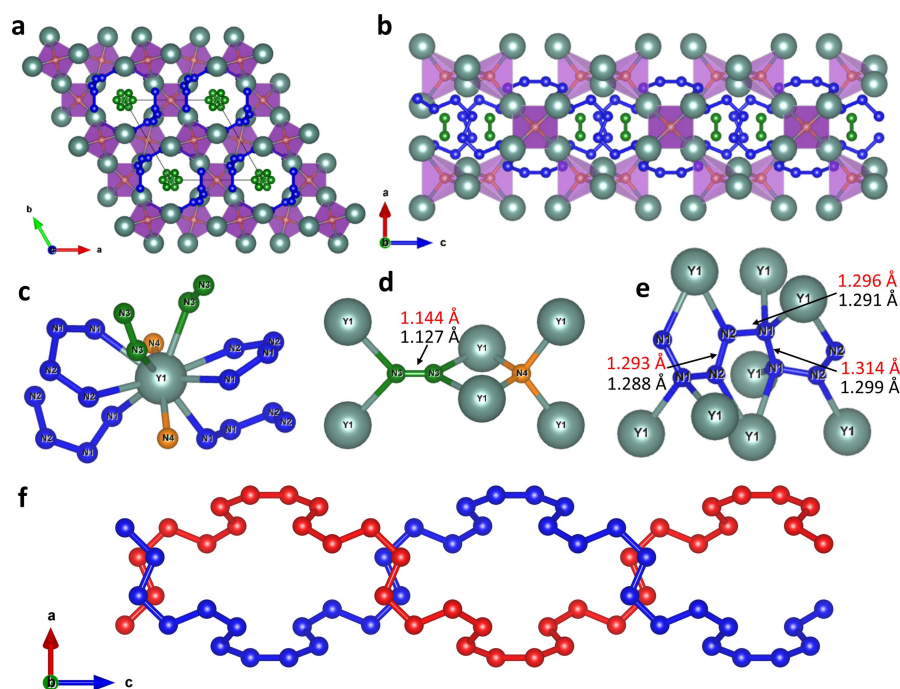


Figure 3. Crystal structure of Y_2N_{11} . All Y atoms are greenish, blue balls represent nitrogen atoms of the infinite chains, green balls—nitrogen atoms that form dumbbells, orange balls—discrete nitrogen atoms; grey thin lines outline the unit cell. a) A view of the crystal structure along the c -axis. b) A view of the crystal structure along the b -axis. c) The coordination environment of the Y atom. d) The coordination environment of discrete nitrogen atoms and nitrogen dumbbells. e) The coordination environment of polymeric nitrogen chain; values of bond lengths obtained from the experiment are shown in black, while those obtained from the DFT calculations are shown in red. f) Double helix built of two polynitrogen chains running along the c -direction around the 6_2 screw-axis.

the c -direction (shown in blue in Figure 3a,b,e) forming a double helix arrangement (highlighted in blue and red in Figure 3f) around the 6_2 screw-axis. The crystal-chemical formula of Y_2N_{11} may be written as $Y_2N(N_4)_2(N_2)$.

It appears that Y_2N_{11} is isostructural to previously reported Hf_2N_{11} (space group $P6_422$) synthesized by laser-heating Hf in nitrogen at 105 GPa.^[26] The difference in the oxidation states of the cations Y^{3+} and Hf^{4+} in the isostructural compounds should lead to the difference in charge states of the corresponding nitrogen units. Indeed, taking into account that in the Hf_2N_{11} structure at 105 GPa the N–N distance in N_2 dimers is equal to 1.186 Å, and the average N–N distance in polynitrogen chains is 1.32 Å, the charge distribution was proposed as $(Hf^{4+})_2N^{3-}(N_4^{2-})_2(N_2^-)$.^[26] In Y_2N_{11} at 100(1) GPa, the N–N distance in N_2 dimers is 1.13 Å 1.127(15), and the average N–N distance in polynitrogen chains is 1.29 Å, noticeably shorter than those in Hf_2N_{11} , indicating smaller charges on the nitrogen species. Since the N–N distance in N_2 dimers is longer than that in the triple-bonded non-charged N_2 molecule, but shorter than the bond length in N_2^- , one can suggest the $N_2^{0.5-}$ charge state for the dumbbells. Contrary to Hf_2N_{11} , the N–N distances in the polynitrogen chains in Y_2N_{11} are almost equal and the length corresponds to a bond order between 1 and 1.5. Thus, one can assume the following charge distribution: $(Y^{3+})_2N^{3-}(N_4^{1.25-})_2(N_2^{0.5-})$. This example demonstrates that the π -system of polynitrogen chains is flexible in terms of charge accommodation.

Inorganic double helices are extremely rare^[48–50] and the fact that such an arrangement of nitrogen atoms in the compounds was observed for the second time at about 100 GPa may indicate the existence of such a class of polynitrides under high pressure. Furthermore, the structure of Y_2N_{11} can be considered as a host–guest, where yttrium and discrete nitrogen atoms form a β -quartz-type host framework (Figure 3), where inside and around the channels are guest nitrogen dimers and a polynitrogen double helix. Therefore, perhaps β -quartz-motifs could serve as a template for the synthesis of other inorganic double helices.

In order to get a deeper insight into the chemistry and physical properties of the novel compounds, further DFT-based calculations were performed (see Supporting Information for details). As mentioned above, variable-cell structural relaxations for both compounds at the synthesis pressure closely reproduced structural parameters and bond lengths obtained from the experimental data. Phonon dispersion relations calculated in harmonic approximation show that both YN_6 and Y_2N_{11} phases are dynamically stable at 100 GPa (Figure 4a and Figure 4d). To estimate the thermodynamic stability of the novel phases, a static enthalpy convex-hull for all known yttrium nitrides was calculated at 100 GPa. Within the used approximations, YN_6 lies on the convex hull together with YN and Y_5N_{14} , while Y_2N_{11} lays 189 meV per atom above the convex hull (Figure S2). Being smaller than $k_B T$ at synthesis temperature (3000 K, 258 meV), this suggests that the structure repre-

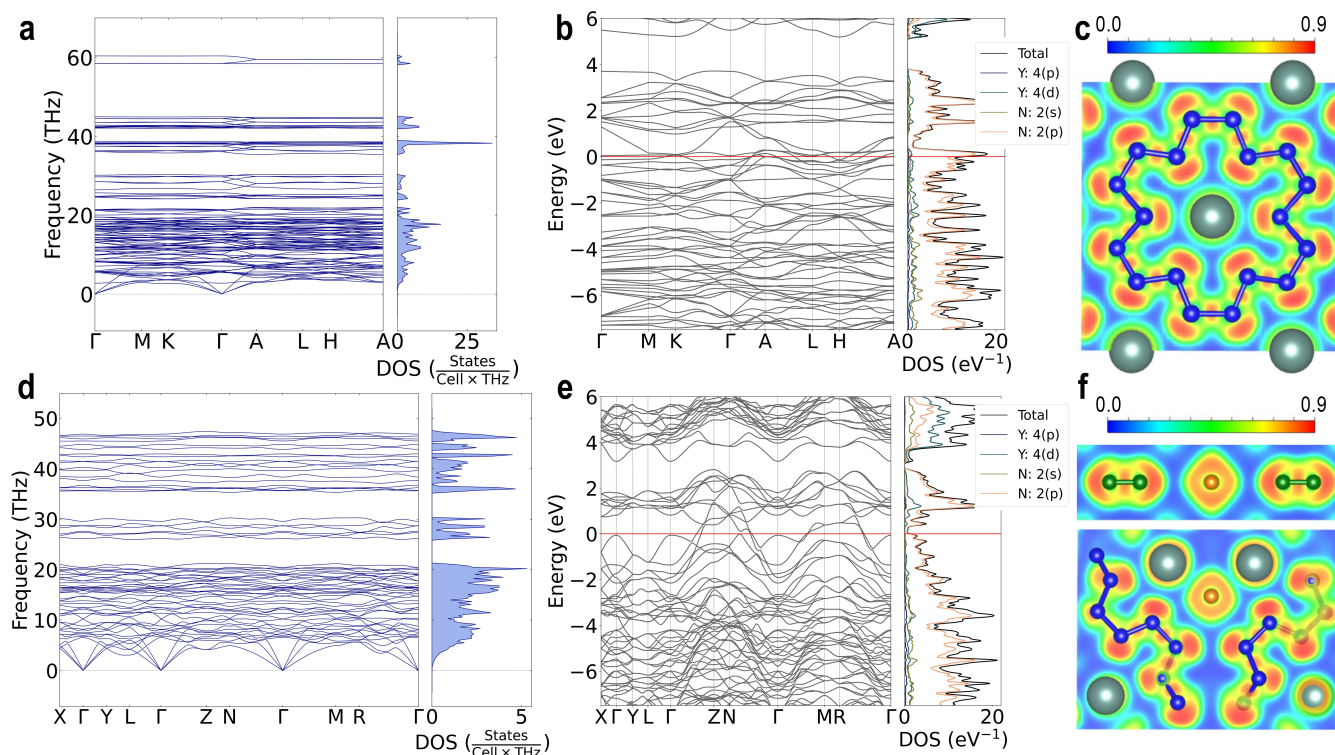


Figure 4. Calculated properties of YN_6 and Y_2N_{11} at 100 GPa. YN_6 : a) Phonon dispersions, b) electron density of states (red line indicates the Fermi level), c) electron localization function calculated in (4 0 -1) plane. Y_2N_{11} : d) The phonon dispersions, e) the electron density of states (red line indicates a Fermi level), f) the electron localization function calculated in (0 0 1) plane (upper figure) or in (3 -2 0) plane (bottom figure).

sents a local minimum in the potential energy landscape at synthesis conditions which is preserved as a meta-stable state under rapid T-quench to room temperature.

The agreement between theory and experiment at the synthesis pressure created the basis for the further analysis of chemistry and physical properties. To obtain an equation of state for YN_6 and Y_2N_{11} , variable-cell structure relaxations for both compounds were performed at target pressures between 0–150 GPa (using 10 GPa steps). Both structures were found to keep their respective symmetry in the relaxations within the full pressure range considered, however, the calculated phonon dispersion curves of YN_6 and Y_2N_{11} at atmospheric pressure show imaginary modes indicating dynamical instability at $T=0$ K (Figures S3 and S4). A 3rd order Birch–Murnaghan equation of state was subsequently fitted to the obtained energy-volume-points (see Supporting Information). The obtained bulk moduli are lower than the bulk moduli of other experimentally known yttrium nitrides, YN and Y_5N_{14} , and the bulk modulus decreases with the decrease of yttrium content: $K_0(\text{YN})=151.0$ GPa^[51] > $K_0(\text{Y}_5\text{N}_{14})=137.0$ GPa^[8] > $K_0(\text{Y}_2\text{N}_{11})=115.7$ GPa > $K_0(\text{YN}_6)=92.6$ GPa. It is also worth noting that the bulk modulus of Y_2N_{11} is significantly lower than the bulk modulus of the isostructural Hf_2N_{11} compound ($K_0(\text{Hf}_2\text{N}_{11})=193$ GPa^[26]) due to the higher compressibility of $\text{M}^{3+}\text{-N}$ bonds in Y_2N_{11} compared to $\text{M}^{4+}\text{-N}$ bonds in Hf_2N_{11} .

The calculated electron localization functions for YN_6 and Y_2N_{11} at 100 GPa demonstrate a strong covalent

bonding between nitrogen atoms in the N_{18} macrocycles, polynitrogen chains and nitrogen dimers (Figure 4c,f). At the same time, there is no obvious sign of covalent bonding between nitrogen and yttrium atoms and there is no sign of electron localization between these atoms, as expected for electrides.^[52] The N–N bond orders estimated from the crystal-chemical analysis were corroborated by calculated crystal orbital bond index^[53] (Tables S4 and S5). The computed electron density of states shows that both phases are metals (Figure 4b and Figure 4e). Remarkably, the main electronic contribution at the Fermi level comes from the nitrogen *p*-states, with an almost negligible contribution from yttrium states. The metallicity through the nitrogen π -system explains the observation of non-standard charges and bond multiplicities in the nitrogen units. Worth noting is also that the anion-driven metallicity was found for the majority of high-pressure di- and poly-nitrides,^[2,7,8,25,26,54] which, therefore, seems to be a regular phenomenon for high-pressure nitrides.

In conclusion, at 1 Mbar pressure, we have discovered two novel yttrium polynitrides YN_6 and Y_2N_{11} , which are built from extremely unique nitrogen structural units: N_{18} macrocycles and double helix polynitrogen chains, respectively. The discovery of such compounds encourages further exploration of the remarkable inorganic chemistry of polynitrides. Moreover, the ability of nitrogen to form such structural units shows that perhaps humanity is on the verge of opening a new branch of chemistry—nitrogen organic chemistry under ultrahigh pressure.

Acknowledgements

The authors acknowledge the European Synchrotron Radiation Facility (ESRF) for the provision of beamtime at the ID11 beamline and the using laser-heating setup of ID18 beamline. Computations were performed at the Leibniz Supercomputing Center of the Bavarian Academy of Sciences and the Humanities, and the research center for scientific computing at the University of Bayreuth. DL thanks the Alexander von Humboldt Foundation, the Deutsche Forschungsgemeinschaft (DFG, project LA-4916/1-1) and the UKRI Future Leaders Fellowship (MR/V025724/1) for financial support. ND and LD thank the Federal Ministry of Education and Research, Germany (BMBF, grant no. 05K19WC1) and the Deutsche Forschungsgemeinschaft (DFG projects DU 954-11/1, DU 393-9/2, DU 393-13/1) for financial support. ND and IAA also thank the Swedish Government Strategic Research Area in Materials Science on Functional Materials at Linköping University (Faculty Grant SFO-Mat-LiU No. 2009 00971). IAA and FT are supported by the Swedish Research Council (VR) Grant No. 2019-05600. IAA acknowledges support from the Knut and Alice Wallenberg Foundation (Wallenberg Scholar grant no. KAW-2018.0194). Computations were enabled by resources provided by the Swedish National Infrastructure for Computing (SNIC) using Dardel at the PDC Center for High Performance Computing, KTH Royal Institute of Technology and LUMI at the IT Center for Science (CSC), Finland through grant SNIC 2022/6-10 and SNIC 2021/37-10, respectively. For the purpose of open access, the author has applied a Creative Commons Attribution (CC BY) licence to any Author Accepted Manuscript version arising from this submission. Open Access funding enabled and organized by Projekt DEAL.

Conflict of Interest

The authors declare no conflict of interest.

Data Availability Statement

The data that support the findings of this study are available in the Supporting Information of this article.

Keywords: High-Pressure Chemistry · Inorganic Double Helix · Macrocycles · Polynitrides

- [1] D. Laniel, G. Weck, G. Gaiffe, G. Garbarino, P. Loubeyre, *J. Phys. Chem. Lett.* **2018**, *9*, 1600–1604.
- [2] M. Bykov, K. R. Tasca, I. G. Batyrev, D. Smith, K. Glazyrin, S. Chariton, M. Mahmood, A. F. Goncharov, *Inorg. Chem.* **2020**, *59*, 14819–14826.
- [3] V. S. Bhadram, D. Y. Kim, T. A. Strobel, *Chem. Mater.* **2016**, *28*, 1616–1620.
- [4] M. Bykov, S. Chariton, H. Fei, T. Fedotenko, G. Aprilis, A. V. Ponomareva, F. Tasnádi, I. A. Abrikosov, B. Merle, P. Feldner, S. Vogel, W. Schnick, V. B. Prakapenka, E. Greenberg, M. Hanfland, A. Pakhomova, H.-P. Liermann, T. Katsura, N. Dubrovinskaia, L. Dubrovinsky, *Nat. Commun.* **2019**, *10*, 2994.
- [5] A. F. Young, C. Sanloup, E. Gregoryanz, S. Scandolo, R. J. Hemley, H. K. Mao, *Phys. Rev. Lett.* **2006**, *96*, 155501.
- [6] J. C. Crowhurst, A. F. Goncharov, B. Sadigh, C. L. Evans, P. G. Morrall, J. L. Ferreira, A. J. Nelson, *Science* **2006**, *311*, 1275–1278.
- [7] D. Laniel, B. Winkler, T. Fedotenko, A. Aslandukova, A. Aslandukov, S. Vogel, T. Meier, M. Bykov, S. Chariton, K. Glazyrin, V. Milman, V. Prakapenka, W. Schnick, L. Dubrovinsky, N. Dubrovinskaia, *Phys. Rev. Mater.* **2022**, *6*, 023402.
- [8] A. Aslandukov, A. Aslandukova, D. Laniel, I. Koemets, T. Fedotenko, L. Yuan, G. Steinle-Neumann, K. Glazyrin, M. Hanfland, L. Dubrovinsky, N. Dubrovinskaia, *J. Phys. Chem. C* **2021**, *125*, 18077–18084.
- [9] S. B. Schneider, R. Frankovsky, W. Schnick, *Inorg. Chem.* **2012**, *51*, 2366–2373.
- [10] K. Niwa, R. Fukui, T. Terabe, T. Kawada, D. Kato, T. Sasaki, K. Soda, M. Hasegawa, *Eur. J. Inorg. Chem.* **2019**, 3753–3757.
- [11] W. Chen, J. S. Tse, J. Z. Jiang, *J. Phys. Condens. Matter* **2010**, *22*, 015404.
- [12] K. Niwa, T. Yamamoto, T. Sasaki, M. Hasegawa, *Phys. Rev. Mater.* **2019**, *3*, 53601.
- [13] K. Niwa, T. Terabe, D. Kato, S. Takayama, M. Kato, K. Soda, M. Hasegawa, *Inorg. Chem.* **2017**, *56*, 6410–6418.
- [14] M. Wessel, R. Dronskowski, *J. Am. Chem. Soc.* **2010**, *132*, 2421–2429.
- [15] K. Niwa, K. Suzuki, S. Muto, K. Tatsumi, K. Soda, T. Kikegawa, M. Hasegawa, *Chem. Eur. J.* **2014**, *20*, 13885–13888.
- [16] K. Niwa, D. Dzivenko, K. Suzuki, R. Riedel, I. Troyan, M. Eremets, M. Hasegawa, *Inorg. Chem.* **2014**, *53*, 697–699.
- [17] D. Laniel, B. Winkler, E. Koemets, T. Fedotenko, M. Bykov, E. Bykova, L. Dubrovinsky, N. Dubrovinskaia, *Nat. Commun.* **2019**, *10*, 4515.
- [18] D. Laniel, G. Weck, P. Loubeyre, *Inorg. Chem.* **2018**, *57*, 10685–10693.
- [19] B. A. Steele, E. Stavrou, J. C. Crowhurst, J. M. Zaug, V. B. Prakapenka, I. I. Oleynik, *Chem. Mater.* **2017**, *29*, 735–741.
- [20] M. Bykov, E. Bykova, S. Chariton, V. B. Prakapenka, I. G. Batyrev, M. F. Mahmood, A. F. Goncharov, *Dalton Trans.* **2021**, *50*, 7229–7237.
- [21] N. P. Salke, K. Xia, S. Fu, Y. Zhang, E. Greenberg, V. B. Prakapenka, J. Liu, J. Sun, J.-F. Lin, *Phys. Rev. Lett.* **2021**, *126*, 65702.
- [22] Y. Wang, M. Bykov, I. Chepkasov, A. Samtsevich, E. Bykova, X. Zhang, S. Jiang, E. Greenberg, S. Chariton, V. B. Prakapenka, A. R. Oganov, A. F. Goncharov, *Nat. Chem.* **2022**, *14*, 794–800.
- [23] D. Laniel, F. Trybel, Y. Yin, T. Fedotenko, S. Khandarkhaeva, A. I. Abrikosov, T. Bin Masood, C. Giacobbe, E. L. Bright, K. Glazyrin, M. Hanfland, I. Hotz, I. A. Abrikosov, L. Dubrovinsky, *arXiv:2112.09857* **2022**.
- [24] M. Bykov, E. Bykova, G. Aprilis, K. Glazyrin, E. Koemets, I. Chuvashova, I. Kuppenko, C. McCammon, M. Mezouar, V. Prakapenka, H.-P. Liermann, F. Tasnádi, A. V. Ponomareva, I. A. Abrikosov, N. Dubrovinskaia, L. Dubrovinsky, *Nat. Commun.* **2018**, *9*, 2756.
- [25] M. Bykov, E. Bykova, E. Koemets, T. Fedotenko, G. Aprilis, K. Glazyrin, H.-P. Liermann, A. V. Ponomareva, J. Tidholm, F. Tasnádi, I. A. Abrikosov, N. Dubrovinskaia, L. Dubrovinsky, *Angew. Chem. Int. Ed.* **2018**, *57*, 9048–9053; *Angew. Chem.* **2018**, *130*, 9186–9191.
- [26] M. Bykov, S. Chariton, E. Bykova, S. Khandarkhaeva, T. Fedotenko, A. V. Ponomareva, J. Tidholm, F. Tasnádi, I. A. Abrikosov, P. Sedmak, V. Prakapenka, M. Hanfland, H. P. Liermann, M. Mahmood, A. F. Goncharov, N. Dubrovinskaia,

- L. Dubrovinsky, *Angew. Chem. Int. Ed.* **2020**, *59*, 10321–10326; *Angew. Chem.* **2020**, *132*, 10407–10412.
- [27] M. Bykov, E. Bykova, A. V. Ponomareva, I. A. Abrikosov, S. Chariton, V. B. Prakapenka, M. F. Mahmood, L. Dubrovinsky, A. F. Goncharov, *Angew. Chem. Int. Ed.* **2021**, *60*, 9003–9008; *Angew. Chem.* **2021**, *133*, 9085–9090.
- [28] D. Laniel, A. A. Aslandukova, A. N. Aslandukov, T. Fedotenko, S. Chariton, K. Glazyrin, V. B. Prakapenka, L. S. Dubrovinsky, N. Dubrovinskaia, *Inorg. Chem.* **2021**, *60*, 14594–14601.
- [29] M. Bykov, T. Fedotenko, S. Chariton, D. Laniel, K. Glazyrin, M. Hanfland, J. S. Smith, V. B. Prakapenka, M. F. Mahmood, A. F. Goncharov, A. V. Ponomareva, F. Tasnádi, A. I. Abrikosov, T. Bin Masood, I. Hotz, A. N. Rudenko, M. I. Katsnelson, N. Dubrovinskaia, L. Dubrovinsky, I. A. Abrikosov, *Phys. Rev. Lett.* **2021**, *126*, 175501.
- [30] L. Li, K. Bao, X. Zhao, T. Cui, *J. Phys. Chem. C* **2021**, *125*, 24605–24612.
- [31] J. Lin, F. Wang, Q. Rui, J. Li, Q. Wang, X. Wang, *Matter Radiat. Extrem.* **2022**, *7*, 038401.
- [32] Y. Chen, X. Cai, H. Wang, H. Wang, H. Wang, *Sci. Rep.* **2018**, *8*, 10670.
- [33] S. Yu, B. Huang, Q. Zeng, A. R. Oganov, L. Zhang, G. Frapper, *J. Phys. Chem. C* **2017**, *121*, 11037–11046.
- [34] X. Wang, Y. Wang, M. Miao, X. Zhong, J. Lv, T. Cui, J. Li, L. Chen, C. J. Pickard, Y. Ma, *Phys. Rev. Lett.* **2012**, *109*, 175502.
- [35] J. Lin, D. Peng, Q. Wang, J. Li, H. Zhu, X. Wang, *Phys. Chem. Chem. Phys.* **2021**, *23*, 6863–6870.
- [36] S. Duwal, Y.-J. Ryu, M. Kim, C.-S. Yoo, S. Bang, K. Kim, N. H. Hur, *J. Chem. Phys.* **2018**, *148*, 134310.
- [37] J. Y. Miao, Z. S. Lu, F. Peng, C. Lu, *Chin. Phys. Lett.* **2021**, *38*, 066201.
- [38] F. Jiao, C. Zhang, W. Xie, *Phys. Chem. Chem. Phys.* **2021**, *23*, 7313–7320.
- [39] C. P. Kempter, N. H. Krikorian, J. C. McGuire, *J. Phys. Chem.* **1957**, *61*, 1237–1238.
- [40] Deposition Numbers 2173746 and 2173750 contain the supplementary crystallographic data for this paper. These data are provided free of charge by the joint Cambridge Crystallographic Data Centre and Fachinformationszentrum Karlsruhe Access Structures service.
- [41] W. Radecka-Paryzek, *Inorg. Chim. Acta* **1981**, *54*, 251–253.
- [42] W. A. Rabanal-León, J. A. Murillo-López, D. Páez-Hernández, R. Arratia-Pérez, *J. Phys. Chem. A* **2015**, *119*, 9931–9940.
- [43] M. A. Fik-Jaskółka, I. Pospieszna-Markiewicz, G. N. Roviello, M. Kubicki, W. Radecka-Paryzek, V. Patroniak, *Inorg. Chem.* **2021**, *60*, 2122–2126.
- [44] B. A. Steele, I. I. Oleynik, *J. Phys. Chem. A* **2017**, *121*, 8955–8961.
- [45] M. I. Eremets, A. G. Gavriliuk, I. A. Trojan, D. A. Dzivenko, R. Boehler, *Nat. Mater.* **2004**, *3*, 558–563.
- [46] W. T. Bell, F. Guzzo, *J. Am. Chem. Soc.* **1984**, *106*, 6112–6114.
- [47] K. Kihara, *Eur. J. Mineral.* **1990**, *2*, 63–78.
- [48] V. Soghomonian, Q. Chen, R. C. Haushalter, J. Zubieta, C. J. O'Connor, *Science* **1993**, *259*, 1596–1599.
- [49] A. K. Jissy, A. Datta, *J. Phys. Chem. Lett.* **2013**, *4*, 1018–1022.
- [50] D. Pfister, K. Schäfer, C. Ott, B. Gerke, R. Pöttgen, O. Janka, M. Baumgartner, A. Efimova, A. Hohmann, P. Schmidt, S. Venkatachalam, L. van Wüllen, U. Schürmann, L. Kienle, V. Duppel, E. Parzinger, B. Miller, J. Becker, A. Holleitner, R. Wehrich, T. Nilges, *Adv. Mater.* **2016**, *28*, 9783–9791.
- [51] S. Zerroug, F. Ali Sahraoui, N. Bouarissa, *Appl. Phys. A* **2009**, *97*, 345–350.
- [52] S. G. Dale, E. R. Johnson, *J. Phys. Chem. A* **2018**, *122*, 9371–9391.
- [53] P. C. Müller, C. Ertural, J. Hempelmann, R. Dronskowski, *J. Phys. Chem. C* **2021**, *125*, 7959–7970.
- [54] M. Bykov, E. Bykova, A. V. Ponomareva, F. Tasnádi, S. Chariton, V. B. Prakapenka, K. Glazyrin, J. S. Smith, M. F. Mahmood, I. A. Abrikosov, A. F. Goncharov, *ACS Nano* **2021**, *15*, 13539–13546.

Manuscript received: May 20, 2022

Accepted manuscript online: June 21, 2022

Version of record online: July 13, 2022

Supporting Information

Anionic N₁₈ Macrocycles and a Polynitrogen Double Helix in Novel Yttrium Polynitrides YN₆ and Y₂N₁₁ at 100 GPa

A. Aslandukov, F. Trybel, A. Aslandukova, D. Laniel, T. Fedotenko, S. Khandarkhaeva, G. Aprilis, C. Giacobbe, E. Lawrence Bright, I. A. Abrikosov, L. Dubrovinsky, N. Dubrovinskaia*

SUPPORTING INFORMATION

Experimental Procedures

Sample preparation. The BX90-type large X-ray aperture DAC^[1] equipped with Boehler-Almax type diamonds^[2] (culet diameter is 120 μm) was used in the experiment. The sample chamber was formed by pre-indenting of a rhenium gasket to ~ 20 μm thickness and drilling a hole of ~ 60 μm in diameter in the center of the indentation. Two pieces of yttrium (99.9%, Sigma Aldrich) were placed in a sample chamber, then molecular nitrogen was loaded using a high-pressure gas loading system (1300 bars).^[3] The sample was compressed to ~ 100 GPa and laser-heated ($\lambda = 1064$ nm) up to 3000(200) K using the home-made double-sided laser-heating system at BGI,^[4] as well as the double-sided laser heating system of ID18 beamline of the ESRF (Grenoble, France).^[5] The temperature during laser-heating was determined by the blackbody radiation fit. The pressure in the cell was determined using the equation of state of Re^[6] and additionally monitored by the Raman signal from the diamond anvils.^[7]

X-ray diffraction. XRD measurements were performed at ID11 beamline of the ESRF (Grenoble, France) with the X-ray beam ($\lambda = 0.2852$ Å) focused down to 0.5×0.5 μm^2 , and the XRD patterns were collected on a Eiger2X CdTe 4M hybrid photon counting pixel detector. For single-crystal XRD measurements, the sample was rotated around a vertical ω axis in a range of $\pm 36^\circ$. The XRD images were collected with an angular step of $\Delta\omega = 0.25^\circ$ and an exposure time of 3s/frame. The CrysAlis^{Pro} software package was used for the analysis of the single-crystal XRD data (peak hunting, indexing, data integration, frame scaling, and absorption correction). To calibrate the instrumental model in the CrysAlis^{Pro} software, *i.e.* the sample-to-detector distance, detector's origin, offsets of the goniometer angles, and rotation of both the X-ray beam and detector around the instrument axis, we used a single crystal of orthoenstatite [(Mg_{1.93}Fe_{0.06})(Si_{1.93}Al_{0.06})O₆, *Pbca* space group, $a = 8.8117(2)$ Å, $b = 5.18320(10)$ Å, and $c = 18.2391(3)$ Å]. The DAFi program^[8] was used for the search of reflections' groups belonging to individual single-crystal domains. Using the OLEX2 software package,^[9] the structures were solved with the ShelXT structure solution program^[10] using intrinsic phasing and refined with the ShelXL^[11] refinement package using least-squares minimization. Crystal structure visualization was made with the VESTA software.^[12]

Density functional theory calculations. Kohn-Sham density function theory based structural relaxations and electronic structure calculations were performed with the QUANTUM ESPRESSO package^[13–15] using the projector augmented wave approach.^[16] We used the generalized gradient approximation by Perdew-Burke-Ernzerhof (PBE)^[17] for exchange and correlation, with the corresponding potential files: for Y the 3d electrons and lower and for N the 1s electrons are treated as scalar-relativistic core states. Convergence tests with a threshold of 1 meV per atom in energy and 1 meV/Å per atom for forces led to a Monkhorst-Pack^[18] k-point grid of $8 \times 8 \times 24$ for YN₆, $12 \times 12 \times 12$ for Y₂N₁₁, $8 \times 8 \times 16$ for Y₅N₁₄, $8 \times 8 \times 8$ for YN, $16 \times 16 \times 16$ for *cg*-N, and $8 \times 8 \times 3$ for *hR24*-Y. For all calculations a cutoff for the wave-function expansion of 80 Ry and a gaussian smearing of 0.005 Ry was used. Phonon calculations were performed with PHONOPY^[19] in $2 \times 2 \times 2$ supercells with respectively adjusted k-points. The crystal orbital bond index (COBI)^[20] was calculated using LOBSTER v4.1.0 software^[21].

We performed variable cell relaxations (lattice parameters and atomic positions) on all experimental structures to optimize the atomic coordinates and the cell vectors until the total forces were smaller than 10^{-4} eV/Å per atom and the deviation from the experimental pressure was below 0.1 GPa. Furthermore, we calculated equation of states (EOS) by performing variable cell relaxations to respective target pressures until forces are $< 10^{-3}$ eV/Å and pressure is matched within 0.1 GPa. A third order Birch Murnaghan EOS was fitted to the calculated energy versus volume points. We obtained

$$\begin{array}{llll} \text{YN}_6: & K_0 = 92.6 \text{ GPa}, & K' = 5.13, & V_0 = 423.59 \text{ \AA}^3 \\ \text{Y}_2\text{N}_{11}: & K_0 = 115.7 \text{ GPa}, & K' = 4.38, & V_0 = 401.48 \text{ \AA}^3 \end{array}$$

SUPPORTING INFORMATION

Results

Table S1. Structure refinement details of YN₆ at 100(1) GPa. The full crystallographic dataset was deposited to the CCDC under the deposition number 2173746.

Chemical formula	YN ₆						
Temperature (K)	293						
Pressure (GPa)	100(1)						
Crystal data							
Mr	172.97						
ρ (g/cm ³)	6.180						
Crystal system, space group	monoclinic, C2/c						
a (Å)	9.667(3)						
b (Å)	8.7071(15)						
c (Å)	3.3592(9)						
β (°)	99.52(3)						
V (Å ³)	278.86(12)						
Z	6						
Radiation type	X-ray, $\lambda = 0.2852$ Å						
μ (mm ⁻¹)	2.823						
Data collection							
No. of measured, independent and observed [$I > 2\sigma(I)$] reflections	918/648/526						
R _{int}	1.17%						
($\sin \theta/\lambda$) _{max} (Å ⁻¹)	1.205						
Refinement							
R[F ² > 3 σ (F ²)], wR(F ²), GOF	0.0470, 0.1270, 1.023						
data/parameters ratio	648/53						
$\Delta\rho_{\max}$, $\Delta\rho_{\min}$ (e Å ⁻³)	2.83, -1.96						
Atomic positions							
Atom	Wyckoff site	Fractional atomic coordinates					
		x	y	z			
Y1	2a	0	0	0			
Y2	4i	0.34719(6)	0	0.28733(18)			
N1	4i	0.1516(6)	0	0.5598(16)			
N2	8j	0.3011(4)	0.3817(3)	0.1879(12)			
N3	8j	0.3391(4)	0.2562(4)	0.3655(12)			
N4	8j	0.0804(5)	0.2245(3)	0.2976(12)			
N5	8j	0.0469(5)	0.3630(3)	0.1695(12)			
Anisotropic displacement parameters							
Atom	U_{11} (Å ²)	U_{22} (Å ²)	U_{33} (Å ²)	U_{12} (Å ²)	U_{13} (Å ²)	U_{23} (Å ²)	U_{eq} (Å ²)
Y1	0.0114(4)	0.0047(2)	0.0117(3)	0	-0.0038(3)	0	0.00990(19)
Y2	0.0111(3)	0.0047(2)	0.0119(2)	0	-0.0039(2)	0	0.00991(16)
N1	0.012(3)	0.0069(16)	0.011(2)	0	-0.003(2)	0	0.0105(12)
N2	0.009(2)	0.0063(11)	0.0112(13)	-0.0002(7)	-0.0039(13)	-0.0003(7)	0.0096(8)
N3	0.010(2)	0.0070(13)	0.0148(17)	0.0004(7)	-0.0028(16)	0.0000(7)	0.0112(9)
N4	0.0108(19)	0.0062(11)	0.0132(15)	0.0020(7)	-0.0046(14)	0.0002(7)	0.0108(8)
N5	0.012(2)	0.0068(12)	0.0129(15)	-0.0012(8)	-0.0032(14)	0.0005(7)	0.0112(8)

SUPPORTING INFORMATION

Table S2. Structure refinement details of Y_2N_{11} at 100(1) GPa. The full crystallographic dataset was deposited to the CCDC under the deposition number 2173750.

Chemical formula	Y ₂ N ₁₁						
Temperature (K)	293						
Pressure (GPa)	100(1)						
Crystal data							
Mr	331.93						
ρ (g/cm ³)	6.104						
Crystal system, space group	hexagonal, <i>P6₂22</i>						
a (Å)	6.478(4)						
c (Å)	7.454(6)						
V (Å ³)	270.9(4)						
Z	3						
Radiation type	X-ray, $\lambda = 0.2852$ Å						
μ (mm ⁻¹)	2.900						
Data collection							
No. of measured, independent and observed [$I > 2\sigma(I)$] reflections	1111/744/551						
R _{int}	4.94%						
($\sin \theta/\lambda$) _{max} (Å ⁻¹)	1.222						
Refinement							
R[F ² > 3 σ (F ²)], wR(F ²), GOF	0.0517, 0.1278, 1.004						
data/parameters ratio	685/32						
$\Delta\rho_{\text{max}}$, $\Delta\rho_{\text{min}}$ (e Å ⁻³)	1.73, -1.85						
Atomic positions							
Atom	Wyckoff site	Fractional atomic coordinates					
		x	y	z			
Y1	6j	0.20989(7)	0.41978(14)	0.5			
N1	12k	0.2661(9)	0.4451(9)	0.0785(8)			
N2	12k	0.1052(9)	0.3831(10)	0.2012(7)			
N3	6g	0.0870(11)	0	0			
N4	3c	0.5	0	0			
Anisotropic displacement parameters							
Atom	U_{11} (Å ²)	U_{22} (Å ²)	U_{33} (Å ²)	U_{12} (Å ²)	U_{13} (Å ²)	U_{23} (Å ²)	U_{eq} (Å ²)
Y1	0.00700(18)	0.0076(2)	0.0107(2)	0.00379(12)	-0.00008(18)	0	0.00836(14)
N1	0.0077(15)	0.0067(16)	0.0097(17)	0.0032(14)	-0.0004(12)	-0.0001(13)	0.0082(7)
N2	0.0066(16)	0.011(2)	0.0086(19)	0.0042(14)	0.0023(12)	-0.0003(13)	0.0090(8)
N3	0.0088(16)	0.007(2)	0.015(3)	0.0033(10)	0.0016(12)	0.003(2)	0.0104(10)
N4	0.0027(16)	0.008(3)	0.007(3)	0.0040(15)	0	0	0.0054(11)

SUPPORTING INFORMATION

Table S3. Experimentally determined crystallographic data for the YN_6 and Y_2N_{11} phases at 100(1) GPa compared with the corresponding DFT-relaxed structures. Note that pressure was fixed in theoretical simulations, while the volume of the unit cells, lattice parameters and equilibrium state parameters were calculated.

	YN_6		Y_2N_{11}	
	Exp.	Calc.	Exp.	Calc.
Space group	$C2/c$	$C2/c$	$P6_222$	$P6_222$
Volume	278.86(12) Å ³	286.19 Å ³	270.9(4) Å ³	275.7 Å ³
Lattice parameters	a = 9.667(3) Å b = 8.7071(15) Å c = 3.3592(9) Å $\alpha = 90^\circ$ $\beta = 99.52(3)^\circ$ $\gamma = 90^\circ$	a = 9.7902 Å b = 8.7467 Å c = 3.3938 Å $\alpha = 90^\circ$ $\beta = 100.01^\circ$ $\gamma = 90^\circ$	a = 6.478(4) Å b = 6.478(4) Å c = 7.454(6) Å $\alpha = 90^\circ$ $\beta = 90^\circ$ $\gamma = 120^\circ$	a = 6.4863 Å b = 6.4863 Å c = 7.5667 Å $\alpha = 90^\circ$ $\beta = 90^\circ$ $\gamma = 120^\circ$
Atomic positions	Y1 x 0 y 0 z 0	Y1 x 0.00000 y 0.00000 z 0.00000	Y1 x 0.20989(7) y 0.41978(14) z 0.5	Y1 x 0.20842 y 0.41667 z 0.50000
	Y2 x 0.34719(6) y 0 z 0.28733(18)	Y2 x 0.34799 y 0.00000 z 0.28283	N1 x 0.2661(9) y 0.4451(9) z 0.0785(8)	N1 x 0.26628 y 0.44517 z 0.07838
	N1 x 0.1516(6) y 0 z 0.5598(16)	N1 x 0.15206 y 0.00000 z 0.56359	N2 x 0.1052(9) y 0.3831(10) z 0.2012(7)	N2 x 0.10570 y 0.38217 z 0.20044
	N2 x 0.3011(4) y 0.3817(3) z 0.1879(12)	N2 x 0.30237 y 0.38133 z 0.18711	N3 x 0.0870(11) y 0 z 0	N3 x 0.08823 y 0.00000 z 0.00000
	N3 x 0.3391(4) y 0.2562(4) z 0.3655(12)	N3 x 0.33794 y 0.25598 z 0.36799	N4 x 0.5 y 0 z 0	N4 x 0.50000 y 0.00000 z 0.00000
	N4 x 0.0804(5) y 0.2245(3) z 0.2976(12)	N4 x 0.07877 y 0.22361 z 0.29871		
	N5 x 0.0469(5) y 0.3630(3) z 0.1695(12)	N5 x 0.04678 y 0.36250 z 0.16765		

SUPPORTING INFORMATION

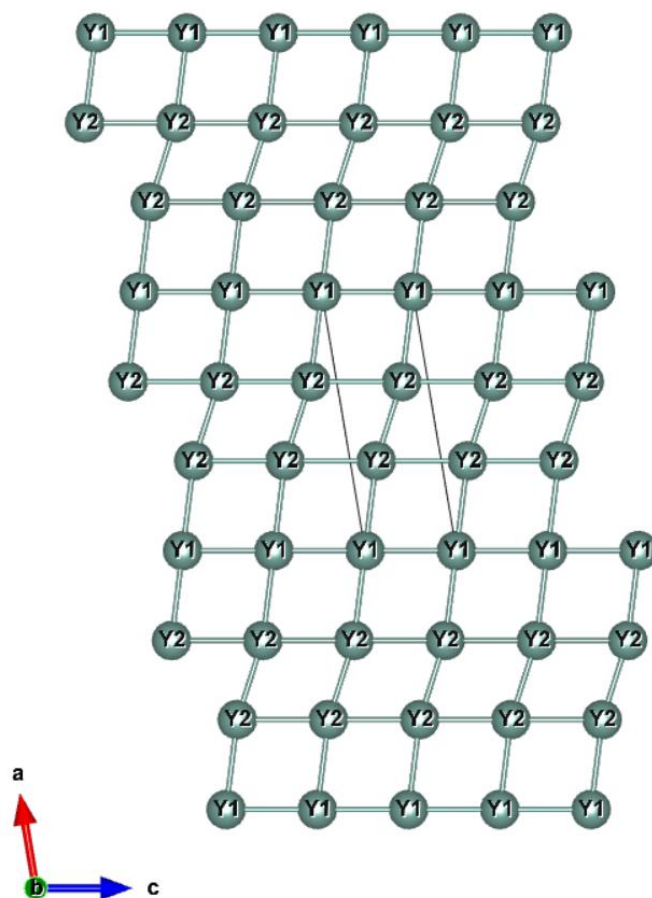


Figure S1. A layer of Y atoms in the ac plane in the YN_6 structure.

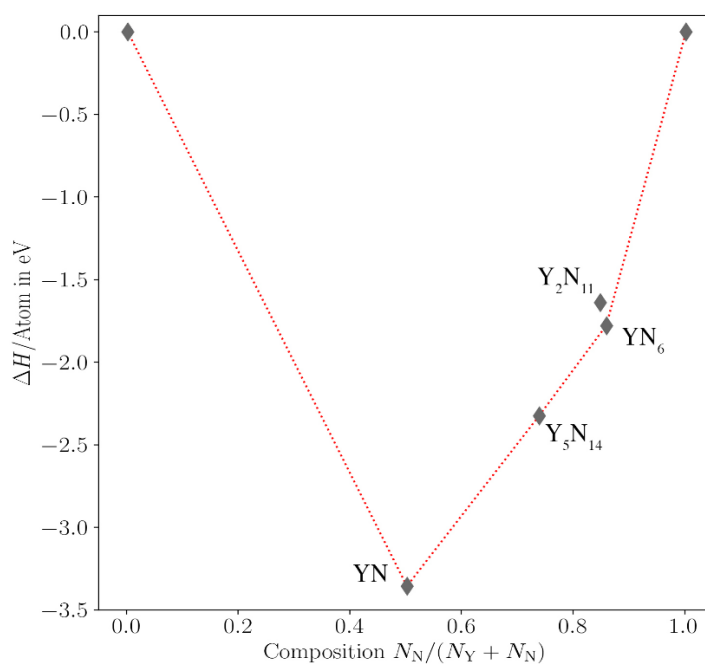


Figure S2. The calculated convex hull in the Y-N binary system for known yttrium nitrides at 100 GPa. Static enthalpies were calculated for Y ($hR24$ structure^[22]), nitrogen ($cg-N$ structure^[23]), YN (rocksalt structure), Y_5N_{14} ^[24] and two compounds, YN_6 and Y_2N_{11} , from the current study. The phases YN, Y_5N_{14} and YN_6 lie on the convex hull.

SUPPORTING INFORMATION

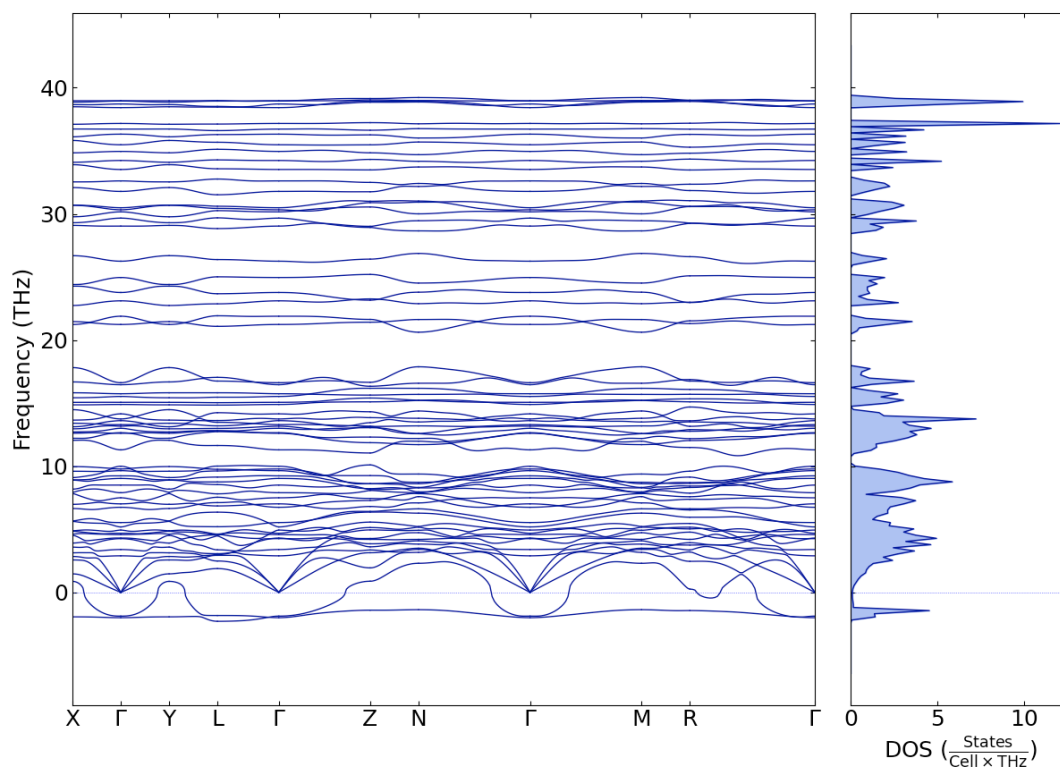


Figure S3. Phonon dispersions of YN_6 at 1 bar.

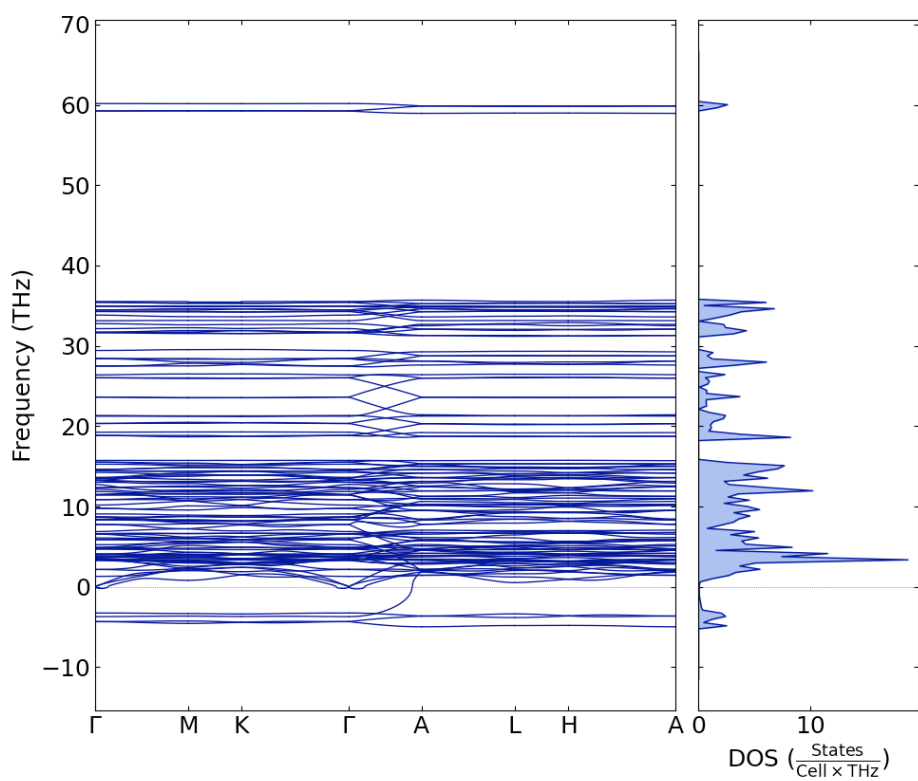


Figure S4. Phonon dispersions of Y_2N_{11} at 1 bar.

SUPPORTING INFORMATION

Table S4. Crystal orbital bond index of nitrogen-nitrogen bonds in N₁₈ macrocycle in YN₆

Bond	Bond length	Bond index COBI	Bond order estimated from crystal-chemical analysis
N1-N2	1.364	0.996	1
N2-N3	1.275	1.232	1.5
N3-N4	1.287	1.256	1.5
N4-N5	1.313	1.122	1.125
N5-N5	1.331	1.043	1

Table S5. Crystal orbital bond index of nitrogen-nitrogen bonds in polynitrogen chains and nitrogen dimers in Y₂N₁₁

Bond	Bond length	Bond index COBI	Bond order estimated from crystal-chemical analysis
N1-N1 (chains)	1.315	1.092	between 1 and 1.5
N1-N2 (chains)	1.296	1.184	between 1 and 1.5
N2-N2 (chains)	1.293	1.242	between 1 and 1.5
N3-N3 (dimers)	1.145	2.051	2.75

References

- [1] I. Kantor, V. Prakapenka, A. Kantor, P. Dera, A. Kurnosov, S. Sinogeikin, N. Dubrovinskaia, L. Dubrovinsky, *Rev. Sci. Instrum.* **2012**, *83*, 125102.
- [2] R. Boehler, *Rev. Sci. Instrum.* **2006**, *77*, 2004–2007.
- [3] A. Kurnosov, I. Kantor, T. Boffa-Ballaran, S. Lindhardt, L. Dubrovinsky, A. Kuznetsov, B. H. Zehnder, *Rev. Sci. Instrum.* **2008**, *79*, 045110.
- [4] T. Fedotenko, L. Dubrovinsky, G. Aprilis, E. Koemets, A. Snigirev, I. Snigireva, A. Barannikov, P. Ershov, F. Cova, M. Hanfland, N. Dubrovinskaia, *Rev. Sci. Instrum.* **2019**, *90*, 104501.
- [5] I. Kупenko, L. Dubrovinsky, N. Dubrovinskaia, C. McCammon, K. Glazyrin, E. Bykova, T. B. Ballaran, R. Sinmyo, A. I. Chumakov, V. Potapkin, A. Kantor, R. Rüffer, M. Hanfland, W. Crichton, M. Merlini, *Rev. Sci. Instrum.* **2012**, *83*, 124501.
- [6] S. Anzellini, A. Dewaele, F. Occelli, P. Loubeyre, M. Mezouar, *J. Appl. Phys.* **2014**, *115*, 043511.
- [7] Y. Akahama, H. Kawamura, *J. Appl. Phys.* **2006**, *100*, 043516.
- [8] A. Aslandukov, M. Aslandukov, N. Dubrovinskaia, L. Dubrovinsky, *J. Appl. Crystallogr.* **2022**, under review.
- [9] O. V. Dolomanov, L. J. Bourhis, R. J. Gildea, J. A. K. Howard, H. Puschmann, *J. Appl. Crystallogr.* **2009**, *42*, 339–341.
- [10] V. Petríček, M. Dušek, L. Palatinus, *Zeitschrift für Krist.* **2014**, *229*, 345–352.
- [11] G. M. Sheldrick, *Acta Crystallogr. Sect. C Struct. Chem.* **2015**, *71*, 3–8.
- [12] K. Momma, F. Izumi, *J. Appl. Crystallogr.* **2011**, *44*, 1272–1276.
- [13] P. Giannozzi, S. Baroni, N. Bonini, M. Calandra, R. Car, C. Cavazzoni, D. Ceresoli, G. L. Chiarotti, M. Cococcioni, I. Dabo, A. Dal Corso, S. De Gironcoli, S. Fabris, G. Fratesi, R. Gebauer, U. Gerstmann, C. Gougoussis, A. Kokalj, M. Lazzeri, L. Martin-Samos, N. Marzari, F. Mauri, R. Mazzarello, S. Paolini, A. Pasquarello, L. Paulatto, C. Sbraccia, S. Scandolo, G. Sclauzero, A. P. Seitsonen, A. Smogunov, P. Umari, R. M. Wentzcovitch, *J. Phys. Condens. Matter* **2009**, *21*, 395502.
- [14] P. Giannozzi, O. Andreussi, T. Brumme, O. Bunau, M. B. Nardelli, M. Calandra, R. Car, C. Cavazzoni, D. Ceresoli, M. Cococcioni, others, *J. Phys. Condens. Matter* **2017**, *29*, 465901.
- [15] P. Giannozzi, O. Baseggio, P. Bonfà, D. Brunato, R. Car, I. Carnimeo, C. Cavazzoni, S. De Gironcoli, P. Delugas, F. Ferrari Ruffino, A. Ferretti, N. Marzari, I. Timrov, A. Urru, S. Baroni, *J. Chem. Phys.* **2020**, *152*, 154105.
- [16] P. E. Blöchl, *Phys. Rev. B* **1994**, *50*, 17953–17979.
- [17] J. P. Perdew, K. Burke, M. Ernzerhof, *Phys. Rev. Lett.* **1996**, *77*, 3865–3868.
- [18] H. J. Monkhorst, J. D. Pack, *Phys. Rev. B* **1976**, *13*, 5188–5192.
- [19] A. Togo, I. Tanaka, *Scr. Mater.* **2015**, *108*, 1–5.
- [20] P. C. Müller, C. Ertural, J. Hempelmann, R. Dronskowski, *J. Phys. Chem. C* **2021**, *125*, 7959–7970.
- [21] R. Nelson, C. Ertural, J. George, V. L. Deringer, G. Hautier, R. Dronskowski, *J. Comput. Chem.* **2020**, *41*, 1931–1940.
- [22] E. J. Pace, S. E. Finnegan, C. V. Storm, M. Stevenson, M. I. McMahon, S. G. MacLeod, E. Plekhanov, N. Bonini, C. Weber, *Phys. Rev. B* **2020**, *102*, 094104.
- [23] M. I. Eremets, A. G. Gavriluk, I. A. Trojan, D. A. Dzivenko, R. Boehler, *Nat. Mater.* **2004**, *3*, 558–563.
- [24] A. Aslandukov, A. Aslandukova, D. Laniel, I. Koemets, T. Fedotenko, L. Yuan, G. Steinle-Neumann, K. Glazyrin, M. Hanfland, L. Dubrovinsky, N. Dubrovinskaia, *J. Phys. Chem. C* **2021**, *125*, 18077–18084.

5.4. Stabilization of N₆ and N₈ anionic units and 2D polynitrogen layers in high-pressure scandium polynitrides

This section contains the following manuscript and the related supplementary material:

“Stabilization of N₆ and N₈ anionic units and 2D polynitrogen layers in high-pressure scandium polynitrides”

A. Aslandukov, A. Aslandukova, D. Laniel, S. Khandarkhaeva, Y. Yin, F. I. Akbar, S. Chariton, V. Prakapenka, E. L. Bright, C. Giacobbe, J. Wright, D. Comboni, M. Hanfland, N. Dubrovinskaia, L. Dubrovinsky

Status: published in *Nature Communications*, 15(1), 2244.

(2024)

Reproduced under the terms and conditions of the Creative Commons ‘CC BY 4.0’

Stabilization of N₆ and N₈ anionic units and 2D polynitrogen layers in high-pressure scandium polynitrides

Received: 23 November 2023

Accepted: 14 February 2024

Published online: 12 March 2024

Check for updates

Andrey Aslandukov^{1,2}✉, Alena Aslandukova¹, Dominique Laniel³, Saiana Khandarkhaeva¹, Yuqing Yin^{2,4}, Fariia I. Akbar¹, Stella Chariton⁵, Vitali Prakapenka⁵, Eleanor Lawrence Bright⁶, Carlotta Giacobbe⁶, Jonathan Wright⁶, Davide Comboni⁶, Michael Hanfland⁶, Natalia Dubrovinskaia^{2,4} & Leonid Dubrovinsky¹

Nitrogen catenation under high pressure leads to the formation of polynitrogen compounds with potentially unique properties. The exploration of the entire spectrum of poly- and oligo-nitrogen moieties is still in its earliest stages. Here, we report on four novel scandium nitrides, Sc₂N₆, Sc₂N₈, ScN₅, and Sc₄N₃, synthesized by direct reaction between yttrium and nitrogen at 78–125 GPa and 2500 K in laser-heated diamond anvil cells. High-pressure synchrotron single-crystal X-ray diffraction reveals that in the crystal structures of the nitrogen-rich Sc₂N₆, Sc₂N₈, and ScN₅ phases nitrogen is catenated forming previously unknown N₆⁶⁻ and N₈⁶⁻ units and $\infty^2(\text{N}_5^{3-})$ anionic corrugated 2D-polynitrogen layers consisting of fused N₁₂ rings. Density functional theory calculations, confirming the dynamical stability of the synthesized compounds, show that Sc₂N₆ and Sc₂N₈ possess an anion-driven metallicity, while ScN₅ is an indirect semiconductor. Sc₂N₆, Sc₂N₈, and ScN₅ solids are promising high-energy-density materials with calculated volumetric energy density, detonation velocity, and detonation pressure higher than those of TNT.

The discovery of nitrogen polymerization under high pressures has significantly extended the nitrogen chemistry. While the polymeric single-bonded nitrogen allotropes are formed only at pressures above 110 GPa^{1–3}, the introduction of electropositive elements facilitates breaking the N₂ triple-bond and initiates nitrogen catenation at significantly lower pressures. Indeed, under high-pressure high-temperature conditions nitrogen easily reacts with metals and forms numerous compounds featuring charged nitrogen N₂^{x-} dimers^{4–19} at low-to-mild pressures (5–50 GPa), or various catenated nitrogen units (e.g. tetranitrogen N₄⁴⁻ units²⁰, pentazolate N₅⁻ rings^{21–23}, N₆ rings^{24–26}, and N₁₈ macrocycle²⁷) and 1D-polynitrogen chains^{20,28–33} at mild-to-high

pressures (>50 GPa). Some of the nitrogen species discovered under high-pressure (e.g. pentazolate-anion, whose first stabilization in bulk was achieved in CsN₅ at 60 GPa²²) were subsequently synthesized by conventional chemistry methods under ambient pressure^{34–36}.

In addition to the discoveries of unique nitrogen entities that push the boundaries of fundamental nitrogen chemistry, nitrides and polynitrides synthesized under high pressure often possess key properties for functional applications such as high hardness⁷, unique electronic properties³³, and high energy density³⁷. Polynitrides with a high nitrogen content are especially promising as high-energy-density materials (HEDM) because their decomposition results in the

¹Bavarian Research Institute of Experimental Geochemistry and Geophysics (BGI), University of Bayreuth, 95440 Bayreuth, Germany. ²Material Physics and Technology at Extreme Conditions, Laboratory of Crystallography, University of Bayreuth, 95440 Bayreuth, Germany. ³Centre for Science at Extreme Conditions and School of Physics and Astronomy, University of Edinburgh, EH9 3FD Edinburgh, United Kingdom. ⁴Department of Physics, Chemistry and Biology (IFM), Linköping University, SE-581 83 Linköping, Sweden. ⁵Center for Advanced Radiation Sources, University of Chicago, Chicago, IL 60637, USA. ⁶European Synchrotron Radiation Facility, 38000 Grenoble, France. ✉e-mail: andrii.aslandukov@uni-bayreuth.de

formation of molecular nitrogen, which is accompanied by a large energy release. The latter is due to a large difference between the energy of the triple intramolecular bond in N_2 and the energy of double and single bonds in polynitrogen units³⁷. For HEDMs the molecular weight of the compound also matters: with other properties being similar, the lighter the elements in the solid, the higher the gravimetric energy density of the compound. Since scandium is the lightest transition metal, its polynitrides may be especially promising as HEDM.

Hitherto, only one binary Sc-N compound is known: cubic scandium nitride ScN with the rock salt structure, which exists at ambient conditions and is predicted to be stable up to ~250 GPa³⁸. There are several theoretical studies^{39–42}, where nitrogen-rich phases with ScN₃, ScN₅, ScN₆, and ScN₇ compositions have been predicted to be stable under 30–110 GPa and may have potential as HEDM (gravimetric energy density ranges from 2.40 kJ/g to 4.23 kJ/g).

In this study, we experimentally investigated the behavior of the Sc-N system at pressures between 50 to 125 GPa and high temperatures. Here we present the synthesis and characterization of four novel Sc-N phases, whose structures were solved and refined on the basis of single-crystal X-ray diffraction. The nitrogen-rich polynitrides Sc₂N₆, Sc₂N₈, and ScN₅ feature a unique nitrogen catenation: previously unknown N₆⁶⁻ and N₈⁶⁻ nitrogen units and $\infty^2(N_5^{3-})$ anionic 2D-polynitrogen layers consisting of fused N₁₂ rings, respectively.

Results and discussion

In this study diamond anvil cells (DACs) loaded with scandium pieces embedded in molecular nitrogen were used (see Methods section for details). Samples were compressed to their target pressures and laser-heated at 2500(300) K. Laser-heating experiments were carried out at pressures of 50(1), 78(2), 96(2), and 125(2) GPa (Supplementary Table 1). After laser-heating, detailed X-ray diffraction maps were collected around the heated spot to pinpoint the location of crystallites most appropriate for single-crystal X-ray diffraction measurements (Fig. 1). Then single-crystal X-ray diffraction data (Supplementary Fig. 1) were collected at the selected positions to identify the phases' crystal structure and chemical composition.

According to the synchrotron single-crystal X-ray diffraction data, only the well-known ScN phase (rock-salt type structure, $a = 4.2492(7)$ Å, $V = 76.72(4)$ Å³ at 50 GPa) was formed at 50 GPa. The obtained volume is in good agreement with the published ScN equation of state³⁸. At 78 GPa, two novel scandium nitrides with chemical formulas Sc₂N₆ and Sc₂N₈ were obtained along with ScN. At 96 GPa, a mixture of ScN, Sc₂N₆, as well as the previously unobserved ScN₅, was obtained. And, finally, at 125 GPa the collected synchrotron

single-crystal X-ray diffraction data and the subsequent crystal structure solution and refinement revealed the formation of the ScN₅ and Sc₂N₈ phases. Overall four novel Sc-N phases were synthesized by chemical reactions of Sc and N₂ at 2500 K in the pressure range of 78 to 125 GPa (Supplementary Fig. 2).

Remarkably, at 50 GPa, scandium behaves like at ambient pressure producing only ScN, while at higher pressures a rich variety of phases was observed. In addition to a significant increase in the chemical potential of nitrogen under high pressure⁴³, another possible reason explaining such difference in chemistry between 50 and 78 GPa is a significant drop in scandium's electronegativity at 60 GPa (Supplementary Fig. 3a) and as a result, scandium is predicted to be the least electronegative atom in 60–110 GPa pressure range⁴⁴. It leads to the significant increase of difference in electronegativity between N and Sc above 60 GPa (Supplementary Fig. 3b), which increases the chemical reactivity of scandium, decreases the potential kinetic barriers of reactions, and leads to the appearance of more local minima in the energy landscape.

The refinement against single-crystal X-ray diffraction data for all synthesized compounds resulted in very good agreement factors (Supplementary Tables 2–6). For cross-validation of the crystal structures, we performed density functional theory (DFT) calculations using the Vienna ab initio simulation package⁴⁵ (see Methods section for details). We carried out variable cell structural relaxations for Sc₂N₆, Sc₂N₈, and ScN₅ and found that the relaxed structural parameters closely reproduce the corresponding experimental values (Supplementary Tables 7–9).

Sc₂N₆ synthesized at 78 GPa (Fig. 2a) crystallizes in the triclinic crystal system (space group $P\bar{1}$ (#2)). The structure of Sc₂N₆ has one Sc and three N distinct atomic positions (see Supplementary Table 3 and the CIF for the full crystallographic data). Nitrogen atoms form isolated “zig-zag” N₆ units (Fig. 2a, b). The existence of this phase was predicted at pressures of 30–100 GPa³⁹.

The structure of Sc₂N₈ (Fig. 2d) has the monoclinic space group $P2_1/c$ (#14) with one Sc and four N distinct atomic positions (see Supplementary Table 4 and the CIF for the full crystallographic data). Nitrogen atoms form isolated “zig-zag” N₈ units (Fig. 2d, e) that have never been observed or predicted.

The bond length analysis of the N₆ and N₈ units suggests that N1-N2, N2-N3 (in N₆ unit) and N1-N2, N2-N3, N4-N4 (in N₈ unit) are single-bonded, while N3-N4 (in N₆ unit) and N3-N4 (in N₈ unit) are double-bonded (Fig. 2b,c,e,f). Then, the charges can be described in a classic ionic approach: the total charge of [N₆]⁶⁻ and [N₈]⁶⁻ units is 6-, which corresponds to the +3 oxidation state of Sc atoms. The angle values and a small difference in bond length indicate the strong electron delocalization (indeed several different resonance Lewis formulas can

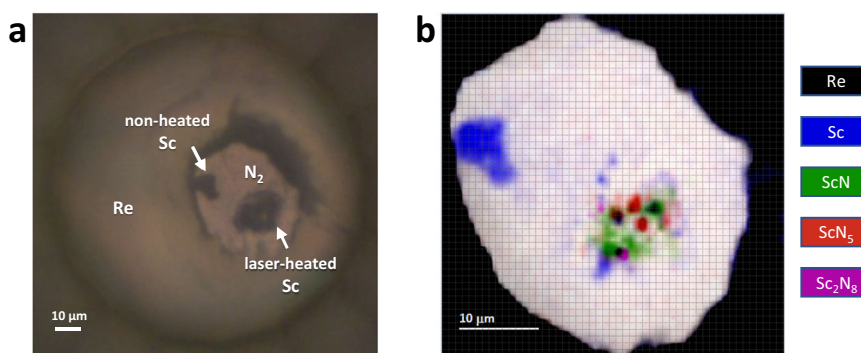


Fig. 1 | Sample chamber of the diamond anvil cell at 96 GPa. a Micro-photo of the sample chamber. **b** 2D X-ray diffraction map (collected with 0.75 μm steps at the ID11 beamline of the ESRF) showing the distribution of the scandium nitride phases (determined by single-crystal XRD) within the heated sample at 96 GPa.

The color intensity is proportional to the intensity of the following reflections: the (1 1 1) and (3 3 1) of ScN for the green regions; the (1 1 1) of ScN₅ for the red regions; the (0 2 1) of Sc₂N₈ for the purple regions.

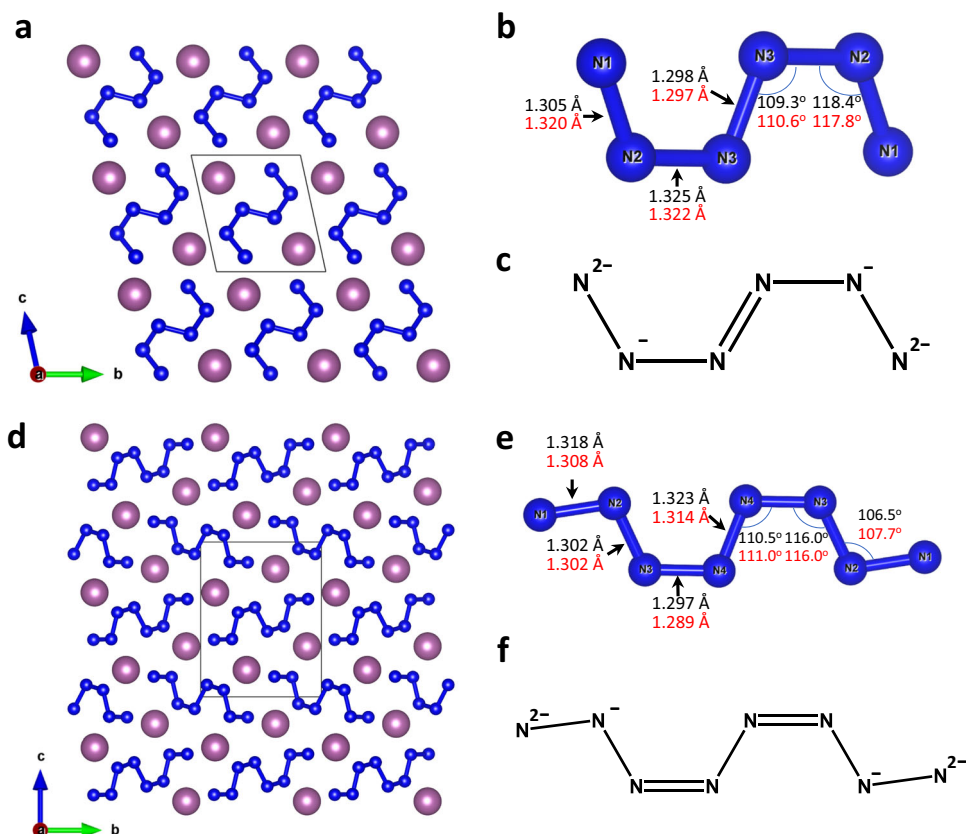


Fig. 2 | Crystal structure of Sc_2N_6 and Sc_2N_8 at 78 GPa. a A view of Sc_2N_6 along the a -axis; **b** an N_6 unit; **c** structural formula of an N_6 unit; **d** a view of Sc_2N_8 along the a -axis; **e** an N_8 unit; **f** structural formula of an N_8 unit. Sc atoms are purple, N atoms

are blue; thin grey lines outline the unit cell. Values of bond lengths and angles obtained from the experiment are shown in black, while those obtained from the DFT calculations are shown in red.

be drawn for N_6 and N_8) and nitrogen atoms cannot be considered as purely sp^2 or sp^3 hybridized.

The two novel catenated nitrogen units N_6^{6-} and N_8^{6-} discovered in this study—being intermediate non-cyclic species between dinitride and 1D-polynitrogen anions—significantly expand the list of anionic nitrogen oligomers (Fig. 3). Notably, all these units are built of an even number of nitrogen atoms suggesting their formation via the polymerization of dinitrogen molecules. The degree of polymerization increases with pressure: dinitrides are synthesized at low pressures (<50 GPa); N_4 , N_6 , N_8 units are obtained at mild pressures (50–80 GPa), while 1D-polynitrogen chains are usually formed above 100 GPa. Since the dinitrogen ($[\text{N}_2]^{x-}$, $x = 0.66, 0.75, 1, 2, 3, 4$), and 1D-polynitrogen ($[\text{N}_x]_{\infty}^{x-}$, $x = 2-6$) anions are able to accumulate different charges, one can expect that the N_6 and N_8 units can also exist in different charge states, and therefore can be found in other metal-nitrogen systems.

The structure of ScN_5 has the monoclinic space group $P2_1/m$ (#11) with one Sc and three N distinct atomic positions (see Supplementary Table 5 and the CIF for the full crystallographic data). Nitrogen atoms form corrugated 2D polymeric $\infty^2(\text{N}_3^{3-})$ layers alternating along the a -axis built of fused N_{12} rings (Fig. 4a). Sc atoms are located in between the layers, in the way that the projection of Sc atoms along the a -axis is in the center of the N_{12} rings (Fig. 4b). Sc atoms are eight-fold coordinated (coordination number CN = 8, coordination polyhedron is a distorted square antiprism) by four N atoms of the lower layer and four N atoms of the upper layer (Fig. 4c).

The analysis of N-N lengths in ScN_5 suggests that all N-N bonds are single bonds (Fig. 4d). All N atoms can be considered as sp^3 -hybridized, which also explains that the values of N-N-N angles in the N_{12} cycles are close to the ideal tetrahedra angle (98.7° – 114.5° , Fig. 4e). N1 atoms make three covalent N-N bonds, while N2 and N3 atoms make only two,

therefore one can suggest a -1 charge on the N2 and N3 atoms. It corresponds to the $+3$ oxidation state of Sc atoms.

Despite the theoretical prediction of four different structures with the ScN_5 composition^{39–41}, the here observed structure was not predicted. Usually in polynitrides nitrogen prefers to form 1D polymeric chains^{20,28–33}, and among all the experimentally synthesized polynitrides up-to-date there is only one discovered polynitride with 2D polynitrogen layers—monoclinic BeN_4 ³³ with layers consisting of the fused N_{10} rings. The polynitrogen layers in ScN_5 can be considered as distorted bp-N layers², where 1/6 atoms are missing (Supplementary Fig. 4).

ScN_5 is isostructural to a family of polyphosphides LnP_5 ($\text{Ln} = \text{La-Lu}$, Y (except Eu and Pm)) known at ambient conditions^{46,47}. It fully obeys the ninth high-pressure chemistry rule of thumb formulated in 1998: “Elements behave at high pressures like the elements below them in the periodic table at lower pressures”⁴⁸. The adoption of this structure type is also advantageous from a geometric point of view, since the ratio of ionic radii $r(\text{N}^{3-})/r(\text{Sc}^{3+}) = 1.97$ in ScN_5 perfectly fits $r(\text{P}^{3-})/r(\text{Y}^{3+}) = 1.95$ in the above-mentioned family member YP_5 .

Sc_4N_3 synthesized at 125 GPa has a well-known anti- Th_3P_4 structure type (space group $I-43d$ (#220)) and contains only distinct, not-catenated N atoms (see Supplementary Table 6, Supplementary Fig. 5, and the CIF for the full crystallographic data), which we do not discuss in detail here. This Sc_4N_3 structure was predicted to be thermodynamically stable above 80 GPa³⁹.

In order to get a deeper insight into the chemistry and the physical properties of the novel compounds, further DFT calculations were performed (see Methods section for details). As mentioned above, variable-cell structural relaxations for the Sc_2N_6 , Sc_2N_8 , and ScN_5 compounds at the synthesis pressure closely reproduced structural

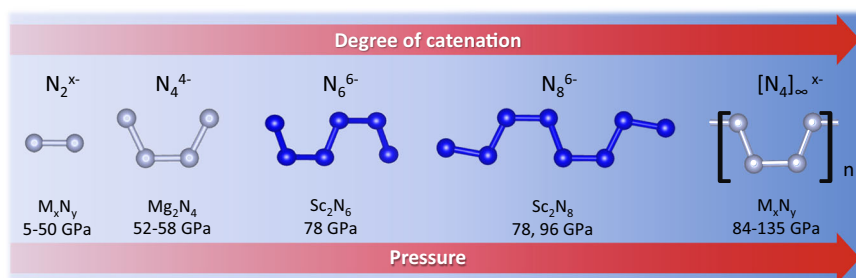


Fig. 3 | Experimentally observed catenated nitrogen units and chains. The units in blue were first discovered in the present study.

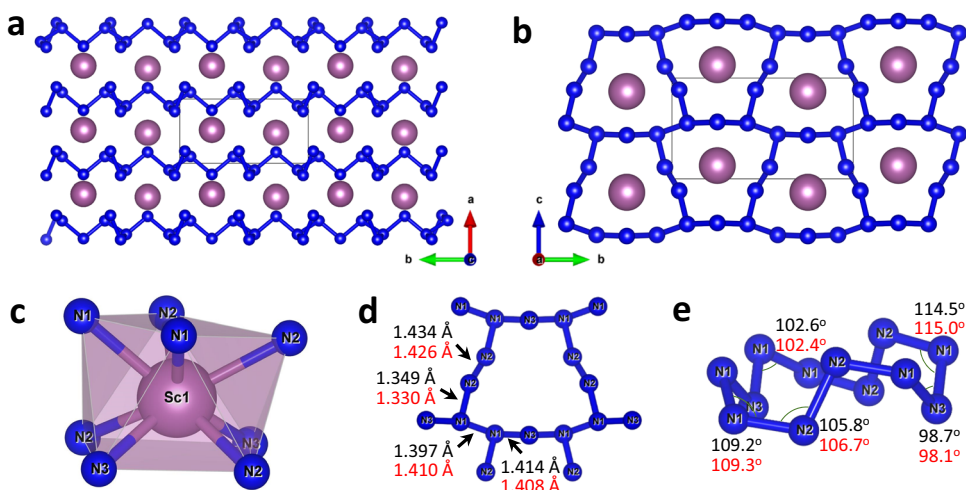


Fig. 4 | Crystal structure of ScN_5 at 96 GPa. **a** A view of the crystal structure along the c -axis. **b** A view of the crystal structure along the a -axis. **c** The coordination environment of the Sc atom. **d** A specific view of N_{12} cycle along the a -axis. **e** A general view of N_{12} cycle. Sc atoms are purple, N atoms are blue; thin grey

lines outline the unit cell. Values of bond lengths and angles obtained from the experiment are shown in black, while those obtained from the DFT calculations are shown in red.

parameters and bond lengths obtained from the experimental data. The phonon dispersion relations calculated in the harmonic approximation show that Sc_2N_6 , Sc_2N_8 , and ScN_5 phases are dynamically stable at 96 GPa and remain dynamically stable at ambient pressure (Supplementary Figs. 6–8). Considering dynamical stability at 1 bar, we have attempted to quench Sc_2N_6 , Sc_2N_8 , ScN_5 phases, however, due to technical limitations of the decompression experiment (see footnote Supplementary Table 1), no conclusion regarding their recoverability could be made. To trace the structures' behavior during the pressure release and to get the equations of state of all synthesized nitrogen-rich high-pressure scandium polynitrides, the full variable-cell structure relaxation for the Sc_2N_6 , Sc_2N_8 , and ScN_5 compounds were performed with 10 GPa pressure steps in the range of 0–150 GPa (Supplementary Fig. 9). The volume-pressure dependences of DFT-relaxed structures of Sc_2N_6 , Sc_2N_8 , and ScN_5 were fitted with a 3rd order Birch-Murnaghan equation of state (Supplementary Fig. 10). The obtained bulk moduli ($K_0(\text{Sc}_2\text{N}_6) = 160$ GPa, $K_0(\text{Sc}_2\text{N}_8) = 173$ GPa, $K_0(\text{ScN}_5) = 205$ GPa) are lower than or comparable to the bulk modulus of known ScN ($K_0(\text{ScN}) = 207$ GPa)³⁸.

Under the same pressure, the volume per atom for all investigated nitrides monotonously linearly decreases with increasing nitrogen content (Supplementary Fig. 11a). Interestingly, the volume per nitrogen atom in the ScN – Sc_2N_6 – Sc_2N_8 – ScN_5 series does not decrease with the degree of nitrogen polymerization (Supplementary Fig. 11b), so nitrogen polymerization probably is a way of crystal structure adaptation to closer N–N contacts.

While the structure of Sc_2N_6 has been predicted³⁹, the crystal structures of Sc_2N_8 and ScN_5 we observed have not been predicted.

Remarkably, four different crystal structures with the ScN_5 composition were proposed^{39–41}, but the one we synthesized in the present study ($P2_1/m$ ScN_5) was not among them. Our calculations of relative formation enthalpies of ScN_5 for various predicted structures (Cm ScN_5 ³⁹, $P-1$ ScN_5 ³⁹, $C2/m$ ScN_5 ⁴⁰ and $P2_1/c$ ScN_5 ⁴¹) with respect to $P2_1/m$ ScN_5 (Supplementary Fig. 12a) in the range of 0 to 150 GPa have shown that above 46 GPa the $P2_1/m$ ScN_5 phase is thermodynamically more stable than all other predicted phases. Below 46 GPa $P-1$ ScN_5 ³⁹ is more favorable. The $C2/m$ ScN_5 ⁴⁰ and $P2_1/c$ ScN_5 ⁴¹ phases are not energetically competitive with $P2_1/m$ ScN_5 in the whole pressure range studied (Supplementary Fig. 12a).

To estimate the thermodynamic stability of the Sc_2N_6 , Sc_2N_8 , and ScN_5 phases, the nitrogen-rich part of the static enthalpy convex hull was calculated at different pressures. Sc_2N_6 and ScN_5 phases were found to be stable at the synthesis pressures (78 and 96 GPa, Supplementary Fig. 13a and Supplementary Fig. 12b), but Sc_2N_8 appears to be out of the convex hull (40 meV and 50 meV per atom above the convex hull at 78 and 96 GPa, respectively). Such insignificant departures from the convex hull, smaller than $k_B T$ at the synthesis temperature (2500 K, 215 meV), suggest that Sc_2N_8 may be thermodynamically stable at high temperatures and preserved as a metastable state under rapid T-quench to room temperature. ScN_5 remains thermodynamically stable at least down to 40 GPa (Supplementary Fig. 13b), and Sc_2N_6 –down to 30 GPa (Supplementary Fig. 13c), while at 20 GPa all nitrogen-rich scandium phases are out of the convex-hull (Supplementary Fig. 13d).

The calculated electron localization functions for Sc_2N_6 , Sc_2N_8 , and ScN_5 demonstrate a strong covalent bonding between nitrogen

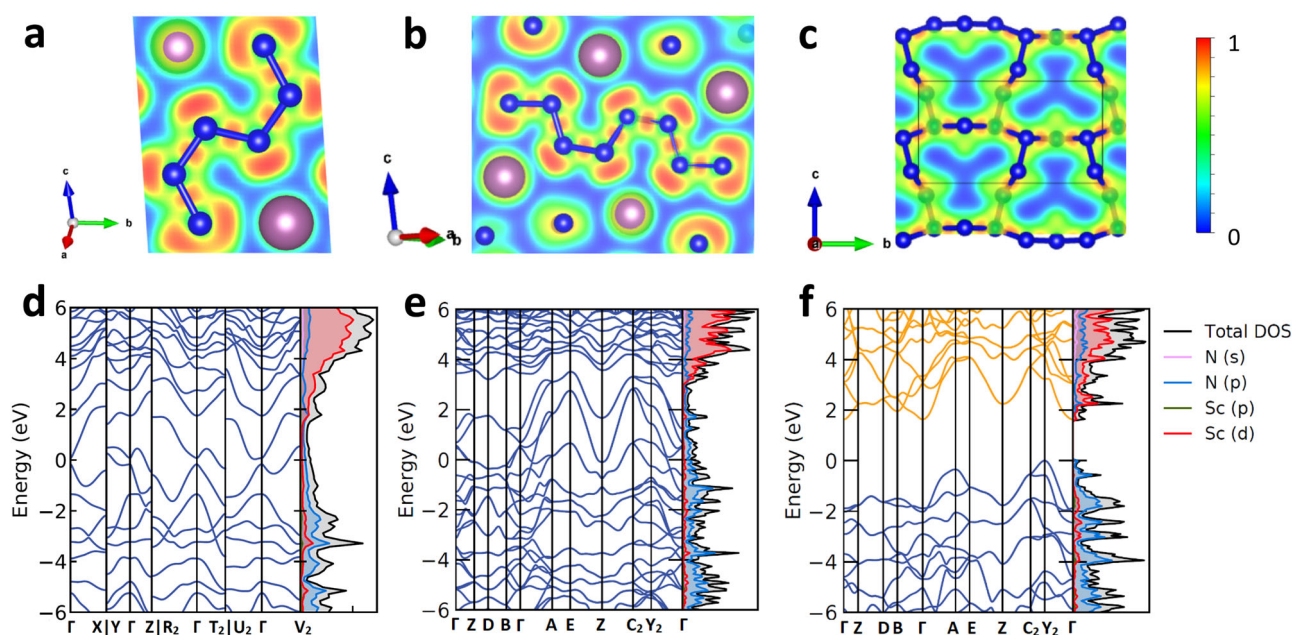


Fig. 5 | Calculated electronic properties of Sc_2N_6 at 78 GPa, and Sc_2N_8 , ScN_5 at 96 GPa. Electron localization function calculated for (a) Sc_2N_6 in the (3 0 2) plane, (b) Sc_2N_8 in the (-2 4 1) plane, and (c) ScN_5 in the (1 0 0) plane. The electron density of states of (d) Sc_2N_6 , (e) Sc_2N_8 , and (f) ScN_5 .

atoms within the N_6 , N_8 units, and 2D-polynitrogen layers (Fig. 5a–c), while there is no covalent bonding between nitrogen and scandium atoms. The computed electron density of states (DOS) shows that Sc_2N_6 and Sc_2N_8 are metals (Fig. 5d, e) with an anion-driven metallicity¹⁰, since the main electronic contribution at the Fermi level comes from the nitrogen p -states. At the same time, ScN_5 is an indirect semiconductor with a band gap of 1.8 eV at 96 GPa (Fig. 5f). One can explain such different electronic properties considering the chemical bonding in these compounds. In ScN_5 there are only single N–N bonds, which means all π^* antibonding nitrogen molecular orbitals are fully filled, whereas, in Sc_2N_6 and Sc_2N_8 , containing delocalized π -bonds within N_6^{6-} and N_8^{6-} units, π^* antibonding nitrogen states are partially filled and can conduct electrons through the π^* -band. A similar trend of electronic properties with respect to the presence of N–N π -bonds is observed for many known polynitrides^{27–33}. Among all known polynitrides there are only two compounds with solely σ N–N bonds: TaN_5 , which contains single-bonded branched polynitrogen chains³¹, and $m\text{-BeN}_4$, which contains single-bonded 2D-polynitrogen layers³³. Both compounds are semiconductors, as reported for TaN_5 ³¹, and calculated for $m\text{-BeN}_4$ in the present study (Supplementary Fig. 14). Other polynitrides contain N–N π -bonds and the majority of them (tr- BeN_4 , FeN_4 , $\alpha\text{-ZnN}_4$, $\beta\text{-ZnN}_4$, TaN_4 , $\text{ReN}_8 \cdot x\text{N}_2$, $\text{WN}_8 \cdot \text{N}_2$, $\text{Os}_5\text{N}_{28} \cdot 3\text{N}_2$, $\text{Hf}_4\text{N}_{20} \cdot \text{N}_2$, Hf_2N_{11} , Y_2N_{11} , YN_6)^{27–33} exhibit an anion-driven metallicity.

Considering the dynamical stability of Sc_2N_6 , Sc_2N_8 , and ScN_5 at ambient pressure, these phases might be preserved at ambient conditions as metastable and potentially can serve as high-energy-density materials. The key metrics of energetic materials' performance⁴⁹, such as volumetric and gravimetric energy densities, detonation velocity, and detonation pressure, were estimated for Sc_2N_6 , Sc_2N_8 , and ScN_5 (Table 1) considering their decomposition to ScN and molecular nitrogen at 1 bar (see Methods section for details).

The energy densities and explosive performance increase from Sc_2N_6 to ScN_5 along with the increase in nitrogen content. Due to the higher density of scandium nitrides compared to organic explosives, they possess extremely high volumetric energy densities that are higher than the typical energy density of TNT. The estimated gravimetric energy densities are lower than that of TNT, but higher than those of many other polynitrides³¹ since scandium is a light metal. The estimated detonation velocity and detonation pressure of scandium

polynitrides are also higher than those of TNT. Thus, the Sc_2N_6 , Sc_2N_8 , and ScN_5 are promising high-energy-density materials.

To summarize, in this study, four novel Sc–N phases— Sc_2N_6 , Sc_2N_8 , ScN_5 , and Sc_4N_3 —were synthesized from Sc and N_2 by laser-heating at 2500 K at pressures between 78 and 125 GPa. Nitrogen-rich scandium polynitrides Sc_2N_6 , Sc_2N_8 , and ScN_5 demonstrate a unique nitrogen catenation: they feature N_6 units, N_8 units, and 2D polynitrogen $\infty^2(\text{N}_5^{2-})$ layers consisting of N_{12} fused rings, respectively. DFT calculations showed that all three scandium polynitrides are dynamically stable at the synthesis pressure as well as at 1 bar. Sc_2N_6 and Sc_2N_8 are metals with the main electronic contribution at the Fermi level that comes from the nitrogen p -states, while ScN_5 is an indirect semiconductor. Synthesized Sc_2N_6 , Sc_2N_8 , and ScN_5 compounds are promising high-energy-density materials with volumetric energy densities, detonation velocities, and detonation pressures higher than those of TNT.

One can expect that the N_6 and N_8 units will be stabilized at ambient conditions in the future, considering a positive example of CsN_5 high-pressure synthesis and subsequent stabilization of the N_5^- anion at atmospheric pressure. It may not only open access to novel high-energy-density materials but also to analogues of Li- and Mg-metalorganic compounds that are currently widely used in organic synthesis. N_6 and N_8 units, if used as building blocks in organic chemistry, may provide new routes for the targeted synthesis of novel N-heteroatomic organic, metalorganic, and coordination compounds.

Methods

Sample preparation

The BX90-type large X-ray aperture DACs⁵² equipped with Boehler-Almax type diamonds⁵³ (culet diameters are 250, 120, and 80 μm) were used in the experiments. The sample chambers were formed by pre-indenting of rhenium gaskets to 20, 18, and 15 μm thickness and laser-drilling a hole of 115, 60 and 40 μm , respectively, in diameter in the center of the indentation. A DAC equipped with 250- μm culet anvils was used for the experiment at 50(1) GPa; a DAC equipped with 120- μm culet anvils was used for experiments at 78(2) and 96(2); and a DAC equipped with 80- μm culet anvils was used for the experiment at 125(2) GPa. A piece of scandium (99.9%, Sigma Aldrich) was placed in a sample chamber, then molecular nitrogen (purity grade N5.0) was

Table 1 | Characteristics of Sc₂N₆, Sc₂N₈, ScN₅ and TNT as energetic materials

Compound	Density ρ , g/cm ³	Energy density		Detonation velocity V_d , km/s	Detonation pressure P_d , GPa
		gravimetric GED, kJ/g	volumetric VED, kJ/cm ³		
Sc ₂ N ₆	3.65	2.28	8.31	6.9	30
Sc ₂ N ₈	3.58	3.07	11.0	8.3	43
ScN ₅	3.71	3.76	14.0	9.8	60
TNT	1.64 ⁵⁰	4.3 ⁵¹	7.2 ⁵¹	6.9 ⁵⁰	19 ⁵⁰

loaded using a BGI high-pressure gas loading system (1300 bars)⁵⁴. The sizes of the scandium pieces were $40 \times 40 \times 8 \mu\text{m}^3$ for $250 \mu\text{m}$ culet anvils and not bigger than $15 \times 15 \times 5 \mu\text{m}^3$ for DACs with anvils of all other sizes. The samples were compressed to target pressure (50(1), 78(2), 96(2), and 125(2) GPa) and then laser-heated up to 2500(200) K using a home-made double-sided laser-heating system equipped with two YAG lasers ($\lambda = 1064 \text{ nm}$) and the IsoPlane SCT 320 spectrometer with a 1024×2560 PI-MAX 4 camera for the collection of thermal emission spectra from the heated spot⁵⁵. The temperature during the laser heating was determined by fitting of sample's thermal emission spectra to the grey body approximation of Planck's radiation function in a given wavelength range (570–830 nm). The pressure in the DACs was determined using the Raman signal from the diamond anvils⁵⁶ and monitored additionally by X-ray diffraction of the Re gasket edge using the rhenium equation of state⁵⁷.

X-ray diffraction

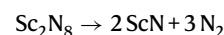
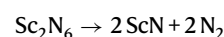
The X-ray diffraction studies were done at the ID11 beamline ($\lambda = 0.2843 \text{ \AA}$ and $\lambda = 0.2846 \text{ \AA}$) and ID15b beamline ($\lambda = 0.4100 \text{ \AA}$) of the Extreme Brilliant Source European Synchrotron Radiation Facility (EBS-ESRF) as well as at the GSECARS 13IDD beamline of the APS ($\lambda = 0.2952 \text{ \AA}$). At ID11 beamline of ESRF the X-ray beam was focused down to $0.75 \times 0.75 \mu\text{m}^2$ and data was collected with Eiger2X CdTe 4 M hybrid photon counting pixel detector. At ID15b beamline of ESRF the X-ray beam was focused down to $1.5 \times 1.5 \mu\text{m}^2$ and data was collected with Eiger2X CdTe 9 M hybrid photon counting pixel detector. At 13IDD beamline of APS the X-ray beam was focused down to $2 \times 2 \mu\text{m}^2$ and data was collected with Pilatus 1 M detector. In order to determine the position of the polycrystalline sample on which the single-crystal X-ray diffraction acquisition is obtained, a full X-ray diffraction mapping of the pressure chamber was achieved. The sample position displaying the most and the strongest single-crystal reflections belonging to the phase of interest was chosen for the collection of single-crystal data, collected in step-scans of 0.5° from -36° to $+36^\circ$. The CrysAlis^{Pro} software package⁵⁸ was used for the analysis of the single-crystal XRD data (peak hunting, indexing, data integration, frame scaling, and absorption correction). To calibrate an instrumental model in the CrysAlis^{Pro} software, i.e., the sample-to-detector distance, detector's origin, offsets of the goniometer angles, and rotation of both the X-ray beam and detector around the instrument axis, we used a single crystal of orthoenstatite [(Mg_{1.93}Fe_{0.06})(Si_{1.93}Al_{0.06})O₆, *Pbca* space group, $a = 8.8117(2) \text{ \AA}$, $b = 5.18320(10) \text{ \AA}$, and $c = 18.2391(3) \text{ \AA}$]. The DAFI program was used for the search of reflection's groups belonging to the individual single crystal domains⁵⁹. Using the OLEX2 software package⁶⁰, the structures were solved with the ShelXT structure solution program⁶¹ using intrinsic phasing and refined with the ShelXL⁶² refinement package using least-squares minimization. Crystal structure visualization was made with the VESTA software⁶³.

Theoretical calculations

First-principles calculations were performed using the framework of density functional theory (DFT) as implemented in the Vienna Ab initio Simulation Package (VASP)⁶⁴. The Projector-Augmented-Wave (PAW) method⁶⁵ was used to expand the electronic wave function in plane

waves. The Generalized Gradient Approximation (GGA) functional is used for calculating the exchange-correlation energies, as proposed by Perdew–Burke–Ernzerhof (PBE)⁶⁶. The recommended PAW potentials “Sc_{sv}” and “N” with the following valence configurations of $3s^2 3p^6 4s^2 3d^1$ for Sc and $2s^2 2p^3$ for N were used. We used the Monkhorst–Pack scheme with $10 \times 10 \times 10$ for ScN, $12 \times 8 \times 8$ for Sc₂N₆, $10 \times 6 \times 4$ for Sc₂N₈, $12 \times 6 \times 12$ for ScN₅ *k*-points for Brillouin zone sampling, and the plane-wave kinetic energy cutoff was set to 800 eV, with which total energies are converged to better than 2 meV/atom. The electronic convergence criterion was set to $\Delta E = 10^{-8} \text{ eV}$, this minimized the interatomic forces to $F_{\text{atom}} < 10^{-3} \text{ eV/\AA}$. For electron band structure calculations the 1.5–2 fold denser *k*-points grids were used. The finite displacement method, as implemented in PHONOPY⁶⁷, was used to calculate phonon frequencies and phonon band structures. The $4 \times 3 \times 3$, $3 \times 2 \times 2$, and $3 \times 2 \times 3$ supercells with $4 \times 4 \times 4$ *k*-points grids for Sc₂N₆, Sc₂N₈, and ScN₅, respectively, were used for phonon calculations and displacement amplitudes were of 0.01 Å.

The gravimetric and volumetric energy densities of Sc₂N₆, Sc₂N₈, and ScN₅ were calculated considering the enthalpy change ΔH for the following chemical decomposition reactions at ambient pressure at 0 K (the *Fm-3m*-ScN and α -N₂ structures of products were used in the calculations since they are the most stable polymorphs at such conditions):



The detonation velocity (V_d , km/s) and detonation pressure (P_d , GPa) of the Sc₂N₆, Sc₂N₈, and ScN₅ were estimated by the Kamlet–Jacobs empirical equations⁵⁰:

$$V_d = (N \cdot M^{0.5} \cdot \text{GED}^{0.5})^{0.5} \cdot (1.011 + 1.312\rho) \quad (1)$$

$$P_d = 1.588 \cdot N \cdot M^{0.5} \cdot \text{GED}^{0.5} \cdot \rho^2 \quad (2)$$

where N is the number of moles of gaseous detonation product (nitrogen gas) per gram of explosive, M is the molar mass (28 g/mol) of nitrogen gas, GED is gravimetric energy density in cal/g, and ρ is density in g/cm³.

Data availability

The full crystallographic data for structures reported in this article have been deposited at the Inorganic Crystal Structure Database (ICSD) under deposition numbers CSD 2252030–2252036. These data can be obtained from CCDC's and FIZ Karlsruhe's free service for viewing and retrieving structures (<https://www.ccdc.cam.ac.uk/structures/>). The crystallographic information (CIF files, FCF files, and the corresponding CheckCIF reports) is also available as Source data. All other datasets generated and/or analyzed during the current

study are available from the corresponding author upon request. Source data are provided with this paper.

References

1. Eremets, M. I., Gavriluk, A. G., Trojan, I. A., Dzivenko, D. A. & Boehler, R. Single-bonded cubic form of nitrogen. *Nat. Mater.* **3**, 558–563 (2004).
2. Laniel, D. et al. High-pressure polymeric nitrogen allotrope with the black phosphorus structure. *Phys. Rev. Lett.* **124**, 216001 (2020).
3. Laniel, D., Geneste, G., Weck, G., Mezouar, M. & Loubeyre, P. Hexagonal layered polymeric nitrogen phase synthesized near 250 GPa. *Phys. Rev. Lett.* **122**, 66001 (2019).
4. Laniel, D., Weck, G., Gaiffe, G., Garbarino, G. & Loubeyre, P. High-pressure synthesized lithium pentazolate compound metastable under ambient conditions. *J. Phys. Chem. Lett.* **9**, 1600–1604 (2018).
5. Bykov, M. et al. Dinitrogen as a universal electron acceptor in solid-state chemistry: an example of uncommon metallic compounds $\text{Na}_3(\text{N}_2)_4$ and NaN_2 . *Inorg. Chem.* **59**, 14819–14826 (2020).
6. Bhadram, V. S., Kim, D. Y. & Strobel, T. A. High-pressure synthesis and characterization of incompressible titanium pernitride. *Chem. Mater.* **28**, 1616–1620 (2016).
7. Bykov, M. et al. High-pressure synthesis of ultraincompressible hard rhenium nitride pernitride $\text{Re}_2(\text{N}_2)(\text{N})_2$ stable at ambient conditions. *Nat. Commun.* **10**, 2994 (2019).
8. Young, A. F. et al. Synthesis of novel transition metal nitrides IrN_2 and OsN_2 . *Phys. Rev. Lett.* **96**, 155501 (2006).
9. Crowhurst, J. C. et al. Synthesis and characterization of the nitrides of platinum and iridium. *Science*. **311**, 1275–1278 (2006).
10. Laniel, D. et al. High-pressure $\text{Na}_3(\text{N}_2)_4$, $\text{Ca}_3(\text{N}_2)_4$, $\text{Sr}_3(\text{N}_2)_4$, and $\text{Ba}(\text{N}_2)_3$ featuring nitrogen dimers with noninteger charges and anion-driven metallicity. *Phys. Rev. Mater.* **6**, 023402 (2022).
11. Aslandukov, A. et al. High-pressure yttrium nitride, Y_5N_{14} , featuring three distinct types of nitrogen dimers. *J. Phys. Chem. C* **125**, 18077–18084 (2021).
12. Schneider, S. B., Frankovsky, R. & Schnick, W. Synthesis of alkaline earth diazenides $\text{M}_{\text{AE}}\text{N}_2$ ($\text{M}_{\text{AE}} = \text{Ca}, \text{Sr}, \text{Ba}$) by controlled thermal decomposition of azides under high pressure. *Inorg. Chem.* **51**, 2366–2373 (2012).
13. Niwa, K. et al. High-pressure synthesis and phase stability of nickel pernitride. *Eur. J. Inorg. Chem.* **2019**, 3753–3757 (2019).
14. Chen, W., Tse, J. S. & Jiang, J. Z. Stability, elastic and electronic properties of palladium nitride. *J. Phys. Condens. Matter* **22**, 015404 (2010).
15. Niwa, K., Yamamoto, T., Sasaki, T. & Hasegawa, M. High-pressure synthesis, crystal growth, and compression behavior of hexagonal CrN_2 having one-dimensionally aligned nitrogen dimer. *Phys. Rev. Mater.* **3**, 53601 (2019).
16. Niwa, K. et al. Highly coordinated iron and cobalt nitrides synthesized at high pressures and high temperatures. *Inorg. Chem.* **56**, 6410–6418 (2017).
17. Wessel, M. & Dronskowski, R. Nature of N-N bonding within high-pressure noble-metal pernitrides and the prediction of lanthanum pernitride. *J. Am. Chem. Soc.* **132**, 2421–2429 (2010).
18. Niwa, K. et al. Discovery of the last remaining binary platinum-group pernitride RuN_2 . *Chemistry* **20**, 13885–13888 (2014).
19. Niwa, K. et al. High pressure synthesis of marcasite-type rhodium pernitride. *Inorg. Chem.* **53**, 697–699 (2014).
20. Laniel, D. et al. Synthesis of magnesium-nitrogen salts of poly-nitrogen anions. *Nat. Commun.* **10**, 4515 (2019).
21. Laniel, D., Weck, G. & Loubeyre, P. Direct reaction of nitrogen and lithium up to 75 GPa: synthesis of the Li_3N , LiN , LiN_2 , and LiN_5 compounds. *Inorg. Chem.* **57**, 10685–10693 (2018).
22. Steele, B. A. et al. High-pressure synthesis of a pentazolate salt. *Chem. Mater.* **29**, 735–741 (2017).
23. Bykov, M. et al. Stabilization of pentazolate anions in the high-pressure compounds Na_2N_5 and NaN_5 and in the sodium pentazolate framework $\text{NaN}_5\cdot\text{N}_2$. *Dalt. Trans.* **50**, 7229–7237 (2021).
24. Salke, N. P. et al. Tungsten hexanitride with single-bonded arm-chairlike hexazine structure at high pressure. *Phys. Rev. Lett.* **126**, 65702 (2021).
25. Wang, Y. et al. Stabilization of hexazine rings in potassium polynitride at high pressure. *Nat. Chem.* **14**, 794–800 (2022).
26. Laniel, D. et al. Aromatic hexazine $[\text{N}_6]^{4-}$ anion featured in the complex structure of the high-pressure potassium nitrogen compound K_9N_{56} . *Nat. Chem.* **15**, 641–646 (2023).
27. Aslandukov, A. et al. Anionic N_{18} macrocycles and a polynitrogen double helix in novel yttrium polynitrides YN_6 and Y_2N_{11} at 100 GPa. *Angew. Chemie Int. Ed.* **61**, e202207469 (2022).
28. Bykov, M. et al. Fe-N system at high pressure reveals a compound featuring polymeric nitrogen chains. *Nat. Commun.* **9**, 2756 (2018).
29. Bykov, M. et al. High-pressure synthesis of a nitrogen-rich inclusion compound $\text{ReN}_8\cdot x\text{N}_2$ with conjugated polymeric nitrogen chains. *Angew. Chemie Int. Ed.* **57**, 9048–9053 (2018).
30. Bykov, M. et al. High-pressure synthesis of metal-inorganic frameworks $\text{Hf}_4\text{N}_{20}\cdot\text{N}_2$, $\text{WN}_8\cdot\text{N}_2$, and $\text{Os}_5\text{N}_{28}\cdot 3\text{N}_2$ with polymeric nitrogen linkers. *Angew. Chemie Int. Ed.* **59**, 10321–10326 (2020).
31. Bykov, M. et al. Stabilization of polynitrogen anions in tantalum-nitrogen compounds at high pressure. *Angew. Chemie* **133**, 9085–9090 (2021).
32. Laniel, D. et al. High-pressure synthesis of the $\beta\text{-Zn}_3\text{N}_2$ nitride and the $\alpha\text{-ZnN}_4$ and $\beta\text{-ZnN}_4$ polynitrogen compounds. *Inorg. Chem.* **60**, 14594–14601 (2021).
33. Bykov, M. et al. High-pressure synthesis of dirac materials: layered van der Waals bonded BeN_4 polymorph. *Phys. Rev. Lett.* **126**, 175501 (2021).
34. Zhang, C., Sun, C., Hu, B., Yu, C. & Lu, M. Synthesis and characterization of the pentazolate anion cyclo-N_5^- in $(\text{N}_5)_6(\text{H}_3\text{O})_3(\text{NH}_4)_4\text{Cl}$ - SUPPLEMENTARY. *Science* **355**, 374–376 (2017).
35. Xu, Y. et al. A series of energetic metal pentazolate hydrates. *Nature* **549**, 78–81 (2017).
36. Zhang, C. et al. A symmetric $\text{Co}(\text{N}_5)_2(\text{H}_2\text{O})_4\cdot 4\text{H}_2\text{O}$ high-nitrogen compound formed by cobalt(II) cation trapping of a cyclo-N_5^- anion. *Angew. Chemie Int. Ed.* **56**, 4512–4514 (2017).
37. Jiao, F., Zhang, C. & Xie, W. Energy density of high-pressure nitrogen-rich MN_x compounds. *Phys. Chem. Chem. Phys.* **23**, 7313–7320 (2021).
38. Berkok, H., Tebboune, A. & Belkaid, M. N. Structural properties and new phase transitions of ScN using FP-LMTO method. *Phys. B Condens. Matter* **406**, 3836–3840 (2011).
39. Aslam, M. A. & Ding, Z. J. Prediction of Thermodynamically Stable Compounds of the Sc-N System under High Pressure. *ACS Omega* **3**, 11477–11485 (2018).
40. Lin, J. et al. Stable nitrogen-rich scandium nitrides and their bonding features under ambient conditions. *Phys. Chem. Chem. Phys.* **23**, 6863–6870 (2021).
41. Wei, S. et al. A novel high-pressure phase of ScN_5 with higher stability predicted from first-principles calculations. *J. Phys. Condens. Matter* **33**, 475401 (2021).
42. Guo, Y. et al. Polymerization of nitrogen in two theoretically predicted high-energy compounds ScN_6 and ScN_7 under modest pressure. *New J. Phys.* **24**, 083015 (2022).
43. Alkhalidi, H. & Kroll, P. Chemical potential of nitrogen at high pressure and high temperature: application to nitrogen and nitrogen-rich phase diagram calculations. *J. Phys. Chem. C* **123**, 7054–7060 (2019).
44. Rahm, M., Cammi, R., Ashcroft, N. W. & Hoffmann, R. Squeezing all elements in the periodic table: electron configuration and

- electronegativity of the atoms under compression. *J. Am. Chem. Soc.* **141**, 10253–10271 (2019).
45. Kresse, G. & Furthmüller, J. Efficiency of ab-initio total energy calculations for metals and semiconductors using a plane-wave basis set. *Comput. Mater. Sci.* **6**, 15–50 (1996).
 46. Hulliger, F. Chapter 33 rare earth pnictides. *Handb. Phys. Chem. Rare Earths* **4**, 153–236 (1979).
 47. Shatruk, M. Synthesis of phosphides. *ACS Symp. Ser.* **1333**, 103–134 (2019).
 48. Prewitt, C. T. & Downs, R. T. High-pressure crystal chemistry. *Rev. Mineral.* **37**, 283–318 (1998).
 49. O’Sullivan, O. T. & Zdilla, M. J. Properties and promise of catenated nitrogen systems as high-energy-density materials. *Chem. Rev.* **120**, 5682–5744 (2020).
 50. Politzer, P. & Murray, J. S. The Kamlet-Jacobs parameter φ : a measure of intrinsic detonation potential. *Propellants Explos. Pyrotech.* **44**, 844–849 (2019).
 51. Zhang, J., Oganov, A. R., Li, X. & Niu, H. Pressure-stabilized hafnium nitrides and their properties. *Phys. Rev. B* **95**, 1–5 (2017).
 52. Kantor, I. et al. BX90: a new diamond anvil cell design for X-ray diffraction and optical measurements. *Rev. Sci. Instrum.* **83**, 125102 (2012).
 53. Boehler, R. New diamond cell for single-crystal x-ray diffraction. *Rev. Sci. Instrum.* **77**, 2004–2007 (2006).
 54. Kurnosov, A. et al. A novel gas-loading system for mechanically closing of various types of diamond anvil cells. *Rev. Sci. Instrum.* **79**, 045110 (2008).
 55. Fedotenko, T. et al. Laser heating setup for diamond anvil cells for in situ synchrotron and in house high and ultra-high pressure studies. *Rev. Sci. Instrum.* **90**, 104501 (2019).
 56. Akahama, Y. & Kawamura, H. Pressure calibration of diamond anvil Raman gauge to 310 GPa. *J. Appl. Phys.* **100**, 043516 (2006).
 57. Anzellini, S., Dewaele, A., Occelli, F., Loubeyre, P. & Mezouar, M. Equation of state of rhenium and application for ultra high pressure calibration. *J. Appl. Phys.* **115**, 043511 (2014).
 58. Rigaku Oxford Diffraction, CrysAlisPro Software system (2015).
 59. Aslandukov, A., Aslandukov, M., Dubrovinskaia, N. & Dubrovinsky, L. Domain auto finder (DAFI) program: the analysis of single-crystal X-ray diffraction data from polycrystalline samples. *J. Appl. Crystallogr.* **55**, 1383–1391 (2022).
 60. Dolomanov, O. V., Bourhis, L. J., Gildea, R. J., Howard, J. A. K. & Puschmann, H. OLEX2: a complete structure solution, refinement and analysis program. *J. Appl. Crystallogr.* **42**, 339–341 (2009).
 61. Sheldrick, G. M. SHELXT - Integrated space-group and crystal-structure determination. *Acta Crystallogr. Sect. A Found. Crystallogr.* **71**, 3–8 (2015).
 62. Sheldrick, G. M. Crystal structure refinement with SHELXL. *Acta Crystallogr. Sect. C Struct. Chem.* **71**, 3–8 (2015).
 63. Momma, K. & Izumi, F. VESTA 3 for three-dimensional visualization of crystal, volumetric and morphology data. *J. Appl. Crystallogr.* **44**, 1272–1276 (2011).
 64. Kresse, G. & Furthmüller, J. Efficient iterative schemes for ab initio total-energy calculations using a plane-wave basis set. *Phys. Rev. B* **54**, 11169–11186 (1996).
 65. Kresse, G. & Joubert, D. From ultrasoft pseudopotentials to the projector augmented-wave method. *Phys. Rev. B* **59**, 1758–1775 (1999).
 66. Perdew, J. P., Burke, K. & Ernzerhof, M. Generalized gradient approximation made simple. *Phys. Rev. Lett.* **77**, 3865–3868 (1996).
 67. Togo, A. & Tanaka, I. First principles phonon calculations in materials science. *Scr. Mater.* **108**, 1–5 (2015).

Acknowledgements

The authors thank Prof. Björn Winkler for useful discussions. The authors acknowledge the Advanced Photon Source (APS) for the provision of beamtime at the 13ID-D beamline and the European Synchrotron Radiation Facility (ESRF) for the provision of beamtime at the ID11 and ID15b beamlines. Portions of this work were performed at GeoSoilEnviroCARS (The University of Chicago, Sector 13), Advanced Photon Source (APS), Argonne National Laboratory. GeoSoilEnviroCARS was supported by the National Science Foundation – Earth Sciences (EAR – 1634415). This research used resources of the Advanced Photon Source, a U.S. Department of Energy (DOE) Office of Science User Facility operated for the DOE Office of Science by Argonne National Laboratory under Contract No. DE-AC02-06CH11357. Computations were performed at the Leibniz Supercomputing Center of the Bavarian Academy of Sciences and the Humanities, and the research center for scientific computing at the University of Bayreuth. D.L. thanks the UKRI Future Leaders Fellowship (MR/V025724/1) for financial support. N.D. and L.D. thank the Deutsche Forschungsgemeinschaft (DFG projects DU 945/15-1, LA 4916/1-1, DU 954–11/1, DU 393–9/2, DU 393–13/1) for financial support. N.D. also thanks the Swedish Government Strategic Research Area in Materials Science on Functional Materials at Linköping University (Faculty Grant SFO-Mat-LiU No. 2009 00971). For the purpose of open access, the authors have applied a Creative Commons Attribution (CC BY) licence to any Author Accepted Manuscript version arising from this submission. Open access is funded by the Open Access Publishing Fund of the University of Bayreuth.

Author contributions

An.A., L.D., and N.D. designed the research. An.A. and Al.A. prepared the high-pressure experiments. An.A., Al.A., D.L., S.K., Y.Y., F.I.A., S.C., V.P., E.L.B., C.G., J. W., D.C., M.H. performed the synchrotron X-ray diffraction experiments. An.A. processed the synchrotron X-ray diffraction data. An.A. and Al.A. performed the theoretical calculations. An.A. and L.D. contextualized the data interpretation. An.A., L.D., and N.D. prepared the first draft of the paper with contributions from all other authors. All the authors commented on successive drafts and have given approval to the final version of the paper.

Funding

Open Access funding enabled and organized by Projekt DEAL.

Competing interests

The authors declare no competing interests.

Additional information

Supplementary information The online version contains supplementary material available at <https://doi.org/10.1038/s41467-024-46313-9>.

Correspondence and requests for materials should be addressed to Andrey Aslandukov.

Peer review information *Nature Communications* thanks the anonymous reviewer(s) for their contribution to the peer review of this work. A peer review file is available.

Reprints and permissions information is available at <http://www.nature.com/reprints>

Publisher’s note Springer Nature remains neutral with regard to jurisdictional claims in published maps and institutional affiliations.

Open Access This article is licensed under a Creative Commons Attribution 4.0 International License, which permits use, sharing, adaptation, distribution and reproduction in any medium or format, as long as you give appropriate credit to the original author(s) and the source, provide a link to the Creative Commons licence, and indicate if changes were made. The images or other third party material in this article are included in the article's Creative Commons licence, unless indicated otherwise in a credit line to the material. If material is not included in the article's Creative Commons licence and your intended use is not permitted by statutory regulation or exceeds the permitted use, you will need to obtain permission directly from the copyright holder. To view a copy of this licence, visit <http://creativecommons.org/licenses/by/4.0/>.

© The Author(s) 2024

Supporting Information

Stabilization of N₆ and N₈ anionic units and 2D polynitrogen layers in high-pressure scandium polynitrides

Andrey Aslandukov^{1,2*}, Alena Aslandukova¹, Dominique Laniel³, Saiana Khandarkhaeva¹, Yuqing Yin², Fariia I. Akbar¹, Stella Chariton⁴, Vitali Prakapenka⁴, Eleanor Lawrence Bright⁵, Carlotta Giacobbe⁵, Jonathan Wright⁵, Davide Comboni⁵, Michael Hanfland⁵, Natalia Dubrovinskaia^{2,6} Leonid Dubrovinsky¹

¹ Bavarian Research Institute of Experimental Geochemistry and Geophysics (BGI), University of Bayreuth, Universitaetstrasse 30, 95440 Bayreuth, Germany

² Material Physics and Technology at Extreme Conditions, Laboratory of Crystallography, University of Bayreuth, 95440 Bayreuth, Germany

³ Centre for Science at Extreme Conditions and School of Physics and Astronomy, University of Edinburgh, EH9 3FD Edinburgh, United Kingdom

⁴ Center for Advanced Radiation Sources, University of Chicago, Chicago, Illinois 60637, USA

⁵ European Synchrotron Radiation Facility, BP 220, 38043 Grenoble Cedex, France

⁶ Department of Physics, Chemistry and Biology (IFM), Linköping University, SE-581 83, Linköping, Sweden

*Correspondence to andrii.aslandukov@uni-bayreuth.de

Supplementary Tables

Supplementary Table 1. List of the samples investigated in the present study

Sample	Culet size, μm	Reaction mixture	Temperature, K	Pressure, GPa		Reaction products	Attempt to decompress
				Raman diamond edge	Re EoS		
DAC#1	250	Sc + N ₂	2500(200)	50(1)	50(1)	ScN	No
DAC#2 ¹	120	Sc + N ₂	2500(200)	78(2)	79(2)	ScN, Sc ₂ N ₆ , Sc ₂ N ₈	Yes ²
			2500(200)	96(2)	98(2)	ScN, Sc ₂ N ₈ , ScN ₅	
DAC#3	80	Sc + N ₂	2500(200)	125(2)	125(2)	Sc ₄ N ₃ , ScN ₅	No

¹Two scandium pieces were loaded into the sample chamber of DAC#2. One of the pieces was laser heated at 96(2) GPa, while another one at 78(2) GPa.

²In order to check the recoverability of Sc₂N₆, Sc₂N₈, ScN₅ phases DAC#2 was decompressed. Unfortunately, at 50(2) GPa nitrogen pressure transmitting medium went out through microcracks in the diamond resulting in the complete gasket closure and dropping pressure to 1 atm. The sample could not be found afterward, therefore no conclusion regarding the recoverability of Sc₂N₆, Sc₂N₈, and ScN₅ can be made. Unfortunately, it is a technical limitation of the decompression experiment started from the pressures above ~70 GPa in a gas pressure transmitting medium. It is a typical behavior of the culets (*i.e.* 120 μm or smaller) of double-bevel diamonds: above ~70 GPa the square-like cracks appear around the culet, and during the decompression in a gas-pressure transmitting medium diffuses into the crack resulting in a crack expansion and cell depressurization.

Supplementary Table 2. Structure refinement details of ScN at 50 GPa. The full crystallographic data was deposited to the ICSD under the deposition number CSD 2252036. The A and B alerts revealed by CheckCIF are listed and explained after the table.

Chemical formula	ScN				
Temperature (K)	293				
Pressure (GPa)	50(2)				
Crystal data					
Mr	58.97				
ρ (g/cm ³)	5.105				
Crystal system, space group	cubic, <i>Fm-3m</i>				
a (Å)	4.2492(7)				
V (Å ³)	76.72(4)				
Z	4				
Radiation type	X-ray, $\lambda = 0.29521$ Å				
μ (mm ⁻¹)	0.709				
Data collection					
No. of measured, independent and observed [$I > 2\sigma(I)$] reflections	40/19/19				
R _{int}	6.88%				
($\sin \theta/\lambda$) _{max} (Å ⁻¹)	0.849				
Refinement					
R[F ² > 4 σ (F ²)], wR(F ²), GOF	3.41%, 7.72%, 1.202				
data/parameters ratio	19/3				
$\Delta\rho_{\max}, \Delta\rho_{\min}$ (e Å ⁻³)	0.630, -1.025				
Atomic positions and equivalent isotropic ADPs					
Atom	Wyckoff site	Fractional atomic coordinates			U _{eq} (Å ²)
		x	y	z	
Sc1	4a	0	0	0	U _{eq} = 0.0070(7)
N1	4b	0.5	0.5	0.5	U _{eq} = 0.0051(14)

Datablock: ScN_50GPa

PLAT088_ALERT_3_B Poor Data / Parameter Ratio 6.33 Note

- Author Response: This measurement was performed at high pressure. The diamond anvil cell metallic body typically shadows more than 60% of the reflections.

PLAT113_ALERT_2_B ADDSYM Suggests Possible Pseudo/New Space Group Pm-3m Check

- Author Response: Fm-3m spacegroup is correct.

Supplementary Table 3. Structure refinement details of Sc₂N₆ at 78 GPa. The full crystallographic data was deposited to the ICSD under the deposition number CSD 2252033. The A and B alerts revealed by CheckCIF are listed and explained after the table.

Chemical formula		Sc ₂ N ₆			
Temperature (K)		293			
Pressure (GPa)		78(2)			
Crystal data					
Mr		173.98			
ρ (g/cm ³)		5.092			
Crystal system, space group		triclinic, <i>P</i> -1			
a (Å)		2.9170(3)			
b (Å)		4.3283(10)			
c (Å)		4.812(2)			
α (°)		99.36(3)			
β (°)		104.29(2)			
γ (°)		99.517(15)			
V (Å ³)		56.73(3)			
Z		1			
Radiation type		X-ray, $\lambda = 0.2846$ Å			
μ (mm ⁻¹)		0.471			
Data collection					
No. of measured, independent and observed [$I > 2\sigma(I)$] reflections		302/224/213			
R_{int}		0.25%			
$(\sin \theta/\lambda)_{\text{max}}$ (Å ⁻¹)		1.121			
Refinement					
R[$F^2 > 4\sigma(F^2)$], wR(F^2), GOF		4.12%, 12.34%, 1.188			
data/parameters ratio		224/22			
$\Delta\rho_{\text{max}}, \Delta\rho_{\text{min}}$ (e Å ⁻³)		0.564, -0.707			
Atomic positions and equivalent isotropic (or isotropic) ADPs					
Atom	Wyckoff site	Fractional atomic coordinates			U _{iso} or U _{eq} (Å ²)
		x	y	z	
Sc1	2i	0.41540(12)	0.79589(14)	0.1946(2)	U _{eq} = 0.0054(7)
N1	2i	0.2595(7)	0.2909(8)	0.1278(14)	U _{iso} = 0.0072(3)
N2	2i	0.1124(7)	0.1685(9)	0.3293(14)	U _{iso} = 0.0083(4)
N3	2i	0.0020(7)	0.3614(8)	0.5348(13)	U _{iso} = 0.0074(4)

Datablock: Sc₂N₆_78GPa

PLAT029_ALERT_3_A _diffn_measured_fraction_theta_full value Low . 0.293 Why?

- Author Response: This measurement was performed at high pressure which, due to the high pressure apparatus, limits the theta range. Indeed, the diamond anvil cell metallic body typically shadows more than 60% of the reflections.

PLAT911_ALERT_3_B Missing FCF Refl Between Thmin & STh/L= 0.600 143 Report

- Author Response: This measurement was performed at high pressure which, due to the high pressure apparatus, limits the theta range. Indeed, the diamond anvil cell metallic body typically shadows more than 60% of the reflections.

Supplementary Table 4. Structure refinement details of Sc₂N₈ at 78 and 96 GPa. The full crystallographic data were deposited to the ICSD under the deposition numbers CSD 2252034 and CSD 2252035. The A and B alerts revealed by CheckCIF are listed and explained after the table.

Chemical formula	Sc ₂ N ₈			Sc ₂ N ₈	
Temperature (K)	293			293	
Pressure (GPa)	78(2)			96(2)	
Crystal data					
Mr	202.0			202.0	
ρ (g/cm ³)	4.857			4.994	
Crystal system, space group	monoclinic, <i>P</i> 2 ₁ / <i>c</i>			monoclinic, <i>P</i> 2 ₁ / <i>c</i>	
a (Å)	3.3278(6)			3.2884(16)	
b (Å)	5.6802(8)			5.6390(9)	
c (Å)	7.3964(4)			7.342(2)	
β (°)	98.905(9)			99.36(4)	
V (Å ³)	138.13(3)			134.32(8)	
Z	2			2	
Radiation type	X-ray, $\lambda = 0.2846$ Å			X-ray, $\lambda = 0.2843$ Å	
μ (mm ⁻¹)	0.401			0.411	
Data collection					
No. of measured, independent and observed [<i>I</i> > 2 σ (<i>I</i>)] reflections	946/575/429			388/320/215	
R _{int}	2.40%			2.01%	
($\sin \theta/\lambda$) _{max} (Å ⁻¹)	1.161			1.045	
Refinement					
R[F ² > 4 σ (F ²)], wR(F ²), GOF	4.38%, 11.78%, 1.074			4.11%, 11.07%, 1.009	
data/parameters ratio	575/46			320/26	
$\Delta\rho_{\max}$, $\Delta\rho_{\min}$ (e Å ⁻³)	1.147, -0.722			0.552, -0.584	
Atomic positions and equivalent isotropic ADPs at 78(2) GPa					
Atom	Wyckoff site	Fractional atomic coordinates			U _{eq} (Å ²)
		x	y	z	
Sc1	4e	0.1326(2)	0.87943(11)	0.32610(6)	U _{eq} = 0.00742(15)
N1	4e	0.3159(11)	0.6093(5)	0.1307(3)	U _{eq} = 0.0087(5)
N2	4e	0.3777(10)	0.2554(5)	0.3724(3)	U _{eq} = 0.0077(5)
N3	4e	0.3769(10)	0.1903(5)	0.0434(3)	U _{eq} = 0.0078(5)
N4	4e	0.0859(10)	0.0525(5)	0.0761(3)	U _{eq} = 0.0077(5)
Atomic positions and equivalent isotropic (or isotropic) ADPs at 96(2) GPa					
Atom	Wyckoff site	Fractional atomic coordinates			U _{iso} or U _{eq} (Å ²)
		x	y	z	
Sc1	4e	0.1314(3)	0.88020(12)	0.32608(14)	U _{eq} = 0.0084(3)
N1	4e	0.3111(15)	0.6111(6)	0.1312(6)	U _{iso} = 0.0100(6)
N2	4e	0.3781(17)	0.2583(5)	0.3726(6)	U _{iso} = 0.0096(6)
N3	4e	0.3759(16)	0.1906(5)	0.0444(5)	U _{iso} = 0.0090(6)
N4	4e	0.0891(17)	0.0513(6)	0.0773(6)	U _{iso} = 0.0099(6)

Datablock: Sc₂N₈_78GPa

PLAT029_ALERT_3_A _diffn_measured_fraction_theta_full value Low . 0.545 Why?

- Author Response: This measurement was performed at high pressure which, due to the high pressure apparatus, limits the theta range. Indeed, the diamond anvil cell metallic body typically shadows more than 60% of the reflections.

PLAT911_ALERT_3_B Missing FCF Refl Between Thmin & STh/L= 0.600 111 Report

- Author Response: This measurement was performed at high pressure which, due to the high pressure apparatus, limits the theta range. Indeed, the diamond anvil cell metallic body typically shadows more than 60% of the reflections.

Datablock: Sc₂N₈_96GPa

PLAT029_ALERT_3_A _diffn_measured_fraction_theta_full value Low . 0.407 Why?

- Author Response: This measurement was performed at high pressure which, due to the high pressure apparatus, limits the theta range. Indeed, the diamond anvil cell metallic body typically shadows more than 60% of the reflections.

PLAT911_ALERT_3_B Missing FCF Refl Between Thmin & STh/L= 0.600 144 Report

- Author Response: This measurement was performed at high pressure which, due to the high pressure apparatus, limits the theta range. Indeed, the diamond anvil cell metallic body typically shadows more than 60% of the reflections.

Supplementary Table 5. Structure refinement details of ScN₅ at 96 and 125 GPa. The full crystallographic data were deposited to the ICSD under the deposition numbers CSD 2252030 and CSD 2252031. The A and B alerts revealed by CheckCIF are listed and explained after the table.

Chemical formula		ScN ₅			ScN ₅
Temperature (K)		293			293
Pressure (GPa)		96(2)			125(2)
Crystal data					
Mr		115.01			115.01
ρ (g/cm ³)		4.971			5.282
Crystal system, space group		monoclinic, <i>P</i> 2 ₁ / <i>m</i>			monoclinic, <i>P</i> 2 ₁ / <i>m</i>
a (Å)		3.3225(6)			3.203(5)
b (Å)		6.440(3)			6.3576(8)
c (Å)		3.7067(4)			3.6943(6)
β (°)		104.339(13)			105.99(6)
V (Å ³)		76.84(4)			72.31(12)
Z		2			2
Radiation type		X-ray, $\lambda = 0.2843$ Å			X-ray, $\lambda = 0.4100$ Å
μ (mm ⁻¹)		0.373			0.373
Data collection					
No. of measured, independent and observed [<i>I</i> > 2 σ (<i>I</i>)] reflections		446/264/202			172/106/98
R _{int}		3.21%			2.02%
$(\sin \theta/\lambda)_{\max}$ (Å ⁻¹)		1.067			0.876
Refinement					
R[F ² > 4 σ (F ²)], wR(F ²), GOF		3.63%, 8.77%, 1.008			4.43%, 11.96%, 1.154
data/parameters ratio		264/31			106/15
$\Delta\rho_{\max}, \Delta\rho_{\min}$ (e Å ⁻³)		0.724, -0.789			0.605, -0.668
Atomic positions and equivalent isotropic ADPs at 96(2) GPa					
Atom	Wyckoff site	Fractional atomic coordinates			U _{eq} (Å ²)
		x	y	z	
Sc1	2e	0.4779(2)	0.25	0.13202(18)	U _{eq} = 0.0076(3)
N1	4f	0.1061(6)	0.5835(8)	0.4462(5)	U _{eq} = 0.0082(9)
N2	4f	0.1897(7)	0.5396(8)	0.1165(5)	U _{eq} = 0.0099(10)
N3	2e	0.1740(10)	0.25	0.5651(8)	U _{eq} = 0.0078(13)
Atomic positions and isotropic ADPs at 125(2) GPa					
Atom	Wyckoff site	Fractional atomic coordinates			U _{iso} (Å ²)
		x	y	z	
Sc1	2e	0.4623(11)	0.25	0.1205(3)	U _{iso} = 0.0102(4)
N1	4f	0.102(4)	0.5853(6)	0.4492(11)	U _{iso} = 0.0106(8)
N2	4f	0.187(4)	0.5457(6)	0.1196(10)	U _{iso} = 0.0109(8)
N3	2e	0.184(5)	0.25	0.5551(15)	U _{iso} = 0.0097(10)

Datablock: ScN₅_96GPa

PLAT029_ALERT_3_A _diffn_measured_fraction_theta_full value Low . 0.547 Why?

- Author Response: This measurement was performed at high pressure which, due to the high pressure apparatus, limits the theta range. Indeed, the diamond anvil cell metallic body typically shadows more than 60% of the reflections.

PLAT911_ALERT_3_B Missing FCF Refl Between Thmin & STh/L= 0.600 68 Report

- Author Response: This measurement was performed at high pressure which, due to the high pressure apparatus, limits the theta range. Indeed, the diamond anvil cell metallic body typically shadows more than 60% of the reflections.

Datablock: ScN₅_125GPa

ATOM007_ALERT_1_A _atom_site_aniso_label is missing Unique label identifying the atom site.

- Author Response: Due to poor data/parameter ratio it is not possible to refine atoms in the anisotropic approximation.

PLAT029_ALERT_3_A _diffrn_measured_fraction_theta_full value Low . 0.392 Why?

- Author Response: This measurement was performed at high pressure which, due to the high pressure apparatus, limits the theta range. Indeed, the diamond anvil cell metallic body typically shadows more than 60% of the reflections.

PLAT088_ALERT_3_B Poor Data / Parameter Ratio 7.07 Note

- Author Response: Low number of reflections due to low quality of the crystallite under higher-than-megabar pressure and due to limitations of the high pressure apparatus.

PLAT149_ALERT_3_B s.u. on the beta Angle is Too Large 0.06 Degree

- Author Response: The precision of beta angle determination is a bit lower than usual, because of insufficient statistics. The reason is the low number of reflections, especially at high angles, due to low quality of the crystallite under higher-than-megabar pressure and due to limitations of the high pressure apparatus.

PLAT911_ALERT_3_B Missing FCF Refl Between Thmin & STh/L= 0.600 64 Report

- Author Response: This measurement was performed at high pressure which, due to the high pressure apparatus, limits the theta range. Indeed, the diamond anvil cell metallic body typically shadows more than 60% of the reflections.

Supplementary Table 6. Structure refinement details of Sc₄N₃ at 125 GPa. The full crystallographic data was deposited to the ICSD under the deposition number CSD 2252032. No A or B alerts were revealed by CheckCIF.

Chemical formula		Sc ₄ N ₃			
Temperature (K)		293			
Pressure (GPa)		125(2)			
Crystal data					
Mr		221.87			
ρ (g/cm ³)		6.301			
Crystal system, space group		cubic, <i>I</i> -43 <i>d</i>			
a (Å)		6.1613(13)			
V (Å ³)		233.89(15)			
Z		4			
Radiation type		X-ray, $\lambda = 0.4100$ Å			
μ (mm ⁻¹)		2.232			
Data collection					
No. of measured, independent and observed [$I > 2\sigma(I)$] reflections		246/83/80			
R_{int}		2.55%			
$(\sin \theta/\lambda)_{\text{max}}$ (Å ⁻¹)		0.8740			
Refinement					
R[$F^2 > 4\sigma(F^2)$], wR(F^2), GOF		2.66%, 6.37%, 1.078			
data/parameters ratio		83/6			
$\Delta\rho_{\text{max}}, \Delta\rho_{\text{min}}$ (e Å ⁻³)		0.481, -0.534			
Atomic positions and equivalent isotropic ADPs					
Atom	Wyckoff site	Fractional atomic coordinates			U_{eq} (Å ²)
		x	y	z	
Sc1	16c	0.06784(8)	0.06784(8)	0.06784(8)	$U_{\text{eq}} = 0.0080(3)$
N1	12a	0	0.25	0.375	$U_{\text{eq}} = 0.0095(11)$

Supplementary Table 7. Experimentally determined crystallographic data for Sc₂N₆ at 78 GPa in comparison with the corresponding DFT-relaxed structure. Note that pressure was fixed in theoretical simulations, while volume of the unit cell, lattice parameters and equilibrium state parameters were calculated.

	Exp.	Calc.
Space group	<i>P</i> -1	<i>P</i> -1
Volume	56.73(3) Å ³	57.25 Å ³
Lattice parameters	a = 2.9170(3) Å b = 4.3283(10) Å c = 4.812(2) Å α = 99.36(3)° β = 104.29(2)° γ = 99.517(15)°	a = 2.9135 Å b = 4.3291 Å c = 4.8517 Å α = 99.04° β = 104.02° γ = 99.731°
Atomic positions	Sc1 x 0.41540(12) y 0.79589(14) z 0.1946(2)	Sc1 x 0.41668 y 0.79662 z 0.19583
	N1 x 0.2595(7) y 0.2909(8) z 0.1278(14)	N1 x 0.25922 y 0.29398 z 0.12654
	N2 x 0.1124(7) y 0.1685(9) z 0.3293(14)	N2 x 0.10949 y 0.16759 z 0.32841
	N3 x 0.0020(7) y 0.3614(8) z 0.5348(13)	N3 x 0.00298 y 0.36034 z 0.53232

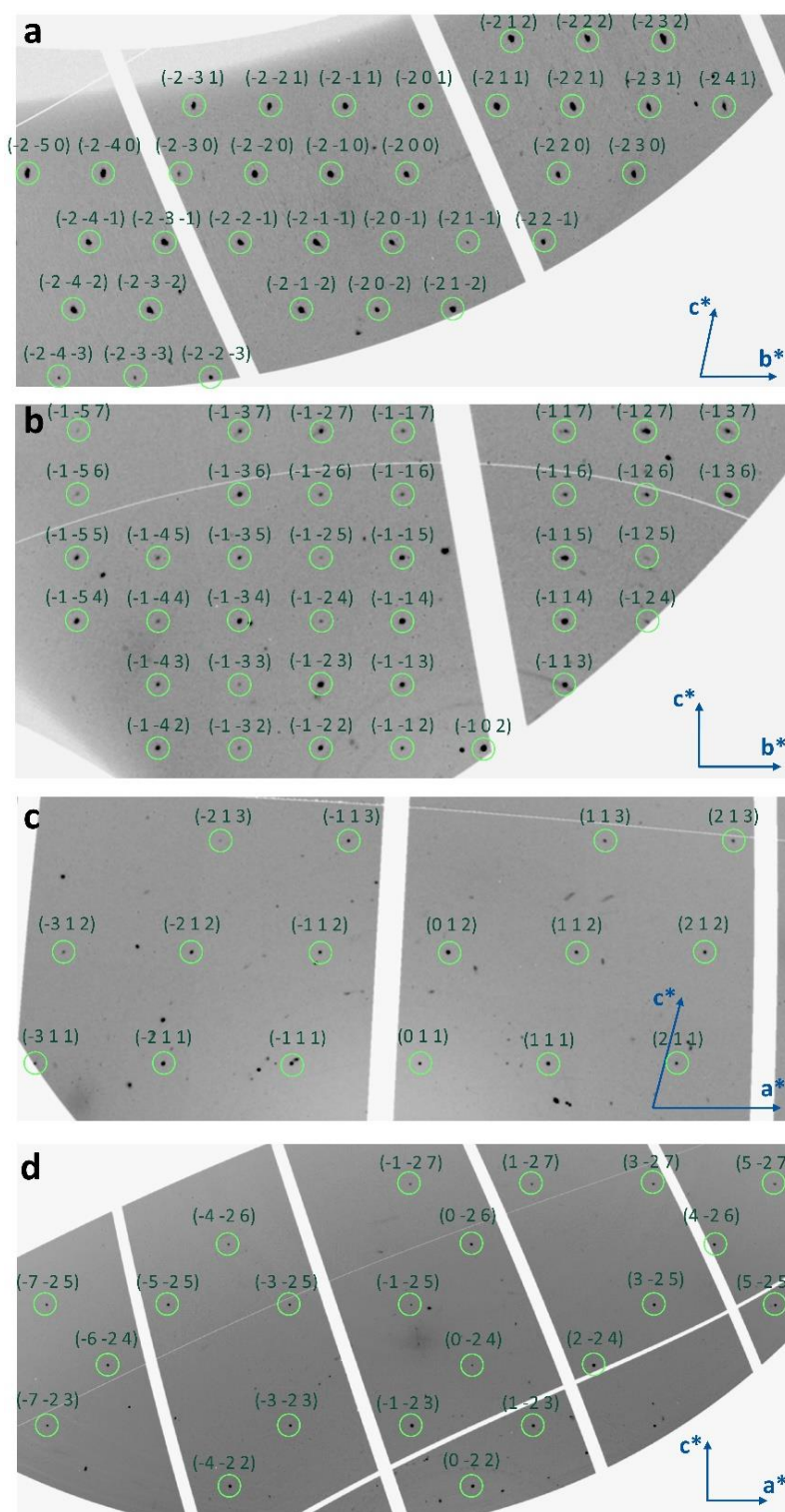
Supplementary Table 8. Experimentally determined crystallographic data for Sc₂N₈ at 96 GPa in comparison with the corresponding DFT-relaxed structure. Note that pressure was fixed in theoretical simulations, while volume of the unit cell, lattice parameters and equilibrium state parameters were calculated.

	Exp.	Calc.
Space group	<i>P</i> 2 ₁ / <i>c</i>	<i>P</i> 2 ₁ / <i>c</i>
Volume	134.32(8)Å ³	133.59 Å ³
Lattice parameters	a = 3.2884(16) Å b = 5.6390(9) Å c = 7.342(2) Å β = 99.36°	a = 3.3081 Å b = 5.5730 Å c = 7.3612 Å β = 100.14°
Atomic positions	Sc1 x 0.1314(3) y 0.8802(1) z 0.3261(1)	Sc1 x 0.1291 y 0.8826 z 0.3270
	N1 x 0.3111(15) y 0.6111(6) z 0.1312(6)	N1 x 0.3159 y 0.6148 z 0.1332
	N2 x 0.3781(17) y 0.2583(5) z 0.3726(6)	N2 x 0.3754 y 0.2576 z 0.3723
	N3 x 0.3759(16) y 0.1906(5) z 0.0444(5)	N3 x 0.3775 y 0.1905 z 0.0441
	N4 x 0.0891(17) y 0.0513(6) z 0.0773(6)	N4 x 0.0855 y 0.0545 z 0.0755

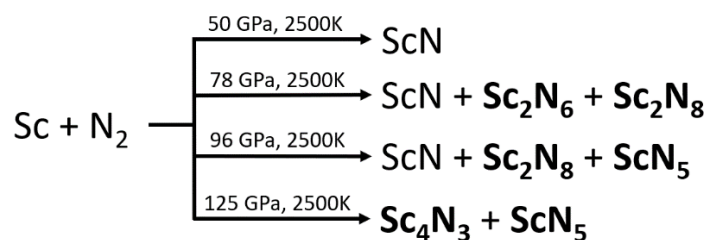
Supplementary Table 9. Experimentally determined crystallographic data for ScN₅ phase at 96 GPa in comparison with the corresponding DFT-relaxed structure. Note that pressure was fixed in theoretical simulations, while volumes of the unit cells, lattice parameters and equilibrium state parameters were calculated.

	Exp.	Calc.
Space group	$P2_1/m$	$P2_1/m$
Volume	76.84(4) Å ³	76.53 Å ³
Lattice parameters	a = 3.3225(6) Å b = 6.440(3) Å c = 3.7067(4) Å $\beta = 104.339(13)^\circ$	a = 3.3273 Å b = 6.4281 Å c = 3.6955 Å $\beta = 104.491^\circ$
Atomic positions	Sc1	Sc1
	x 0.4779(2)	x 0.4796
	y 0.25	y 0.2500
	z 0.13202(18)	z 0.1338
	N1	N1
	x 0.1061(6)	x 0.1052
	y 0.5835(8)	y 0.5845
	z 0.4462(5)	z 0.4439
	N2	N2
	x 0.1897(7)	x 0.1868
	y 0.5396(8)	y 0.5405
	z 0.1165(5)	z 0.1180
N3	N3	
x 0.1740(10)	x 0.1744	
y 0.25	y 0.2500	
z 0.5651(8)	z 0.5652	

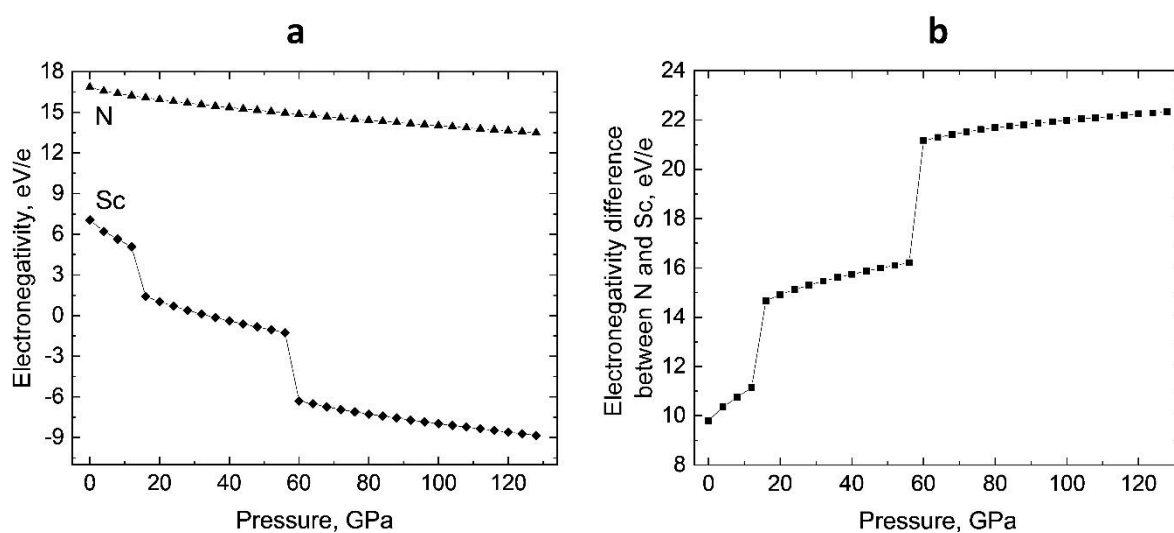
Supplementary figures



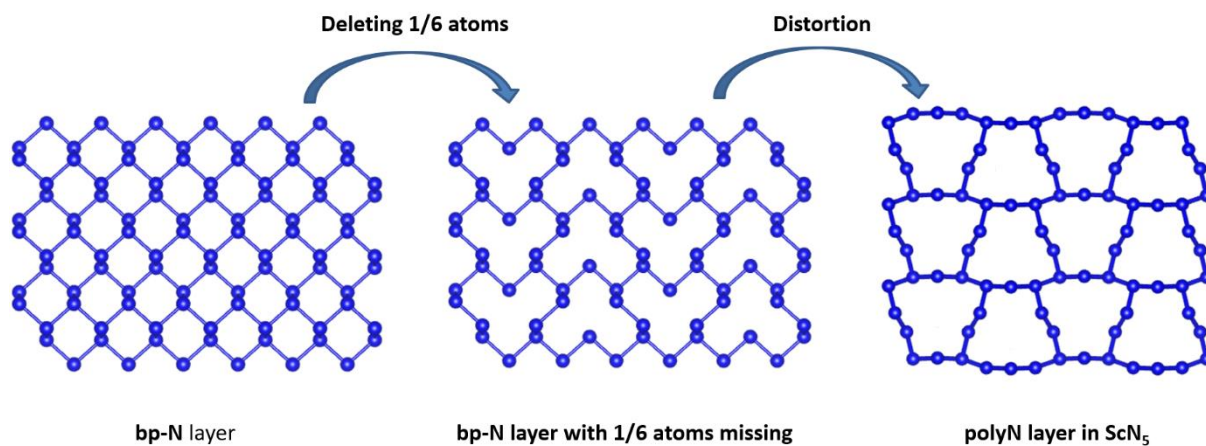
Supplementary Figure 1. The slices of the reciprocal space (also called unwarps) for a given (hkl) plane of a given crystallite, reconstructed from the experimental single-crystal XRD datasets in CrysAlis^{Pro} software, demonstrating the quality of single-crystal reflections: (a) $(-2kl)$ plane of Sc_2N_6 at 78 GPa, (b) $(-1kl)$ plane of Sc_2N_8 at 78 GPa, (c) $(h1l)$ plane of ScN_5 at 96 GPa and (d) $(h-2l)$ plane of Sc_4N_3 at 125 GPa. The green-encircled reflections correspond to the crystallites of (a) Sc_2N_6 , (b) Sc_2N_8 , (c) ScN_5 , or (d) Sc_4N_3 whose structure was determined. The reflections that are not encircled belong to other crystallites of the same Sc-N phase or of other Sc-N phases present in multiphase multigrain samples.



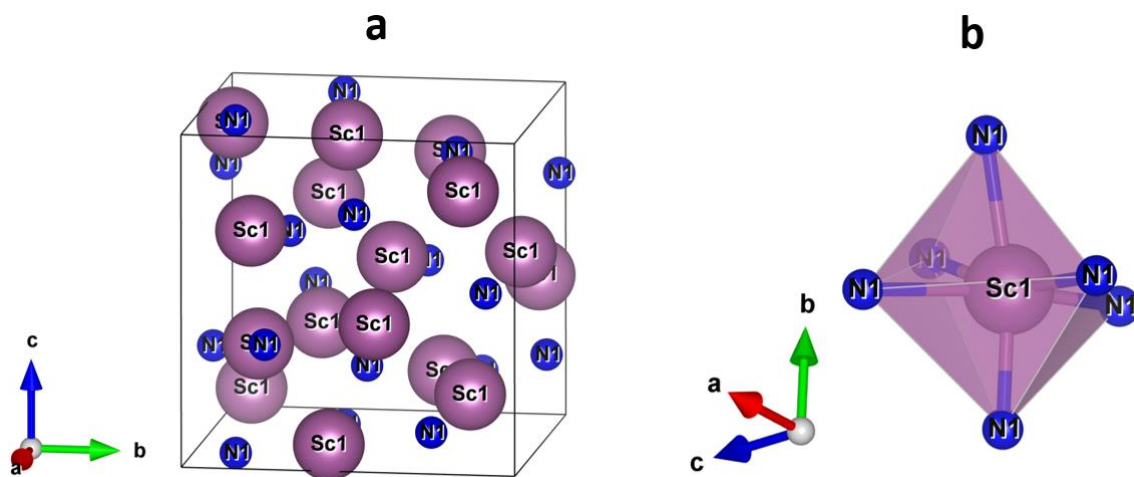
Supplementary Figure 2. Summary of the high-pressure high-temperature induced reactions of Sc and N₂ studied in this paper.



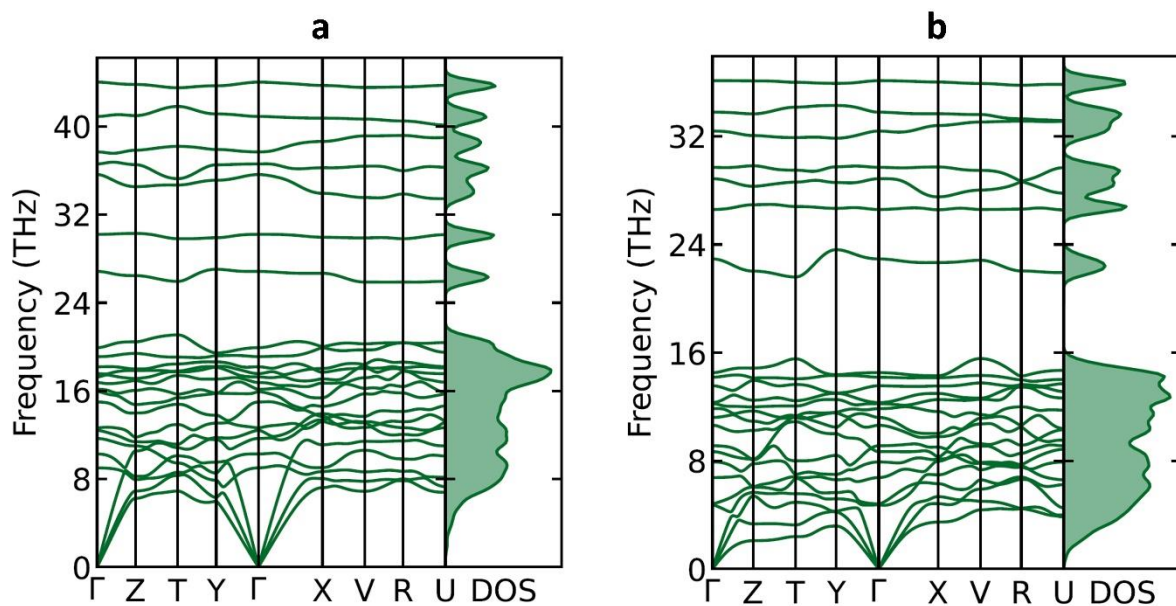
Supplementary Figure 3. Pressure dependence of the (a) electronegativity of N and Sc elements and (b) electronegativity difference between N and Sc according to ¹, where the electronegativity is defined as the average electron energy. This scale might be roughly connected to the Pauling electronegativity scale, where 1 Pauling unit \approx 6 eV/e.¹ At 60 GPa electronegativity difference between N and Sc increases by \sim 5 eV/e, changing from 16.2 to 21.2 eV/e.



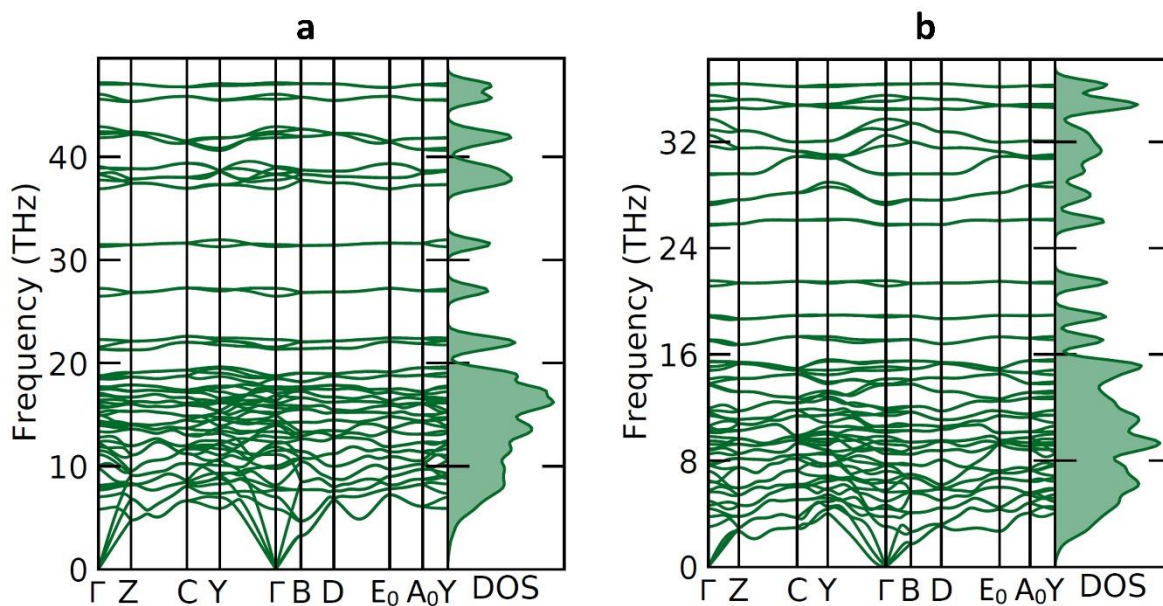
Supplementary Figure 4. The evolution of the bp-N layer to the polynitrogen layer in ScN₅.



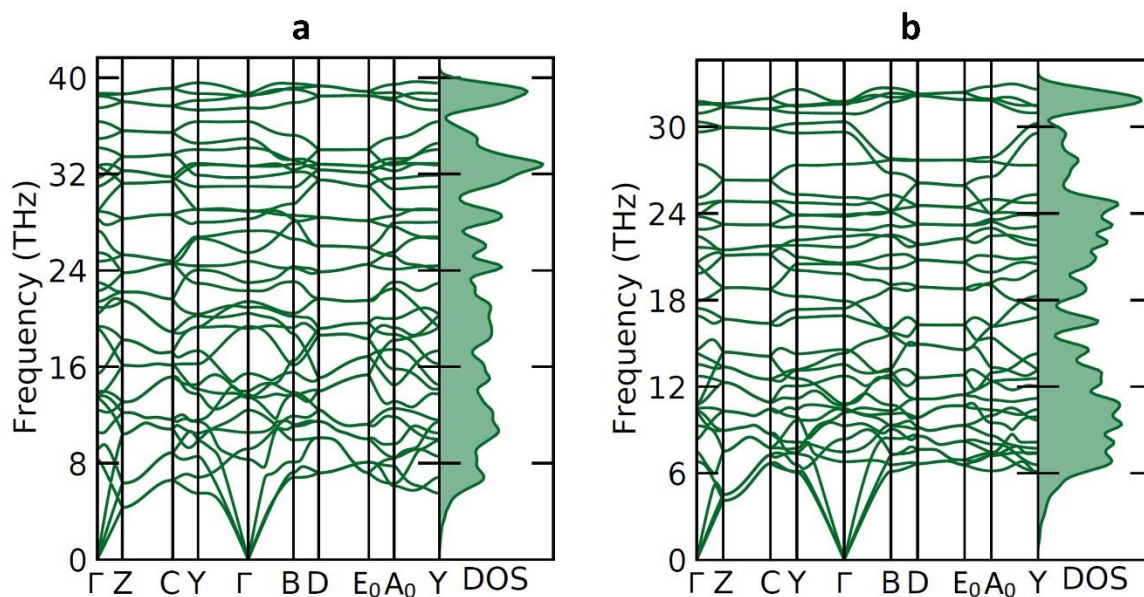
Supplementary Figure 5. Crystal structure of Sc₄N₃. Sc atoms are purple, N atoms are blue; grey thin lines outline the unit cell. (a) A general view of the crystal structure. (b) The coordination polyhedron of Sc atom: distorted octahedron with three Sc-N distances of 2.0332(7) Å and three Sc-N distances of 2.2396(7) Å at 125 GPa.



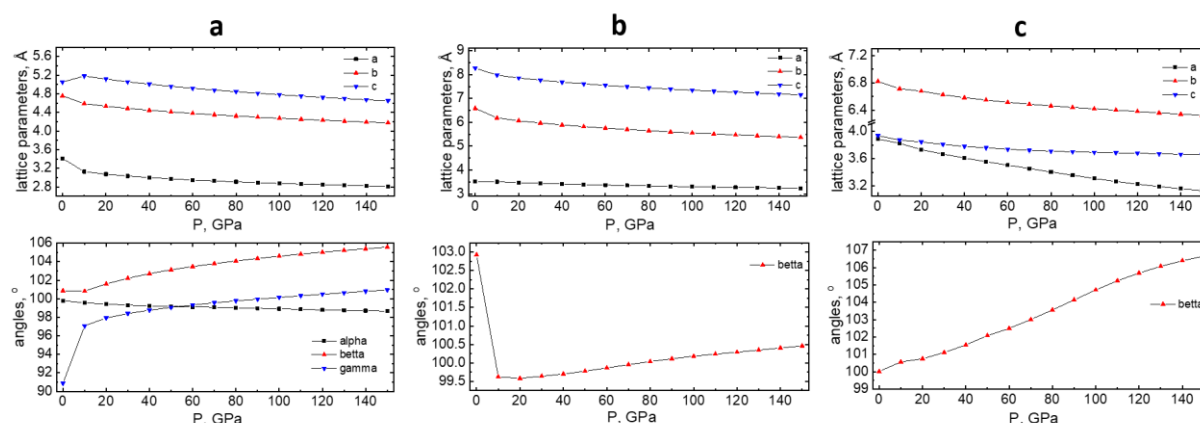
Supplementary Figure 6. Phonon dispersions of Sc_2N_6 at (a) 78 GPa and (b) 1 bar.



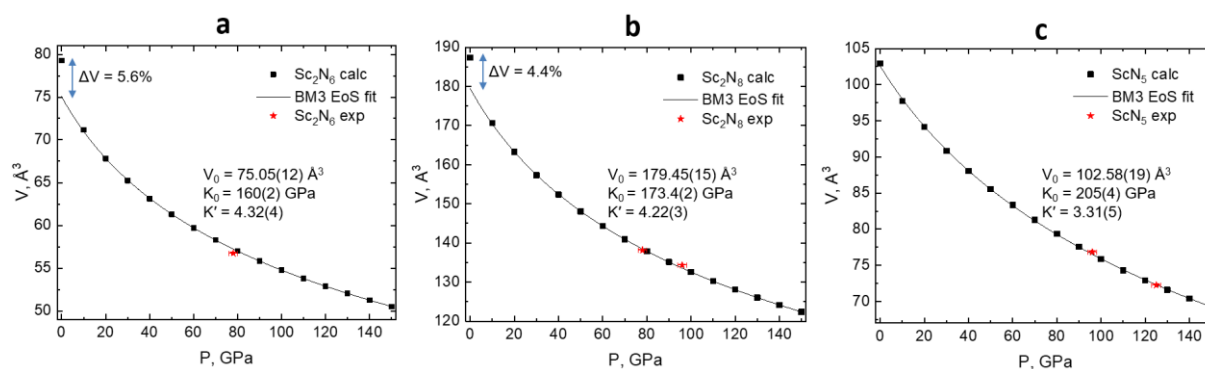
Supplementary Figure 7. Phonon dispersions of Sc_2N_8 at (a) 96 GPa and (b) 1 bar.



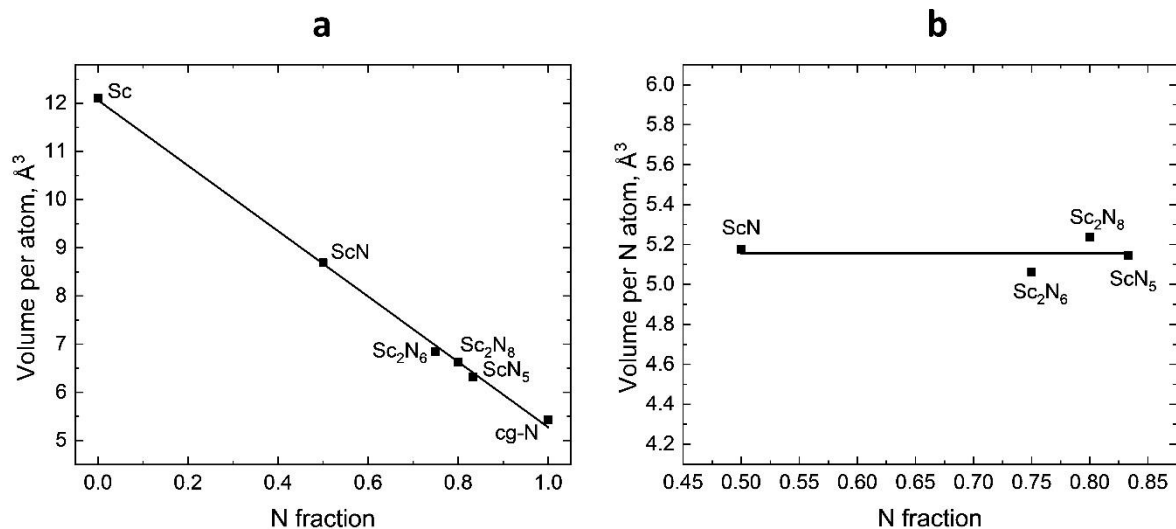
Supplementary Figure 8. Phonon dispersions of ScN₅ at (a) 96 GPa and (b) 1 bar.



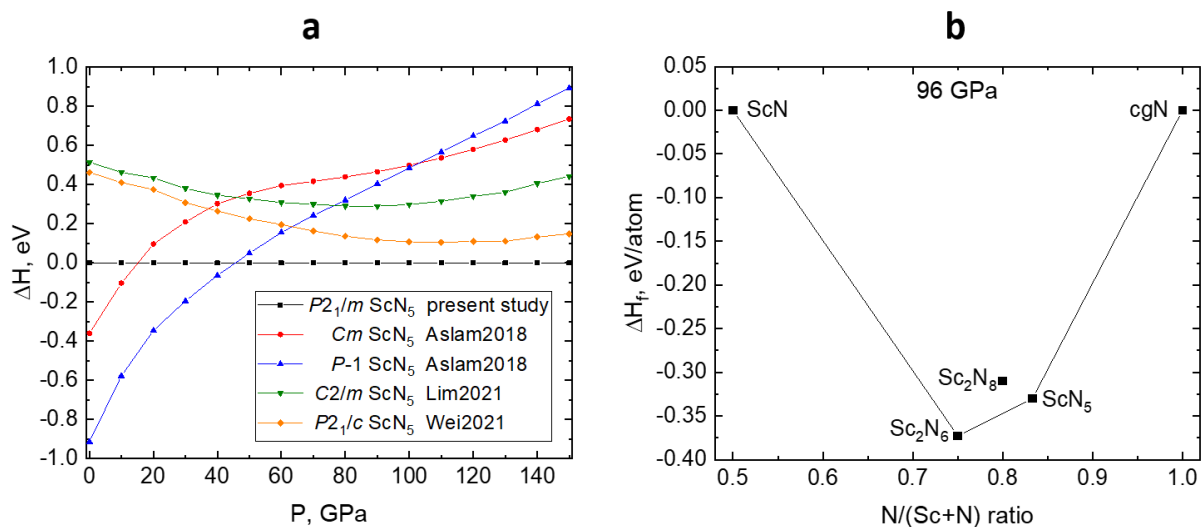
Supplementary Figure 9. The dependence of the unit cell parameters on pressure of (a) Sc₂N₆, (b) Sc₂N₈, and (c) ScN₅ obtained from DFT. The jump of lattice parameters of Sc₂N₆ and Sc₂N₈ between 1 bar and 10 GPa may indicate the isostructural phase transitions. A comparison of the corresponding DFT-relaxed crystal structures at 1 bar and 10 GPa shows that the geometry of N₆ and N₈ units does not change, while the scandium coordination environment changes significantly due to a significant increase of some Sc-N distances.



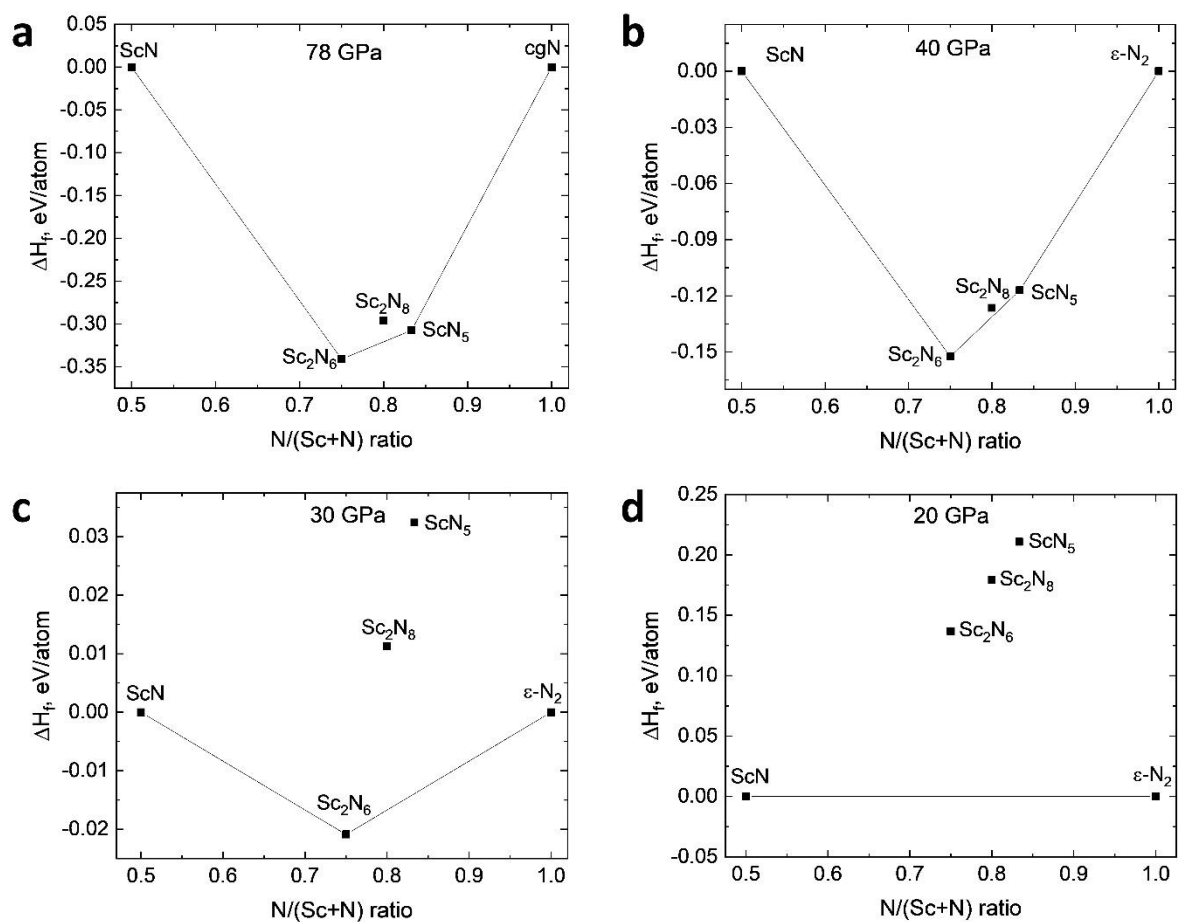
Supplementary Figure 10. Pressure dependence of the unit cell volume for (a) Sc₂N₆, (b) Sc₂N₈, and (c) ScN₅. The black square symbols represent calculated data points obtained from DFT, the red star symbols represent experimental data points obtained from SC-XRD data. The black lines are fits of the DFT data with the 3rd order Birch-Murnaghan equation of state. For Sc₂N₆ and Sc₂N₈ the point at 1 bar was not included in the fit.



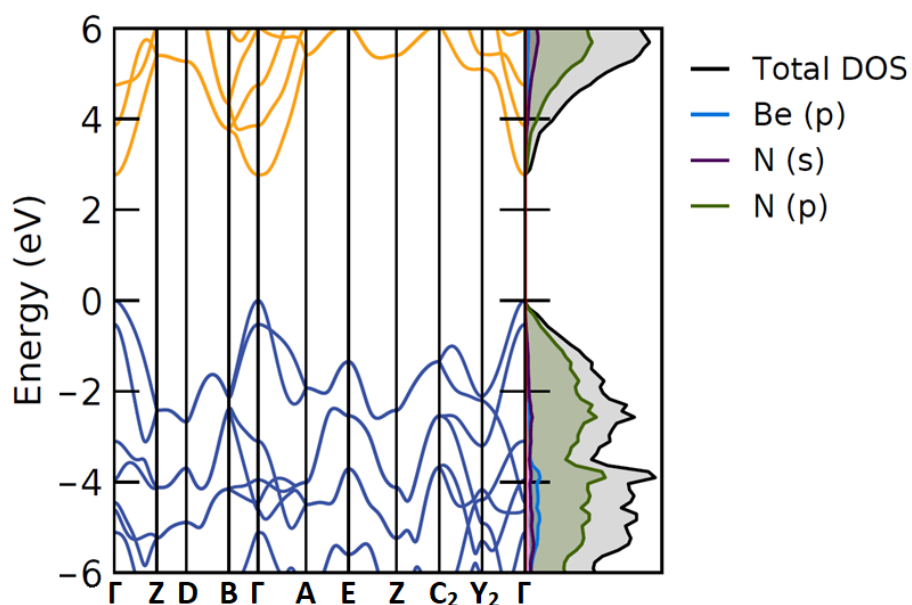
Supplementary Figure 11. (a) Volume per atom for scandium nitrides at 100 GPa. (b) Volume per nitrogen atom for scandium nitrides at 100 GPa. Note: the volume of a scandium atom was considered to be equal, in each phase, to the volume per atom in the scandium metal according to the published equation of state.²



Supplementary Figure 12. (a) Calculated relative formation enthalpies of ScN_5 for various predicted structures (Cm ScN_5 ,³ $P-1$ ScN_5 ,³ $C2/m$ ScN_5 ,⁴ and $P2_1/c$ ScN_5 ,⁵) with respect to $P2_1/m$ ScN_5 synthesized in the present study. (b) The calculated nitrogen-rich part of the convex hull in the Sc-N binary system for known scandium nitrides at 96 GPa. The phases Sc_2N_6 and ScN_5 lie on the convex hull and are thus thermodynamically stable, while Sc_2N_8 is metastable since it is out of the convex hull.



Supplementary Figure 13. The calculated nitrogen-rich part of the convex hull in the Sc-N binary system for known scandium nitrides at (a) 78 GPa, (b) 40 GPa, (c) 30 GPa and (d) 20 GPa



Supplementary Figure 14. The electron density of states of $m\text{-BeN}_4$ ⁶

Supplementary References

1. Rahm, M., Cammi, R., Ashcroft, N. W. & Hoffmann, R. Squeezing All Elements in the Periodic Table: Electron Configuration and Electronegativity of the Atoms under Compression. *J. Am. Chem. Soc.* **141**, 10253–10271 (2019).
2. Fujihisa, H. *et al.* Incommensurate composite crystal structure of scandium-II. *Phys. Rev. B* **72**, 132103 (2005).
3. Aslam, M. A. & Ding, Z. J. Prediction of Thermodynamically Stable Compounds of the Sc-N System under High Pressure. *ACS Omega* **3**, 11477–11485 (2018).
4. Lin, J. *et al.* Stable nitrogen-rich scandium nitrides and their bonding features under ambient conditions. *Phys. Chem. Chem. Phys.* **23**, 6863–6870 (2021).
5. Wei, S. *et al.* A novel high-pressure phase of ScN₅ with higher stability predicted from first-principles calculations. *J. Phys. Condens. Matter* **33**, 475401 (2021).
6. Bykov, M. *et al.* High-Pressure Synthesis of Dirac Materials: Layered van der Waals Bonded BeN₄ Polymorph. *Phys. Rev. Lett.* **126**, 175501 (2021).

5.5. Stabilization of the CN_3^{5-} anion in recoverable high-pressure $\text{Ln}_3\text{O}_2(\text{CN}_3)$ ($\text{Ln} = \text{La, Eu, Gd, Tb, Ho, Yb}$) oxoguanidates

This section contains the following manuscript and the related supplementary material:

“Stabilization of the CN_3^{5-} anion in recoverable high-pressure $\text{Ln}_3\text{O}_2(\text{CN}_3)$ ($\text{Ln} = \text{La, Eu, Gd, Tb, Ho, Yb}$) oxoguanidates,”

A. Aslandukov, P.L. Jurzick, M. Bykov, A. Aslandukova, A. Chanyshv, D. Laniel, Y. Yin, F.I. Akbar, S. Khandarkhaeva, T. Fedotenko, K. Glazirin, S. Chariton, V. Prakapenka, F. Wilhelm, A. Rogalev, D. Comboni, M. Hanfland, N. Dubrovinskaia, L. Dubrovinsky

Status: published in *Angewandte Chemie*, 135(47), e202311516

(2023)

Reproduced under the terms and conditions of the Creative Commons ‘CC BY 4.0’


CN₃ Ions Hot Paper

 How to cite: *Angew. Chem. Int. Ed.* **2023**, *62*, e202311516
doi.org/10.1002/anie.202311516

Stabilization Of The CN₃⁵⁻ Anion In Recoverable High-pressure Ln₃O₂(CN₃) (Ln = La, Eu, Gd, Tb, Ho, Yb) Oxoguanidates

Andrey Aslandukov,* Pascal L. Jurzick, Maxim Bykov, Alena Aslandukova, Artem Chanyshv, Dominique Laniel, Yuqing Yin, Fariia I. Akbar, Saiana Khandarkhaeva, Timofey Fedotenko, Konstantin Glazyrin, Stella Chariton, Vitali Prakapenka, Fabrice Wilhelm, Andrei Rogalev, Davide Comboni, Michael Hanfland, Natalia Dubrovinskaia, and Leonid Dubrovinsky

Abstract: A series of isostructural Ln₃O₂(CN₃) (Ln = La, Eu, Gd, Tb, Ho, Yb) oxoguanidates was synthesized under high-pressure (25–54 GPa) high-temperature (2000–3000 K) conditions in laser-heated diamond anvil cells. The crystal structure of this novel class of compounds was determined via synchrotron single-crystal X-ray diffraction (SCXRD) as well as corroborated by X-ray absorption near edge structure (XANES) measurements and density functional theory (DFT) calculations. The Ln₃O₂(CN₃) solids are composed of the hitherto unknown CN₃⁵⁻ guanidinate anion—deprotonated guanidine. Changes in unit cell volumes and compressibility of Ln₃O₂(CN₃) (Ln = La, Eu, Gd, Tb, Ho, Yb) compounds are found to be dictated by the lanthanide contraction phenomenon. Decompression experiments show that Ln₃O₂(CN₃) compounds are recoverable to ambient conditions. The stabilization of the CN₃⁵⁻ guanidinate anion at ambient conditions provides new opportunities in inorganic and organic synthetic chemistry.

Inorganic ternary metal–C–N compounds with covalently bonded C–N anions encompass important classes of solids. The most investigated classes are cyanides (CN⁻)^[1,2] and carbodiimides (NCN²⁻)^[3–9] although more complex anions (i.e. dicyanamides,^[10,11] tricyanomethanides,^[12] and acetonitriletrifide^[13]) are known. Inorganic cyanides have applications in gold mining, metal finishing, electroplating^[14] and also can be used as reactants or/and catalysts in organic syntheses.^[15] Inorganic carbodiimides exhibit interesting optical properties, making them useful in optoelectronics and photonics^[3–5] and have a potential for energy storage and conversion, e.g. as electrode materials for lithium-ion

batteries, fuel cells, and supercapacitors.^[6–9] While CN⁻ and CN₂²⁻ anions are well-known, the next members of this anionic series—i.e. the CN₃⁵⁻ anion, a derivative of guanidine, and CN₄⁸⁻, a derivative of hypothetical tetraamino-methane—have not been discovered yet, although discussed in the literature.^[16,17]

Here, we present the first stabilization of the CN₃⁵⁻ guanidinate anion in the Ln₃O₂(CN₃) (Ln = La, Eu, Gd, Tb, Ho, Yb) family of compounds. Unexpectedly, these compounds were discovered while studying the polynitride chemistry of rare earth elements. A series of Ln₃O₂(CN₃) oxoguanidates were synthesized at pressures and temper-

[*] A. Aslandukov, A. Aslandukova, Dr. A. Chanyshv, F. I. Akbar, Dr. S. Khandarkhaeva, Prof. L. Dubrovinsky
Bayerisches Geoinstitut, University of Bayreuth
Universitätsstrasse 30, 95440 Bayreuth (Germany)
E-mail: andrii.aslandukov@uni-bayreuth.de

A. Aslandukov, Dr. Y. Yin, Prof. N. Dubrovinskaia
Material Physics and Technology at Extreme Conditions, Laboratory of Crystallography, University of Bayreuth,
Universitätsstrasse 30, 95440 Bayreuth (Germany)

P. L. Jurzick, Dr. M. Bykov
Institute of Inorganic Chemistry, University of Cologne,
Greinstrasse 6, 50939 Cologne (Germany)

Dr. D. Laniel
Centre for Science at Extreme Conditions and School of Physics and Astronomy, University of Edinburgh
EH9 3FD Edinburgh, United Kingdom

Dr. T. Fedotenko, Dr. K. Glazyrin
Deutsches Elektronen-Synchrotron DESY
Notkestrasse 85, 22607 Hamburg (Germany)

Dr. S. Chariton, Prof. V. Prakapenka
Center for Advanced Radiation Sources, University of Chicago
Chicago, Illinois 60637 (USA)

Dr. F. Wilhelm, Dr. A. Rogalev, Dr. D. Comboni, Dr. M. Hanfland
European Synchrotron Radiation Facility
BP 220, 38043 Grenoble Cedex (France)

Prof. N. Dubrovinskaia
Department of Physics, Chemistry and Biology (IFM), Linköping University
SE-581 83 Linköping (Sweden)

© 2023 The Authors. Angewandte Chemie International Edition published by Wiley-VCH GmbH. This is an open access article under the terms of the Creative Commons Attribution License, which permits use, distribution and reproduction in any medium, provided the original work is properly cited.

atures of 25 to 54 GPa and 2000–3000 K, respectively, from molecular nitrogen and metals (La, Gd, Tb, Ho) contaminated by oxygen, as well as from O-contaminated azides $\text{Eu}(\text{N}_3)_2$ and $\text{Yb}(\text{N}_3)_2$ in a laser-heated diamond anvil cell (DAC). The crystal structures of $\text{Ln}_3\text{O}_2(\text{CN}_3)$ oxoguanidates were determined and refined on the basis of single-crystal X-ray diffraction (SCXRD) and corroborated by X-ray absorption near edge structure (XANES) measurements and by density functional theory (DFT) calculations. The family of $\text{Ln}_3\text{O}_2(\text{CN}_3)$ compounds and CN_3^{5-} anion were found to be quenchable to ambient conditions.

Among all synthesized compounds, the best SCXRD data quality was obtained for $\text{La}_3\text{O}_2(\text{CN}_3)$, therefore we will first discuss the crystal structure of $\text{La}_3\text{O}_2(\text{CN}_3)$ and its evolution on decompression and then discuss other $\text{Ln}_3\text{O}_2(\text{CN}_3)$ ($\text{Ln} = \text{Eu}, \text{Gd}, \text{Tb}, \text{Ho}, \text{Yb}$) family members and the trends in their crystal-chemistry.

For the high-pressure high-temperature synthesis of the $\text{La}_3\text{O}_2(\text{CN}_3)$ compound, pieces of lanthanum were loaded in air (leading to the partial oxidization of the metal) into the sample chamber of DACs, the latter then were gas-loaded with molecular nitrogen (see Methods section for details). In two independent experiments, the samples were compressed to 54(1) and 25(1) GPa and laser-heated to 2500(200) K. According to synchrotron SCXRD data, in both experiments the same novel solid, adopting an unexpected $\text{La}_3\text{O}_2(\text{CN}_3)$ composition, was synthesized, and its crystal structure was determined. It was found to have the orthorhombic space group $Pnma$ (#62) and lattice parameters $a = 9.2875(7)$ Å, $b = 6.8259(5)$ Å, $c = 6.149(2)$ Å at 54(1) GPa and $a = 9.795(2)$ Å, $b = 7.0062(11)$ Å, $c = 6.3699(11)$ Å at 25(1) GPa (see Tables S1–S2 and the CIFs for the full crystallographic data^[18]). The carbon atom in $\text{La}_3\text{O}_2(\text{CN}_3)$ comes from the diamond anvil; the latter being able to act as a carbon source and participating in the chemical reactions is well known.^[19–21]

After the $\text{La}_3\text{O}_2(\text{CN}_3)$ synthesis at 54(1) GPa, the sample was decompressed in a few pressure steps down to ambient pressure, when the DAC was opened in air. SCXRD reflections from $\text{La}_3\text{O}_2(\text{CN}_3)$ crystallites could be traced down to ambient conditions and persisted after air exposure (Table S3 and CIF for the full crystallographic data^[18]). Thus, $\text{La}_3\text{O}_2(\text{CN}_3)$ is recoverable to ambient conditions and, at least for some time, resistant to atmospheric oxygen and moisture. One can assume that the presence of O^{2-} anions in the phase plays an important role in its stability at ambient conditions.

Although it is often difficult to distinguish C/N/O atoms in the crystal structure from the SCXRD data, in the present study it was successfully done based on the value of the R_1 agreement factor, the ADPs ratio, interatomic distances, and the charge balance. A detailed justification of the structure model is provided in Supplementary Discussion 1 of the Supporting Information. The structure model was confirmed by supporting DFT calculations using the Vienna ab initio simulation package.^[22] DFT calculations show that the relaxed structural parameters for $\text{La}_3\text{O}_2(\text{CN}_3)$ (Table S4) closely reproduce the corresponding experimental values at 54(1) GPa, as well as at 1 bar. Phonon dispersion relations

calculated in the harmonic approximation show that the $\text{La}_3\text{O}_2(\text{CN}_3)$ phase is dynamically stable at 54 GPa (Figure S1a), as well as at ambient pressure (Figure S1b).

Under high pressure, the elements can behave differently than under ambient conditions, featuring exotic chemistry and unusual oxidation states.^[23–25] Therefore, in this study, to be sure in charge balance considerations, the +3 oxidation state of lanthanum in $\text{La}_3\text{O}_2(\text{CN}_3)$ was confirmed by synchrotron La L_{II} edge XANES measurements at the ID12 beamline at ESRF. The position of the lanthanum white line in $\text{La}_3\text{O}_2(\text{CN}_3)$ matches the white line position of the reference sample (La_2O_3), indicating the same +3 oxidation state of La in these compounds (Figure 1). The structure of $\text{La}_3\text{O}_2(\text{CN}_3)$ (Figure 2a–c) has two La, one C, two N, and two O distinct crystallographic atomic positions. Carbon and nitrogen atoms form planar trigonal CN_3 units (Figure 2d, e), while both oxygen atoms are isolated distinct atoms. O1 atoms are surrounded by six La atoms at the apexes of a distorted octahedron. The O1La₆ octahedra are interconnected with each other by common vertices, forming a three-dimensional framework, whereas the CN_3 triangles and isolated O2 atoms are positioned in the voids between the octahedra (Figure 2b, c).

La1 atoms are coordinated by five N atoms and four O atoms (the coordination number $\text{CN} = 9$, the coordination polyhedron is a distorted capped square antiprism), while La2 atoms are eight-fold coordinated by four N atoms and four O atoms (coordination number $\text{CN} = 8$, the coordination polyhedron is irregular) (Figure S2).

Compared to the $\text{HNC}(\text{NH}_2)_2$ guanidine molecule, which has two types of C–N bonds: two single C–N bonds ($d_{\text{C–N}} = 1.36$ Å) and one double C=N bond ($d_{\text{C–N}} = 1.30$ Å), the deprotonated CN_3^{5-} unit (Figure 2d, e) in $\text{La}_3\text{O}_2(\text{CN}_3)$ has three almost equal C–N bonds indicating the delocalization

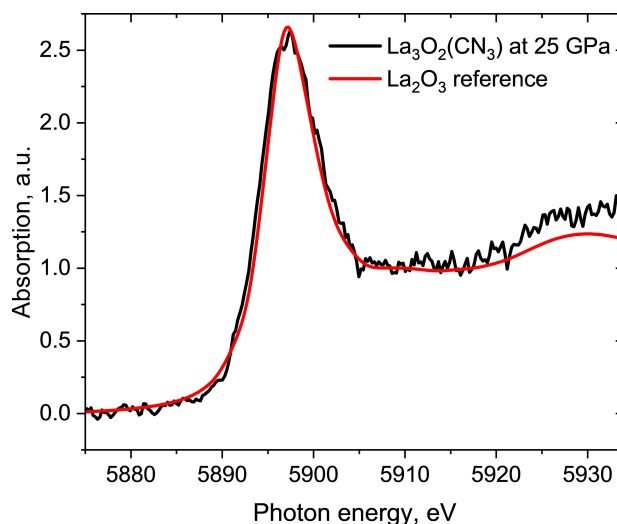


Figure 1. La L_{II} edge XANES spectra of $\text{La}_3\text{O}_2(\text{CN}_3)$ sample at 25 GPa and La_2O_3 reference sample at ambient conditions. The position of white lines is 5897 eV in both spectra. The low signal-to-noise ratio in the spectrum of $\text{La}_3\text{O}_2(\text{CN}_3)$ is because the measurements were carried out in a DAC, and 2 mm-thick diamonds absorb 98% of the X-ray radiation at these energies.

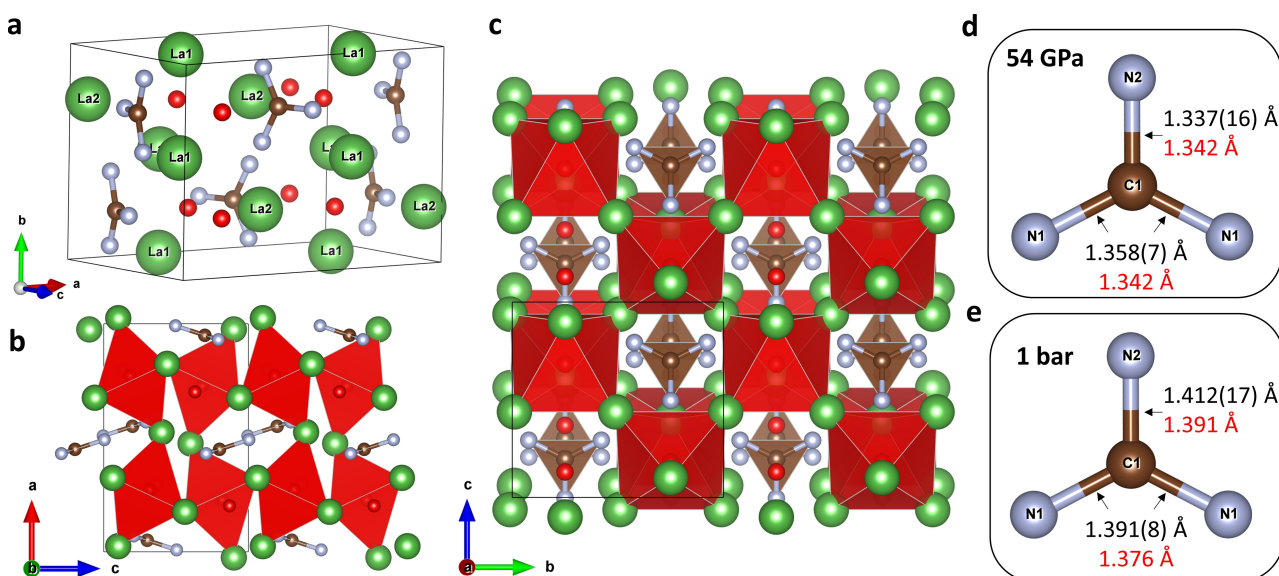


Figure 2. Crystal structure of $\text{La}_3\text{O}_2(\text{CN}_3)$. (a) A general view. (b) A view along the b -axis. (c) A view along the a -axis. (d) CN_3 unit at 54 GPa. (e) CN_3 unit at 1 bar. La atoms are green, C atoms are brown, N atoms are gray, and O atoms are red. Red distorted octahedra correspond to $\text{O}1\text{La}_6$. Thin grey lines outline the unit cell. The bond length values obtained from experiments are shown in black, while those obtained from the DFT calculations are shown in red.

of π -bond. The average length of the C–N bond in CN_3^{5-} at 1 bar is $d_{\text{C-N}} \approx 1.40 \text{ \AA}$, which is longer than an average C–N distance in guanidine ($d_{\text{C-N}} = 1.34 \text{ \AA}$). At the same time, the average length of the C–N bond in CN_3^{5-} at 1 bar is between those of a typical single C–N bond ($d_{\text{C-N}} \approx 1.47 \text{ \AA}$) and a bond of the order of 1.5 (in pyridine $d_{\text{C-N}} = 1.35 \text{ \AA}$), suggesting an expected bond order of 1.33 (Figure 2d). The C–N bond in CN_3^{5-} is longer than C–O and N–O bonds in the well-known trigonal CO_3^{2-} carbonate ($d_{\text{C-O}} = 1.27\text{--}1.29 \text{ \AA}$) and NO_3^- nitrate anions ($d_{\text{N-O}} = 1.24\text{--}1.26 \text{ \AA}$) at 1 bar, respectively.

There are known at ambient conditions quaternary Ln–C–N–O compounds with a stable stoichiometry $\text{Ln}_2\text{O}_2\text{CN}_2$: $I4/mmm\text{-La}_2\text{O}_2\text{CN}_2$ ^[26] and $P\text{-}3m1\text{-Ln}_2\text{O}_2(\text{CN}_2)$ (Ln = Ce, Pr, Nd, Sm, Eu, Gd, Dy, Ho, Er, Tm, Yb).^[27,28] The crystal structures of $\text{Ln}_2\text{O}_2\text{CN}_2$ compounds consist of $\text{Ln}_2\text{O}_2^{2+}$ layers and linear CN_2^{2-} anions at the interlayer positions oriented whether along^[26] or perpendicular^[27,28] to the layers. Thus, the structure motif of $\text{Ln}_2\text{O}_2\text{CN}_2$ compounds completely differs from those of $\text{La}_3\text{O}_2(\text{CN}_3)$.

The crystal structure of the $\text{La}_3\text{O}_2(\text{CN}_3)$ compound has similarities with that of the $\text{La}_3(\text{SiN}_3\text{O})\text{O}$ oxonitridosilicate^[29] (Figure 3a, b). Both structures are based on OLA_6 octahedra framework. While Si atoms form $[\text{SiN}_3\text{O}]^{7-}$ tetrahedra in $\text{La}_3(\text{SiN}_3\text{O})\text{O}$, carbon atoms in $\text{La}_3\text{O}_2(\text{CN}_3)$ prefer a trigonal coordination, and the (CN_3O) ensemble of atoms thereby exists as a CN_3^{5-} unit and a distinct O^{2-} anion (Figure 3c, d).

The calculated electron localization function for $\text{La}_3\text{O}_2(\text{CN}_3)$ confirms the expected covalent bonding between carbon and nitrogen atoms within the CN_3 units (Figure 4a). There is no electron localization between C1 and O2 atoms (Figure 4b) that corroborates the absence of covalent interactions between the CN_3 unit and the O2

atom, and thus there is no CN_3O tetrahedron in the studied material. A reason for that important difference in the crystal chemistry of carbon and silicon is the smaller radius of carbon, which therefore prefers a lower coordination number than its group neighbor silicon at ambient conditions. It is a well-known difference between carbonates and silicates at ambient conditions: carbon forms trigonal CO_3^{2-} groups, while silicon prefers SiO_4 tetrahedra. Only under sufficient compression (at least to 20 GPa) carbon starts to behave like silicon and form CO_4^{4-} tetrahedral anions.^[30–34] The recent high-pressure high-temperature synthesis of C_3N_4 polymorphs^[21] shows that, above 70 GPa, CN_4 tetrahedra can also be formed. Our experimental results demonstrate that 54 GPa is not a sufficient pressure for the formation of tetra-coordinated carbon with C–N bonds. However, one can expect the stabilization of CN_4^{8-} units or/and the formation of polycarbonitrides built of corner/edge-sharing CN_4 tetrahedra in ternary M–C–N systems at pressures above 70 GPa.

The structure evolution and compressibility of $\text{La}_3\text{O}_2(\text{CN}_3)$ were studied experimentally upon the decompression from 54(1) GPa down to 1 bar, as well as using DFT by variable-cell structure relaxation in the pressure range of 0 to 100 GPa. The lattice parameters and unit cell volume of $\text{La}_3\text{O}_2(\text{CN}_3)$ extracted from the SCXRD data collected upon the decompression are closely reproduced by DFT (Figure 5).

The evolution of the a , b , and c lattice parameters (Figure 5a) shows an anisotropic response of $\text{La}_3\text{O}_2(\text{CN}_3)$ to pressure: its compressibility along the three main directions increases in the following order: $a > c > b$ (it is also clear from the evolution of the a/a_0 , b/b_0 , c/c_0 ratio with pressure, Figure S3). One can explain the greater compressibility along the a direction due to the larger spacing between

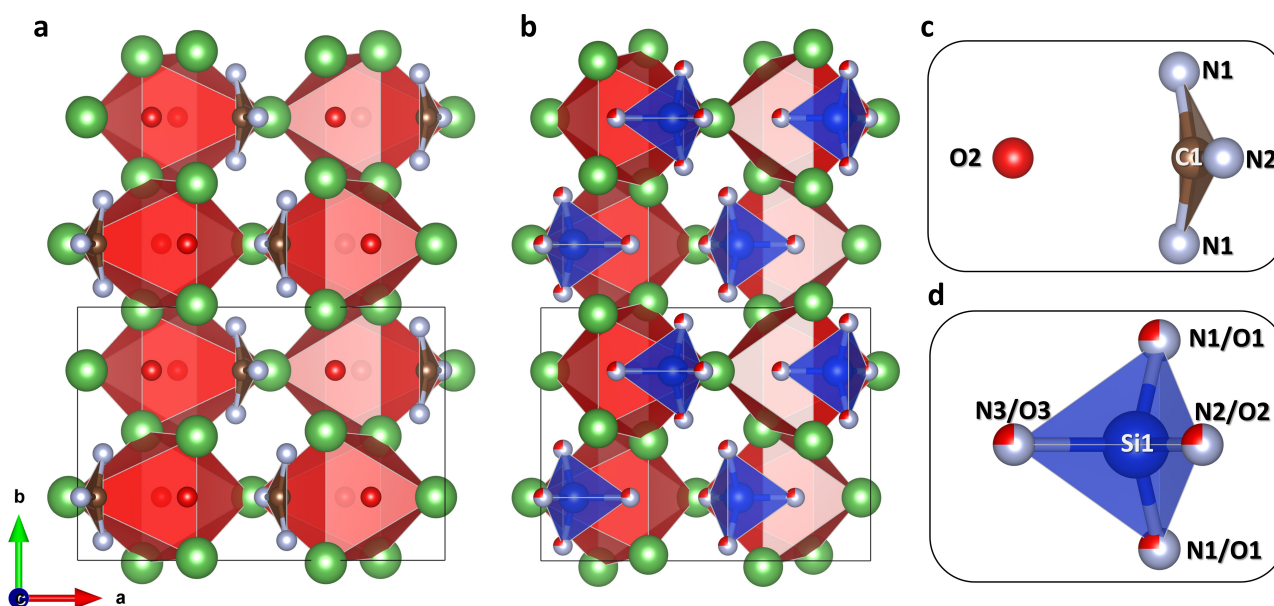


Figure 3. Comparison of the structures of $\text{La}_3\text{O}_2(\text{CN}_3)$ and $\text{La}_3(\text{SiN}_3\text{O})\text{O}$ oxonitridosilicate. (a) Crystal structure of $\text{La}_3\text{O}_2(\text{CN}_3)$ viewed along the c -axis. (b) Crystal structure of $\text{La}_3(\text{SiN}_3\text{O})\text{O}^{[29]}$ viewed along the c -axis. (c) and (d) The arrangements of CN_3O and SiN_3O ensembles of atoms in both compounds. La atoms are green, C atoms are brown, N atoms are gray, O atoms are red, and Si atoms are blue. Red distorted octahedra correspond to O1La_6 octahedra. Thin grey lines outline the unit cell.

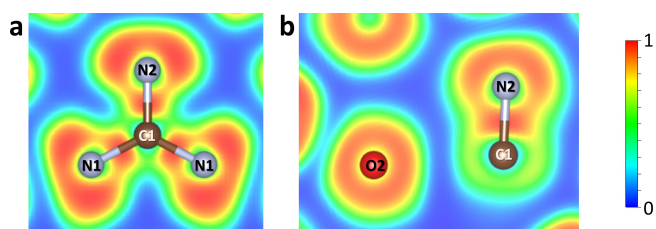


Figure 4. Cross sections of the electron localization function calculated for $\text{La}_3\text{O}_2(\text{CN}_3)$. (a) In the plane of a CN_3^{5-} unit. (b) In the (010) plane containing C1, N2, and O2 atoms.

O1La_6 octahedra in that direction (Figure 1b). The coordination numbers and coordination polyhedra of La1 and La2 atoms do not change in the studied pressure range.

The fitting of the $\text{La}_3\text{O}_2(\text{CN}_3)$ experimental pressure-volume data with a 2nd order Birch-Murnaghan equation of state yields a bulk modulus of $K_0 = 146(3)$ GPa ($V_0 = 493.95 \text{ \AA}^3$ was fixed), a value that agrees well with the bulk modulus $K_0 = 139.1(5)$ GPa ($V_0 = 498.16 \text{ \AA}^3$ was fixed) obtained by fitting the pressure-volume points of $\text{La}_3\text{O}_2(\text{CN}_3)$ DFT-relaxed structures from 0 to 100 GPa with the 2nd order Birch-Murnaghan equation of state (Figure 5b).

The synthesis of the other $\text{Ln}_3\text{O}_2(\text{CN}_3)$ ($\text{Ln} = \text{Eu}, \text{Gd}, \text{Tb}, \text{Ho}, \text{Yb}$) family members was done under similar high-pressure high-temperature conditions (pressures of 25 to 54 GPa and temperatures of 2000–3000 K) from partially oxidized metals (Gd, Tb, Ho) and nitrogen as well as from oxygen-contaminated azides $\text{Eu}(\text{N}_3)_2$ and $\text{Yb}(\text{N}_3)_2$ in a laser-heated DAC (Table S1). The crystal structures of $\text{Ln}_3\text{O}_2(\text{CN}_3)$ ($\text{Ln} = \text{Eu}, \text{Gd}, \text{Tb}, \text{Ho}, \text{Yb}$) oxoguanidates were also determined based on SCXRD (Tables S6–S13).

The fact that $\text{Ln}_3\text{O}_2(\text{CN}_3)$ phases were obtained for different lanthanides at different pressures and from different precursors demonstrates the stability of such a structure type and chemical composition.

It should be noted that contrary to the case of $\text{La}_3\text{O}_2(\text{CN}_3)$, the crystal structure refinements for $\text{Ln}_3\text{O}_2(\text{CN}_3)$ ($\text{Ln} = \text{Eu}, \text{Gd}, \text{Tb}, \text{Ho}, \text{Yb}$) indicate a possible splitting of the C1 atom between two crystallographic positions (see Supplementary Discussion 2). While models with split C1 atom position resulted in a slightly lower R_1 agreement factor, we cannot exclude that this is an artifact of the limited quality of X-ray diffraction data collected in the DACs. The investigation of this phenomenon requires additional studies. Here we will consider the structure models without splitting for all $\text{Ln}_3\text{O}_2(\text{CN}_3)$ ($\text{Ln} = \text{Eu}, \text{Gd}, \text{Tb}, \text{Ho}, \text{Yb}$) compounds.

The structural evolution of these compounds with pressure was also studied by DFT calculations (Figures S4–S8). For $\text{Tb}_3\text{O}_2(\text{CN}_3)$ and $\text{Ho}_3\text{O}_2(\text{CN}_3)$, the decompression down to 1 bar was done, and the experimentally observed P – V dependence is well-reproduced by DFT calculations (Figs. S6 and S7). For $\text{Ln} = \text{Gd}, \text{Tb}, \text{Ho}$ the recoverability of the synthesized compounds was examined, and they were found to be recoverable, just like $\text{La}_3\text{O}_2(\text{CN}_3)$ (Tables S7, S10, and S12). The volume of the $\text{Ln}_3\text{O}_2(\text{CN}_3)$ unit cell at the same pressure decreases when going through the sequence $\text{La} \rightarrow \text{Eu} \rightarrow \text{Gd} \rightarrow \text{Tb} \rightarrow \text{Ho} \rightarrow \text{Yb}$, as expected due to the lanthanide contraction (Figure 6a). Moreover, the correlation between the unit cell volume and ionic radii³ is linear, which is similar to known classes of lanthanide compounds (e.g. nitrides, Figure S9).

The behavior of the CN_3^{5-} anion under compression was investigated both experimentally and theoretically for all

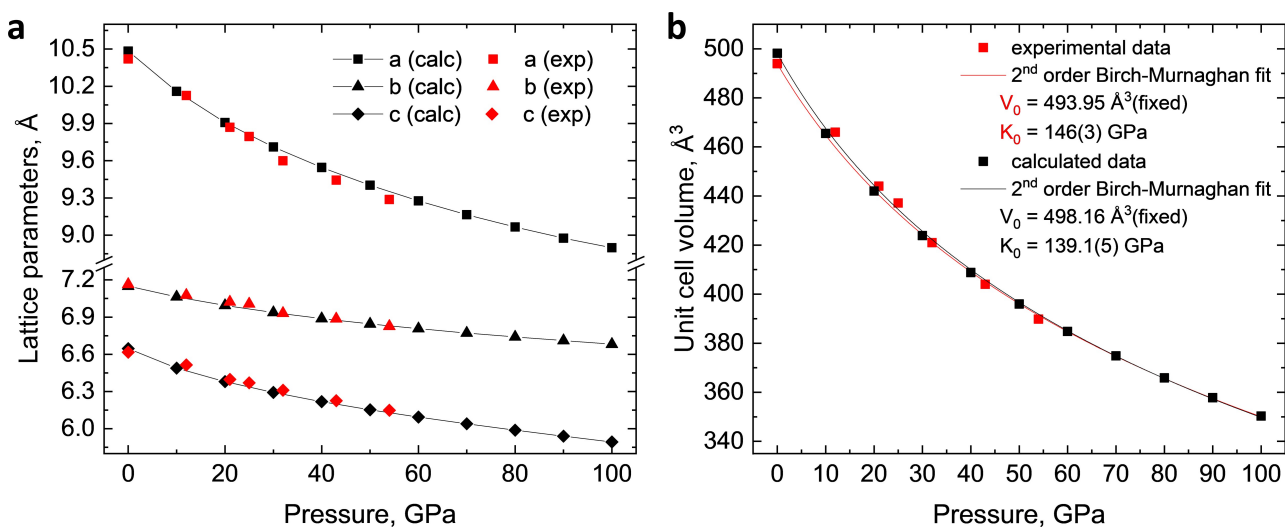


Figure 5. Compressional behavior of the La₃O₂(CN₃) structure. (a) Experimental (red squares, triangles, and diamonds) and calculated (black squares, triangles, and diamonds) pressure dependence of the La₃O₂(CN₃) lattice parameters. (b) Experimental (red squares) and calculated (black squares) pressure dependence of the La₃O₂(CN₃) unit cell volume and the fit of the experimental P–V data (red curve) using a 2nd order Birch-Murnaghan equation of state. Errors in the experimental data are within the symbol size. The calculated P–V data also can be fitted using the 3rd order Birch-Murnaghan equation of state, yielding *K*₀ = 131.3(9) GPa, *K*' = 4.36(4) with fixed *V*₀ = 498.16 Å³.

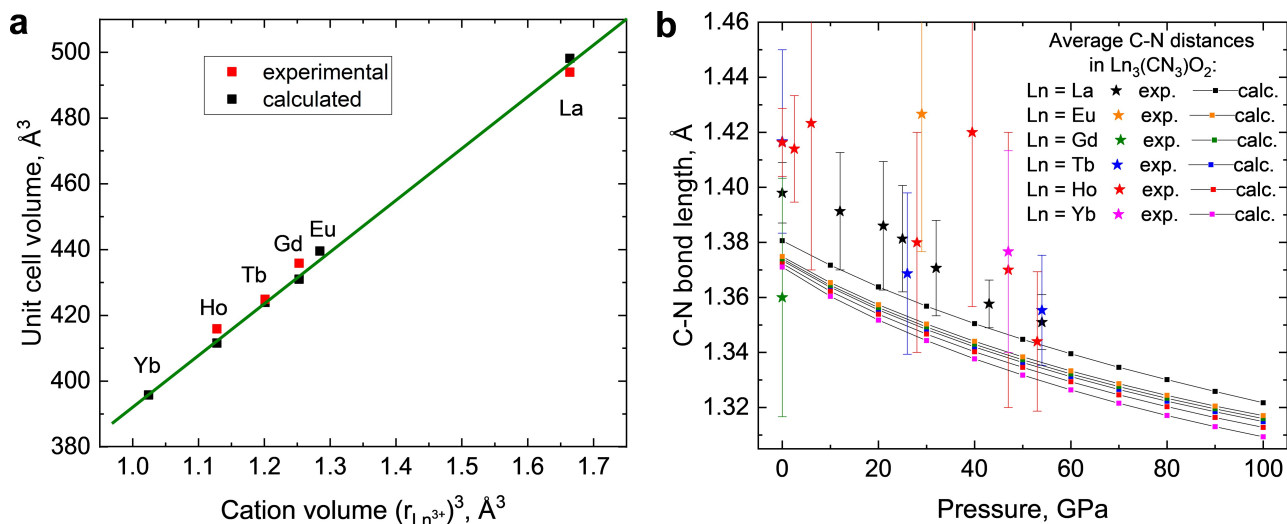


Figure 6. Comparison of crystallographic characteristics of the studied Ln₃O₂(CN₃) compounds at 1 bar and in the range up to 100 GPa. (a) The volume of the Ln₃O₂(CN₃) unit cell at 1 bar versus the volume of lanthanide ion (ionic radii are taken from <http://abulafia.mt.ic.ac.uk/shannon/ptable.php> (original reference^[35]) for CN = 8). (b) The average C–N bond length within the CN₃⁵⁻ unit in Ln₃O₂(CN₃) (Ln = La, Eu, Gd, Tb, Ho, Yb) at different pressures.

Ln₃O₂(CN₃) (Ln = La, Eu, Gd, Tb, Ho, Yb) phases (Figure 6b). Due to significant uncertainties in C–N distances extracted from the experimental data, no remarkable differences in the C–N bond lengths dependent on a lanthanide cation at the same pressure was noted, but there is a general trend of a small decrease of the C–N bond length upon compression. The analysis of theoretical data provides a more resolved picture: regardless of a cation, C–N bonds become shorter by ≈ 0.04 Å upon compression from 1 bar to 100 GPa, and furthermore, a small and monotonous contraction of the C–N bond length in CN₃⁵⁻ is noted when going from lanthanum to ytterbium. At the same time, metal-

nonmetal distances change significantly depending on both the pressure and the cation (Figure S10), indicating that the decrease in the unit cell volume is primarily attributed to the decrease in the volume of the Ln coordination polyhedra. Due to this reason, the calculated bulk moduli of Ln₃O₂(CN₃) solids decrease along the Ln = La–Eu–Gd–Tb–Ho–Yb lanthanide row (Table S14, Figure S11).

To conclude, a series of recoverable Ln₃O₂(CN₃) (Ln = La, Eu, Gd, Tb, Ho, Yb) oxoguanidates was synthesized under high-pressure high-temperature conditions. The fact that the Ln₃O₂(CN₃) phases were obtained for different

lanthanides, under different pressures, and from different precursors, demonstrates the stability of such a structure type and chemical composition. Despite the significant difference in ionic radii of La^{3+} and Yb^{3+} , all studied $\text{Ln}_3\text{O}_2(\text{CN}_3)$ compounds are isostructural and the only difference in their crystal chemistry is the unit cell volumes and interatomic distances decreasing due to the lanthanides' contraction. The lanthanide contraction also dictates the slight decrease in compressibility of $\text{Ln}_3\text{O}_2(\text{CN}_3)$ compounds going from $\text{Ln}=\text{La}$ to $\text{Ln}=\text{Yb}$. These solids all feature the hitherto unknown CN_3^{5-} guanidinate anion—i.e. deprotonated guanidine. This discovery extends the list of carbon-nitrogen inorganic anions and may open up new synthesis routes in inorganic and organic chemistry. Also, based on the analysis of carbon crystal-chemical behavior under pressure and its comparison with silicon crystal chemistry, one can expect the stabilization of currently unknown CN_4^{8-} unit or/and formation of polycarbonitrides built of corner/edge-sharing CN_4 tetrahedra in ternary M–C–N systems at pressures above 70 GPa.

Note: At the same time, the high-pressure synthesis of SbCN_3 antimony nitridocarbonate was carried out by another group,^[36] which demonstrates the universality of a high-pressure approach for the stabilization of CN_3^{5-} guanidinate anion.

Acknowledgements

The authors thank Prof. Björn Winkler for useful discussions. The authors acknowledge the Deutsches Elektronen-Synchrotron (DESY, PETRA III) for the provision of beamtime at the P02.2 beamline, the European Synchrotron Radiation Facility (ESRF) for the provision of beamtime at the ID15b and ID12 beamlines. Portions of this work were performed at GeoSoilEnviroCARS (The University of Chicago, Sector 13), Advanced Photon Source (APS), Argonne National Laboratory. GeoSoilEnviroCARS is supported by the National Science Foundation – Earth Sciences (EAR – 1634415). This research used resources of the Advanced Photon Source, a U.S. Department of Energy (DOE) Office of Science User Facility operated for the DOE Office of Science by Argonne National Laboratory under Contract No. DE-AC02-06CH11357. Computations were performed at the Leibniz Supercomputing Center of the Bavarian Academy of Sciences and the Humanities, and the research center for scientific computing at the University of Bayreuth. M.B. acknowledges the support of Deutsche Forschungsgemeinschaft (DFG Emmy-Noether project BY112/2-1). D.L. thanks the UKRI Future Leaders Fellowship (MR/V025724/1) for financial support. N.D. and L.D. thank the Deutsche Forschungsgemeinschaft (DFG projects DU 954-11/1, DU 393-9/2, DU 393-13/1; DU 945/15-1) for financial support. N.D. also thanks the Swedish Government Strategic Research Area in Materials Science on Functional Materials at Linköping University (Faculty Grant SFO-Mat-LiU No. 2009 00971). For the purpose of open access, the authors have applied a Creative Commons Attribution (CC BY) license to any Author Accepted Manuscript version

arising from this submission. Open Access funding enabled and organized by Projekt DEAL.

Conflict of Interest

The authors declare no conflict of interest.

Data Availability Statement

The data that support the findings of this study are available in the supplementary material of this article. Additional references are cited within the Supporting Information.^[37-60]

Keywords: Diamond Anvil Cell · Guanidinate · High Pressure · Lanthanides · Single-Crystal X-Ray Diffraction

- [1] B. M. Chadwick, A. G. Sharpe, *Rev. Inorg. Chem.* **1966**, pp. 83–176.
- [2] A. Schulz, J. Surkau, *Rev. Inorg. Chem.* **2023**, *43*, 49–188.
- [3] C. Braun, L. Mereacre, W. Hua, T. Stürzer, I. Ponomarev, P. Kroll, A. Slabon, Z. Chen, Y. Damour, X. Rocquefelte, J. Halet, S. Indris, *ChemElectroChem* **2020**, *7*, 4550–4561.
- [4] M. Kubus, C. Castro, D. Enselsing, T. Jüstel, *Opt. Mater.* **2016**, *59*, 126–129.
- [5] Q. Liu, Y. Liu, G. Dai, L. Tian, J. Xu, G. Zhao, N. Zhang, Y. Fang, *Appl. Surf. Sci.* **2015**, *357*, 745–749.
- [6] M. T. Sougrati, A. Darwiche, X. Liu, A. Mahmoud, R. P. Hermann, S. Jouen, L. Monconduit, R. Dronskowski, L. Stievano, *Angew. Chem. Int. Ed.* **2016**, *55*, 5090–5095.
- [7] A. Eguía-Barrio, E. Castillo-Martínez, X. Liu, R. Dronskowski, M. Armand, T. Rojo, *J. Mater. Chem. A* **2016**, *4*, 1608–1611.
- [8] K. Chen, M. Fehse, A. Laurita, J. J. Arayamparambil, M. T. Sougrati, L. Stievano, R. Dronskowski, *Angew. Chem. Int. Ed.* **2020**, *59*, 3718–3723.
- [9] M. T. Sougrati, J. J. Arayamparambil, X. Liu, M. Mann, A. Slabon, L. Stievano, R. Dronskowski, *Dalton Trans.* **2018**, *47*, 10827–10832.
- [10] B. Jürgens, E. Irran, W. Schnick, *J. Solid State Chem.* **2001**, *157*, 241–249.
- [11] B. Jürgens, E. Irran, W. Schnick, *J. Solid State Chem.* **2005**, *178*, 72–78.
- [12] K. E. Bessler, C. C. Gatto, M. J. de, A. Sales, L. L. Romualdo, J. A. Ellena, *Main Group Met. Chem.* **2007**, *30*, 135–142.
- [13] W. P. Clark, A. Köhn, R. Niewa, *Angew. Chem. Int. Ed.* **2020**, *59*, 339–342.
- [14] R. R. Dash, A. Gaur, C. Balomajumder, *J. Hazard. Mater.* **2009**, *163*, 1–11.
- [15] D. Kieslich, J. Christoffers, *Synthesis* **2021**, *53*, 3485–3496.
- [16] D. Luo, X. Qiao, R. Dronskowski, *Angew. Chem. Int. Ed.* **2021**, *60*, 486–492.
- [17] O. A. Gapurenko, T. N. Griбанова, R. M. Minyaev, V. I. Minkin, *Russ. J. Org. Chem.* **2007**, *43*, 685–690.
- [18] Deposition numbers 2286275, 2286276, and 2286277 contain the supplementary crystallographic data for this paper. These data are provided free of charge by the joint Cambridge Crystallographic Data Centre and Fachinformationszentrum Karlsruhe Access Structures service.
- [19] Y. Yin, F. I. Akbar, E. Bykova, A. Aslandukova, D. Laniel, A. Aslandukov, M. Bykov, M. Hanfland, G. Garbarino, Z. Jia, L. Dubrovinsky, N. Dubrovinskaia, *Commun. Chem.* **2022**, *5*, 122.

- [20] F. I. Akbar, A. Aslandukova, A. Aslandukov, Y. Yin, F. Trybel, S. Khandarkhaeva, T. Fedotenko, D. Laniel, M. Bykov, E. Bykova, N. Dubrovinskaia, L. Dubrovinsky, *Front. Chem.* **2023**, *11*, 1210081.
- [21] D. Laniel, F. Trybel, A. Aslandukov, S. Khandarkhaeva, T. Fedotenko, Y. Yin, F. Tasnádi, A. V. Ponomareva, G. Weck, F. I. Akbar, B. Winkler, A. Néri, S. Chariton, C. Giacobbe, J. Wright, G. Garbarino, B. Wehinger, A. Pakhomova, M. Mezouar, V. Prakapenka, V. Milman, W. Schnick, I. A. Abrikosov, L. Dubrovinsky, N. Dubrovinskaia, *Adv. Mater.* **2023**, <https://doi.org/10.1002/adma.202308030>.
- [22] G. Kresse, J. Furthmüller, *Comput. Mater. Sci.* **1996**, *6*, 15–50.
- [23] W. Grochala, R. Hoffmann, J. Feng, N. W. Ashcroft, *Angew. Chem. Int. Ed.* **2007**, *46*, 3620–3642.
- [24] M. Miao, Y. Sun, E. Zurek, H. Lin, *Nat. Chem. Rev.* **2020**, *4*, 508–527.
- [25] M. Rahm, R. Cammi, N. W. Ashcroft, R. Hoffmann, *J. Am. Chem. Soc.* **2019**, *141*, 10253–10271.
- [26] Y. Hashimoto, M. Takahashi, S. Kikkawa, F. Kanamaru, *J. Solid State Chem.* **1995**, *114*, 592–594.
- [27] Y. Hashimoto, M. Takahashi, S. Kikkawa, F. Kanamaru, *J. Solid State Chem.* **1996**, *125*, 37–42.
- [28] M. Li, W. Yuan, J. Wang, C. Gu, H. Zhao, *Powder Diffr.* **2007**, *22*, 59–63.
- [29] D. Durach, W. Schnick, *Eur. J. Inorg. Chem.* **2015**, 4095–4100.
- [30] V. Cerantola, E. Bykova, I. Kupaenko, M. Merlini, L. Ismailova, C. McCammon, M. Bykov, A. I. Chumakov, S. Petitgirard, I. Kantor, V. Svitlyk, J. Jacobs, M. Hanfland, M. Mezouar, C. Prescher, R. Rüffer, V. B. Prakapenka, L. Dubrovinsky, *Nat. Commun.* **2017**, *8*, 15960.
- [31] D. Laniel, J. Binck, B. Winkler, S. Vogel, T. Fedotenko, S. Chariton, V. Prakapenka, V. Milman, W. Schnick, L. Dubrovinsky, N. Dubrovinskaia, *Acta Crystallogr. Sect. B* **2021**, *77*, 131–137.
- [32] D. Spahr, J. Binck, L. Bayarjargal, R. Luchitskaia, W. Morgenroth, D. Comboni, V. Milman, B. Winkler, *Inorg. Chem.* **2021**, *60*, 5419–5422.
- [33] J. Binck, D. Laniel, L. Bayarjargal, S. Khandarkhaeva, T. Fedotenko, A. Aslandukov, K. Glazyrin, V. Milman, S. Chariton, V. B. Prakapenka, N. Dubrovinskaia, L. Dubrovinsky, B. Winkler, *Am. Mineral.* **2022**, *107*, 336–342.
- [34] P. N. Gavryushkin, N. S. Martirosyan, S. V. Rashchenko, D. N. Sagatova, N. E. Sagatov, A. I. Semerikova, T. M. Fedotenko, K. D. Litasov, *JETP Lett.* **2022**, *116*, 477–484.
- [35] R. D. Shannon, *Acta Crystallogr. Sect. A* **1976**, *32*, 751–767.
- [36] L. Brüning, N. Jena, E. Bykova, P. L. Jurzick, N. T. Flosbach, M. Mezouar, M. Hanfland, N. Giordano, T. Fedotenko, B. Winkler, I. A. Abrikosov, M. Bykov, *Angew. Chem. Int. Ed.* **2023**, *62*, e202311519.
- [37] I. Kantor, V. Prakapenka, A. Kantor, P. Dera, A. Kurnosov, S. Sinogeikin, N. Dubrovinskaia, L. Dubrovinsky, *Rev. Sci. Instrum.* **2012**, *83*, 125102.
- [38] R. Boehler, *Rev. Sci. Instrum.* **2006**, *77*, 2004–2007.
- [39] A. Kurnosov, I. Kantor, T. Boffa-Ballaran, S. Lindhardt, L. Dubrovinsky, A. Kuznetsov, B. H. Zehnder, *Rev. Sci. Instrum.* **2008**, *79*, 045110.
- [40] G. Aprilis, C. Strohm, I. Kupaenko, S. Linhardt, A. Laskin, D. M. Vasiukov, V. Cerantola, E. G. Koemets, C. McCammon, A. Kurnosov, A. I. Chumakov, R. Rüffer, N. Dubrovinskaia, L. Dubrovinsky, *Rev. Sci. Instrum.* **2017**, *88*, 084501.
- [41] T. Fedotenko, L. Dubrovinsky, G. Aprilis, E. Koemets, A. Snigirev, I. Snigireva, A. Barannikov, P. Ershov, F. Cova, M. Hanfland, N. Dubrovinskaia, *Rev. Sci. Instrum.* **2019**, *90*, 104501.
- [42] Y. Akahama, H. Kawamura, *J. Appl. Phys.* **2006**, *100*, 043516.
- [43] S. Anzellini, A. Dewaele, F. Occelli, P. Loubeyre, M. Mezouar, *J. Appl. Phys.* **2014**, *115*, 043511.
- [44] *Rigaku Oxford Diffraction, CrysAlisPro Software (2015)*. **2015**, DOI 10.1063/1.2372734.
- [45] A. Aslandukov, M. Aslandukov, N. Dubrovinskaia, L. Dubrovinsky, *J. Appl. Crystallogr.* **2022**, *55*, 1383–1391.
- [46] O. V. Dolomanov, L. J. Bourhis, R. J. Gildea, J. A. K. Howard, H. Puschmann, *J. Appl. Crystallogr.* **2009**, *42*, 339–341.
- [47] V. Petríček, M. Dušek, L. Palatinus, *Zeitschrift für Krist.* **2014**, *229*, 345–352.
- [48] G. M. Sheldrick, *Acta Crystallogr. Sect. C Struct. Chem.* **2015**, *71*, 3–8.
- [49] K. Momma, F. Izumi, *J. Appl. Crystallogr.* **2011**, *44*, 1272–1276.
- [50] J. Gonzalez-Platas, M. Alvaro, F. Nestola, R. Angel, *J. Appl. Crystallogr.* **2016**, *49*, 1377–1382.
- [51] G. Kresse, J. Furthmüller, *Phys. Rev. B* **1996**, *54*, 11169–11186.
- [52] G. Kresse, D. Joubert, *Phys. Rev. B - Condens. Matter Mater. Phys.* **1999**, *59*, 1758–1775.
- [53] J. P. Perdew, K. Burke, M. Ernzerhof, *Phys. Rev. Lett.* **1996**, *77*, 3865–3868.
- [54] A. Togo, I. Tanaka, *Scr. Mater.* **2015**, *108*, 1–5.
- [55] S. Yu, B. Huang, Q. Zeng, A. R. Oganov, L. Zhang, G. Frapper, *J. Phys. Chem. C* **2017**, *121*, 11037–11046.
- [56] S. Wei, D. Li, Z. Liu, X. Li, F. Tian, D. Duan, B. Liu, T. Cui, *Phys. Chem. Chem. Phys.* **2017**, *19*, 9246–9252.
- [57] Y. Chen, X. Cai, H. Wang, H. Wang, H. Wang, *Sci. Rep.* **2018**, *8*, 10670.
- [58] X. Shi, Z. Yao, B. Liu, *J. Phys. Chem. C* **2020**, *124*, 4044–4049.
- [59] X. Du, Y. Yao, J. Wang, Q. Yang, G. Yang, *J. Chem. Phys.* **2021**, *154*, 054706.
- [60] W. C. Hamilton, *Acta Crystallogr.* **1965**, *18*, 502–510.

Manuscript received: August 8, 2023

Accepted manuscript online: September 28, 2023

Version of record online: October 16, 2023

Supporting Information

Stabilization Of The CN_3^{5-} Anion In Recoverable High-pressure $\text{Ln}_3\text{O}_2(\text{CN}_3)$ (Ln = La, Eu, Gd, Tb, Ho, Yb) Oxoguanidates

A. Aslandukov, P. L. Jurzick, M. Bykov, A. Aslandukova, A. Chanyshv, D. Laniel, Y. Yin, F. I. Akbar, S. Khandarkhaeva, T. Fedotenko, K. Glazyrin, S. Chariton, V. Prakapenka, F. Wilhelm, A. Rogalev, D. Comboni, M. Hanfland, N. Dubrovinskaia, L. Dubrovinsky*

Methods

Sample preparation. The BX90-type large X-ray aperture diamond anvil cells^[1] equipped with Boehler-Almax type diamonds^[2] (culet diameter is 250 μm) were used in the experiments. The sample chamber was formed by pre-indenting a rhenium gasket to 20–25 μm thickness and drilling a hole of 110–125 μm in diameter in the center of the indentation. The pieces of lanthanides (La, Gd, Tb, Ho) (99.9%, ChemPur or smart-elements) were placed in the sample chambers of individual DACs in air, then molecular nitrogen was loaded using a high-pressure gas loading system (1300 bars)^[3]. The metal pieces were exposed to air during the loading into DAC. The exposure time depends on the loading but always was between 20 min and 1 hour. The investigation of the metal pieces exposed to air for 20 min by powder XRD at a home diffractometer showed that corresponding rare-earth oxides were detectable in the powder pattern at the level of ~3–5wt%. This is an estimation of minimal contamination by oxides. The sample chambers of another two DACs were loaded with solid $\text{Eu}(\text{N}_3)_2$ and $\text{Yb}(\text{N}_3)_2$ compounds, whose syntheses will be described elsewhere, in the glovebox. The samples were compressed to target pressure (Table S1) and laser-heated ($\lambda = 1064 \text{ nm}$) to 2000–3000 K using double-sided laser-heating systems BGI (University of Bayreuth, Bayreuth, Germany)^[4,5] or of P02.2 beamline (Petra III, DESY, Hamburg, Germany). The temperature during laser heating was determined by the blackbody radiation fit. The initial pressure in the sample chambers, as well as pressure upon the decompression of some of the cells, was determined by the Raman signal from the diamond anvils^[6] and additionally monitored by the diffraction of Re gasket edge using the equation of state of Re.^[7]

X-ray diffraction. The X-ray diffraction studies were done at the P02.2 beamline of Petra III, DESY ($\lambda = 0.2904 \text{ \AA}$ or 0.2905 \AA depending on the experiment); ID15b beamline ($\lambda = 0.4104 \text{ \AA}$) of the Extreme Brilliant Source European Synchrotron Radiation Facility (EBS-ESRF); as well as at the GSECARS 13IDD beamline of the APS ($\lambda = 0.2952 \text{ \AA}$). At P02.2 beamline of DESY the X-ray beam was focused down to $2 \times 2 \mu\text{m}^2$ and data was collected with a PerkinElmer 1621 XRD flat-panel detector. At ID15b beamline of ESRF the X-ray beam was focused down to $3 \times 3 \mu\text{m}^2$ and data was collected with Eiger2X CdTe 9M hybrid photon counting pixel detector. At 13IDD beamline of APS the X-ray beam was focused down to $2 \times 2 \mu\text{m}^2$ and data was collected with Pilatus 1M detector. In order to determine the position of the polycrystalline sample on which the single-crystal X-ray diffraction acquisition is obtained, a full X-ray diffraction mapping of the pressure chamber was achieved. The sample position displaying the most and the strongest single-crystal reflections belonging to the phase of interest was chosen for the collection of single-crystal data, collected in step-scans of 0.5° from -36° to $+36^\circ$. The CrysAlis^{Pro} software package^[8] was used for the analysis of the single-crystal XRD data (peak hunting, indexing, data integration, frame scaling, and absorption correction). To calibrate an instrumental model in the CrysAlis^{Pro} software, i.e., the sample-to-detector distance, detector's origin, offsets of the goniometer angles, and rotation of both the X-ray beam and detector around the instrument axis, we used a single crystal of orthoenaite [(Mg_{1.93}Fe_{0.06})(Si_{1.93}Al_{0.06})O₆, *Pbca* space group, $a = 8.8117(2) \text{ \AA}$, $b = 5.18320(10) \text{ \AA}$, and $c = 18.2391(3) \text{ \AA}$]. The DAFI program was used for the search of reflection's groups belonging to the individual single crystal domains.^[9] Using the OLEX2 software package,^[10] the structures were solved with the ShelXT structure solution program^[11] using intrinsic phasing and refined with the ShelXL^[12] refinement package using least-squares minimization. Crystal structure visualization was made with the VESTA software.^[13] The equations of state were obtained by fitting the pressure-volume dependence data using the EoSFit7-GUI.^[14]

XANES. The x-ray absorption near edge structure (XANES) experiments at the La L_{II} edge ($\sim 5.9 \text{ keV}$) were performed at the beamline ID12 of the ESRF in Grenoble. The beam was focused down to $5 \times 5 \mu\text{m}^2$ using two parabolic two-dimensional refractive beryllium lenses having a parabola apex radius of 50 μm fixing the focal distance to be at 2.0 m. The beam size has been checked to remain constant within the La L_{II} -edge energy range. The XANES spectra were recorded via the total fluorescence yield using a photodiode in backscattering geometry. The XANES spectra were collected from the $\text{La}_3\text{O}_2(\text{CN}_3)$ sample in DAC#2 at 25 GPa and from La_2O_3 reference sample at ambient conditions.

Theoretical Calculations. First-principles calculations were performed using the framework of density functional theory (DFT) as implemented in the Vienna Ab initio Simulation Package (VASP).^[15] The Projector-Augmented-Wave (PAW) method^[16] was used to expand the electronic wave function in plane waves. The Generalized Gradient Approximation (GGA) functional is used for calculating the exchange-correlation energies, as proposed by Perdew–Burke–Ernzerhof (PBE).^[17] The PAW potentials “C”, “N” and “O” with the following valence configurations $2s^2 2p^2$ for C, $2s^2 2p^3$ for N, $2s^2 2p^4$ for O were used for non-metal atoms. For lanthanum “La” PAW potential was used with the $5s^2 5p^6 5d^1 6s^2$ valence configuration, while for Ln = Eu, Gd, Tb, Ho, Yb the “Ln_3” PAW potentials were used, in which non-valence 4 *f*-electrons are kept frozen in the core. We used the Monkhorst–Pack scheme with $4 \times 6 \times 6$ *k*-points for Brillouin zone sampling for all $\text{Ln}_3\text{O}_2(\text{CN}_3)$ compounds, and the plane-wave kinetic energy cutoff was set to 800 eV, with which total energies are converged to better than 2 meV/atom. The 0 K harmonic phonon calculations were performed using the finite displacement approach implemented into PHONOPY.^[18] Converged phonon dispersions were achieved using a $(1 \times 2 \times 2)$ supercell with 144 atoms and $6 \times 4 \times 4$ Monkhorst–Pack *k*-point sampling.

SUPPORTING INFORMATION

Supplementary Discussion 1. The justification of the selected La₃O₂(CN₃) structure model.

The crystal structure solution unambiguously suggested two positions of La atoms and five positions of C/N/O non-metal atoms (two positions of distinct atoms (X1 and X2) and three positions in an AZ₃ planar trigonal unit, in general, La₃X1X2(AZ₃)). The assignment of C/N/O atoms required a more detailed analysis, which is described below.

First, the atoms in the AZ₃ planar trigonal unit were determined. The well-known trigonal CO₃²⁻ carbonate and NO₃⁻ nitrate anions were ruled out because they did not fit the A-Z distances: $d_{(A-X)} \approx 1.35 \text{ \AA}$ at 54 GPa and $d_{(A-X)} \approx 1.40 \text{ \AA}$ at 1 bar, while C-O and N-O distances in CO₃²⁻ and NO₃⁻ ($d_{C-O} = 1.27\text{-}1.29 \text{ \AA}$ and $d_{N-O} = 1.24\text{-}1.26 \text{ \AA}$ at 1 bar) are significantly shorter. Therefore, we considered two other options: (1) an NN₃⁴⁻ unit, which was theoretically predicted in several studies^[19–23] with $d_{N-N} = 1.35 \text{ \AA}$ at 40 GPa and (2) an CN₃⁵⁻ unit. Carbon, nitrogen and oxygen atoms were tested for X1 and X2. The results of the analysis of the crystal structure refinement are summarized in Table SD1.1. Upon preliminary analysis, the possibility of the X1 and X2 positions occupation by carbon atoms was ruled out due to much worse R₁ and ADPs values, so we do not include these models in Table SD1.1.

Table SD1.1. Analysis of the structure refinements of different “La₃X1X2(AZ₃)” models at 54(1) GPa.

Model La ₃ X1X2(AZ ₃)	R ₁ , %	U _{eq} ADPs ¹					Max/min ADP ratio	Distances, Å		Charge balance ²	
		“A”	“Z1”	“Z2”	“X1”	“X2”		“A-Z1”	“A-Z2”	cations	anions
La ₃ NN(NN ₃)	2.81	N 0.027	N 0.006	N 0.009	N 0.003	N 0.005	9.0	1.35	1.35	+9	-10
La ₃ NO(NN ₃)	2.78	N 0.028	N 0.006	N 0.009	N 0.003	O 0.010	9.3	1.36	1.33	+9	-9
La ₃ ON(NN ₃)	2.76	N 0.025	N 0.006	N 0.008	O 0.006	N 0.005	5.0	1.36	1.35	+9	-9
La ₃ OO(NN ₃)	2.66	N 0.023	N 0.006	N 0.008	O 0.006	O 0.010	3.8	1.34	1.36	+9	-8
La ₃ NN(CN ₃)	2.70	C 0.016	N 0.006	N 0.008	N 0.003	N 0.005	5.3	1.35	1.35	+9	-11
La ₃ NO(CN ₃)	2.65	C 0.015	N 0.006	N 0.008	N 0.003	O 0.010	5.0	1.35	1.34	+9	-10
La ₃ ON(CN ₃)	2.61	C 0.013	N 0.006	N 0.007	O 0.006	N 0.005	2.6	1.35	1.36	+9	-10
La ₃ OO(CN ₃)	2.53	C 0.013	N 0.006	N 0.007	O 0.006	O 0.010	2.2	1.36	1.34	+9	-9
La ₃ O(O _{0.25} N _{0.75})(CN _{2.25} O _{0.75})	2.60	C 0.013	$\frac{3}{4}$ N $\frac{1}{4}$ O 0.007	$\frac{3}{4}$ N $\frac{1}{4}$ O 0.009	O 0.006	$\frac{3}{4}$ N $\frac{1}{4}$ O 0.006	2.2	1.35	1.35	+9	-9

¹U_{eq} ADPs of both La1 and La2 were U_{eq} ≈ 0.007 in each structure model.

²Charges were calculated in classic ionic considerations.

The colors represent the reliability of the analyzed parameters: green – good, orange – acceptable, and red – inadequate. The uncertainty of the U_{eq} ADPs and of the “A-Z” distances are omitted for clarity.

The A-Z bond lengths in the AZ₃ unit were found to be the same within the uncertainty for all tested structure models. All models with NN₃⁴⁻ units have central nitrogen atoms with relatively large ADPs, which results in a huge max/min ADPs ratio of non-metal atoms, indicating that the structure models are not correct. Models with CN₃⁵⁻ unit have smaller ADP values of carbon atoms, resulting in a good max/min ADPs ratio. The R₁ factor also drops down compared to structure models with NN₃⁴⁻ unit. The lowest R₁ factor and smallest max/min ADPs ratio were achieved with a La₃O₂(CN₃) structure model. Moreover, only this composition among all models containing CN₃⁵⁻ units is reasonable from charge balance considerations.

For La₃O₂(CN₃) composition we also tested La₃O(O_{0.25}N_{0.75})(CN_{2.25}O_{0.75}) model, where N1, N2, and O2 positions are mixed-occupied with N and O in an atomic ratio of $\frac{3}{4}:\frac{1}{4}$, similar to the proposed model for La₃(SiN₃O) oxonitridosilicate.^[24] This change resulted in a slight increase of R₁ factor, indicating that the mixed-occupied model is not preferable.

Table SD1.2. The results of DFT analysis of different La₃X1X2(AZ₃) structure models at 1 bar

Model	Unit cell volume		Dynamical stability
	V _{exp} , Å ³	V _{calc} , Å ³	
La ₃ NN(NN ₃)	493.95(9)	515.67	No
La ₃ OO(NN ₃)	493.95(9)	498.92	No
La ₃ NN(CN ₃)	493.95(9)	512.71	Yes
La ₃ OO(CN ₃)	493.95(9)	498.16	Yes

DFT calculations additionally corroborate the validity of a La₃O₂(CN₃) model. We compared the relaxed structure models of the potential compositions, at 1 bar, in terms of (1) dynamical stability, and (2) discrepancy between the experimental

SUPPORTING INFORMATION

and calculated unit cell volumes (Table SD1.2). Phonon calculations show that all relaxed models with NN_3^{4-} unit have imaginary phonon frequencies and therefore are dynamically unstable at 1 bar (Fig. SD1.1). On the other hand, models comprised of CN_3^{5-} units are dynamically stable (Fig. SD1.2) and the $\text{La}_3\text{O}_2(\text{CN}_3)$ composition has the best agreement between experimental and calculated unit cell volumes.

Thus, both detailed structure refinement analysis and DFT calculations unambiguously show that the selected $\text{La}_3\text{O}_2(\text{CN}_3)$ structure model is correct.

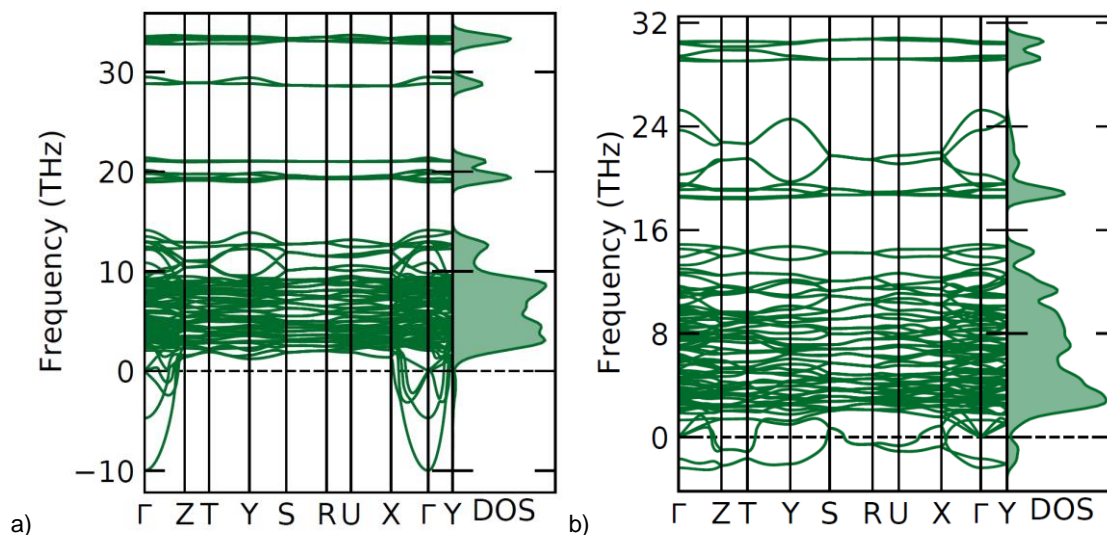


Figure SD1.1. Phonon dispersion curves for (a) $\text{La}_3\text{N}_2(\text{NN}_3)$ and (b) $\text{La}_3\text{O}_2(\text{NN}_3)$ along the high symmetry directions in the Brillouin zone and the phonon density of states at ambient pressure.

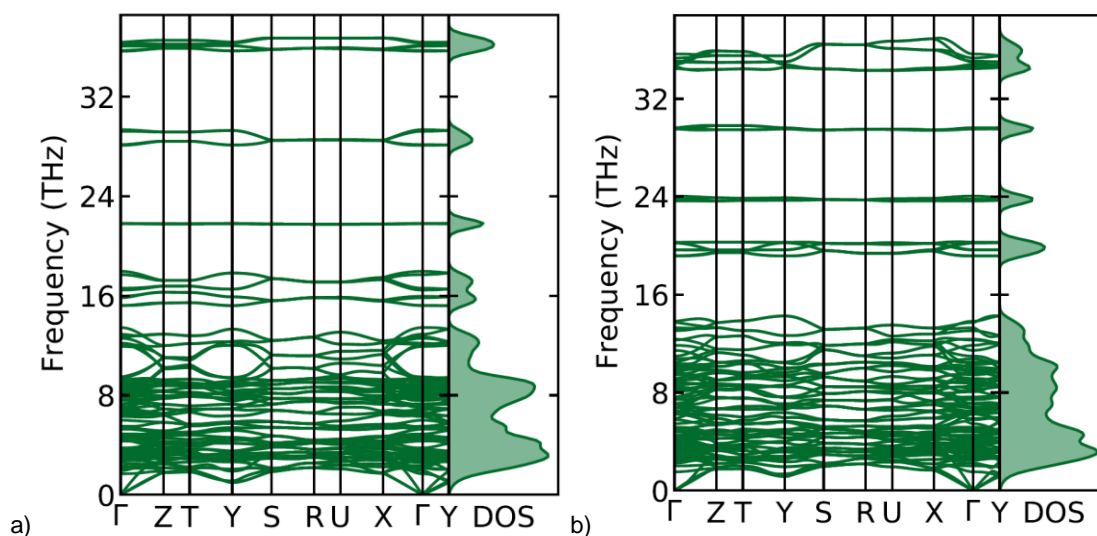


Figure SD1.2. Phonon dispersion curves for (a) $\text{La}_3\text{N}_2(\text{CN}_3)$ and (b) $\text{La}_3\text{O}_2(\text{CN}_3)$ along the high symmetry directions in the Brillouin zone and the phonon density of states at ambient pressure.

SUPPORTING INFORMATION

Supplementary Discussion 2. Possible splitting of C1 atom position in $\text{Ln}_3\text{O}_2(\text{CN}_3)$ ($\text{Ln} = \text{Eu}, \text{Gd}, \text{Tb}, \text{Ho}, \text{Yb}$) structures.

Contrary to the case of $\text{La}_3\text{O}_2(\text{CN}_3)$, for all other lanthanide cations considered in the present study, the refinements of $\text{Ln}_3\text{O}_2(\text{CN}_3)$ ($\text{Ln} = \text{Eu}, \text{Gd}, \text{Tb}, \text{Ho}, \text{Yb}$) crystal structures suggests a residual electronic density peak at the same position (Fig. SD2.1a).

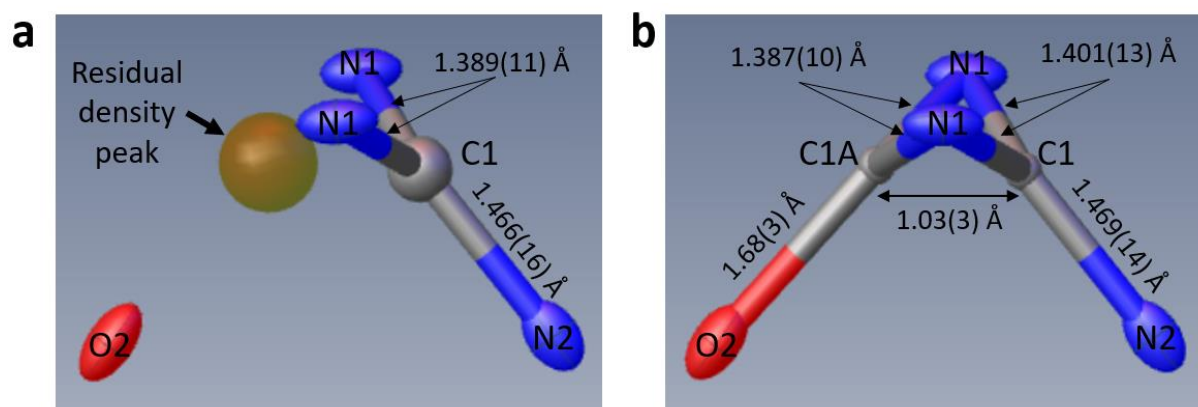


Figure SD2.1. A part of the crystal structure of $\text{Ho}_3\text{O}_2(\text{CN}_3)$ at 1 bar: a) model with a non-split C1 atom and b) model with a split C1 atom (the chemical occupancies of C1 and C1A positions are 0.696(18) and 0.304(18), respectively).

Due to a too short distance from the C1 atom to this residual electronic density peak, as well as insufficient electron density, the simultaneous presence of two C atoms with full occupancy is unreasonable. Therefore, we considered the splitting of C1 between two crystallographic positions (Fig. SD2.1b). This model has a frustrated carbon atom between two CN_3 and CN_2O planar (or almost planar) trigonal coordination environments. The R_1 value drops down compared to the model with a non-split C1 atom (see Tables S6-S10, S12, S13). Interestingly, in most cases, the chemical occupancy ratio between the C1 and C1A positions was $\sim 2:1$ (see Tables S6-S10, S12, S13). It is important to note that it was not possible to place the C atom in the center of the CN_3O tetrahedra.

Despite the disorder model resulted in a statistically significant^[25] improvement of the R_1 agreement factor, it must be pointed out that the C1A-O2 distance is too long for a C-O single bond, and therefore from a crystal-chemical point of view this model is dubious. We also can not exclude that the appearance of this residual density peak is an artifact of the limited quality of single-crystal X-ray diffraction data collected in the diamond anvil cell. Resolving this question requires additional studies.

Supplementary Figures

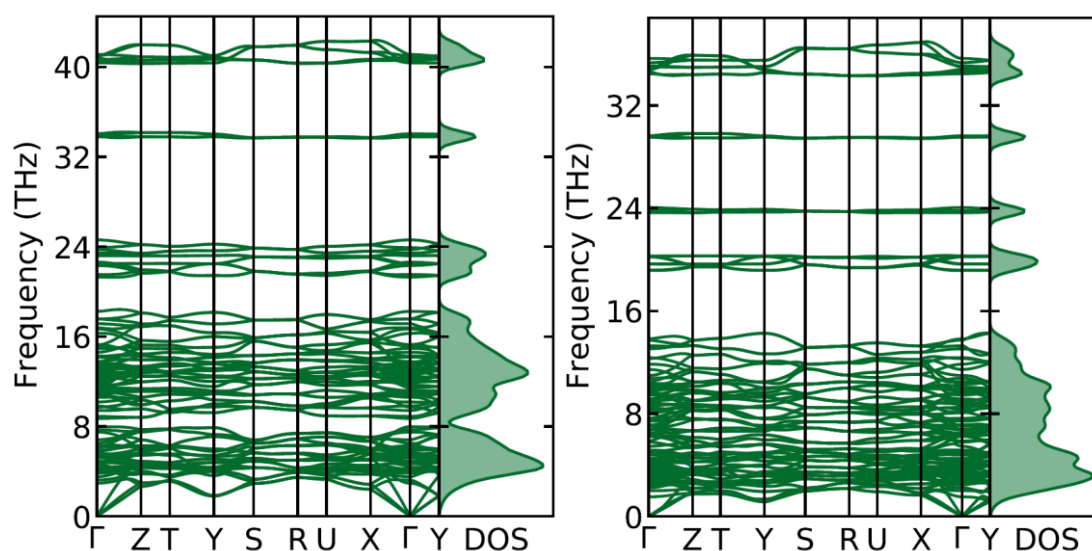


Figure S1. Phonon dispersion curves for $\text{La}_3\text{O}_2(\text{CN}_3)$ along the high symmetry directions in the Brillouin zone and phonon density of states at (a) 54 GPa and (b) ambient pressure.

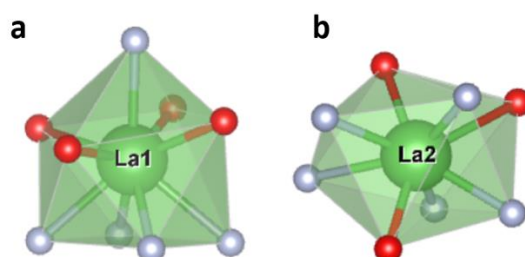


Figure S2. Coordination polyhedra of (a) the La1 atom and (b) the La2 atom in the $\text{La}_3\text{O}_2(\text{CN}_3)$ crystal structure

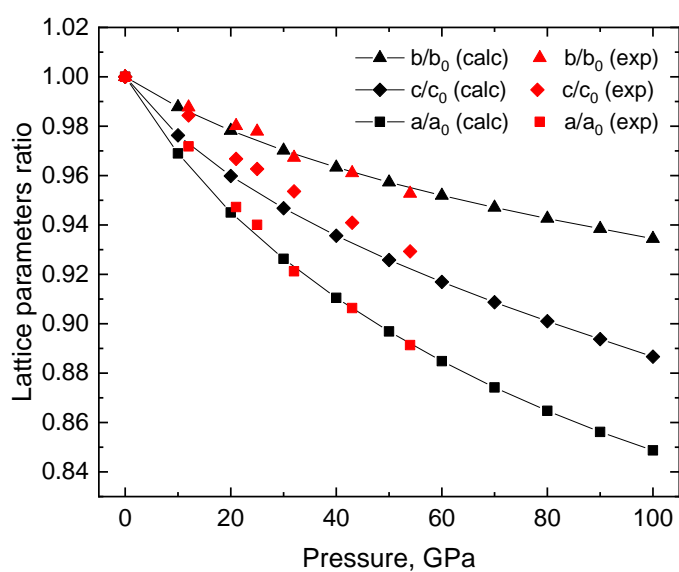


Figure S3. The compressibility of the a , b , and c crystallographic axes of $\text{La}_3\text{O}_2(\text{CN}_3)$. The experimental points are red, and the calculated points are black.

SUPPORTING INFORMATION

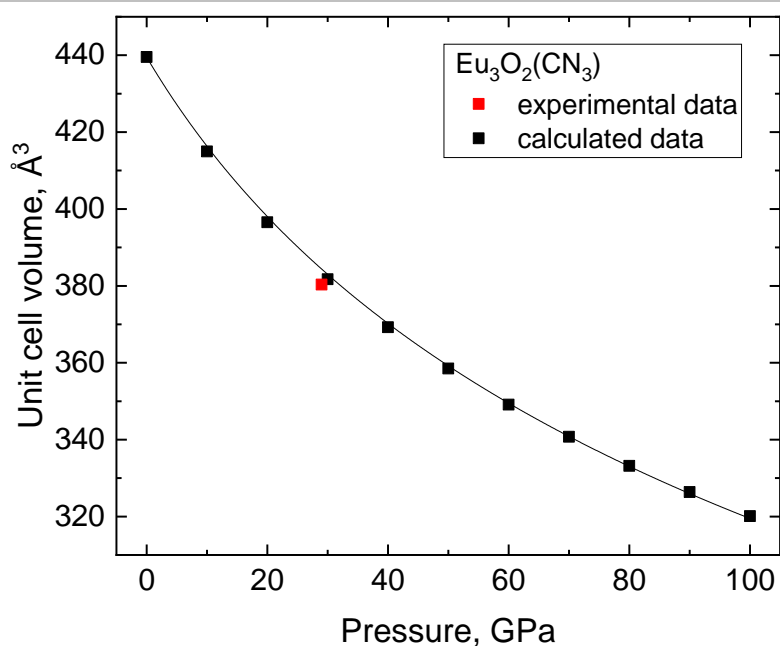


Figure S4. Experimental (red points) and calculated (black points) pressure dependence of the $\text{Eu}_3\text{O}_2(\text{CN}_3)$ unit cell volume. The black curve is the fit of the calculated P-V data using a 2nd order Birch-Murnaghan equation of state, yielding $K_0=131.3(9)$ GPa, $K'=4$ (fixed), and $V_0=498.16 \text{ \AA}^3$ (fixed).

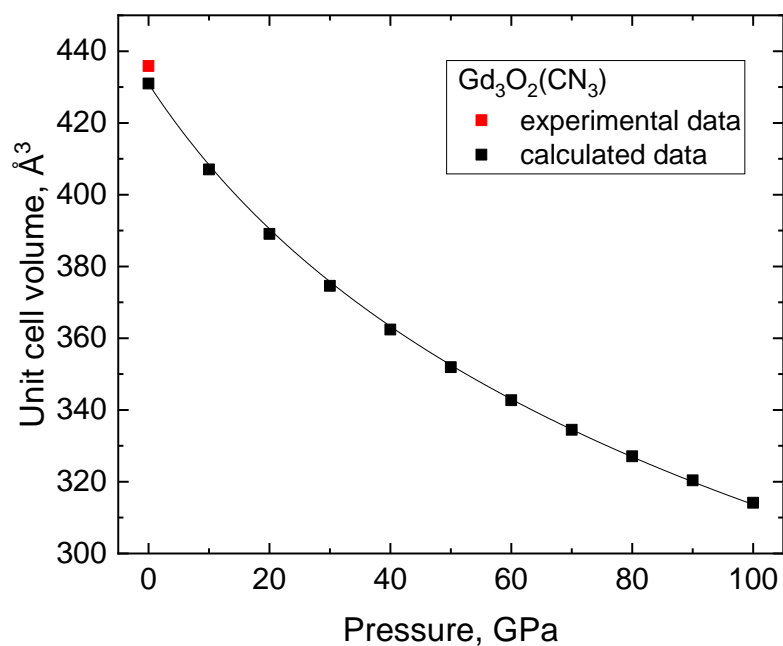


Figure S5. Experimental (red points) and calculated (black points) pressure dependence of the $\text{Gd}_3\text{O}_2(\text{CN}_3)$ unit cell volume. The black curve is the fit of the calculated P-V data using a 2nd order Birch-Murnaghan equation of state, yielding $K_0=131.3(9)$ GPa, $K'=4$ (fixed), and $V_0=498.16 \text{ \AA}^3$ (fixed).

SUPPORTING INFORMATION

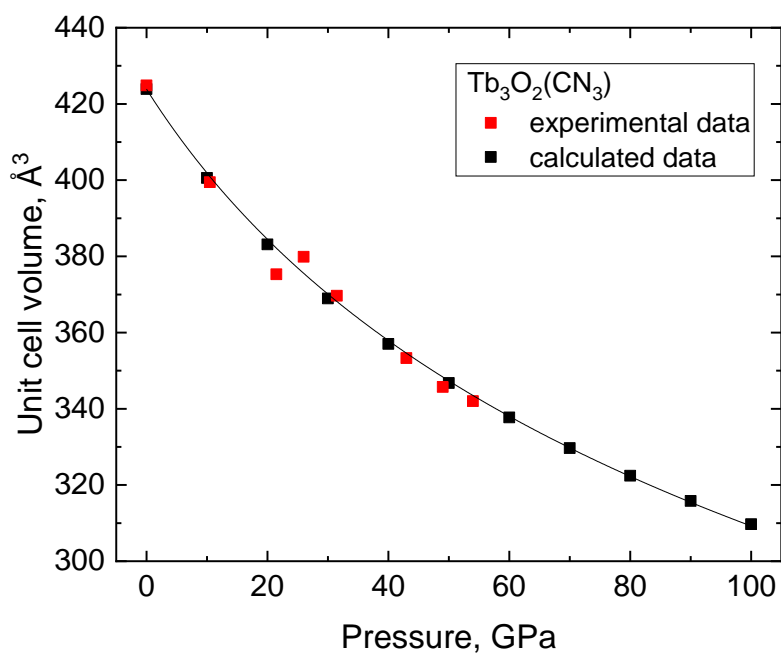


Figure S6. Experimental (red points) and calculated (black points) pressure dependence of the Tb₃O₂(CN₃) unit cell volume. The black curve is the fit of the calculated P-V data using a 2nd order Birch-Murnaghan equation of state, yielding $K_0=131.3(9)$ GPa, $K'=4$ (fixed), and $V_0=498.16 \text{ \AA}^3$ (fixed).

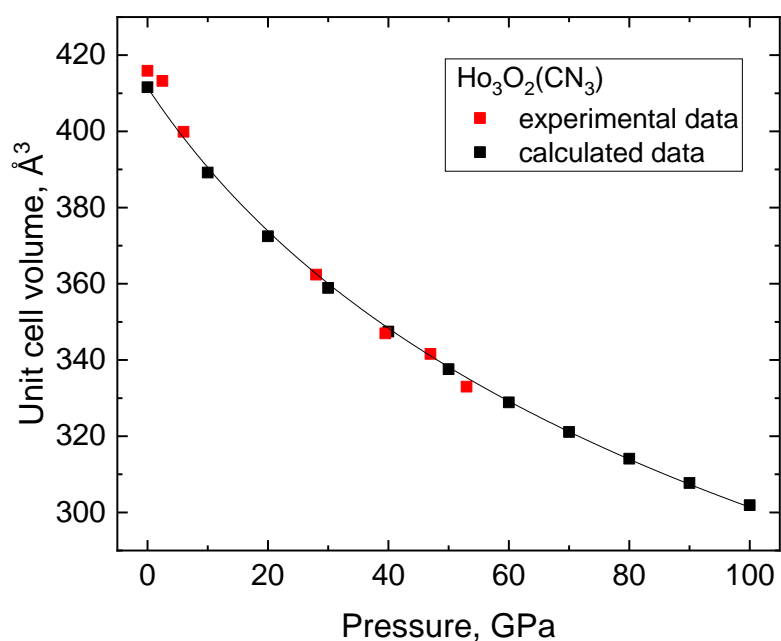


Figure S7. Experimental (red points) and calculated (black points) pressure dependence of the Ho₃O₂(CN₃) unit cell volume. The black curve is the fit of the calculated P-V data using a 2nd order Birch-Murnaghan equation of state, yielding $K_0=131.3(9)$ GPa, $K'=4$ (fixed), and $V_0=498.16 \text{ \AA}^3$ (fixed).

SUPPORTING INFORMATION

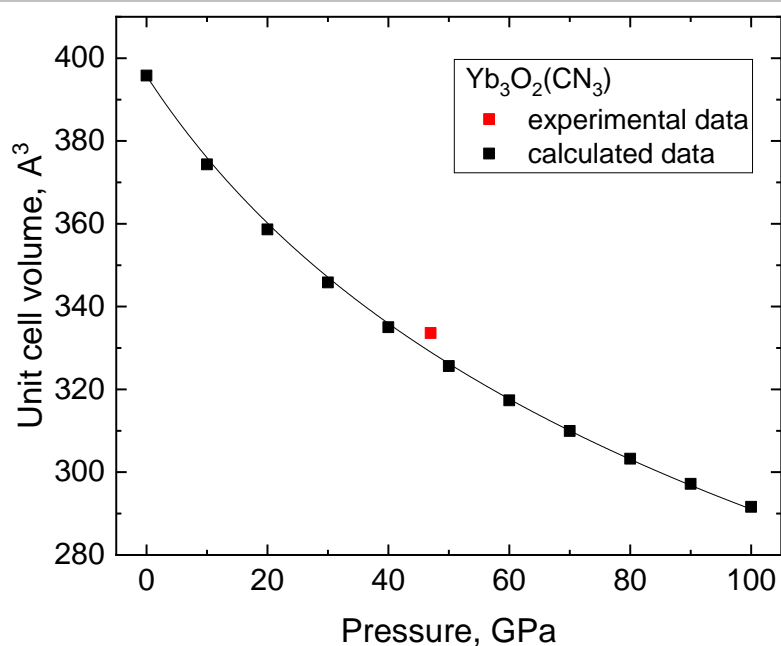


Figure S8. Experimental (red points) and calculated (black points) pressure dependence of the $\text{Yb}_3\text{O}_2(\text{CN}_3)$ unit cell volume. The black curve is the fit of the calculated P-V data using a 2nd order Birch-Murnaghan equation of state, yielding $K_0=131.3(9)$ GPa, $K'=4$ (fixed), and $V_0=498.16 \text{ \AA}^3$ (fixed).

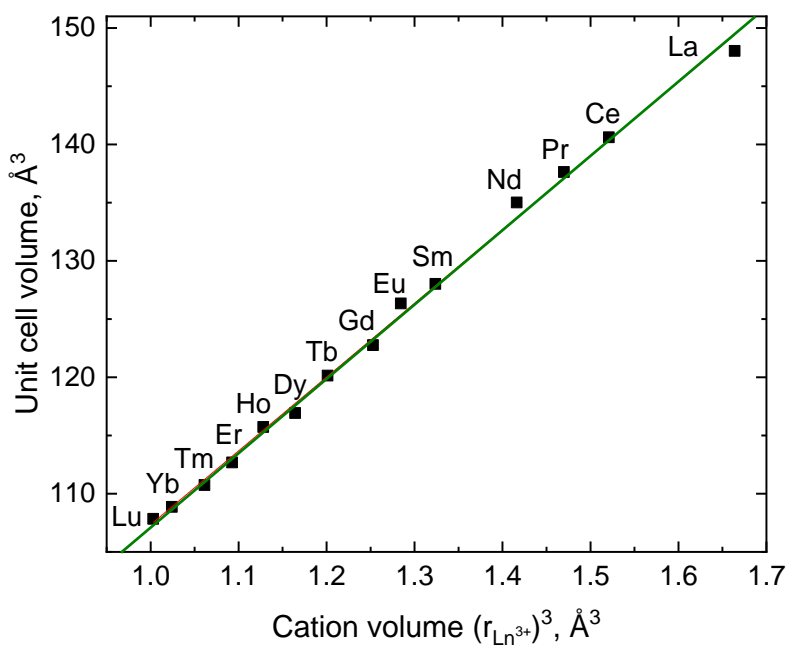


Figure S9. The linear dependence of the unit cell volume of LnN compounds at 1 bar versus the volume of the lanthanide ion (ionic radii are taken from <http://abulafia.mt.ic.ac.uk/shannon/ptable.php> for CN = 8).

SUPPORTING INFORMATION

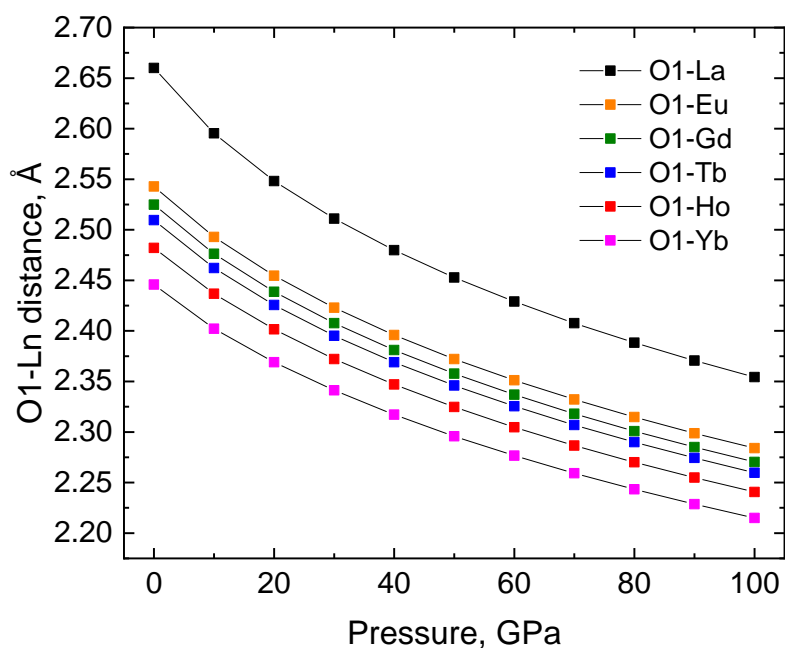


Figure S10. The calculated average O1-Ln bond length within the O1Ln₆ octahedra in Ln₃O₂(CN₃) (Ln = La, Eu, Gd, Tb, Ho, Yb) solids, at different pressures.

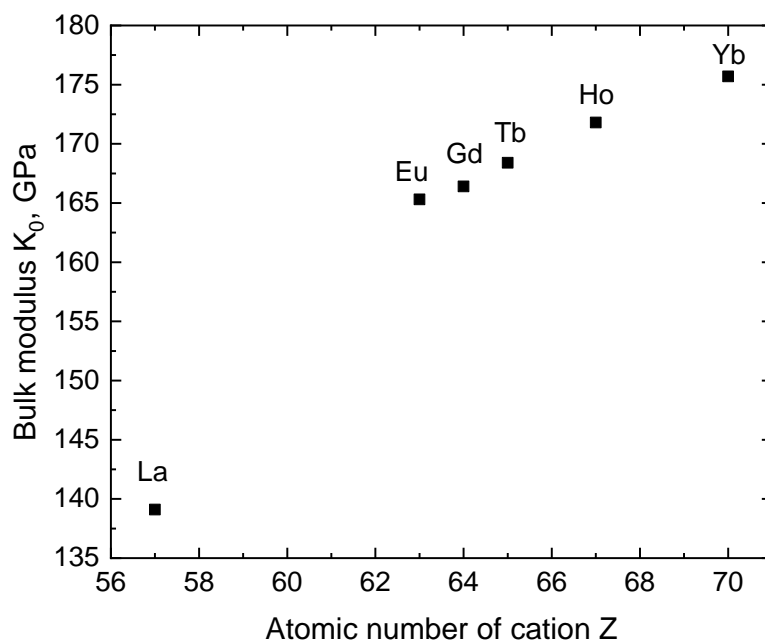


Figure S11. Calculated bulk moduli for Ln₃O₂(CN₃) (Ln = La, Eu, Gd, Tb, Ho, Yb) solids, extracted from 2nd order Birch-Murnaghan equation of state fits.

SUPPORTING INFORMATION

Supplementary Tables

Table S1. List of the samples investigated in the present study

Sample	Reaction mixture ¹	Pressure, GPa	Temperature, K	Decompression experiment
DAC#1	"La" + N ₂	54(1)	2500(500)	Yes
DAC#2	"La" + N ₂	25(1)	2500(500)	No
DAC#3	"Tb" + N ₂	54(1)	2500(500)	Yes
DAC#4	"Tb" + N ₂	26(1)	2500(500)	No
DAC#5	"Gd" + N ₂	50(1)	2500(500)	Yes ²
DAC#6	"Ho" + N ₂	53(1)	3000(500)	Yes
DAC#7	"Eu(N ₃) ₂ "	29(1)	2000(500)	No
DAC#8	"Yb(N ₃) ₂ "	47(1)	2000(500)	No

¹The quotation marks indicate the nominal composition. In fact, the samples were O-contaminated.

²The Gd₃O₂(CN₃) phase was detected only at the last step of the decompression experiment – at ambient conditions. It was not found at higher pressures, presumably because of the presence of other strong-diffracting phases. However, as these phases were no longer visible at ambient conditions due to their decompression, Gd₃O₂(CN₃) could be identified.

SUPPORTING INFORMATION

Table S2. Structure refinement details of La₃O₂(CN₃) at 54(1) GPa. The full crystallographic dataset was deposited to the CSD under the deposition number 2286277.

Crystal data							
Chemical formula		La ₃ O ₂ (CN ₃)					
Temperature (K)		293					
Pressure (GPa)		54(1)					
Mr		502.77					
ρ (g/cm ³)		8.566					
Crystal system, space group		orthorhombic, <i>Pnma</i>					
a (Å)		9.2875(7)					
b (Å)		6.8259(5)					
c (Å)		6.149(2)					
V (Å ³)		389.84(14)					
Z		4					
Radiation type		X-ray, $\lambda = 0.2904$ Å					
Data collection							
No. of measured, independent and observed [$I > 2\sigma(I)$] reflections		2095/703/635					
R _{int}		3.56%					
$(\sin \theta/\lambda)_{\max}$ (Å ⁻¹)		0.999					
Refinement							
R[F ² > 3 σ (F ²)], wR(F ²), GOF		2.53%, 5.47%, 1.009					
data/parameters ratio		703/49					
$\Delta\rho_{\max}, \Delta\rho_{\min}$ (e Å ⁻³)		1.920, -2.181					
Atomic positions							
Atom	Wyckoff site	Fractional atomic coordinates					
		x	y	z			
La1	8d	0.32330(2)	0.01466(3)	0.07787(8)			
La2	4c	0.47616(3)	0.25	0.60594(11)			
O1	4c	0.2334(4)	0.25	0.8268(14)			
O2	4c	0.2943(4)	0.25	0.3672(15)			
N1	8d	0.0696(3)	0.0736(4)	0.2059(12)			
N2	4c	0.0081(4)	0.25	0.5113(17)			
C1	4c	0.0469(5)	0.25	0.305(2)			
Anisotropic displacement parameters							
Atom	U_{11} (Å ²)	U_{22} (Å ²)	U_{33} (Å ²)	U_{12} (Å ²)	U_{13} (Å ²)	U_{23} (Å ²)	U_{eq} (Å ²)
La1	0.00470(10)	0.00516(9)	0.0099(4)	0.00069(9)	-0.00023(9)	-0.00007(4)	0.00660(14)
La2	0.00537(12)	0.00479(11)	0.0091(6)	0	-0.00011(12)	0	0.00642(18)
O1	0.0048(13)	0.0084(13)	0.003(7)	0	0.0011(16)	0	0.006(2)
O2	0.0094(15)	0.0080(14)	0.012(8)	0	0.0032(19)	0	0.010(2)
N1	0.0065(11)	0.0066(11)	0.005(6)	-0.0005(14)	-0.0018(13)	0.0005(6)	0.0061(17)
N2	0.0048(16)	0.0082(15)	0.007(9)	0	-0.0022(19)	0	0.007(3)
C1	0.009(2)	0.0094(19)	0.020(12)	0	-0.002(3)	0	0.013(4)

SUPPORTING INFORMATION

Table S3. Structure refinement details of La₃O₂(CN₃) at 25(1) GPa. The full crystallographic dataset was deposited to the CSD under the deposition number 2286275.

Crystal data							
Chemical formula	La ₃ O ₂ (CN ₃)						
Temperature (K)	293						
Pressure (GPa)	25(1)						
Mr	502.77						
ρ (g/cm ³)	7.640						
Crystal system, space group	orthorhombic, <i>Pnma</i>						
a (Å)	9.795(2)						
b (Å)	7.0062(11)						
c (Å)	6.3699(11)						
V (Å ³)	437.13(14)						
Z	4						
Radiation type	X-ray, $\lambda = 0.2904$ Å						
Data collection							
No. of measured, independent and observed [$I > 2\sigma(I)$] reflections	1416/594/477						
R _{int}	5.53%						
($\sin \theta/\lambda$) _{max} (Å ⁻¹)	0.713						
Refinement							
R[F ² > 3 σ (F ²)], wR(F ²), GOF	4.45%, 9.86%, 1.044						
data/parameters ratio	594/32						
$\Delta\rho_{\max}$, $\Delta\rho_{\min}$ (e Å ⁻³)	2.524, -2.277						
Atomic positions							
Atom	Wyckoff site	Fractional atomic coordinates					
		x	y	z			
La1	8d	0.32371(8)	0.01220(9)	0.07030(10)			
La2	4c	0.47499(11)	0.25	0.60416(15)			
O1	4c	0.2281(13)	0.25	0.8242(19)			
O2	4c	0.2956(12)	0.25	0.3636(18)			
N1	8d	0.0698(11)	0.0742(14)	0.2068(15)			
N2	4c	0.0082(13)	0.25	0.507(2)			
C1	4c	0.051(2)	0.25	0.306(3)			
Anisotropic displacement parameters							
Atom	U_{11} (Å ²)	U_{22} (Å ²)	U_{33} (Å ²)	U_{12} (Å ²)	U_{13} (Å ²)	U_{23} (Å ²)	U_{eq} or U_{iso} (Å ²)
La1	0.0155(4)	0.0061(4)	0.0107(4)	0.00118(19)	0.0001(2)	-0.0006(2)	0.0155(4)
La2	0.0181(6)	0.0061(5)	0.0123(4)	0	-0.0023(4)	0	0.0181(6)
O1							0.015(2)
O2							0.011(2)
N1							0.0132(19)
N2							0.009(2)
C1							0.026(4)

SUPPORTING INFORMATION

Table S4. Structure refinement details of La₃O₂(CN₃) at 1 bar. The full crystallographic dataset was deposited to the CSD under the deposition number 2286276.

Crystal data							
Chemical formula	La ₃ O ₂ (CN ₃)						
Temperature (K)	293						
Pressure (GPa)	1 bar						
Mr	502.77						
ρ (g/cm ³)	6.761						
Crystal system, space group	orthorhombic, <i>Pnma</i>						
a (Å)	10.4195(5)						
b (Å)	7.1644(3)						
c (Å)	6.6169(12)						
V (Å ³)	493.95(9)						
Z	4						
Radiation type	X-ray, $\lambda = 0.2904$ Å						
Data collection							
No. of measured, independent and observed [$I > 2\sigma(I)$] reflections	2185/848/477						
R_{int}	4.16%						
$(\sin \theta/\lambda)_{\text{max}}$ (Å ⁻¹)	0.862						
Refinement							
$R[F^2 > 3\sigma(F^2)]$, $wR(F^2)$, GOF	3.16%, 7.79%, 1.020						
data/parameters ratio	848/49						
$\Delta\rho_{\text{max}}$, $\Delta\rho_{\text{min}}$ (e Å ⁻³)	2.285, -1.830						
Atomic positions							
Atom	Wyckoff site	Fractional atomic coordinates					
		x	y	z			
La1	8d	0.32434(2)	0.01033(4)	0.06190(7)			
La2	4c	0.47527(3)	0.25	0.60030(11)			
O1	4c	0.2279(5)	0.25	0.8179(15)			
O2	4c	0.2985(5)	0.25	0.3693(14)			
N1	8d	0.0693(4)	0.0784(5)	0.2071(12)			
N2	4c	0.0084(5)	0.25	0.5038(16)			
C1	4c	0.0506(6)	0.25	0.301(2)			
Anisotropic displacement parameters							
Atom	U_{11} (Å ²)	U_{22} (Å ²)	U_{33} (Å ²)	U_{12} (Å ²)	U_{13} (Å ²)	U_{23} (Å ²)	U_{eq} (Å ²)
La1	0.00929(14)	0.00728(13)	0.0099(4)	0.00136(11)	-0.00051(9)	-0.00082(6)	0.00884(15)
La2	0.00981(15)	0.00633(15)	0.0092(5)	0	0.00140(12)	0	0.00845(17)
O1	0.0117(18)	0.0118(17)	0.023(7)	0	-0.006(2)	0	0.016(2)
O2	0.015(2)	0.018(2)	0.007(8)	0	-0.001(2)	0	0.013(2)
N1	0.0236(18)	0.0065(13)	0.004(6)	-0.0018(17)	-0.0036(18)	-0.0009(10)	0.0115(17)
N2	0.0072(19)	0.009(2)	0.021(8)	0	-0.002(2)	0	0.012(2)
C1	0.009(2)	0.013(2)	0.026(10)	0	-0.002(3)	0	0.016(3)

SUPPORTING INFORMATION

Table S5. Experimentally determined crystallographic data for $\text{La}_3\text{O}_2(\text{CN}_3)$ at 54(1) GPa and 1 bar compared with the corresponding DFT-relaxed structures. Note that pressure was fixed in theoretical simulations, while the volume of the unit cells, lattice parameters and equilibrium state parameters were calculated.

Pressure	54 GPa		1 bar	
Exp./Calc.	Exp.	Calc.	Exp.	Calc.
Space group	<i>Pnma</i>	<i>Pnma</i>	<i>Pnma</i>	<i>Pnma</i>
Volume	389.84(14) Å ³	389.83 Å ³	493.95(9) Å ³	498.16 Å ³
Lattice parameters	a = 9.2875(7) Å b = 6.8259(5) Å c = 6.149(2) Å $\alpha = 90^\circ$ $\beta = 90^\circ$ $\gamma = 90^\circ$	a = 9.3333 Å b = 6.8238 Å c = 6.1209 Å $\alpha = 90^\circ$ $\beta = 90^\circ$ $\gamma = 90^\circ$	a = 10.4195(5) Å b = 7.1644(3) Å c = 6.6169(12) Å $\alpha = 90^\circ$ $\beta = 90^\circ$ $\gamma = 90^\circ$	a = 10.4839 Å b = 7.1497 Å c = 6.6460 Å $\alpha = 90^\circ$ $\beta = 90^\circ$ $\gamma = 90^\circ$
Atomic positions	La1 x 0.32330(2) y 0.01466(3) z 0.07787(8)	La1 x 0.32207 y 0.01489 z 0.08023	La1 x 0.32434(2) y 0.01033(4) z 0.06190(7)	La1 x 0.32382 y 0.00898 z 0.06165
	La2 x 0.47616(3) y 0.25 z 0.60594(11)	La2 x 0.47799 y 0.25 z 0.60844	La2 x 0.47527(3) y 0.25 z 0.60030(11)	La2 x 0.47581 y 0.25 z 0.60091
	O1 x 0.2334(4) y 0.25 z 0.8268(14)	O1 x 0.23533 y 0.25 z 0.82501	O1 x 0.2279(5) y 0.25 z 0.8179(15)	O1 x 0.22798 y 0.25 z 0.81953
	O2 x 0.2943(4) y 0.25 z 0.3672(15)	O2 x 0.29669 y 0.25 z 0.37046	O2 x 0.2985(5) y 0.25 z 0.3693(14)	O2 x 0.29808 y 0.25 z 0.37844
	N1 x 0.0696(3) y 0.0736(4) z 0.2059(12)	N1 x 0.06979 y 0.07400 z 0.20527	N1 x 0.0693(4) y 0.0784(5) z 0.2071(12)	N1 x 0.06710 y 0.07937 z 0.20813
	N2 x 0.0081(4) y 0.25 z 0.5113(17)	N2 x 0.00921 y 0.25 z 0.50819	N2 x 0.0084(5) y 0.25 z 0.5038(16)	N2 x 0.00856 y 0.25 z 0.49867
	C1 x 0.0469(5) y 0.25 z 0.305(2)	C1 x 0.05542 y 0.25 z 0.30062	C1 x 0.0506(6) y 0.25 z 0.301(2)	C1 x 0.04976 y 0.25 z 0.299746

SUPPORTING INFORMATION

Table S6. Structure refinement details of $\text{Eu}_3\text{O}_2(\text{CN}_3)$ at 29 GPa.

Crystal data						
Chemical formula		$\text{Eu}_3\text{O}_2(\text{CN}_3)$				
Temperature (K)		293				
Pressure (GPa)		29(1)				
Mr		541.92				
ρ (g/cm ³)		9.463				
Crystal system, space group		orthorhombic, <i>Pnma</i>				
a (Å)		9.3222(7)				
b (Å)		6.7074(5)				
c (Å)		6.083(6)				
V (Å ³)		380.4(4)				
Z		4				
Radiation type		X-ray, $\lambda = 0.2905\text{Å}$				
Data collection						
No. of measured, independent and observed [$I > 2\sigma(I)$] reflections		1434/ 516/ 452				
R_{int}		3.11%				
$(\sin \theta/\lambda)_{\text{max}}$ (Å ⁻¹)		1.071				
Refinement						
Structure model		model with a non-split C1 atom		model with split C1 atom		
R[F ² > 4 σ (F ²)], wR(F ²), GOF		3.55%, 9.96%, 1.159		3.32%, 8.90%, 1.074		
data/parameters ratio		516/39		516/39		
$\Delta\rho_{\text{max}}, \Delta\rho_{\text{min}}$ (e Å ⁻³)		2.827, -1.831		1.880, -1.753		
Atomic positions and equivalent isotropic (or isotropic) ADPs for the model with a non-split C1 atom						
Atom	Wyckoff site	Fractional atomic coordinates			Occupancy	U_{eq} or U_{iso} (Å ²)
		x	y	z		
Eu1	8d	0.32594(4)	0.01157(6)	0.0641(2)	1	$U_{\text{eq}} = 0.0115(5)$
Eu2	4c	0.47582(6)	0.25	0.5986(3)	1	$U_{\text{eq}} = 0.0113(6)$
O1	4c	0.2263(7)	0.25	0.817(3)	1	$U_{\text{iso}} = 0.014(7)$
O2	4c	0.2953(10)	0.25	0.354(4)	1	$U_{\text{iso}} = 0.013(9)$
N1	8d	0.0767(6)	0.0681(10)	0.193(3)	1	$U_{\text{iso}} = 0.0119(10)$
N2	4c	0.0024(9)	0.25	0.528(4)	1	$U_{\text{iso}} = 0.0082(14)$
C1	4c	0.0511(18)	0.25	0.318(10)	1	$U_{\text{iso}} = 0.028(3)$
Atomic positions and equivalent isotropic (or isotropic) ADPs for the model with split C1 atom						
Atom	Wyckoff site	Fractional atomic coordinates			Occupancy	U_{eq} or U_{iso} (Å ²)
		x	y	z		
Eu1	8d	0.32595(4)	0.01154(5)	0.06401(18)	1	$U_{\text{eq}} = 0.0117(4)$
Eu2	4c	0.47582(5)	0.25	0.5986(3)	1	$U_{\text{eq}} = 0.0112(6)$
O1	4c	0.2267(7)	0.25	0.816(3)	1	$U_{\text{iso}} = 0.0076(10)$
O2	4c	0.2953(9)	0.25	0.357(4)	1	$U_{\text{iso}} = 0.013(8)$
N1	8d	0.0762(6)	0.0680(9)	0.193(3)	1	$U_{\text{iso}} = 0.0116(9)$
N2	4c	0.0028(8)	0.25	0.528(4)	1	$U_{\text{iso}} = 0.0078(13)$
C1	4c	0.0504(15)	0.25	0.309(8)	0.67(3)	$U_{\text{iso}} = 0.013(2)$
C1A	4c	0.135(3)	0.25	0.261(16)	0.33(3)	$U_{\text{iso}} = 0.013(2)$

SUPPORTING INFORMATION

Table S7. Structure refinement details of Gd₃O₂(CN₃) at 1 bar.

Crystal data						
Chemical formula		Gd ₃ O ₂ (CN ₃)				
Temperature (K)		293				
Pressure (bar)		1				
Mr		557.79				
ρ (g/cm ³)		8.501				
Crystal system, space group		orthorhombic, <i>Pnma</i>				
a (Å)		9.939(2)				
b (Å)		6.849(3)				
c (Å)		6.4028(14)				
V (Å ³)		435.8(2)				
Z		4				
Radiation type		X-ray, $\lambda = 0.2904\text{Å}$				
Data collection						
No. of measured, independent and observed [$I > 2\sigma(I)$] reflections		1254/ 679 / 399				
R _{int}		10.97 %				
$(\sin \theta/\lambda)_{\max}$ (Å ⁻¹)		0.806				
Refinement						
Structure model		model with a non-split C1 atom		model with split C1 atom		
R[F ² > 4 σ (F ²)], wR(F ²), GOF		6.86%, 18.22%, 0.950		6.76%, 17.96%, 0.939		
data/parameters ratio		679/32		679/35		
$\Delta\rho_{\max}, \Delta\rho_{\min}$ (e Å ⁻³)		4.060, -3.935		3.950, -3.915		
Atomic positions and equivalent isotropic (or isotropic) ADPs for the model with a non-split C1 atom						
Atom	Wyckoff site	Fractional atomic coordinates			Occupancy	U _{eq} or U _{iso} (Å ²)
		x	y	z		
Gd1	8d	0.32446(11)	0.0087(2)	0.05350(16)	1	U _{eq} = 0.0176(4)
Gd2	4c	0.47615(15)	0.25	0.6008(2)	1	U _{eq} = 0.0162(4)
O1	4c	0.225(2)	0.25	0.819(3)	1	U _{iso} = 0.021(4)
O2	4c	0.294(3)	0.25	0.354(4)	1	U _{iso} = 0.030(6)
N1	8d	0.075(2)	0.084(4)	0.196(3)	1	U _{iso} = 0.030(4)
N2	4c	0.010(2)	0.25	0.510(4)	1	U _{iso} = 0.018(5)
C1	4c	0.050(3)	0.25	0.300(5)	1	U _{iso} = 0.022(6)
Atomic positions and equivalent isotropic (or isotropic) ADPs for the model with split C1 atom						
Atom	Wyckoff site	Fractional atomic coordinates			Occupancy	U _{eq} or U _{iso} (Å ²)
		x	y	z		
Gd1	8d	0.32450(11)	0.0086(2)	0.05352(16)	1	U _{eq} = 0.0178(4)
Gd2	4c	0.47620(15)	0.25	0.6007(2)	1	U _{eq} = 0.0163(4)
O1	4c	0.224(2)	0.25	0.819(3)	1	U _{iso} = 0.021(4)
O2	4c	0.294(3)	0.25	0.355(4)	1	U _{iso} = 0.033(6)
N1	8d	0.075(2)	0.085(4)	0.198(3)	1	U _{iso} = 0.029(4)
N2	4c	0.008(2)	0.25	0.511(4)	1	U _{iso} = 0.019(5)
C1	4c	0.049(3)	0.25	0.299(5)	0.72(6)	U _{iso} = 0.008(5)
C1A	4c	0.138(8)	0.25	0.238(12)	0.28(6)	U _{iso} = 0.008(5)

SUPPORTING INFORMATION

Table S8. Structure refinement details of Tb₃O₂(CN₃) at 54 GPa

Crystal data						
Chemical formula		Tb ₃ O ₂ (CN ₃)				
Temperature (K)		293				
Pressure (GPa)		54				
Mr		562.80				
ρ (g/cm ³)		10.930				
Crystal system, space group		orthorhombic, <i>Pnma</i>				
a (Å)		8.8178(19)				
b (Å)		6.564(6)				
c (Å)		5.909(2)				
V (Å ³)		342.0(3)				
Z		4				
Radiation type		X-ray, $\lambda = 0.29521$ Å				
Data collection						
No. of measured, independent and observed [$I > 2\sigma(I)$] reflections		878/ 426 / 379				
R _{int}		1.57%				
$(\sin \theta/\lambda)_{\max}$ (Å ⁻¹)		0.890				
Refinement						
Structure model		model with a non-split C1 atom		model with split C1 atom		
R[F ² > 4 σ (F ²)], wR(F ²), GOF		3.86%, 10.95%, 1.069		3.66%, 10.40%, 1.070		
data/parameters ratio		426/32		426/35		
$\Delta\rho_{\max}, \Delta\rho_{\min}$ (e Å ⁻³)		3.361, -2.780		3.270, -2.828		
Atomic positions and equivalent isotropic (or isotropic) ADPs for the model with a non-split C1 atom						
Atom	Wyckoff site	Fractional atomic coordinates			Occupancy	U _{eq} or U _{iso} (Å ²)
		x	y	z		
Tb1	4c	0.32452(6)	0.01311(13)	0.07054(8)	1	U _{eq} = 0.0074(3)
Tb2	8d	0.47511(9)	0.25	0.60314(11)	1	U _{eq} = 0.0072(3)
O1	4c	0.2294(11)	0.25	0.8208(17)	1	U _{iso} = 0.0055(18)
O2	4c	0.2904(16)	0.25	0.355(2)	1	U _{iso} = 0.017(2)
N1	8d	0.0711(10)	0.070(2)	0.1966(14)	1	U _{iso} = 0.0081(15)
N2	4c	0.0034(13)	0.25	0.522(2)	1	U _{iso} = 0.006(2)
C1	4c	0.054(2)	0.25	0.298(3)	1	U _{iso} = 0.021(4)
Atomic positions and equivalent isotropic (or isotropic) ADPs for the model with split C1 atom						
Atom	Wyckoff site	Fractional atomic coordinates			Occupancy	U _{eq} or U _{iso} (Å ²)
		x	y	z		
Tb1	4c	0.32451(5)	0.01314(12)	0.07054(7)	1	U _{eq} = 0.0074(2)
Tb2	8d	0.47512(8)	0.25	0.60313(10)	1	U _{eq} = 0.0072(3)
O1	4c	0.2294(10)	0.25	0.8211(16)	1	U _{iso} = 0.0061(17)
O2	4c	0.2915(15)	0.25	0.356(2)	1	U _{iso} = 0.017(2)
N1	8d	0.0704(9)	0.071(2)	0.1973(13)	1	U _{iso} = 0.0080(14)
N2	4c	0.0032(12)	0.25	0.5225(19)	1	U _{iso} = 0.006(2)
C1	4c	0.053(2)	0.25	0.300(3)	0.68(4)	U _{iso} = 0.006(3)
C1A	4c	0.137(5)	0.25	0.265(6)	0.32(4)	U _{iso} = 0.006(3)

SUPPORTING INFORMATION

Table S9. Structure refinement details of Tb₃O₂(CN₃) at 26 GPa.

Crystal data						
Chemical formula		Tb ₃ O ₂ (CN ₃)				
Temperature (K)		293				
Pressure (GPa)		26				
Mr		562.80				
ρ (g/cm ³)		9.840				
Crystal system, space group		orthorhombic, <i>Pnma</i>				
a (Å)		9.399(9)				
b (Å)		6.6399(10)				
c (Å)		6.0873(6)				
V (Å ³)		379.9(4)				
Z		4				
Radiation type		X-ray, $\lambda = 0.41015\text{Å}$				
Data collection						
No. of measured, independent and observed [$I > 2\sigma(I)$] reflections		1112 / 382 / 297				
R _{int}		4.53%				
$(\sin \theta/\lambda)_{\max}$ (Å ⁻¹)		0.906				
Refinement						
Structure model		model with a non-split C1 atom		model with split C1 atom		
R[F ² > 4 σ (F ²)], wR(F ²), GOF		4.32%, 11.09 %, 1.063		4.27%, 11.19%, 1.024		
data/parameters ratio		382/32		492/35		
$\Delta\rho_{\max}, \Delta\rho_{\min}$ (e Å ⁻³)		2.635, -2.405		2.704, -2.198		
Atomic positions and equivalent isotropic (or isotropic) ADPs for the model with a non-split C1 atom						
Atom	Wyckoff site	Fractional atomic coordinates			Occupancy	U _{eq} or U _{iso} (Å ²)
		x	y	z		
Tb1	4c	0.3232(2)	0.01037(11)	0.06292(13)	1	U _{eq} = 0.0139(8)
Tb2	8d	0.4759(3)	0.25	0.60687(16)	1	U _{eq} = 0.0149(11)
O1	4c	0.222(5)	0.25	0.814(3)	1	U _{iso} = 0.020(4)
O2	4c	0.301(5)	0.25	0.357(3)	1	U _{iso} = 0.016(3)
N1	8d	0.072(3)	0.0714(17)	0.1960(17)	1	U _{iso} = 0.008(2)
N2	4c	-0.001(5)	0.25	0.513(3)	1	U _{iso} = 0.014(4)
C1	4c	0.056(6)	0.25	0.298(3)	1	U _{iso} = 0.015(4)
Atomic positions and equivalent isotropic (or isotropic) ADPs for the model with split C1 atom						
Atom	Wyckoff site	Fractional atomic coordinates			Occupancy	U _{eq} or U _{iso} (Å ²)
		x	y	z		
Tb1	4c	0.3233(2)	0.01040(11)	0.06291(13)	1	U _{eq} = 0.0137(8)
Tb2	8d	0.4759(3)	0.25	0.60689(16)	1	U _{eq} = 0.0152(11)
O1	4c	0.223(5)	0.25	0.814(3)	1	U _{iso} = 0.021(3)
O2	4c	0.301(4)	0.25	0.357(3)	1	U _{iso} = 0.016(3)
N1	8d	0.072(3)	0.0713(17)	0.1957(17)	1	U _{iso} = 0.009(2)
N2	4c	0.000(4)	0.25	0.514(3)	1	U _{iso} = 0.013(3)
C1	4c	0.051(8)	0.25	0.305(5)	0.73(7)	U _{iso} = 0.003(4)
C1A	4c	0.13(2)	0.25	0.253(13)	0.27(7)	U _{iso} = 0.003(4)

SUPPORTING INFORMATION

Table S10. Structure refinement details of Tb₃O₂(CN₃) at 1 bar.

Crystal data						
Chemical formula		Tb ₃ O ₂ (CN ₃)				
Temperature (K)		293				
Pressure (bar)		1				
Mr		562.80				
ρ (g/cm ³)		8.798				
Crystal system, space group		orthorhombic, <i>Pnma</i>				
a (Å)		9.8390(4)				
b (Å)		6.8043(8)				
c (Å)		6.3464(4)				
V (Å ³)		424.88(6)				
Z		4				
Radiation type		X-ray, $\lambda = 0.41004\text{Å}$				
Data collection						
No. of measured, independent and observed [$I > 2\sigma(I)$] reflections		846/ 492 / 384				
R _{int}		2.14%				
$(\sin \theta/\lambda)_{\max}$ (Å ⁻¹)		0.769				
Refinement						
Structure model		model with a non-split C1 atom		model with split C1 atom		
R[F ² > 4 σ (F ²)], wR(F ²), GOF		4.50%, 12.03%, 1.027		4.27%, 11.19%, 1.024		
data/parameters ratio		492/32		492/35		
$\Delta\rho_{\max}, \Delta\rho_{\min}$ (e Å ⁻³)		2.811, -2.523		2.704, -2.198		
Atomic positions and equivalent isotropic (or isotropic) ADPs for the model with a non-split C1 atom						
Atom	Wyckoff site	Fractional atomic coordinates			Occupancy	U _{eq} or U _{iso} (Å ²)
		x	y	z		
Tb1	4c	0.32343(7)	0.00880(12)	0.05353(13)	1	U _{eq} = 0.0189(3)
Tb2	8d	0.47683(10)	0.25	0.60061(15)	1	U _{eq} = 0.0164(3)
O1	4c	0.2229(15)	0.25	0.813(3)	1	U _{iso} = 0.021(3)
O2	4c	0.2992(18)	0.25	0.359(3)	1	U _{iso} = 0.030(4)
N1	8d	0.0785(13)	0.071(2)	0.194(2)	1	U _{iso} = 0.024(3)
N2	4c	0.0012(16)	0.25	0.510(3)	1	U _{iso} = 0.024(4)
C1	4c	0.052(3)	0.25	0.289(5)	1	U _{iso} = 0.035(6)
Atomic positions and equivalent isotropic (or isotropic) ADPs for the model with split C1 atom						
Atom	Wyckoff site	Fractional atomic coordinates			Occupancy	U _{eq} or U _{iso} (Å ²)
		x	y	z		
Tb1	4c	0.32342(7)	0.00878(11)	0.05348(12)	1	U _{eq} = 0.0189(3)
Tb2	8d	0.47685(10)	0.25	0.60064(15)	1	U _{eq} = 0.0165(3)
O1	4c	0.2233(14)	0.25	0.813(2)	1	U _{iso} = 0.021(3)
O2	4c	0.3002(16)	0.25	0.357(3)	1	U _{iso} = 0.027(3)
N1	8d	0.0779(12)	0.074(2)	0.194(2)	1	U _{iso} = 0.023(2)
N2	4c	0.0010(16)	0.25	0.510(3)	1	U _{iso} = 0.024(4)
C1	4c	0.050(3)	0.25	0.289(4)	0.68(4)	U _{iso} = 0.014(4)
C1A	4c	0.147(5)	0.25	0.224(9)	0.32(4)	U _{iso} = 0.014(4)

SUPPORTING INFORMATION

Table S11. Structure refinement details of Ho₃O₂(CN₃) at 53 GPa.

Crystal data						
Chemical formula		Ho ₃ O ₂ (CN ₃)				
Temperature (K)		293				
Pressure (GPa)		53				
Mr		580.83				
ρ (g/cm ³)		11.586				
Crystal system, space group		orthorhombic, <i>Pnma</i>				
a (Å)		8.7617(19)				
b (Å)		6.487(2)				
c (Å)		5.8586(7)				
V (Å ³)		333.00(14)				
Z		4				
Radiation type		X-ray, $\lambda = 0.2901\text{Å}$				
Data collection						
No. of measured, independent and observed [$I > 2\sigma(I)$] reflections		1512 / 662 / 459				
R _{int}		2.88 %				
$(\sin \theta/\lambda)_{\max}$ (Å ⁻¹)		1.038				
Refinement						
Structure model		model with a non-split C1 atom				
R[F ² > 4 σ (F ²)], wR(F ²), GOF		3.85%, 9.78%, 1.081				
data/parameters ratio		662/32				
$\Delta\rho_{\max}, \Delta\rho_{\min}$ (e Å ⁻³)		5.384, -4.830				
Atomic positions and equivalent isotropic (or isotropic) ADPs for the model with a non-split C1 atom						
Atom	Wyckoff site	Fractional atomic coordinates			Occupancy	U _{eq} or U _{iso} (Å ²)
		x	y	z		
Ho1	4c	0.32419(7)	0.01310(12)	0.07024(8)	1	U _{eq} = 0.00780(18)
Ho2	8d	0.47499(10)	0.25	0.60337(13)	1	U _{eq} = 0.00704(14)
O1	4c	0.2264(17)	0.25	0.819(2)	1	U _{iso} = 0.012(2)
O2	4c	0.2920(18)	0.25	0.353(2)	1	U _{iso} = 0.016(3)
N1	8d	0.0699(12)	0.067(2)	0.1994(15)	1	U _{iso} = 0.009(2)
N2	4c	0.0034(18)	0.25	0.520(2)	1	U _{iso} = 0.0072(15)
C1	4c	0.056(2)	0.25	0.290(5)	1	U _{iso} = 0.033(6)

SUPPORTING INFORMATION

Table S12. Structure refinement details of $\text{Ho}_3\text{O}_2(\text{CN}_3)$ at 1 bar.

Crystal data						
Chemical formula		$\text{Ho}_3\text{O}_2(\text{CN}_3)$				
Temperature (K)		293				
Pressure (bar)		1				
Mr		580.83				
ρ (g/cm ³)		9.276				
Crystal system, space group		orthorhombic, <i>Pnma</i>				
a (Å)		9.7962(5)				
b (Å)		6.7318(8)				
c (Å)		6.3066(3)				
V (Å ³)		415.90(6)				
Z		4				
Radiation type		X-ray, $\lambda = 0.2905\text{Å}$				
Data collection						
No. of measured, independent and observed [$I > 2\sigma(I)$] reflections		2153/ 863 / 697				
R_{int}		1.96%				
$(\sin \theta/\lambda)_{\text{max}}$ (Å ⁻¹)		0.908				
Refinement						
Structure model		model with a non-split C1 atom		model with split C1 atom		
$R[F^2 > 4\sigma(F^2)]$, $wR(F^2)$, GOF		2.82%, 7.96%, 1.083		2.57%, 6.97%, 1.063		
data/parameters ratio		863/46		863/49		
$\Delta\rho_{\text{max}}$, $\Delta\rho_{\text{min}}$ (e Å ⁻³)		4.059, -2.045		2.934, -2.135		
Atomic positions and equivalent isotropic (or isotropic) ADPs for the model with a non-split C1 atom						
Atom	Wyckoff site	Fractional atomic coordinates			Occupancy	U_{eq} or U_{iso} (Å ²)
		x	y	z		
Ho1	4c	0.32204(3)	0.00820(7)	0.05145(5)	1	$U_{\text{eq}} = 0.01184(11)$
Ho2	8d	0.47778(4)	0.25	0.60101(7)	1	$U_{\text{eq}} = 0.01014(12)$
O1	4c	0.2233(7)	0.25	0.8094(10)	1	$U_{\text{eq}} = 0.0144(18)$
O2	4c	0.2974(9)	0.25	0.3562(14)	1	$U_{\text{eq}} = 0.025(3)$
N1	8d	0.0793(7)	0.0711(15)	0.1922(9)	1	$U_{\text{eq}} = 0.0184(18)$
N2	4c	0.0025(8)	0.25	0.5127(18)	1	$U_{\text{eq}} = 0.018(2)$
C1	4c	0.0505(11)	0.25	0.2925(17)	1	$U_{\text{iso}} = 0.023(3)$
Atomic positions and equivalent isotropic (or isotropic) ADPs for the model with split C1 atom						
Atom	Wyckoff site	Fractional atomic coordinates			Occupancy	U_{eq} or U_{iso} (Å ²)
		x	y	z		
Ho1	4c	0.32205(3)	0.00822(6)	0.05145(4)	1	$U_{\text{eq}} = 0.01181(10)$
Ho2	8d	0.47778(4)	0.25	0.60102(6)	1	$U_{\text{eq}} = 0.01008(11)$
O1	4c	0.2232(6)	0.25	0.8100(9)	1	$U_{\text{eq}} = 0.0145(16)$
O2	4c	0.2982(7)	0.25	0.3554(11)	1	$U_{\text{eq}} = 0.023(2)$
N1	8d	0.0781(6)	0.0714(13)	0.1920(8)	1	$U_{\text{eq}} = 0.0186(16)$
N2	4c	0.0022(6)	0.25	0.5132(16)	1	$U_{\text{eq}} = 0.018(2)$
C1	4c	0.0496(9)	0.25	0.2922(15)	0.696(18)	$U_{\text{iso}} = 0.0076(14)$
C1A	4c	0.147(2)	0.25	0.231(3)	0.304(18)	$U_{\text{iso}} = 0.0076(14)$

SUPPORTING INFORMATION

Table S13. Structure refinement details of Yb₃O₂(CN₃) at 47 GPa.

Crystal data						
Chemical formula		Yb ₃ O ₂ (CN ₃)				
Temperature (K)		293				
Pressure (GPa)		47(1)				
Mr		605.16				
ρ (g/cm ³)		12.048				
Crystal system, space group		orthorhombic, <i>Pnma</i>				
a (Å)		8.8785(12)				
b (Å)		6.4071(5)				
c (Å)		5.8647(19)				
V (Å ³)		333.62(12)				
Z		4				
Radiation type		X-ray, $\lambda = 0.2905\text{Å}$				
Data collection						
No. of measured, independent and observed [$I > 2\sigma(I)$] reflections		1333/ 655 / 573				
R _{int}		1.51%				
$(\sin \theta/\lambda)_{\max}$ (Å ⁻¹)		1.060				
Refinement						
Structure model		model with non-split C1 atom		model with split C1 atom		
R[F ² > 4 σ (F ²)], wR(F ²), GOF		2.75%, 7.06%, 1.115		2.41%, 5.87%, 1.111		
data/parameters ratio		655/39		651/45		
$\Delta\rho_{\max}, \Delta\rho_{\min}$ (e Å ⁻³)		6.111, -3.163		2.416, -2.692		
Atomic positions and equivalent isotropic (or isotropic) ADPs for the model with a non-split C1 atom						
Atom	Wyckoff site	Fractional atomic coordinates			Occupancy	U _{eq} or U _{iso} (Å ²)
		x	y	z		
Yb1	8d	0.32577(4)	0.01113(4)	0.06362(8)	1	U _{eq} = 0.00702(12)
Yb2	4c	0.47536(5)	0.25	0.59993(11)	1	U _{eq} = 0.00647(14)
O1	4c	0.2244(8)	0.25	0.8170(19)	1	U _{eq} = 0.0063(17)
O2	4c	0.2949(12)	0.25	0.3540(3)	1	U _{eq} = 0.015(3)
N1	8d	0.0792(6)	0.0647(8)	0.1923(15)	1	U _{iso} = 0.0064(8)
N2	4c	0.0017(9)	0.25	0.526(2)	1	U _{iso} = 0.0078(13)
C1	4c	0.064(3)	0.25	0.308(7)	1	U _{iso} = 0.047(5)
Atomic positions and equivalent isotropic (or isotropic) ADPs for the model with split C1 atom						
Atom	Wyckoff site	Fractional atomic coordinates			Occupancy	U _{eq} or U _{iso} (Å ²)
		x	y	z		
Yb1	8d	0.32577(4)	0.01109(4)	0.06362(8)	1	U _{eq} = 0.00701(10)
Yb2	4c	0.47536(5)	0.25	0.60002(11)	1	U _{eq} = 0.00633(12)
O1	4c	0.2233(8)	0.25	0.8192(19)	1	U _{eq} = 0.0072(15)
O2	4c	0.2952(12)	0.25	0.3538(3)	1	U _{eq} = 0.015(2)
N1	8d	0.0791(6)	0.0653(8)	0.1926(15)	1	U _{eq} = 0.0066(7)
N2	4c	0.0016(9)	0.25	0.526(2)	1	U _{eq} = 0.011(2)
C1	4c	0.0556(3)	0.25	0.291(7)	0.54(3)	U _{iso} = 0.0081(17)
C1A	4c	0.1405(4)	0.25	0.251(8)	0.46(3)	U _{iso} = 0.0081(17)

SUPPORTING INFORMATION

Table S14. Parameters of the Birch-Murnaghan equation of state fit of Ln₃O₂(CN₃) (Ln = La, Eu, Gd, Tb, Ho, Yb) DFT-relaxed structures

Compound	V ₀ , Å ³	Parameters of Birch-Murnaghan equation of state fit			
		2 nd order		3 rd order	
		K ₀ , GPa	K'	K ₀ , GPa	K'
La ₃ O ₂ (CN ₃)	498.161 (fixed)	139.1(5)	4 (fixed)	131.3(9)	4.36(4)
Eu ₃ O ₂ (CN ₃)	439.557 (fixed)	165.3(6)	4 (fixed)	156.0(5)	4.41(2)
Gd ₃ O ₂ (CN ₃)	430.982 (fixed)	166.4(5)	4 (fixed)	157.8(6)	4.37(3)
Tb ₃ O ₂ (CN ₃)	423.928 (fixed)	168.4(5)	4 (fixed)	159.8(7)	4.37(3)
Ho ₃ O ₂ (CN ₃)	411.558 (fixed)	171.8(6)	4 (fixed)	162.5(7)	4.40(3)
Yb ₃ O ₂ (CN ₃)	395.793 (fixed)	175.7(7)	4 (fixed)	165.0(9)	4.46(4)

References

- [1] I. Kantor, V. Prakapenka, A. Kantor, P. Dera, A. Kurnosov, S. Sinogeikin, N. Dubrovinskaia, L. Dubrovinsky, *Rev. Sci. Instrum.* 2012, 83, 125102.
- [2] R. Boehler, *Rev. Sci. Instrum.* 2006, 77, 2004–2007.
- [3] A. Kurnosov, I. Kantor, T. Boffa-Ballaran, S. Lindhardt, L. Dubrovinsky, A. Kuznetsov, B. H. Zehnder, *Rev. Sci. Instrum.* 2008, 79, 045110.
- [4] G. Aprilis, C. Strohm, I. Kuppenko, S. Linhardt, A. Laskin, D. M. Vasiukov, V. Cerantola, E. G. Koemets, C. McCammon, A. Kurnosov, A. I. Chumakov, R. Rüffer, N. Dubrovinskaia, L. Dubrovinsky, *Rev. Sci. Instrum.* 2017, 88, 084501.
- [5] T. Fedotenko, L. Dubrovinsky, G. Aprilis, E. Koemets, A. Snigirev, I. Snigireva, A. Barannikov, P. Ershov, F. Cova, M. Hanfland, N. Dubrovinskaia, *Rev. Sci. Instrum.* 2019, 90, 104501.
- [6] Y. Akahama, H. Kawamura, *J. Appl. Phys.* 2006, 100, 043516.
- [7] S. Anzellini, A. Dewaele, F. Occelli, P. Loubeyre, M. Mezouar, *J. Appl. Phys.* 2014, 115, 043511.
- [8] *Rigaku Oxford Diffraction, CrysAlisPro Softw. Syst. (2015)*. 2015, DOI 10.1063/1.2372734.
- [9] A. Aslandukov, M. Aslandukov, N. Dubrovinskaia, L. Dubrovinsky, *J. Appl. Crystallogr.* 2022, 55, 1383–1391.
- [10] O. V. Dolomanov, L. J. Bourhis, R. J. Gildea, J. A. K. Howard, H. Puschmann, *J. Appl. Crystallogr.* 2009, 42, 339–341.
- [11] V. Petríček, M. Dušek, L. Palatinus, *Zeitschrift für Krist.* 2014, 229, 345–352.
- [12] G. M. Sheldrick, *Acta Crystallogr. Sect. C Struct. Chem.* 2015, 71, 3–8.
- [13] K. Momma, F. Izumi, *J. Appl. Crystallogr.* 2011, 44, 1272–1276.
- [14] J. Gonzalez-Platas, M. Alvaro, F. Nestola, R. Angel, *J. Appl. Crystallogr.* 2016, 49, 1377–1382.
- [15] G. Kresse, J. Furthmüller, *Phys. Rev. B - Condens. Matter Mater. Phys.* 1996, 54, 11169–11186.
- [16] G. Kresse, D. Joubert, *Phys. Rev. B - Condens. Matter Mater. Phys.* 1999, 59, 1758–1775.
- [17] J. P. Perdew, K. Burke, M. Ernzerhof, *Phys. Rev. Lett.* 1996, 77, 3865–3868.
- [18] A. Togo, I. Tanaka, *Scr. Mater.* 2015, 108, 1–5.
- [19] S. Yu, B. Huang, Q. Zeng, A. R. Oganov, L. Zhang, G. Frapper, *J. Phys. Chem. C* 2017, 121, 11037–11046.
- [20] S. Wei, D. Li, Z. Liu, X. Li, F. Tian, D. Duan, B. Liu, T. Cui, *Phys. Chem. Chem. Phys.* 2017, 19, 9246–9252.
- [21] Y. Chen, X. Cai, H. Wang, H. Wang, H. Wang, *Sci. Rep.* 2018, 8, 10670.
- [22] X. Shi, Z. Yao, B. Liu, *J. Phys. Chem. C* 2020, 124, 4044–4049.
- [23] X. Du, Y. Yao, J. Wang, Q. Yang, G. Yang, *J. Chem. Phys.* 2021, 154, 054706.
- [24] D. Durach, W. Schnick, *Eur. J. Inorg. Chem.* 2015, 2015, 4095–4100.
- [25] W. C. Hamilton, *Acta Crystallogr.* 1965, 18, 502–510.

5.6. Synthesis of LaCN_3 , TbCN_3 , CeCN_5 and TbCN_5 polycarbonitrides at megabar pressures

This section contains the following manuscript and the related supplementary material:

“Synthesis of LaCN_3 , TbCN_3 , CeCN_5 and TbCN_5 polycarbonitrides at megabar pressures”

A. Aslandukov, A. Liang, A. Ehn, F. Trybel, Y. Yin, A. Aslandukova, F. I. Akbar, U. Ranieri, J. Spender, R. T. Howie, E. L. Bright, J. Wright, G. Garbarino, M. Mezouar, T. Fedotenko, I. A. Abrikosov, N. Dubrovinskaia, L. Dubrovinsky, D. Laniel.

Status: published in *Journal of the American Chemical Society*, 146(26), 18161–18171

(2024)

Reproduced under the terms and conditions of the Creative Commons ‘CC BY 4.0’

Synthesis of LaCN_3 , TbCN_3 , CeCN_5 , and TbCN_5 Polycarbonitrides at Megabar Pressures

Andrey Aslandukov,^{*,∇} Akun Liang,^{*,∇} Amanda Ehn, Florian Trybel, Yuqing Yin, Alena Aslandukova, Fariia I. Akbar, Umbertoluca Ranieri, James Spender, Ross T. Howie, Eleanor Lawrence Bright, Jonathan Wright, Michael Hanfland, Gaston Garbarino, Mohamed Mezouar, Timofey Fedotenko, Igor A. Abrikosov, Natalia Dubrovinskaia, Leonid Dubrovinsky, and Dominique Laniel

Cite This: *J. Am. Chem. Soc.* 2024, 146, 18161–18171

Read Online

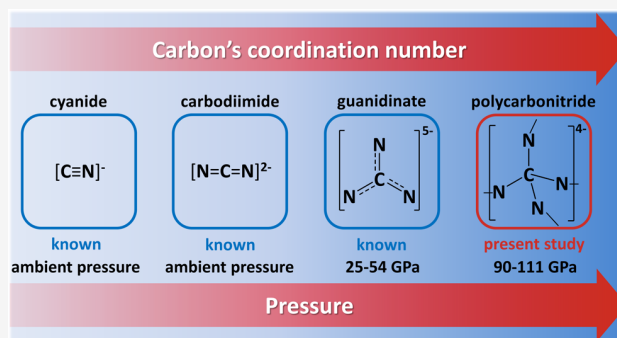
ACCESS |

Metrics & More

Article Recommendations

Supporting Information

ABSTRACT: Inorganic ternary metal–C–N compounds with covalently bonded C–N anions encompass important classes of solids such as cyanides and carbodiimides, well known at ambient conditions and composed of $[\text{CN}]^-$ and $[\text{CN}_2]^{2-}$ anions, as well as the high-pressure formed guanidates featuring $[\text{CN}_3]^{5-}$ anion. At still higher pressures, carbon is expected to be 4-fold coordinated by nitrogen atoms, but hitherto, such CN_4 -built anions are missing. In this study, four polycarbonitride compounds (LaCN_3 , TbCN_3 , CeCN_5 , and TbCN_5) are synthesized in laser-heated diamond anvil cells at pressures between 90 and 111 GPa. Synchrotron single-crystal X-ray diffraction (SCXRD) reveals that their crystal structures are built of a previously unobserved anionic single-bonded carbon–nitrogen three-dimensional (3D) framework consisting of CN_4 tetrahedra connected via di- or oligo-nitrogen linkers. A crystal-chemical analysis demonstrates that these polycarbonitride compounds have similarities to lanthanide silicon phosphides. Decompression experiments reveal the existence of LaCN_3 and CeCN_5 compounds over a very large pressure range. Density functional theory (DFT) supports these discoveries and provides further insight into the stability and physical properties of the synthesized compounds.



INTRODUCTION

In recent years, advancements in the high-pressure chemistry of nitrides and carbides have unveiled a wealth of surprises. Indeed, at pressures above 50 GPa, many exotic oligo- and polynitrides (i.e. containing N_4^{4-} , N_6^{6-} , N_8^{6-} anions,^{1,2} N_6 rings,^{3–5} N_{18} macrocycle,⁶ infinite one-dimensional (1D)-polynitrogen chains,^{1,7–12} and two-dimensional (2D)-polynitrogen layers^{2,12}) as well as polycarbides (i.e. containing graphene-, polyacene-, and para-poly(indenoindene)-like ribbons^{13–16}) were discovered. Recently discovered binary carbon nitrides C_3N_4 and CN_2 , built of CN_4 tetrahedra and synthesized at pressures above 70 GPa,¹⁷ possess many remarkable physical properties, such as superhardness, ultra-incompressibility, photoluminescence, piezoelectricity, and superconductivity, making these multifunctional materials candidates for technological applications, considering that they are recoverable to ambient conditions. A recent high-pressure study of the H–C–N system shows that the addition of another element, namely, hydrogen, helps to produce CN_4 tetrahedra frameworks at lower pressures.¹⁸ The addition of metal atoms to carbon nitrides is expected to enable tuning and controlling of the physical properties of such materials.

Therefore, exploration of the ternary metal–C–N systems at high pressures is very promising.

Ternary metal–C–N compounds with covalently bonded C–N anions at ambient conditions encompass important classes of solids such as cyanides (with CN^- anions)^{19,20} and carbodiimides (with NCN^{2-} anions).^{21–27} Recently, this family of species was extended with the discovery of the CN_3^{5-} anion, synthesized at mild pressures (25–54 GPa) and recoverable to ambient conditions.^{28,29} Knowing that C–N compounds built of CN_4 tetrahedra were obtained at pressures above 70 GPa,¹⁷ as well as the fact that mild pressures (up to 54 GPa) are insufficient for the formation of C–N anions with a tetra-coordinated carbon,²⁹ the stabilization of CN_4^{8-} units,³⁰ or/and the formation of polycarbonitrides built of corner/edge-sharing CN_4 tetrahedra in ternary metal–C–N systems are

Received: May 3, 2024
Revised: June 3, 2024
Accepted: June 10, 2024
Published: June 25, 2024



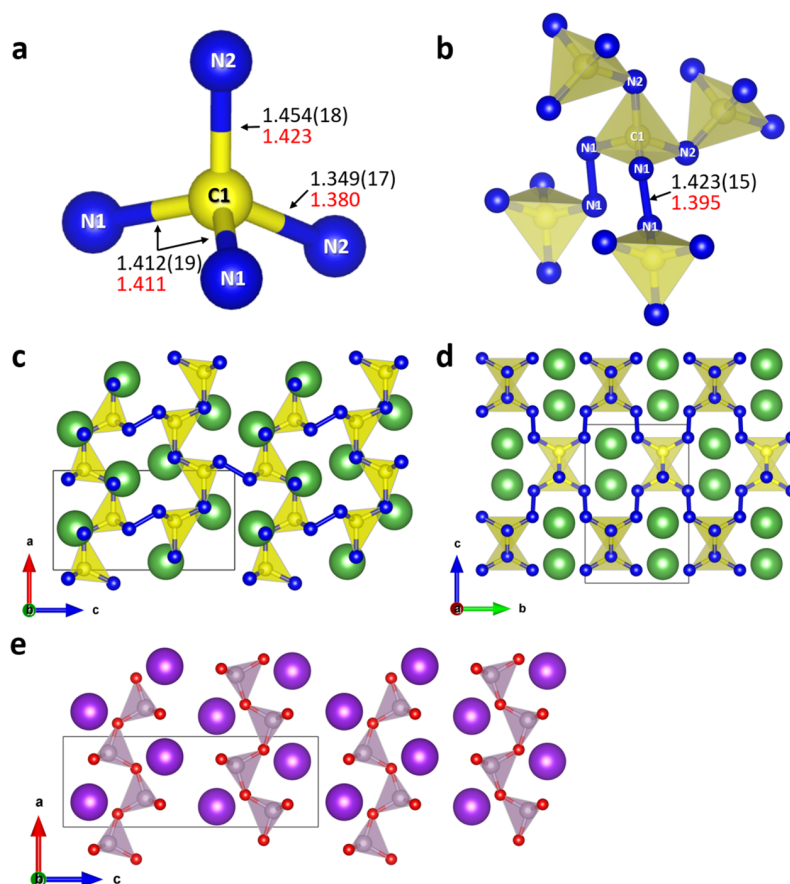


Figure 1. Crystal structure of LaCN_3 at 102(2) GPa and that of the high-temperature phase of $Pnma\text{-KPO}_3$ at ambient pressure. LaCN_3 : (a) Representation of the main building block—the CN_4 tetrahedron. (b) Connectivity of the CN_4 tetrahedra. Values of bond lengths obtained from the experiment are shown in black, while those obtained from the DFT calculations are shown in red. (c, d) Views along the crystallographic b - and a -axes. La atoms are shown as green spheres, C atoms as yellow spheres, and all N atoms (both N1 and N2) as blue spheres; the thin black lines outline the unit cell. (e) Crystal structure of $Pnma\text{-KPO}_3$ at 1 atm³⁴ viewed along the crystallographic b -axis. K atoms are shown as purple spheres, P atoms as gray spheres, and O atoms as red spheres; the thin black lines outline the unit cell.

expected at pressures above 70 GPa. The discovery of such compounds might be interesting not only for chemical and materials sciences but also for planetary sciences since these solids can potentially be formed at the boundaries between the rock core and the methane-ammonia-rich mantle of ice-giant planets.

Here we present the high-pressure, high-temperature synthesis and characterization of four hitherto unknown lanthanide polycarbonitrides, LaCN_3 , TbCN_3 , CeCN_5 , and TbCN_5 , at megabar pressures. Their crystal structures were solved and refined based on synchrotron single-crystal X-ray diffraction, unveiling previously unobserved anionic single-bonded carbon–nitrogen three-dimensional (3D) frameworks consisting of CN_4 tetrahedra connected via di- or oligo-nitrogen linkers. A crystal-chemical analysis demonstrates that polycarbonitride compounds have similarities with lanthanide silicon phosphides. Density functional theory (DFT) calculations cross-validate these discoveries and provide further insight into the stability and physical properties of these compounds.

RESULTS AND DISCUSSION

In this study, diamond anvil cells (DACs) were loaded with rare earth metal pieces (La, Tb, and Ce) embedded in molecular nitrogen (N_2) or cyanuric triazide (C_3N_{12} ; see the

Methods Section for details). The samples were compressed to target pressures between 90 and 111 GPa, and the samples were laser-heated to temperatures reaching 2500 K (Table S1). The resulting multigrain samples, consisting of hundreds of submicron-sized crystallites of the reaction products, were studied by synchrotron single-crystal X-ray diffraction (SCXRD) at the P02.2 beamline of DESY and the ID11, ID15b, and ID27 beamlines of the ESRF. The analysis of the SCXRD data revealed the formation of four metal polycarbonitrides, LaCN_3 , TbCN_3 , CeCN_5 , and TbCN_5 . The refinement against SCXRD data (Figures S1–S4) yields very good agreement factors (see Tables S2–S5 and CIFs for the full crystallographic data). The carbon atoms in the discovered polycarbonitrides originate from the diamond anvils, well known to be able to act as a carbon source and participate in chemical reactions.^{17,28,29,31–33} The description of other reaction products, e.g. binary polynitrides, will be discussed elsewhere.

The isostructural LaCN_3 and TbCN_3 solids crystallize in orthorhombic space group $Pnma$ (#62). The lattice parameters of LaCN_3 are $a = 4.1059(12)$ Å, $b = 4.870(5)$ Å, and $c = 7.4758(15)$ Å at 102(2) GPa, while those of TbCN_3 are $a = 3.9813(15)$ Å, $b = 4.7305(12)$ Å, and $c = 7.2358(15)$ Å at 111(2) GPa. The crystal structure of LaCN_3 at 102(2) GPa is described below as an example (Figure 1). LaCN_3 consists of

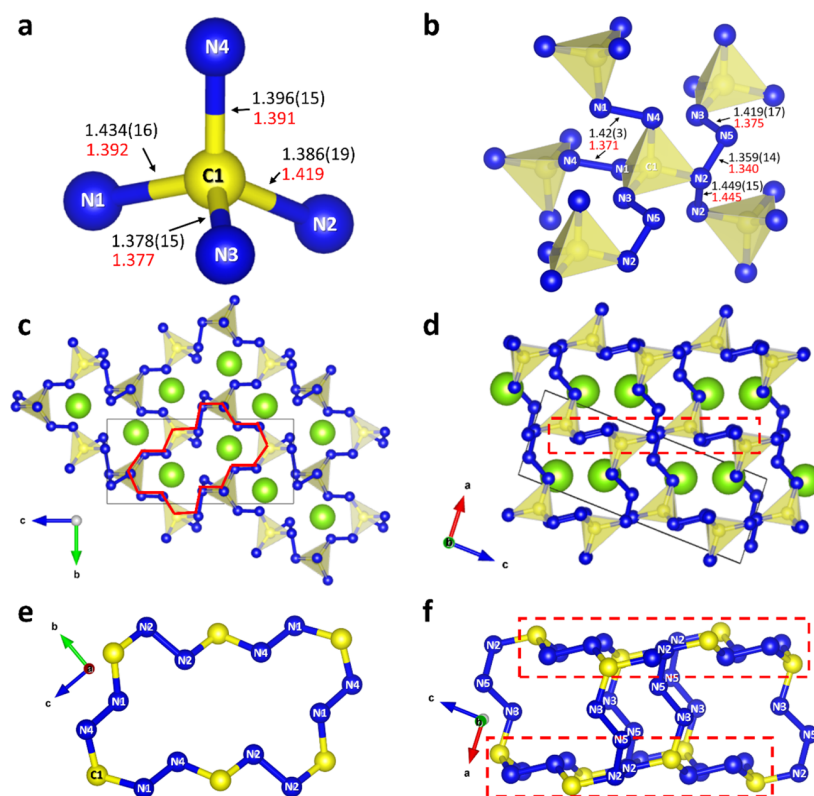


Figure 2. Crystal structure of CeCN_5 at 90(2) GPa. (a) Representation of the main building block—the CN_4 tetrahedron. (b) Connectivity of the CN_4 tetrahedra. Values of bond lengths obtained from the experiment are shown in black, while those obtained from the DFT calculations are shown in red. (c, d) Crystal structure of CeCN_5 viewed along the crystallographic a - and b -axes. The full red line in (c) helps visualize the atoms constituting the C_6N_{12} rings, highlighted in (d) by a red dashed line. The thin black lines outline the unit cell. (e) Depiction of the carbonitride network's C_6N_{12} ring, when viewed along the crystallographic a -axis. (f) Two adjacent C_6N_{12} rings interconnected through N5-N3 dimers, viewed along the crystallographic b -axis. Cerium, carbon, and nitrogen atoms are represented as light green, yellow, and blue spheres, respectively.

four crystallographically distinct atoms: La1, C1, N1, and N2 (see Table S2 and the CIF for the full crystallographic data). Carbon atoms are 4-fold coordinated by nitrogen atoms, forming irregular CN_4 tetrahedra named mirrored sphenoids (Figure 1a). Both N1 and N2 atoms form two single covalent bonds: the N1 atoms form one N1–C1 and one N1–N1 bond between two N1 atoms of different tetrahedra, while the N2 atoms are the common nodes of corner-sharing CN_4 tetrahedra, thus being bonded with two carbon atoms (Figure 1b). The average C–N distance within the CN_4 tetrahedra is $d_{\text{C-N}} = 1.407(9)$ Å, and the N1–N1 bond length between N1 atoms of different tetrahedra is $d_{\text{N-N}} = 1.423(15)$ Å at 102(2) GPa. The average N–C–N and C–N–C/N bond angles are $109.5(4)$ and $111.6(10)^\circ$, respectively. Thus, all nonmetal atoms are sp^3 -hybridized. Lanthanum is 11-fold coordinated by nitrogen atoms. Since all N atoms form two single covalent bonds, each nitrogen atom has a charge of -1 in the fully ionic approximation, in turn implying the expected $+3$ oxidation state for the La atoms. Carbon, which makes four covalent bonds, is neutral. The bond order analysis for TbCN_3 gives the same charge distribution as for LaCN_3 , suggesting a $+3$ oxidation state for Tb, one of two well-known oxidation states for this element. The repeating CN_3^{3-} unit in LaCN_3 and TbCN_3 , as well as its Lewis formula, are presented in Figure S5a,b.

The structure can be described as being built of corner-sharing CN_4 tetrahedra chains running along the crystallographic a -axis. These chains are interconnected through the

N1–N1 single bonds (Figure 1c). Each chain is linked to four other chains, producing a 3D framework (Figure 1d). Lanthanum atoms are located in the voids of this covalent 3D framework and each surrounded by nine CN_4 tetrahedra. The structure of LaCN_3 has similarities with that of the high-temperature $Pnma$ - KPO_3 phase.³⁴ In the latter, atoms are sitting on the same Wyckoff positions as in LaCN_3 , with the nonmetal atoms forming PO_4 tetrahedra arranged in infinite chains along the crystallographic a -axis through corner-sharing (Figure 1e). However, there are no covalent O–O bonds between the chains, and the distance between these PO_4 corner-sharing chains is larger.

The isostructural compounds CeCN_5 and TbCN_5 crystallize in the monoclinic space group $P2_1/n$ (#14) with one lanthanide atom (Ce1 or Tb1), one carbon atom (C1), and five nitrogen atoms (N1 through N5) being crystallographically unique and all located on the $4e$ Wyckoff position (Tables S4 and S5). At a pressure of 90(2) GPa, the lattice parameters of CeCN_5 are as follows: $a = 3.889(1)$ Å, $b = 4.740(1)$ Å, $c = 10.487(6)$ Å, and $\beta = 94.41(4)^\circ$ ($V = 192.72(13)$ Å³). At a pressure of 111(2) GPa, TbCN_5 has lattice parameters of $a = 3.8334(2)$ Å, $b = 4.5221(9)$ Å, $c = 10.3516(5)$ Å, and $\beta = 94.699(5)^\circ$ ($V = 178.84(4)$ Å³). The crystal structure of CeCN_5 at 90(2) GPa is described hereafter as an example of this structure type (Figure 2).

Each C1 atom in the structure of CeCN_5 (Figure 2) is surrounded by four nitrogen atoms (N1–N4), forming a CN_4 tetrahedron with C–N single bonds of lengths ranging from

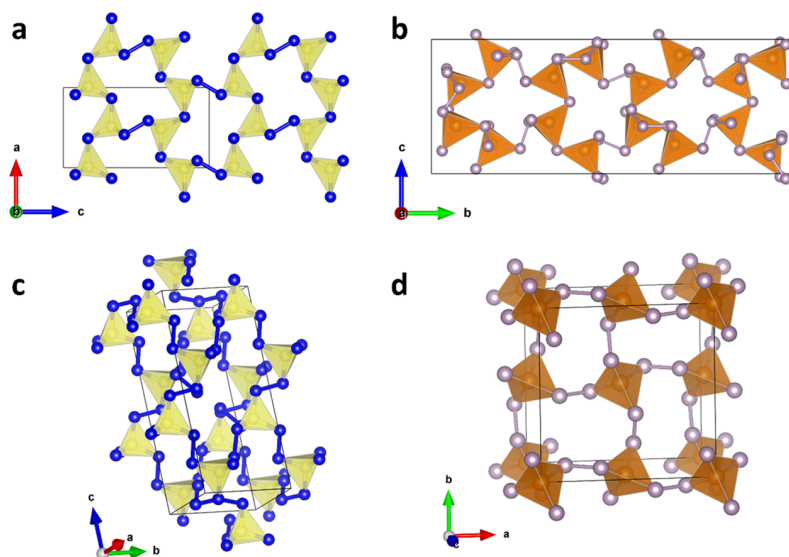


Figure 3. Anionic frameworks of the pairs of compounds with similar connectivity of tetrahedra: (a) $\text{LaCN}_3/\text{TbCN}_3$ and (b) $Cmc2_1\text{-LaSi}_2\text{P}_6$, both built of the 3D framework of corner-sharing CN_4 or SiP_4 tetrahedra connected via N–N or P–P linkers; (c) $\text{CeCN}_5/\text{TbCN}_5$ and (d) $I-42d\text{-Eu}_2\text{SiP}_4$ consisting of CN_4 or SiP_4 tetrahedra linked exclusively via N–N or P–P bonds, producing a 3D framework. The C, N, Si, and P atoms are shown as yellow, blue, light brown, and gray balls, respectively. The thin black lines outline the unit cell.

1.378(15) to 1.434(16) Å (Figure 2a). The N–C–N bond angle varies between $104.4(10)$ and $119.4(13)^\circ$, with an average value of $109.5(5)^\circ$. Among the five crystallographically distinct nitrogen atoms, only N2 forms three bonds (Figure 2b): two with nitrogen atoms and one with the C1 carbon atom, for an average bond angle of $108.1(6)^\circ$. All other nitrogen atoms form two single bonds (Figure 2b): N5—with two nitrogen atoms (bond angle: $103.3(9)^\circ$), while each of the remaining three nitrogen atoms (N1, N3, and N4)—with one nitrogen atom and one carbon atom (bond angles: $109.9(10)$, $115.1(10)$, and $103.8(10)^\circ$, respectively). The 3D polycarbonitride framework in CeCN_5 is built of CN_4 tetrahedra linked by single covalent N2–N2 and N4–N1 bonds as well as through N2–N5–N3 trimer bridges (Figure 2b). Analogously to the LaCN_3 and TbCN_3 compounds, all nonmetal atoms in CeCN_5 and TbCN_5 are sp^3 -hybridized.

When viewed along the a -axis, the structure of CeCN_5 is seen to be composed of large corrugated C_6N_{12} rings. The rings are elongated in a direction close to $[011]$ and arranged in a herringbone pattern (Figure 2c). Each of these C_6N_{12} rings is constituted of six carbon atoms linked through N–N dimers (Figure 2e). There are two distinct dimers within the C_6N_{12} rings, the N2–N2 and the N4–N1 dimers, each with a bond length of 1.449(15) and 1.422(30) Å, respectively, suggesting a single-bond character. Single-bonded N3–N5 dimers (1.419(17) Å) connect the adjacent C_6N_{12} units so that the N3 and N5 atoms are bonded to the C1 and N2 atoms of the C_6N_{12} rings, respectively (Figure 2d,f). Although the N2–N5 bond (1.359(14) Å) is distinctively shorter than other N–N bonds in CeCN_5 , its length is still within the single-bond lengths range.^{2,35,36} Cerium atoms, located between the layers built of C_6N_{12} rings, are 12-fold coordinated with nitrogen, featuring an average bond length of 2.351(11) Å.

With four of the five nitrogen atoms only making two single bonds, it stands to reason that in the ionic approximation, the repeating CN_5 unit bears a charge of -4 , indicative of a $+4$ oxidation state for Ce, one of its two commonly observed oxidation states. In TbCN_5 , the bond order as well as the

hybridization of the C and N is identical to that described in CeCN_5 . Thus, TbCN_5 is composed of the same $[\text{CN}_5]_{\infty}^{4-}$ anion, suggesting a $+4$ oxidation state for Tb, which is also well known for this element. The repeating CN_5^{4-} unit in CeCN_5 and TbCN_5 and its Lewis formula are presented in Figure S5c,d.

Similarly to recently discovered high-pressure C_3N_4 polymorphs,¹⁷ the common building block in LaCN_3 , TbCN_3 , CeCN_5 , and TbCN_5 is the CN_4 tetrahedron. The C–N single-bond lengths and N–C–N bond angles in LaCN_3 , TbCN_3 , CeCN_5 , and TbCN_5 are also similar to those found in the C_3N_4 polymorphs at similar pressures. While the condensed 3D framework in the C_3N_4 solids is built exclusively of corner-sharing tetrahedra, the connectivity of these tetrahedra in the polynitrides discovered here is different. The 3D anionic polycarbonitride framework of LaCN_3 and TbCN_3 is built by corner-sharing CN_4 as well as by N–N bonds (Figure 1b). In the CeCN_5 and TbCN_5 structures, the CN_4 tetrahedra do not have common nodes and are linked only by single covalent nitrogen bonds having two types of linkers: dimers and trimers (Figure 2b).

Among the metal–C–N ternary compounds, hitherto exclusively featuring isolated anions (i.e., cyanides, carbodiimides, and guanidates), the LaCN_3 , TbCN_3 , CeCN_5 , and TbCN_5 solids form a novel unique class of compounds composed of a 3D single-bonded polycarbonitride framework. The geometry of the C–N anions illustrates well how high pressure stabilizes higher coordination numbers of carbon. In the $\text{N}=\text{C}=\text{N}^-$ anion, which is stable under ambient conditions, the C atom is coordinated by two N atoms. At mild pressures (25–54 GPa), the CN_3^{5-} anion is formed with carbon having a coordination number of three. Here, at higher pressures (90–111 GPa), we observe 4-fold coordinated carbon atoms in the crystal structures of LaCN_3 , TbCN_3 , CeCN_5 , and TbCN_5 . Strikingly, despite the theoretical predictions of the high-pressure stabilized CN_4^{8-} orthonitridocarbonate anion,³⁰ we do not observe its formation. This suggests that while CN_4 units are indeed the preferred 3D

building blocks, their concatenation is more favorable than preserving significantly negatively charged anions, such as CN_4^{8-} .

According to the ninth high-pressure chemistry rule of thumb formulated in 1998: "Elements behave at high pressures like the elements below them in the periodic table at lower pressures",³⁷ carbon and nitrogen under high pressure should behave like silicon and phosphorus at lower pressures. Therefore, one can expect similarities between the high-pressure LaCN_3 , TbCN_3 , CeCN_5 , and TbCN_5 compounds and the ternary Ln–C–P, Ln–Si–N, and Ln–Si–P solids (Ln represents lanthanide elements) known under ambient conditions.

To date, there are no known Ln–C–P compounds with covalent C–P frameworks. As for the ternary Ln–Si–N compounds, these belong to the class of nitridosilicates,³⁸ which significantly grew during the last two decades. According to the ICSD, there are six known structure types of lanthanide nitridosilicates: Eu_2SiN_3 ,³⁹ $\text{Eu}_2\text{Si}_2\text{N}_8$,⁴⁰ $\text{Ln}_3\text{Si}_3\text{N}_9$ (Ln = La, Ce, Pr),^{41,42} $\text{Ln}_7\text{Si}_6\text{N}_{15}$ (Ln = La, Ce, Pr),⁴³ $\text{Ln}_3\text{Si}_6\text{N}_{11}$ (Ln = La, Ce, Pr, Nd, Sm),⁴⁴ and LnSi_3N_5 (Ln = La, Ce, Nd).⁴⁴ The crystal structures of all mentioned compounds are built of corner-sharing SiN_4 tetrahedra forming 1D chains (Eu_2SiN_3), 2D layers ($\text{Ln}_3\text{Si}_3\text{N}_9$), or 3D frameworks ($\text{Eu}_2\text{Si}_2\text{N}_8$, $\text{Ln}_7\text{Si}_6\text{N}_{15}$, $\text{Ln}_3\text{Si}_6\text{N}_{11}$, and LnSi_3N_5). Although the building block— SiN_4 tetrahedra—is similar to the CN_4 building block in LaCN_3 , TbCN_3 , CeCN_5 , and TbCN_5 , the important difference is the presence of N–N linkers in the latter, which have never been observed in nitridosilicates.

Considering the building blocks and their connectivity, the closest analogues to the polycarbonitrides discovered here would be ternary Ln–Si–P compounds. According to the ICSD, there are four known structure types of ternary Ln–Si–P compounds built of chains, layers, or 3D frameworks of SiP_4 tetrahedra linked, in particular, by P–P bonds: $P2_1/c\text{-LaSiP}_3$,⁴⁵ $Cmc2_1\text{-LnSi}_2\text{P}_6$ (Ln = La, Ce, Pr),^{46,47} $P2_1/c\text{-La}_2\text{SiP}_4$,⁴⁸ and $I-42d\text{-Eu}_2\text{SiP}_4$.⁴⁹ Although none of them are isotypic to LaCN_3 / TbCN_3 or CeCN_5 / TbCN_5 , some of the anionic motifs of these Ln–Si–P compounds have a tetrahedra connectivity similar to that observed in LaCN_3 / TbCN_3 and CeCN_5 / TbCN_5 . Topologically, the closest analogue to LaCN_3 and TbCN_3 is $Cmc2_1\text{-LaSi}_2\text{P}_6$,⁴⁷ which is built of a 3D framework of corner-sharing SiP_4 tetrahedra and P–P linkers (Figure 3a,b). The closest topological analogue to CeCN_5 and TbCN_5 is $I-42d\text{-Eu}_2\text{SiP}_4$,⁴⁹ which consists of SiP_4 tetrahedra linked exclusively via P–P bonds into a 3D framework (Figure 3c,d).

To get a deeper insight into the stability and physical properties of the novel compounds, DFT calculations were performed using the Vienna Ab initio Simulation Package (VASP)⁵⁰ for LaCN_3 and CeCN_5 . Due to the presence of 4f electrons in Ce and Tb, their compounds require higher-level theory. CeCN_5 can be sufficiently well described with the DFT + U method.⁵¹ However, it has been shown that Tb is not sufficiently well described by DFT + U ⁵² and requires higher-level theory, e.g., DFT + dynamical mean field theory (DMFT).⁵³ The latter is computationally very expensive and requires particular expertise in using it. For this reason, TbCN_3 and TbCN_5 are not investigated through theoretical calculations in this study. The relaxed structure parameters obtained from the variable-cell structure relaxations of LaCN_3 and CeCN_5 compounds closely reproduce the corresponding experimental values (Tables S6 and S7), confirming the validity of our computational methodology.

To trace the structures' behavior at lower pressures and to obtain their equation of state, full variable-cell structure relaxations for the LaCN_3 and CeCN_5 compounds were performed with 10 GPa pressure steps between 0 and 120 GPa (Figure 4). The lattice parameters of LaCN_3 change

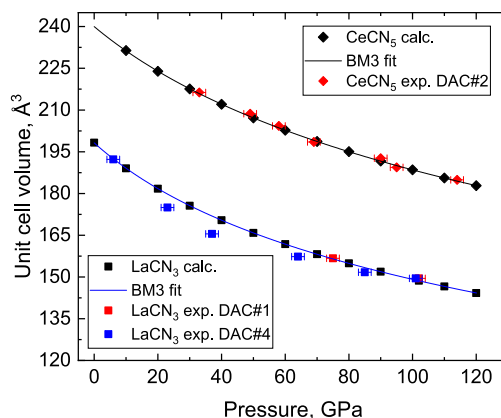


Figure 4. Pressure dependence of the unit cell volume of LaCN_3 and CeCN_5 . The black symbols represent calculated data points obtained from DFT, and the red and blue symbols represent experimental data points obtained from SCXRD data. The black and blue lines are fits of the DFT data with a third-order Birch–Murnaghan equation of state. The parameters of the fit for LaCN_3 are $V_0 = 198.19(4) \text{ \AA}^3$, $K_0 = 192.5(6) \text{ GPa}$, and $K_p = 4.214(12)$, while for CeCN_5 , they are $V_0 = 239.98(9) \text{ \AA}^3$, $K_0 = 250.7(14) \text{ GPa}$, and $K_p = 4.14(3)$.

monotonously in the whole pressure range (Figure S8) and the crystal structure does not undergo any significant changes, indicating the possible recoverability of LaCN_3 to ambient conditions. That is also suggested from phonon calculations: LaCN_3 is dynamically stable both, at the synthesis pressure and at ambient pressure (Figure S6). On the other hand, CeCN_5 is relaxable without structural changes only down to 10 GPa, with its lattice parameters changing monotonously down to that pressure (Figure S9). CeCN_5 is also found to be dynamically stable at its synthesis pressure of 90 and 10 GPa (Figure S7). However, below 10 GPa, full variable-cell structure relaxation resulted in a possible electronic transition in which the 4f electron state is promoted from above the Fermi energy to below (Figure SD1 in Supporting Discussion). It is reminiscent of the promotional model of Zachariassen and Pauling of a $\gamma \leftrightarrow \alpha$ transition in pure Ce,^{54–57} though in CeCN_5 the transition occurs upon decompression and leads to a significant modification of the crystal structure of the compound (Figure SD2 in Supporting Discussion). The above observations make CeCN_5 as well as potentially TbCN_3 and TbCN_5 compounds of high interest for investigations of many-electron effects in these systems at the higher level of the electronic structure theory, e.g., within the DFT + DMFT.⁵³ An accurate theoretical description of the electronic structure and vibrational and structural properties of the compounds with occupied f -states is therefore outside of the scope of the present study.

The volume-pressure dependences of the DFT-relaxed structures of LaCN_3 and CeCN_5 in the pressure range of 0–120 GPa and 10–120 GPa, respectively, were fitted with a third-order Birch–Murnaghan equation of state (Figure 4). The obtained bulk moduli ($K_0(\text{LaCN}_3) = 192.5(6) \text{ GPa}$, $K_0(\text{CeCN}_5) = 250.7(14) \text{ GPa}$) are higher than the bulk moduli

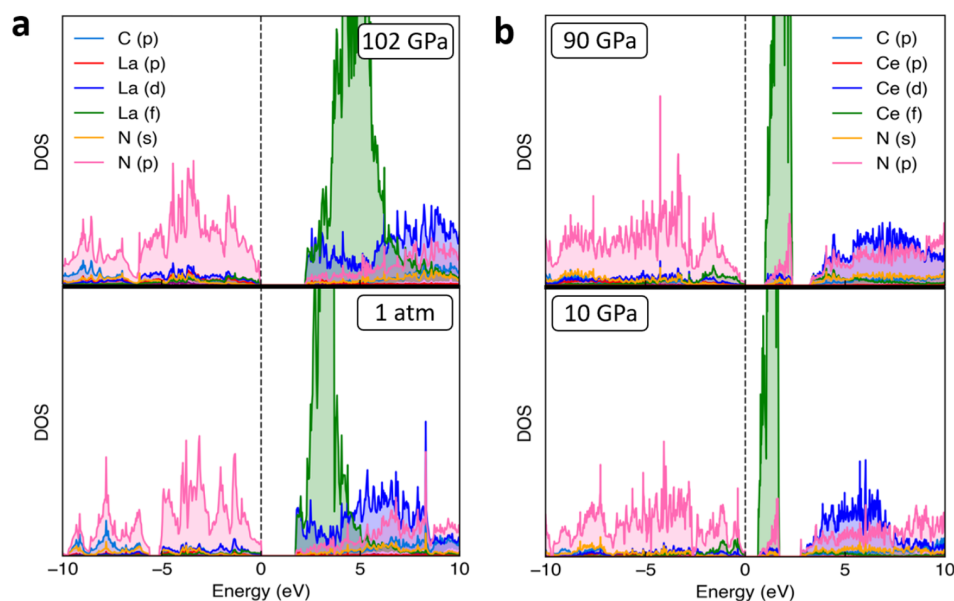


Figure 5. Electron density of states of (a) LaCN_3 at 102 GPa and 1 bar, and (b) CeCN_5 at 90 and 10 GPa.

of known nitrides and carbides of lanthanum (LaN ,⁵⁸ La_2C_3 ,⁵⁹ LaC_2 ⁵⁹) and cerium (CeN ,⁶⁰ CeC ,⁵⁹ Ce_2C_3 ,⁵⁹ CeC_2 ⁵⁹) due to the presence of robust polycarbonitride 3D frameworks with relatively incompressible short C–N and N–N bonds. At the same time, the obtained bulk moduli are lower than the bulk moduli of the ultraincompressible C–N solids,¹⁷ likely because of the dilution of the C–N framework with metal ions. The degree of this dilution is higher in the case of LaCN_3 since the ratio between metal cations and the framework-forming C and N atoms is higher in LaCN_3 than in CeCN_5 , which explains the significant difference in the bulk moduli of LaCN_3 and CeCN_5 . Another reason for the enhancement of K_0 in CeCN_5 compared to the K_0 of LaCN_3 is the smaller size of the Ce^{4+} cation compared to that of La^{3+} and, as a consequence, shorter and less compressible metal–N bonds.

Considering the dynamical stability at 1 bar and the smooth behavior of the lattice parameters of DFT variable-cell relaxed structures down to ambient pressure, a first attempt to experimentally verify the recoverability of LaCN_3 was undertaken. Upon sample decompression, a data point at 75(2) GPa was successfully collected (Table S8). The unit cell volume of LaCN_3 at 75(2) GPa perfectly matches the DFT-calculated equation of state (Figure 4). However, when the pressure was decreased to 50(2) GPa, the sample chamber collapsed, and it was no longer possible to continue the experiment (see footnote of Table S8). After an unsuccessful decompression experiment, another DAC#4 was prepared and loaded with a lanthanum piece embedded in solid cyanuric triazide (C_3N_{12}). Cyanuric triazide serves as a precursor of nitrogen (and might be carbon as well) for the synthesis of LaCN_3 as well as a “hard” solid pressure transmission medium. The same P and T conditions were used for the synthesis: the sample was compressed to 101(2) GPa and laser-heated to temperatures reaching up to 2500 K (Table S1). According to synchrotron single-crystal XRD, the LaCN_3 phase was formed (Table S8). Subsequently, DAC#4 was decompressed, and LaCN_3 was preserved in the cell down to 6(2) GPa. Notably, upon the decompression of DAC#4, the unit cell volume of LaCN_3 lay systematically below the DFT-calculated equation of state curve, due to residual stresses in the hard pressure transmitting

medium (Figure 4). Below 6(2) GPa, the cell was opened in an Ar glovebox and closed again to avoid an interaction with oxygen and moisture. According to the XRD measurements, LaCN_3 was no longer present. Therefore, LaCN_3 exists at least down to 6(2) GPa, but was not found recoverable under ambient conditions.

DAC#2, containing the CeCN_5 compound, was first compressed from 90(2) to 115(2) GPa and then decompressed, allowing data collection from 115(2) to 33(2) GPa. Below that pressure, the sample escaped the experimental chamber, preventing further measurements from being done. In total, seven P – V data points were collected for the CeCN_5 phase, found to persist even down to 33(2) GPa (Table S9). The experimental data agree well with the DFT-calculated equation of state (Figure 4). No decompression experiment was carried out for DAC#3, containing the TbCN_3 and TbCN_5 compounds.

The computed electron densities of states for LaCN_3 and CeCN_5 at the synthesis pressure and at low pressure are shown in Figure 5. LaCN_3 has band gaps of 2.2 and 1.7 eV at 102 GPa and 1 atm, respectively. CeCN_5 has a gap between the valence and conduction bands that is 3.2 eV at the synthesis pressure. Between the valence and conduction bands lie the unoccupied Ce 4f states. The gap from the valence band to the edge of the 4f band is 1 eV, and the 4f peak has a width of 1.4 eV. Upon decompression to 10 GPa, the band gap between the valence and conduction band decreases to 2.7 eV. The gap from the valence band to the 4f band edge is 0.6 eV, and the 4f peak has a width of 1.1 eV. The exact position of the unoccupied 4f peak is influenced by the choice of the U value. A higher value of U shifts the peak away from the Fermi energy. A larger value of U also slightly decreases the gap between the valence and conduction band. A similar effect of shifting the 4f peak and decreasing the band gap has also been observed in studies on CeO_2 .⁵¹ Both LaCN_3 and CeCN_5 compounds demonstrate a pressure-induced band gap opening.

CONCLUSIONS

In this study, the four compounds LaCN_3 , TbCN_3 , CeCN_5 , and TbCN_5 (first representatives of the class of polycarbonitrides) were synthesized in laser-heated diamond anvil cells at pressures between 90(2) and 111(2) GPa. Their crystal structures are built of a covalently single-bonded carbon–nitrogen anionic 3D framework consisting of CN_4 tetrahedra connected via di- or oligo-nitrogen linkers. From a crystal chemistry perspective, the closest ambient condition analogues of these polycarbonitrides are Ln–Si–P metal silicon phosphide ternary compounds.

According to DFT calculations, the CeCN_5 phase is dynamically stable down to 10 GPa and not stable under ambient conditions, while LaCN_3 is (meta)stable under ambient conditions. While experiments did not validate the recoverability of the LaCN_3 solid, one can expect that other high-pressure metal polycarbonitrides built of CN_4 connected only by vertexes or partially N–N connected can be recoverable, analogously to the high-pressure C_3N_4 polymorphs, and CN_2 compound containing N–N bonds. LaCN_3 and CeCN_5 are found to be semiconductors with a pressure-mediated band gap opening.

Due to the presence of hard polycarbonitride 3D frameworks with relatively incompressible short C–N and N–N bonds, LaCN_3 and CeCN_5 exhibit good mechanical properties with the bulk moduli higher than the bulk moduli of known nitrides or carbides of lanthanum and cerium. At the same time, the bulk moduli of lanthanide polycarbonitrides are lower than the bulk moduli of the ultraincompressible C–N solids,¹⁷ and dictated by the degree of dilution of the C–N framework with metal ions having longer and more compressible Ln–N contacts.

METHODS

Sample Preparation. BX90-type DACs⁶¹ equipped with Boehler-Almax type diamonds⁶² of 120 μm (DAC#1, DAC#2, DAC#4) and 80 μm (DAC#3) culet diameter were used in these experiments. The sample chambers were formed by preindenting rhenium gaskets, initially 200 μm in thickness, down to 15–18 μm and laser-drilling a hole of 60 μm (DAC#1, DAC#2, DAC#4) or of 40 μm (DAC#3) in diameter in the center of the indentation. Pieces of lanthanide metals (La, Ce, Tb, 99.9%, Sigma-Aldrich) were placed in the sample chamber of individual DACs (DAC#1, DAC#2, DAC#3) directly in contact with one of the two diamond anvils, and molecular nitrogen was then loaded using high-pressure gas loading systems at the Bayerisch Geoinstitut (BGI, 1300 bar)⁶³ or at the Centre for Science at Extreme Conditions (CSEC, 2000 bar). The Ce metal was loaded into the DAC in an Ar-filled glovebox, while La and Tb were loaded in air. DAC#4 was loaded with a lanthanum piece and solid cyanuric triazide (C_3N_{12}), and the lanthanum piece was placed in contact with one of the two diamond anvils. *Caution: Since the energetic cyanuric triazide compound is to some extent unstable against external stimuli, proper safety precautions should be taken especially when handling the materials in amounts exceeding those that are typically used for an experiment in a DAC. Laboratory personnel should wear protective equipment like grounded shoes, leather coats, Kevlar gloves, ear protection, and face shields.* The samples were compressed to their target pressure (Table S1) and laser-heated ($\lambda = 1064$ nm) up to 2500(500) K using a homemade laser-heating system at BGI⁶⁴ or in CSEC. The temperatures reached during laser heating were determined by fitting the sample's thermal emission spectrum to the gray body approximation of Planck's radiation function in a given wavelength range (570–830 nm). The pressure in the DACs was determined using the Raman signal from the diamond anvils⁶⁵ and additionally monitored by the X-ray diffraction signal of the Re gasket edge using rhenium's equation of state.⁶⁶

X-ray Diffraction. The X-ray diffraction studies were conducted at the P02.2 beamline of Petra III, DESY ($\lambda = 0.2904$ Å); the ID11 beamline ($\lambda = 0.2846$ Å), the ID15b beamline ($\lambda = 0.4099$ Å), and the ID27 beamline ($\lambda = 0.3738$ Å) of the Extreme Brilliant Source European Synchrotron Radiation Facility (EBS-ESRF). At the P02.2 beamline of DESY, the X-ray beam was focused down to $2 \times 2 \mu\text{m}^2$ and data was collected with a PerkinElmer 1621 XRD flat-panel detector. At the ID11 beamline of the ESRF, the X-ray beam was focused down to $0.75 \times 0.75 \mu\text{m}^2$ and data was collected with an Eiger2X CdTe 4 M hybrid photon counting pixel detector. At the ID15b beamline of ESRF, the X-ray beam was focused down to $1.5 \times 1.5 \mu\text{m}^2$ and data was collected with an Eiger2X CdTe 9 M hybrid photon counting pixel detector. At the ID27 beamline of the ESRF, the X-ray beam was focused down to $2 \times 2 \mu\text{m}^2$ and data was collected with an Eiger2X CdTe 9 M hybrid photon counting pixel detector. In order to determine on which sample position the SCXRD data should be collected, a full X-ray diffraction mapping of the pressure chamber was performed. The sample position displaying the most and the strongest single-crystal reflections belonging to the phase of interest was chosen for the collection of single-crystal data, collected in step scans of 0.5° from -36 to $+36^\circ$. The CrysAlis^{Pro} software package⁶⁷ was used for the analysis of the SCXRD data (peak hunting, indexing, data integration, frame scaling, and absorption correction). To calibrate the instrument model in the CrysAlis^{Pro} software, i.e., the sample-to-detector distance, detector's origin, offsets of the goniometer angles, and inclination of both the X-ray beam and detector with regard to the instrument axis, a single crystal of orthoestatite [$(\text{Mg}_{1.93}\text{Fe}_{0.06})(\text{Si}_{1.93}\text{Al}_{0.06})\text{O}_6$, *Pbca* space group, $a = 8.8117(2)$ Å, $b = 5.18320(10)$ Å, and $c = 18.2391(3)$ Å] was used. The DAFI program was used for the search of groups of reflections belonging to individual single-crystal domains.⁶⁸ With the OLEX2 software package,⁶⁹ structures were solved with the ShelXT structure solution program⁷⁰ using intrinsic phasing and refined with the ShelXL⁷¹ refinement package with the least-squares minimization. Crystal structure visualization was made with the VESTA software.⁷²

Theoretical Calculations. Calculations were carried out by the Vienna Ab initio simulation package (VASP),⁵⁰ using the projector augmented wave (PAW) method.⁷³ Table S10 contains information about the used POTCARs. For LaCN_3 , the GGA-PBE functional was used in standard DFT formalism.⁷⁴ For CeCN_5 , due to the presence of localized 4f electrons, the L(S)DA + *U* formalism as formulated by Dudarev et al. was employed to account for the on-site Coulomb repulsion.⁷⁵ The label (S) in L(S)DA + *U*, was omitted for simplicity. In the Dudarev et al. formalism, the LDA + *U* functional takes the form

$$E_{\text{LDA}+U} = E_{\text{LDA}} + \frac{U - J}{2} \sum_{\sigma} [\text{Tr}(\rho^{\sigma}) - \text{Tr}(\rho^{\sigma} \rho^{\sigma})]$$

where ρ is the density matrix of 4f states, and *U* and *J* are the spherically averaged matrix elements of the screened Coulomb electron–electron interaction.⁷⁵ Only the difference between *U* and *J* is significant, and thus, *U* – *J* is simply denoted as *U*. For CeCN_5 , a *U* = 6 eV was used. The value of *U* was chosen based on a semiempirical approach to agree with the experimental values of the lattice constants. The value 6 eV is also justified since values between 5 and 8 eV have been used in previous studies on, for example, pure Ce, Ce impurities in Ag and Pd, and CeO_2 .^{51,54–57,76} For both LaCN_3 and CeCN_5 compounds, spin-polarized calculations were employed to account for possible local magnetic moments. Calculations for structure relaxations and eDOS were done for the LaCN_3 and CeCN_5 compounds with a $6 \times 6 \times 6$ *k*-point mesh according to the Monkhorst–Pack method.⁷⁷ For the relaxations, a Gaussian smearing was used with a smearing of 0.03 eV. For eDOS calculations, the tetrahedron method of Blöchl was used.⁷⁸ The convergence criteria for the energy were set to 10^{-7} eV, and in structure relaxations, the forces on each ion were less than 10^{-3} eV/Å. These settings were used for both LaCN_3 and CeCN_5 . The plane-wave cutoffs were set to 680 eV for LaCN_3 and 740 eV for CeCN_5 . Phonons were calculated with the finite displacement method, with displacements generated by

phonopy.^{79,80} For both LaCN_3 and CeCN_5 , $2 \times 2 \times 2$ supercells were used with a k -mesh of $4 \times 4 \times 4$ k -points. Displacement amplitudes were 0.01 Å, as a default phonopy setting.

■ ASSOCIATED CONTENT

SI Supporting Information

The Supporting Information is available free of charge at <https://pubs.acs.org/doi/10.1021/jacs.4c06068>.

Summary of the performed DAC laser heating experiments; crystallographic information; dependence of the unit cell parameters of LaCN_3 and CeCN_5 with pressure; phonons dispersions; and supplementary discussion of CeCN_5 compound with occupied 4f states (PDF)

Accession Codes

CCDC 2352230–2352233 contain the supplementary crystallographic data for this paper. These data can be obtained free of charge via www.ccdc.cam.ac.uk/data_request/cif, by emailing data_request@ccdc.cam.ac.uk, or by contacting The Cambridge Crystallographic Data Centre, 12 Union Road, Cambridge CB2 1EZ, UK; fax: +44 1223 336033.

■ AUTHOR INFORMATION

Corresponding Authors

Andrey Aslandukov – Bavarian Research Institute of Experimental Geochemistry and Geophysics (BGI), University of Bayreuth, 95440 Bayreuth, Germany; Material Physics and Technology at Extreme Conditions, Laboratory of Crystallography, University of Bayreuth, 95440 Bayreuth, Germany; orcid.org/0000-0003-0988-6066; Email: andrii.aslandukov@uni-bayreuth.de

Akun Liang – Centre for Science at Extreme Conditions and School of Physics and Astronomy, University of Edinburgh, EH9 3FD Edinburgh, United Kingdom; Email: aliang@exseed.ed.ac.uk

Authors

Amanda Ehn – Department of Physics, Chemistry and Biology (IFM), Linköping University, SE-581 83 Linköping, Sweden

Florian Trybel – Department of Physics, Chemistry and Biology (IFM), Linköping University, SE-581 83 Linköping, Sweden

Yuqing Yin – Department of Physics, Chemistry and Biology (IFM), Linköping University, SE-581 83 Linköping, Sweden; orcid.org/0000-0001-8861-8443

Alena Aslandukova – Bavarian Research Institute of Experimental Geochemistry and Geophysics (BGI), University of Bayreuth, 95440 Bayreuth, Germany; orcid.org/0000-0002-4730-4197

Fariia I. Akbar – Bavarian Research Institute of Experimental Geochemistry and Geophysics (BGI), University of Bayreuth, 95440 Bayreuth, Germany

Umbertoluca Ranieri – Centre for Science at Extreme Conditions and School of Physics and Astronomy, University of Edinburgh, EH9 3FD Edinburgh, United Kingdom; orcid.org/0000-0003-2026-6132

James Spender – Centre for Science at Extreme Conditions and School of Physics and Astronomy, University of Edinburgh, EH9 3FD Edinburgh, United Kingdom

Ross T. Howie – Centre for Science at Extreme Conditions and School of Physics and Astronomy, University of Edinburgh, EH9 3FD Edinburgh, United Kingdom

Eleanor Lawrence Bright – European Synchrotron Radiation Facility, 38000 Grenoble, France

Jonathan Wright – European Synchrotron Radiation Facility, 38000 Grenoble, France

Michael Hanfland – European Synchrotron Radiation Facility, 38000 Grenoble, France

Gaston Garbarino – European Synchrotron Radiation Facility, 38000 Grenoble, France

Mohamed Mezouar – European Synchrotron Radiation Facility, 38000 Grenoble, France

Timofey Fedotenko – Photon Science, Deutsches Elektronen-Synchrotron, 22607 Hamburg, Germany

Igor A. Abrikosov – Department of Physics, Chemistry and Biology (IFM), Linköping University, SE-581 83 Linköping, Sweden

Natalia Dubrovinskaia – Material Physics and Technology at Extreme Conditions, Laboratory of Crystallography, University of Bayreuth, 95440 Bayreuth, Germany; Department of Physics, Chemistry and Biology (IFM), Linköping University, SE-581 83 Linköping, Sweden; orcid.org/0000-0002-8256-5675

Leonid Dubrovinsky – Bavarian Research Institute of Experimental Geochemistry and Geophysics (BGI), University of Bayreuth, 95440 Bayreuth, Germany

Dominique Laniel – Centre for Science at Extreme Conditions and School of Physics and Astronomy, University of Edinburgh, EH9 3FD Edinburgh, United Kingdom

Complete contact information is available at: <https://pubs.acs.org/doi/10.1021/jacs.4c06068>

Author Contributions

[†]V.A.A. and A.L. contributed equally to this work.

Notes

The authors declare no competing financial interest.

■ ACKNOWLEDGMENTS

The authors acknowledge the Deutsches Elektronen-Synchrotron (DESY, PETRA III) for the provision of beamtime at the P02.2 beamline, and the European Synchrotron Radiation Facility (ESRF) for the provision of beamtime at the ID11, ID15b, ID27 beamlines. D.L., A.L., and U.R. thank the UKRI Future Leaders Fellowship (MR/V025724/1) for financial support. N.D. and L.D. thank the Deutsche Forschungsgemeinschaft (DFG projects DU 954–11/1, DU 393–9/2, DU 393–13/1; DU 945/15-1) for financial support. N.D., F.T., and I.A.A. also thank the Swedish Government Strategic Research Area in Materials Science on Functional Materials at Linköping University (Faculty Grant SFO-Mat-LiU No. 2009 00971). I.A.A., A.E., and F.T. are supported by the Knut and Alice Wallenberg Foundation (Wallenberg Scholar grant no. KAW-2018.0194). I.A.A. acknowledges support by the Swedish Research Council (VR) Grant No. 2023-05358. Computations were enabled by resources provided by the National Academic Infrastructure for Supercomputing in Sweden (NAISS) using Tetralith at the National Supercomputer Centre, Linköping University and LUMI at the IT Center for Science (CSC), Finland, through grant NAISS 2023/1-11 and NAISS 2023/8-8, respectively. For the purpose of open access, the authors have applied a Creative Commons Attribution (CC BY) licence to any Author Accepted Manuscript version arising from this submission.

REFERENCES

- (1) Laniel, D.; Winkler, B.; Koemets, E.; Fedotenko, T.; Bykov, M.; Bykova, E.; Dubrovinsky, L.; Dubrovinskaia, N. Synthesis of Magnesium-Nitrogen Salts of Polynitrogen Anions. *Nat. Commun.* **2019**, *10* (1), No. 4515.
- (2) Aslandukov, A.; Aslandukova, A.; Laniel, D.; Khandarkhaeva, S.; Yin, Y.; Akbar, F. I.; Chariton, S.; Prakupenka, V.; Bright, E. L.; Giacobbe, C.; Wright, J.; Comboni, D.; Hanfland, M.; Dubrovinskaia, N.; Dubrovinsky, L. Stabilization of N₆ and N₈ Anionic Units and 2D Polynitrogen Layers in High-Pressure Scandium Polynitrides. *Nat. Commun.* **2024**, *15* (1), No. 2244.
- (3) Salke, N. P.; Xia, K.; Fu, S.; Zhang, Y.; Greenberg, E.; Prakupenka, V. B.; Liu, J.; Sun, J.; Lin, J.-F. Tungsten Hexanitride with Single-Bonded Armchairlike Hexazine Structure at High Pressure. *Phys. Rev. Lett.* **2021**, *126* (6), No. 065702.
- (4) Wang, Y.; Bykov, M.; Chepkasov, I.; Samtsevich, A.; Bykova, E.; Zhang, X.; Jiang, S.; Greenberg, E.; Chariton, S.; Prakupenka, V. B.; Oganov, A. R.; Goncharov, A. F. Stabilization of Hexazine Rings in Potassium Polynitride at High Pressure. *Nat. Chem.* **2022**, *14* (7), 794–800.
- (5) Laniel, D.; Trybel, F.; Yin, Y.; Fedotenko, T.; Khandarkhaeva, S.; Aslandukov, A.; Aprilis, G.; Abrikosov, A. I.; Bin Masood, T.; Giacobbe, C.; Bright, E. L.; Glazyrin, K.; Hanfland, M.; Wright, J.; Hotz, I.; Abrikosov, I. A.; Dubrovinsky, L.; Dubrovinskaia, N. Aromatic Hexazine [N₆]⁴⁻ Anion Featured in the Complex Structure of the High-Pressure Potassium Nitrogen Compound K₉N₅₆. *Nat. Chem.* **2023**, *15* (5), 641–646.
- (6) Aslandukov, A.; Trybel, F.; Aslandukova, A.; Laniel, D.; Fedotenko, T.; Khandarkhaeva, S.; Aprilis, G.; Giacobbe, C.; Lawrence Bright, E.; Abrikosov, I. A.; Dubrovinsky, L.; Dubrovinskaia, N. Anionic N₁₈ Macrocycles and a Polynitrogen Double Helix in Novel Yttrium Polynitrides YN₆ and Y₂N₁₁ at 100 GPa. *Angew. Chem., Int. Ed.* **2022**, *61* (34), No. e202207469.
- (7) Bykov, M.; Bykova, E.; Aprilis, G.; Glazyrin, K.; Koemets, E.; Chuvashova, I.; Kuppenko, I.; McCammon, C.; Mezouar, M.; Prakupenka, V.; Liermann, H.-P.; Tasnádi, F.; Ponomareva, A. V.; Abrikosov, I. A.; Dubrovinskaia, N.; Dubrovinsky, L. Fe-N System at High Pressure Reveals a Compound Featuring Polymeric Nitrogen Chains. *Nat. Commun.* **2018**, *9* (1), No. 2756.
- (8) Bykov, M.; Bykova, E.; Koemets, E.; Fedotenko, T.; Aprilis, G.; Glazyrin, K.; Liermann, H.-P.; Ponomareva, A. V.; Tidholm, J.; Tasnádi, F.; Abrikosov, I. A.; Dubrovinskaia, N.; Dubrovinsky, L. High-Pressure Synthesis of a Nitrogen-Rich Inclusion Compound ReN₈xN₂ with Conjugated Polymeric Nitrogen Chains. *Angew. Chem., Int. Ed.* **2018**, *57* (29), 9048–9053.
- (9) Bykov, M.; Chariton, S.; Bykova, E.; Khandarkhaeva, S.; Fedotenko, T.; Ponomareva, A. V.; Tidholm, J.; Tasnádi, F.; Abrikosov, I. A.; Sedmak, P.; Prakupenka, V.; Hanfland, M.; Liermann, H. P.; Mahmood, M.; Goncharov, A. F.; Dubrovinskaia, N.; Dubrovinsky, L. High-Pressure Synthesis of Metal–Inorganic Frameworks Hf₄N₂₀·N₂, WN₈·N₂, and Os₅N₂₈·3N₂ with Polymeric Nitrogen Linkers. *Angew. Chem., Int. Ed.* **2020**, *59* (26), 10321–10326.
- (10) Bykov, M.; Bykova, E.; Ponomareva, A. V.; Abrikosov, I. A.; Chariton, S.; Prakupenka, V. B.; Mahmood, M. F.; Dubrovinsky, L.; Goncharov, A. F. Stabilization of Polynitrogen Anions in Tantalum–Nitrogen Compounds at High Pressure. *Angew. Chem.* **2021**, *133* (16), 9085–9090.
- (11) Laniel, D.; Aslandukova, A.; Aslandukov, A. N.; Fedotenko, T.; Chariton, S.; Glazyrin, K.; Prakupenka, V. B.; Dubrovinsky, L. S.; Dubrovinskaia, N. High-Pressure Synthesis of the β-Zn₃N₂ Nitride and the α-ZnN₄ and β-ZnN₄ Polynitrogen Compounds. *Inorg. Chem.* **2021**, *60* (19), 14594–14601.
- (12) Bykov, M.; Fedotenko, T.; Chariton, S.; Laniel, D.; Glazyrin, K.; Hanfland, M.; Smith, J. S.; Prakupenka, V. B.; Mahmood, M. F.; Goncharov, A. F.; Ponomareva, A. V.; Tasnádi, F.; Abrikosov, A. I.; Bin Masood, T.; Hotz, I.; Rudenko, A. N.; Katsnelson, M. I.; Dubrovinskaia, N.; Dubrovinsky, L.; Abrikosov, I. A. High-Pressure Synthesis of Dirac Materials: Layered van Der Waals Bonded BeN₄ Polymorph. *Phys. Rev. Lett.* **2021**, *126* (17), No. 175501.
- (13) Wang, L.; Dong, X.; Wang, Y.; Zheng, H.; Li, K.; Peng, X.; Mao, H.; Jin, C.; Meng, Y.; Huang, M.; Zhao, Z. Pressure-Induced Polymerization and Disproportionation of Li₂C₂ Accompanied with Irreversible Conductivity Enhancement. *J. Phys. Chem. Lett.* **2017**, *8* (17), 4241–4245.
- (14) Dong, X.; Wang, L.; Li, K.; Zheng, H.; Wang, Y.; Meng, Y.; Shu, H.; Mao, H.; Feng, S.; Jin, C. Tailored Synthesis of the Narrowest Zigzag Graphene Nanoribbon Structure by Compressing the Lithium Acetylide under High Temperature. *J. Phys. Chem. C* **2018**, *122* (35), 20506–20512.
- (15) Khandarkhaeva, S.; Fedotenko, T.; Aslandukova, A.; Akbar, F. I.; Bykov, M.; Laniel, D.; Aslandukov, A.; Ruschewitz, U.; Tobeck, C.; Winkler, B.; Chariton, S.; Prakupenka, V.; Glazyrin, K.; Giacobbe, C.; Bright, E. L.; Belov, M.; Dubrovinskaia, N.; Dubrovinsky, L. Extending Carbon Chemistry at High-Pressure by Synthesis of CaC₂ and Ca₃C₇ with Deprotonated Polyacene- and Para-Poly-(Indenoidene)-like Nanoribbons. *Nat. Commun.* **2024**, *15* (1), No. 2855.
- (16) Akbar, F. I.; Aslandukova, A.; Yin, Y.; Aslandukov, A.; Laniel, D.; Bykova, E.; Bykov, M.; Bright, E. L.; Wright, J.; Comboni, D.; Hanfland, M.; Dubrovinskaia, N.; Dubrovinsky, L. High-Pressure Dysprosium Carbides Containing Carbon Dimers, Trimers, Chains, and Ribbons. *Carbon* **2024**, 119374.
- (17) Laniel, D.; Trybel, F.; Aslandukov, A.; Khandarkhaeva, S.; Fedotenko, T.; Yin, Y.; Miyajima, N.; Tasnádi, F.; Ponomareva, A. V.; Jena, N.; Akbar, F. I.; Winkler, B.; Néri, A.; Chariton, S.; Prakupenka, V.; Milman, V.; Schnick, W.; Rudenko, A. N.; Katsnelson, M. I.; Abrikosov, I. A.; Dubrovinsky, L.; Dubrovinskaia, N. Synthesis of Ultra-Incompressible and Recoverable Carbon Nitrides Featuring CN₄ Tetrahedra. *Adv. Mater.* **2024**, *36* (3), No. 2308030.
- (18) Koller, T. J.; Jin, S.; Krol, V.; Ambach, S. J.; Ranieri, U.; Khandarkhaeva, S.; Spender, J.; McWilliams, S.; Trybel, F.; Giordano, N.; Poreba, T.; Mezouar, M.; Kuang, X.; Lu, C.; Dubrovinsky, L.; Dubrovinskaia, N.; Hermann, A.; Schnick, W.; Laniel, D. Simple Molecules under High-Pressure and High-Temperature Conditions: Synthesis and Characterization of α- and β-C(NH)₂ with Fully sp³-Hybridized Carbon. *Angew. Chem., Int. Ed.* **2024**, *63* (7), No. e202318214.
- (19) Chadwick, B. M.; Sharpe, A. G. Transition Metal Cyanides and Their Complexes. In *Reviews in Inorganic Chemistry*; Elsevier, 1966; Vol. 43, pp 83–176.
- (20) Schulz, A.; Surkau, J. Main Group Cyanides: From Hydrogen Cyanide to Cyanido-Complexes. *Rev. Inorg. Chem.* **2023**, *43* (1), 49–188.
- (21) Braun, C.; Mereacre, L.; Hua, W.; Stürzer, T.; Ponomarev, I.; Kroll, P.; Slabon, A.; Chen, Z.; Damour, Y.; Rocquefelte, X.; Halet, J.; Indris, S. SnCN₂: A Carbodiimide with an Innovative Approach for Energy Storage Systems and Phosphors in Modern LED Technology. *ChemElectroChem* **2020**, *7* (22), 4550–4561.
- (22) Kubus, M.; Castro, C.; Ensling, D.; Jüstel, T. Room Temperature Red Emitting Carbodiimide Compound Ca(CN₂):Mn²⁺. *Opt. Mater.* **2016**, *59*, 126–129.
- (23) Liu, Q.; Liu, Y.; Dai, G.; Tian, L.; Xu, J.; Zhao, G.; Zhang, N.; Fang, Y. Size-Controllable Synthesis of Hierarchical Copper Carbodiimide Microcrystals and Their Pronounced Photoelectric Response under Visible Light. *Appl. Surf. Sci.* **2015**, *357*, 745–749.
- (24) Sougrati, M. T.; Darwiche, A.; Liu, X.; Mahmood, A.; Hermann, R. P.; Jouen, S.; Monconduit, L.; Dronskowski, R.; Stievano, L. Transition-Metal Carbodiimides as Molecular Negative Electrode Materials for Lithium- and Sodium-Ion Batteries with Excellent Cycling Properties. *Angew. Chem., Int. Ed.* **2016**, *55* (16), 5090–5095.
- (25) Eguía-Barrio, A.; Castillo-Martínez, E.; Liu, X.; Dronskowski, R.; Armand, M.; Rojo, T. Carbodiimides: New Materials Applied as Anode Electrodes for Sodium and Lithium Ion Batteries. *J. Mater. Chem. A* **2016**, *4* (5), 1608–1611.

- (26) Chen, K.; Fehse, M.; Laurita, A.; Arayampambal, J. J.; Sougrati, M. T.; Stievano, L.; Dronskowski, R. Quantum-Chemical Study of the FeNCN Conversion-Reaction Mechanism in Lithium- and Sodium-Ion Batteries. *Angew. Chem., Int. Ed.* **2020**, *59* (9), 3718–3723.
- (27) Sougrati, M. T.; Arayampambal, J. J.; Liu, X.; Mann, M.; Slabon, A.; Stievano, L.; Dronskowski, R. Carbodiimides as Energy Materials: Which Directions for a Reasonable Future? *Dalton Trans.* **2018**, *47* (32), 10827–10832.
- (28) Brüning, L.; Jena, N.; Bykova, E.; Jurzick, P. L.; Flosbach, N. T.; Mezouar, M.; Hanfland, M.; Giordano, N.; Fedotenko, T.; Winkler, B.; Abrikosov, I. A.; Bykov, M. Stabilization of Guanidinate Anions $[\text{CN}_3]^{5-}$ in Calcite-Type SbCN_3 . *Angew. Chem., Int. Ed.* **2023**, *62* (47), No. e202311519.
- (29) Aslandukov, A.; Jurzick, P. L.; Bykov, M.; Aslandukova, A.; Chanyshev, A.; Laniel, D.; Yin, Y.; Akbar, F. I.; Khandarkhaeva, S.; Fedotenko, T.; Glazyrin, K.; Chariton, S.; Prakapenka, V.; Wilhelm, F.; Rogalev, A.; Comboni, D.; Hanfland, M.; Dubrovinskaia, N.; Dubrovinsky, L. Stabilization Of The CN_3^{5-} Anion In Recoverable High-pressure $\text{Ln}_3\text{O}_2(\text{CN}_3)$ (Ln = La, Eu, Gd, Tb, Ho, Yb) Oxoguanidates. *Angew. Chem., Int. Ed.* **2023**, *62* (47), No. e202311516.
- (30) Luo, D.; Qiao, X.; Dronskowski, R. Predicting Nitrogen-Based Families of Compounds: Transition-Metal Guanidates TCN_3 (T = V, Nb, Ta) and Ortho-Nitrido Carbonates $\text{T}'_2\text{CN}_4$ (T' = Ti, Zr, Hf). *Angew. Chem., Int. Ed.* **2021**, *60* (1), 486–492.
- (31) Yin, Y.; Akbar, F. I.; Bykova, E.; Aslandukova, A.; Laniel, D.; Aslandukov, A.; Bykov, M.; Hanfland, M.; Garbarino, G.; Jia, Z.; Dubrovinsky, L.; Dubrovinskaia, N. Synthesis of Rare-Earth Metal Compounds through Enhanced Reactivity of Alkali Halides at High Pressures. *Commun. Chem.* **2022**, *5* (1), No. 122.
- (32) Akbar, F. I.; Aslandukova, A.; Aslandukov, A.; Yin, Y.; Trybel, F.; Khandarkhaeva, S.; Fedotenko, T.; Laniel, D.; Bykov, M.; Bykova, E.; Dubrovinskaia, N.; Dubrovinsky, L. High-Pressure Synthesis of Dysprosium Carbides. *Front. Chem.* **2023**, *11*, No. 1210081.
- (33) Laniel, D.; Binck, J.; Winkler, B.; Vogel, S.; Fedotenko, T.; Chariton, S.; Prakapenka, V.; Milman, V.; Schnick, W.; Dubrovinsky, L.; Dubrovinskaia, N. Synthesis, Crystal Structure and Structure–Property Relations of Strontium Orthocarbonate, Sr_2CO_4 . *Acta Crystallogr., Sect. B: Struct. Sci., Cryst. Eng. Mater.* **2021**, *77* (1), 131–137.
- (34) Jost, K. H.; Schulze, H. J. Zur Phasentransformation Des Kaliumpolyphosphates $(\text{KPO}_3)_x$. *Acta Crystallogr., Sect. B: Struct. Crystallogr. Cryst. Chem.* **1969**, *25* (6), 1110–1118.
- (35) Eremets, M. I.; Gavriluk, A. G.; Trojan, I. A.; Dzivenko, D. A.; Boehler, R. Single-Bonded Cubic Form of Nitrogen. *Nat. Mater.* **2004**, *3* (8), 558–563.
- (36) Laniel, D.; Winkler, B.; Fedotenko, T.; Pakhomova, A.; Chariton, S.; Milman, V.; Prakapenka, V.; Dubrovinsky, L.; Dubrovinskaia, N. High-Pressure Polymeric Nitrogen Allotrope with the Black Phosphorus Structure. *Phys. Rev. Lett.* **2020**, *124* (21), No. 216001.
- (37) Prewitt, C. T.; Downs, R. T. High-Pressure Crystal Chemistry. *Rev. Mineral.* **1998**, *37*, 283–318.
- (38) Zeuner, M.; Pagano, S.; Schnick, W. Nitridosilicates and Oxonitridosilicates: From Ceramic Materials to Structural and Functional Diversity. In *Ceramics Science and Technology*; Wiley, 2013; Vol. 4, pp 373–413.
- (39) Zeuner, M.; Pagano, S.; Matthes, P.; Bichler, D.; Johrendt, D.; Harmening, T.; Pöttgen, R.; Schnick, W. Mixed Valence Europium Nitridosilicate $\text{Eu}_2\text{Si}_3\text{N}_5$. *J. Am. Chem. Soc.* **2009**, *131* (31), 11242–11248.
- (40) Huppertz, H.; Schnick, W. $\text{Eu}_2\text{Si}_3\text{N}_8$ and $\text{EuYbSi}_4\text{N}_7$. The First Nitridosilicates with a Divalent Rare Earth Metal. *Acta Crystallogr., Sect. C: Cryst. Struct. Commun.* **1997**, *53* (12), 1751–1753.
- (41) Schmolke, C.; Bichler, D.; Johrendt, D.; Schnick, W. Synthesis and Crystal Structure of the First Chain-Type Nitridosilicates $\text{RE}_2\text{Si}_3\text{N}_9$ (RE = La, Ce). *Solid State Sci.* **2009**, *11* (2), 389–394.
- (42) Lupart, S.; Schnick, W. $\text{Pr}_3\text{Si}_3\text{N}_9$. *Acta Crystallogr., Sect. E: Struct. Rep. Online* **2009**, *65* (6), i43.
- (43) Schmolke, C.; Oeckler, O.; Bichler, D.; Johrendt, D.; Schnick, W. Complex Interrupted Tetrahedral Frameworks in the Nitridosilicates $\text{M}_7\text{Si}_6\text{N}_{15}$ (M = La, Ce, Pr). *Chem. - Eur. J.* **2009**, *15* (36), 9215–9222.
- (44) Woike, M.; Jeitschko, W. Preparation and Crystal Structure of the Nitridosilicates $\text{Ln}_3\text{Si}_6\text{N}_{11}$ (Ln = La, Ce, Pr, Nd, Sm) and LnSi_3N_5 (Ln = Ce, Pr, Nd). *Inorg. Chem.* **1995**, *34* (21), 5105–5108.
- (45) Akopov, G.; Mark, J.; Viswanathan, G.; Lee, S. J.; McBride, B. C.; Won, J.; Perras, F. A.; Paterson, A. L.; Yuan, B.; Sen, S.; Adeyemi, A. N.; Zhang, F.; Wang, C.-Z.; Ho, K.-M.; Miller, G. J.; Kovnir, K. Third Time's the Charm: Intricate Non-Centrosymmetric Polymorphism in LnSiP_3 (Ln = La and Ce) Induced by Distortions of Phosphorus Square Layers. *Dalton Trans.* **2021**, *50* (19), 6463–6476.
- (46) Ono, S.; Hayakawa, H.; Nomura, K. Syntheses of Ln-Si-P (Ln = La, Ce, Pr) Ternary Compounds. *Nippon Kagaku Kaishi* **1976**, No. 11, 1700–1709.
- (47) Sun, Y.; Chen, J.; Yang, S.; Li, B.; Chai, G.; Lin, C.; Luo, M.; Ye, N. LaSiP_3 and LaSi_2P_6 : Two Excellent Rare-Earth Pnictides with Strong SHG Responses as Mid- and Far-Infrared Nonlinear Optical Crystals. *Adv. Opt. Mater.* **2021**, *9* (10), No. 2002176.
- (48) Akopov, G.; Viswanathan, G.; Kovnir, K. Synthesis, Crystal and Electronic Structure of La_2SiP_4 . *Z. Anorg. Allg. Chem.* **2021**, *647* (2–3), 91–97.
- (49) Mark, J.; Dolyński, J.; Tran, N.; Kovnir, K. Crystal and Electronic Structure and Optical Properties of AE_2SiP_4 (AE = Sr, Eu, Ba) and $\text{Ba}_4\text{Si}_3\text{P}_8$. *Z. Anorg. Allg. Chem.* **2019**, *645* (3), 242–247.
- (50) Kresse, G.; Furthmüller, J. Efficient Iterative Schemes for Ab Initio Total-Energy Calculations Using a Plane-Wave Basis Set. *Phys. Rev. B* **1996**, *54* (16), 11169–11186.
- (51) Andersson, D. A.; Simak, S. I.; Johansson, B.; Abrikosov, I. A.; Skorodumova, N. V. Modeling of CeO_2 , Ce_2O_3 , and CeO_{2-x} in the LDA+U Formalism. *Phys. Rev. B* **2007**, *75* (3), No. 035109.
- (52) Loch, I. L. M.; Kvashnin, Y. O.; Rodrigues, D. C. M.; Pereiro, M.; Bergman, A.; Bergqvist, L.; Lichtenstein, A. I.; Katsnelson, M. I.; Delin, A.; Klautau, A. B.; Johansson, B.; Di Marco, I.; Eriksson, O. Standard Model of the Rare Earths Analyzed from the Hubbard I Approximation. *Phys. Rev. B* **2016**, *94* (8), No. 085137.
- (53) Georges, A.; Kotliar, G.; Krauth, W.; Rozenberg, M. J. Dynamical Mean-Field Theory of Strongly Correlated Fermion Systems and the Limit of Infinite Dimensions. *Rev. Mod. Phys.* **1996**, *68* (1), 13–125.
- (54) Lawson, A. W.; Tang, T.-Y. Concerning the High Pressure Allotropic Modification of Cerium. *Phys. Rev.* **1949**, *76* (2), 301–302.
- (55) Coqblin, B.; Blandin, A. Stabilité Des Moments Magnétiques Localisés Dans Les Métaux. *Adv. Phys.* **1968**, *17* (67), 281–366.
- (56) Ramirez, R.; Falicov, L. M. Theory of the α - γ Phase Transition in Metallic Cerium. *Phys. Rev. B* **1971**, *3* (8), 2425–2430.
- (57) Hirst, L. L. Configuration Crossover in 4f Substances under Pressure. *J. Phys. Chem. Solids* **1974**, *35* (9), 1285–1296.
- (58) Ciftci, Y. O.; Çolakoglu, K.; Deligoz, E.; Ozisik, H. The First-Principles Study on the LaN . *Mater. Chem. Phys.* **2008**, *108* (1), 120–123.
- (59) Zhang, H.-n.; Wu, Q.; Hu, Z.; Li, H.; Xiong, H.; Xu, A. First-Principles Study on Stability, Electronic, and Mechanical Properties of La–C and Ce–C Binary Compounds. *J. Iron Steel Res. Int.* **2019**, *26* (7), 771–778.
- (60) Olsen, J. S.; Jørgensen, J.-E.; Gerward, L.; Vaitheeswaran, G.; Kanchara, V.; Svane, A. Compressibility and Structural Stability of CeN from Experiment and Theory. The B1–B2 Transition. *J. Alloys Compd.* **2012**, *533*, 29–32.
- (61) Kantor, I.; Prakapenka, V.; Kantor, A.; Dera, P.; Kurnosov, A.; Sinogeikin, S.; Dubrovinskaia, N.; Dubrovinsky, L. BX90: A New Diamond Anvil Cell Design for X-Ray Diffraction and Optical Measurements. *Rev. Sci. Instrum.* **2012**, *83* (12), No. 125102.
- (62) Boehler, R. New Diamond Cell for Single-Crystal x-Ray Diffraction. *Rev. Sci. Instrum.* **2006**, *77* (11), 2004–2007.

- (63) Kurnosov, A.; Kantor, I.; Boffa-Ballaran, T.; Lindhardt, S.; Dubrovinsky, L.; Kuznetsov, A.; Zehnder, B. H. A Novel Gas-Loading System for Mechanically Closing of Various Types of Diamond Anvil Cells. *Rev. Sci. Instrum.* **2008**, *79* (4), No. 045110.
- (64) Fedotenko, T.; Dubrovinsky, L.; Aprilis, G.; Koemets, E.; Snigirev, A.; Snigireva, I.; Barannikov, A.; Ershov, P.; Cova, F.; Hanfland, M.; Dubrovinskaia, N. Laser Heating Setup for Diamond Anvil Cells for in Situ Synchrotron and in House High and Ultra-High Pressure Studies. *Rev. Sci. Instrum.* **2019**, *90* (10), No. 104501.
- (65) Akahama, Y.; Kawamura, H. Pressure Calibration of Diamond Anvil Raman Gauge to 310 GPa. *J. Appl. Phys.* **2006**, *100* (4), No. 043516.
- (66) Anzellini, S.; Dewaele, A.; Occelli, F.; Loubeyre, P.; Mezouar, M. Equation of State of Rhenium and Application for Ultra High Pressure Calibration. *J. Appl. Phys.* **2014**, *115* (4), No. 043511.
- (67) Rigaku Oxford Diffraction, CrysAlisPro Software System. 2015.
- (68) Aslandukov, A.; Aslandukov, M.; Dubrovinskaia, N.; Dubrovinsky, L. Domain Auto Finder (DAFi) Program: The Analysis of Single-Crystal X-Ray Diffraction Data from Polycrystalline Samples. *J. Appl. Crystallogr.* **2022**, *55* (5), 1383–1391.
- (69) Dolomanov, O. V.; Bourhis, L. J.; Gildea, R. J.; Howard, J. A. K.; Puschmann, H. OLEX2: A Complete Structure Solution, Refinement and Analysis Program. *J. Appl. Crystallogr.* **2009**, *42* (2), 339–341.
- (70) Sheldrick, G. M. SHELXT - Integrated Space-Group and Crystal-Structure Determination. *Acta Crystallogr., Sect. A: Found. Adv.* **2015**, *71* (1), 3–8.
- (71) Sheldrick, G. M. Crystal Structure Refinement with SHELXL. *Acta Crystallogr., Sect. C: Struct. Chem.* **2015**, *71* (1), 3–8.
- (72) Momma, K.; Izumi, F. VESTA 3 for Three-Dimensional Visualization of Crystal, Volumetric and Morphology Data. *J. Appl. Crystallogr.* **2011**, *44* (6), 1272–1276.
- (73) Kresse, G.; Joubert, D. From Ultrasoft Pseudopotentials to the Projector Augmented-Wave Method. *Phys. Rev. B* **1999**, *59* (3), 1758–1775.
- (74) Perdew, J. P.; Burke, K.; Ernzerhof, M. Generalized Gradient Approximation Made Simple. *Phys. Rev. Lett.* **1996**, *77* (18), 3865–3868.
- (75) Dudarev, S. L.; Botton, G. A.; Savrasov, S. Y.; Humphreys, C. J.; Sutton, A. P. Electron-Energy-Loss Spectra and the Structural Stability of Nickel Oxide: An LSDA+U Study. *Phys. Rev. B* **1998**, *57* (3), 1505–1509.
- (76) Dederichs, P. H.; Blügel, S.; Zeller, R.; Akai, H. Ground States of Constrained Systems: Application to Cerium Impurities. *Phys. Rev. Lett.* **1984**, *53* (26), 2512–2515.
- (77) Monkhorst, H. J.; Pack, J. D. Special Points for Brillouin-Zone Integrations. *Phys. Rev. B* **1976**, *13* (12), No. 5188.
- (78) Blöchl, P. E.; Jepsen, O.; Andersen, O. K. Improved Tetrahedron Method for Brillouin-Zone Integrations. *Phys. Rev. B* **1994**, *49* (23), 16223–16233.
- (79) Togo, A.; Chaput, L.; Tadano, T.; Tanaka, I. Implementation Strategies in Phonopy and Phono3py. *J. Phys.: Condens. Matter* **2023**, *35* (35), No. 353001.
- (80) Togo, A. First-Principles Phonon Calculations with Phonopy and Phono3py. *J. Phys. Soc. Jpn.* **2023**, *92* (1), No. 012001.

Supporting information

Synthesis of LaCN₃, TbCN₃, CeCN₅, and TbCN₅ Polycarbonitrides at Megabar Pressures

Andrey Aslandukov^{1,2*}, Akun Liang^{3*}, Amanda Ehn⁴, Florian Trybel⁴, Yuqing Yin⁴, Alena Aslandukova¹, Fariia I. Akbar¹, Umbertolucca Ranieri³, James Spender³, Ross T. Howie³, Eleanor Lawrence Bright⁵, Jonathan Wright⁵, Michael Hanfland⁵, Gaston Garbarino⁵, Mohamed Mezouar⁵, Timofey Fedotenko⁶, Igor A. Abrikosov⁴, Natalia Dubrovinskaia^{2,4}, Leonid Dubrovinsky¹, Dominique Laniel³

¹ Bavarian Research Institute of Experimental Geochemistry and Geophysics (BGI), University of Bayreuth, 95440 Bayreuth, Germany

² Material Physics and Technology at Extreme Conditions, Laboratory of Crystallography, University of Bayreuth, 95440 Bayreuth, Germany

³ Centre for Science at Extreme Conditions and School of Physics and Astronomy, University of Edinburgh, EH9 3FD Edinburgh, United Kingdom

⁴ Department of Physics, Chemistry and Biology (IFM), Linköping University, SE-581 83, Linköping, Sweden

⁵ European Synchrotron Radiation Facility, 38000 Grenoble, France

⁶ Photon Science, Deutsches Elektronen-Synchrotron, 22607 Hamburg, Germany

*Equal contribution. Correspondence to andrii.aslandukov@uni-bayreuth.de and aliang@exseed.ed.ac.uk

Supplementary Tables

Table S1. Summary of the performed DAC laser heating experiments and their reaction conditions for the synthesis of polycarbonitrides.

Sample	Reaction mixture	Temperature, K	Pressure, GPa	Polycarbonitride reaction product
DAC#1	La + N ₂ + C _{diamond} anvil	2500(500)	102(2)	LaCN ₃
DAC#2	Ce + N ₂ + C _{diamond} anvil	2500(500)	90(2)	CeCN ₅
DAC#3	Tb + N ₂ + C _{diamond} anvil	2500(500)	111(2)	TbCN ₃ , TbCN ₅
DAC#4	La + CTA ¹ + C _{diamond} anvil	2500(500)	102(2)	LaCN ₃

¹CTA is cyanuric triazide (C₃N₁₂)

Table S2. Structure refinement details of LaCN₃ at 102(2) GPa. The full crystallographic data was deposited to the ICSD under the deposition number CSD 2352230.

Chemical formula		LaCN ₃			
Temperature (K)		293			
Pressure (GPa)		102(2)			
Crystal data					
Mr		192.95			
ρ (g/cm ³)		8.573			
Crystal system, space group		orthorhombic, <i>Pnma</i>			
a (Å)		4.1059(12)			
b (Å)		4.870(5)			
c (Å)		7.4758(15)			
V (Å ³)		149.49(16)			
Z		4			
Radiation type		X-ray, $\lambda = 0.2846$ Å			
μ (mm ⁻¹)		12.802			
Data collection					
No. of measured, independent and observed [I > 2 σ (I)] reflections		473/198/152			
R _{int}		4.30%			
$(\sin \theta/\lambda)_{\max}$ (Å ⁻¹)		0.769			
Refinement					
R[F ² > 4 σ (F ²)], wR(F ²), GOF		3.67%, 8.31%, 1.078			
data/parameters ratio		198/17			
$\Delta\rho_{\max}, \Delta\rho_{\min}$ (e Å ⁻³)		2.140, -2.327			
Atomic positions and equivalent isotropic (or isotropic) ADPs					
Atom	Wyckoff site	Fractional atomic coordinates			U _{eq} or U _{iso} (Å ²)
		x	y	z	
La1	4c	0.08304(18)	0.25	0.62043(11)	U _{eq} = 0.0057(4)
C1	4c	0.012(3)	0.25	0.1698(17)	U _{iso} = 0.003(2)
N1	8d	0.413(2)	0.007(4)	0.4178(9)	U _{iso} = 0.0042(13)
N2	4c	0.366(3)	0.25	0.1686(14)	U _{iso} = 0.004(2)

Table S3. Structure refinement details of TbCN₃ at 111(2) GPa. The full crystallographic data was deposited to the ICSD under the deposition number CSD 2352231.

Chemical formula		TbCN ₃			
Temperature (K)		293			
Pressure (GPa)		111(2)			
Crystal data					
Mr		212.96			
ρ (g/cm ³)		10.380			
Crystal system, space group		orthorhombic, <i>Pnma</i>			
a (Å)		3.9813(15)			
b (Å)		4.7305(12)			
c (Å)		7.2358(15)			
V (Å ³)		136.28(7)			
Z		4			
Radiation type		X-ray, $\lambda = 0.4099$ Å			
μ (mm ⁻¹)		11.798			
Data collection					
No. of measured, independent and observed [I > 2 σ (I)] reflections		254/144/114			
R _{int}		3.49%			
$(\sin \theta/\lambda)_{\max}$ (Å ⁻¹)		0.853			
Refinement					
R[F ² > 4 σ (F ²), wR(F ²), GOF		4.09%, 9.94%, 1.103			
data/parameters ratio		144/17			
$\Delta\rho_{\max}, \Delta\rho_{\min}$ (e Å ⁻³)		1.729, -2.407			
Atomic positions and equivalent isotropic (or isotropic) ADPs					
Atom	Wyckoff site	Fractional atomic coordinates			U _{eq} or U _{iso} (Å ²)
		x	y	z	
Tb1	4c	0.0863(4)	0.25	0.61802(12)	U _{eq} = 0.0091(4)
C1	4c	0.025(7)	0.25	0.172(3)	U _{iso} = 0.009(4)
N1	8d	0.413(6)	0.501(2)	0.4159(16)	U _{iso} = 0.006(2)
N2	4c	0.379(6)	0.25	0.155(3)	U _{iso} = 0.009(3)

Table S4. Structure refinement details of CeCN₅ at 90(2) GPa. The full crystallographic data was deposited to the ICSD under the deposition number CSD 2352232.

Chemical formula	CeCN ₅				
Temperature (K)	293				
Pressure (GPa)	90(2)				
Crystal data					
Mr	222.18				
ρ (g/cm ³)	7.657				
Crystal system, space group	monoclinic, <i>P</i> 2 ₁ / <i>n</i>				
a (Å)	3.8889(9)				
b (Å)	4.7394(7)				
c (Å)	10.487(6)				
β (°)	94.41(4)				
V (Å ³)	192.72(13)				
Z	4				
Radiation type	X-ray, $\lambda = 0.28457$ Å				
μ (mm ⁻¹)	10.553				
Data collection					
No. of measured, independent and observed [$I > 2\sigma(I)$] reflections	723/423/304				
R_{int}	4.21%				
$(\sin \theta/\lambda)_{\text{max}}$ (Å ⁻¹)	0.833				
Refinement					
$R[F^2 > 4\sigma(F^2)]$, $wR(F^2)$, GOF	3.26%, 6.26%, 0.913				
data/parameters ratio	423/34				
$\Delta\rho_{\text{max}}$, $\Delta\rho_{\text{min}}$ (e Å ⁻³)	1.851, -1.270				
Atomic positions and equivalent isotropic (or isotropic) ADPs					
Atom	Wyckoff site	Fractional atomic coordinates			U_{eq} or U_{iso} (Å ²)
		x	y	z	
Ce1	4 <i>e</i>	0.1469(2)	0.8419(1)	0.1545(1)	$U_{\text{eq}} = 0.0074(2)$
C1	4 <i>e</i>	0.2350(30)	0.1574(17)	0.6261(15)	$U_{\text{iso}} = 0.0083(12)$
N1	4 <i>e</i>	0.1470(30)	0.9171(14)	0.7001(15)	$U_{\text{iso}} = 0.0092(14)$
N2	4 <i>e</i>	0.0340(20)	0.1486(15)	0.5112(12)	$U_{\text{iso}} = 0.0071(11)$
N3	4 <i>e</i>	0.0890(20)	0.3548(15)	0.1255(11)	$U_{\text{iso}} = 0.0077(11)$
N4	4 <i>e</i>	0.1410(30)	0.4090(13)	0.6833(15)	$U_{\text{iso}} = 0.0081(13)$
N5	4 <i>e</i>	0.2280(30)	0.2175(14)	0.0207(14)	$U_{\text{iso}} = 0.0105(14)$

Table S5. Structure refinement details of TbCN₅ at 111(2) GPa. The full crystallographic data was deposited to the ICSD under the deposition number CSD 2352233.

Chemical formula	TbCN ₅				
Temperature (K)	293				
Pressure (GPa)	111(2)				
Crystal data					
Mr	240.98				
ρ (g/cm ³)	8.950				
Crystal system, space group	monoclinic, <i>P2₁/n</i>				
a (Å)	3.8334(2)				
b (Å)	4.5221(9)				
c (Å)	10.3516(5)				
β (°)	94.699(5)				
V (Å ³)	178.84(4)				
Z	4				
Radiation type	X-ray, $\lambda = 0.4099$ Å				
μ (mm ⁻¹)	9.022				
Data collection					
No. of measured, independent and observed [$I > 2\sigma(I)$] reflections	428/286/235				
R_{int}	2.92%				
$(\sin \theta/\lambda)_{\text{max}}$ (Å ⁻¹)	0.866				
Refinement					
$R[F^2 > 4\sigma(F^2)]$, $wR(F^2)$, GOF	4.48%, 11.32%, 1.004				
data/parameters ratio	286/34				
$\Delta\rho_{\text{max}}$, $\Delta\rho_{\text{min}}$ (e Å ⁻³)	2.498, -2.322				
Atomic positions and equivalent isotropic (or isotropic) ADPs					
Atom	Wyckoff site	Fractional atomic coordinates			U_{eq} or U_{iso} (Å ²)
		x	y	z	
Tb1	4e	0.15275(12)	0.8298(3)	0.15535(5)	$U_{\text{eq}} = 0.0047(5)$
C1	4e	0.238(3)	0.180(5)	0.6250(12)	$U_{\text{iso}} = 0.007(2)$
N1	4e	0.147(2)	0.926(4)	0.7006(9)	$U_{\text{iso}} = 0.0040(17)$
N2	4e	0.041(3)	0.155(4)	0.5068(12)	$U_{\text{iso}} = 0.009(2)$
N3	4e	0.090(3)	0.338(4)	0.1240(10)	$U_{\text{iso}} = 0.0042(19)$
N4	4e	0.138(3)	0.427(5)	0.6887(11)	$U_{\text{iso}} = 0.009(2)$
N5	4e	0.219(3)	0.208(5)	0.0188(10)	$U_{\text{iso}} = 0.0072(19)$

Table S6. Experimentally determined crystallographic data for LaCN₃ at 102(2) GPa in comparison with the corresponding DFT-relaxed structure. Note that pressure was fixed to 102 GPa in the theoretical simulations, while the volume of the unit cell, lattice parameters, and equilibrium state parameters were calculated.

	Exp.	Calc.
Space group	<i>Pnma</i>	<i>Pnma</i>
Volume	149.49(16) Å ³	148.63 Å ³
Lattice parameters	a = 4.1059(12) Å b = 4.870(5) Å c = 7.4758(15) Å	a = 4.0900 Å b = 4.8537 Å c = 7.4873 Å
Atomic positions	La1 x 0.08304(18) y 0.25 z 0.62043(11)	La1 x 0.0815 y 0.25 z 0.6219
	C1 x 0.012(3) y 0.25 z 0.1698(17)	C1 x 0.0210 y 0.25 z 0.1690
	N1 x 0.413(2) y 0.007(4) z 0.4178(9)	N1 x 0.4165 y 0.0084 z 0.4190
	N2 x 0.366(3) y 0.25 z 0.1686(14)	N2 x 0.3689 y 0.25 z 0.1664

Table S7. Experimentally determined crystallographic data for CeCN₅ at 90(2) GPa in comparison with the corresponding DFT-relaxed structure. Note that pressure was fixed to 90 GPa in the theoretical simulations, while the volume of the unit cell, lattice parameters and equilibrium state parameters were calculated.

	Exp.	Calc.
Space group	$P2_1/n$	$P2_1/n$
Volume	192.72(13) Å ³	191.66 Å ³
Lattice parameters	a = 3.8889(9) Å b = 4.7394(7) Å c = 10.487(6) Å β = 94.41(4)°	a = 3.8874 Å b = 4.7240 Å c = 10.471 Å β = 94.59°
Atomic positions	Ce1 x 0.1469(2) y 0.8419(1) z 0.1545(1)	Ce1 x 0.1502 y 0.8422 z 0.1540
	C1 x 0.2350(30) y 0.1574(17) z 0.6261(15)	C1 x 0.2600 y 0.1553 z 0.6300
	N1 x 0.1470(30) y 0.9171(14) z 0.7001(15)	N1 x 0.1534 y 0.9191 z 0.7002
	N2 x 0.0340(20) y 0.1486(15) z 0.5112(12)	N2 x 0.0343 y 0.1484 z 0.5119
	N3 x 0.0890(20) y 0.3548(15) z 0.1255(11)	N3 x 0.0928 y 0.3554 z 0.1250
	N4 x 0.1410(30) y 0.4090(13) z 0.6833(15)	N4 x 0.1435 y 0.4063 z 0.6867
	N5 x 0.2280(30) y 0.2175(14) z 0.0207(14)	N5 x 0.2295 y 0.2252 z 0.0231

Table S8. The lattice parameters of LaCN₃ at different pressures.

DAC	Pressure, GPa	a, Å	b, Å	c, Å	Volume, Å ³
DAC#1	102(2) ¹	4.1059(12)	4.870(5)	7.4758(15)	149.49(16)
DAC#1	75(2) ²	4.170(3)	4.950(4)	7.592(10)	156.7(3)
DAC#4	101(2) ¹	4.1252(10)	4.8659(13)	7.448(2)	149.49(7)
DAC#4	85(2)	4.111(8)	4.906(5)	7.523(6)	151.7(3)
DAC#4	64(2)	4.202(5)	4.905(4)	7.632(5)	157.3(2)
DAC#4	37(2)	4.233(5)	5.109(6)	7.652(13)	165.5(4)
DAC#4	23(2)	4.335(3)	5.141(2)	7.851(2)	174.98(16)
DAC#4	6(2)	4.4406(5)	5.3417(7)	8.1055(16)	192.27(5)

¹Pressure of synthesis.

²After the compound's synthesis at 102(2) GPa, the DAC was decompressed from that pressure down to 75(2) GPa. At the next pressure point, 50(2) GPa, the nitrogen pressure transmitting medium went out through microcracks in the diamond resulting in a diamond breaking and the complete gasket closure, with the pressure dropping to 1 atm. The sample could not be found afterwards.

Table S9. The lattice parameters of CeCN₅ at different pressures.

Pressure, GPa	a, Å	b, Å	c, Å	β, °	Volume, Å ³
90(2) ¹	3.889(1)	4.739(1)	10.487(6)	94.41(4)	192.7 (2)
114(2) ²	3.812(1)	4.645(2)	10.464(6)	93.95(3)	184.9(2)
95(2)	3.857(7)	4.707(4)	10.490(8)	93.56(6)	189.4(2)
69(2)	3.9250(16)	4.7804(16)	10.611(5)	94.25(4)	198.5(2)
58(2)	3.9514(10)	4.8448(12)	10.710(3)	94.80(2)	204.3(1)
49(2)	3.9583(12)	4.8827(13)	10.831(6)	94.54(3)	208.7(2)
33(2)	4.0081(15)	4.935(5)	10.960(2)	94.51(2)	216.1(3)

¹Pressure of synthesis.

²After synthesis at 90(2) GPa, the DAC was compressed first to 114(2) GPa, and then decompressed from that pressure down to 33(2) GPa. Below that pressure, one of the diamonds broke, and the sample escaped.

Table S10. POTCARs used for LaCN₃ and CeCN₅.

Compound	Functional	Element	Core	Number of valence electrons
LaCN ₃	PBE	La	[Kr4d]	11
		C	s2p2	4
		N	s2p3	5
CeCN ₅	LDA	Ce	[Kr4d]	12
		C	s2p2	4
		N	s2p3	5

Supplementary Figures

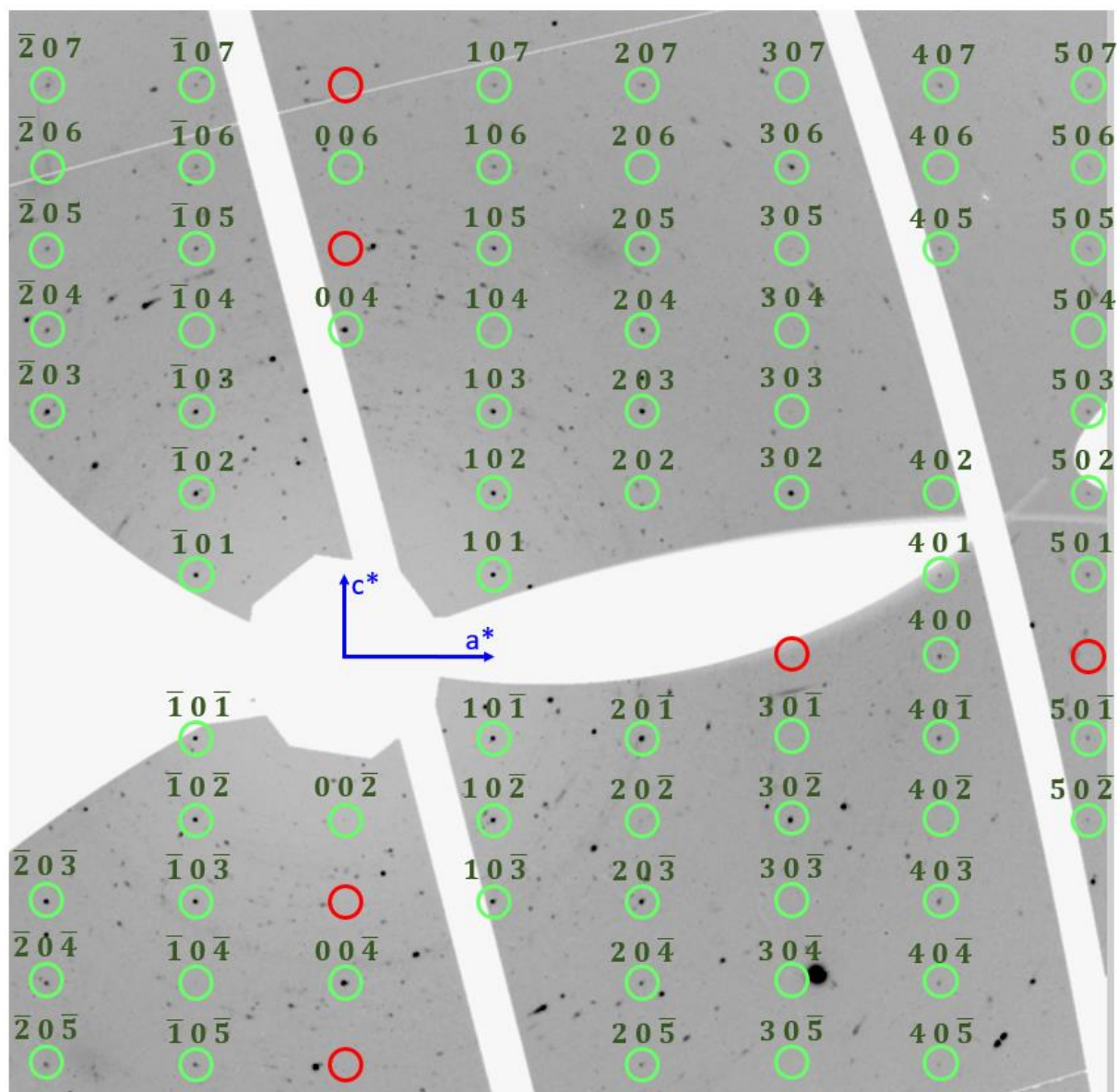


Figure S1. $(h\ 0\ l)$ reciprocal lattice plane of LaCN_3 at 102(2) GPa reconstructed from the experimental SCXRD dataset in the CrysAlis^{Pro} software. The reflections circled in green correspond to the crystallite of LaCN_3 whose structure was determined. The red circles illustrate the positions of the $h\ 0\ 0$ reflections with $h = 2n + 1$ and the $0\ 0\ l$ reflections with $l = 2n + 1$, which are systematically absent in the $Pnma$ space group. The reflections that are not encircled belong to other crystallites of the same LaCN_3 phase or of other binary La-N phases present in the multiphase multigrain sample.

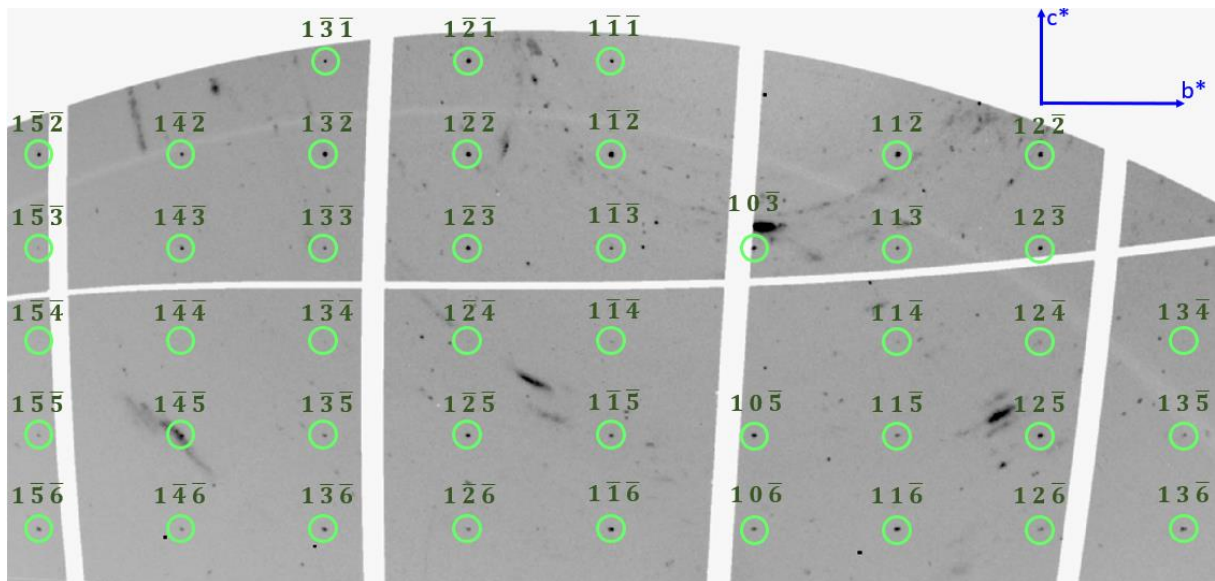


Figure S2. $(1\ k\ l)$ reciprocal lattice plane of TbCN_3 at 111(2) GPa reconstructed from the experimental SCXRD dataset in the CrysAlis^{Pro} software. The reflections circled in green correspond to the crystallite of TbCN_3 whose structure was determined. The reflections that are not encircled belong to other crystallites of the same TbCN_3 phase or of other binary Tb-N phases and TbCN_5 present in the multiphase multigrain sample.

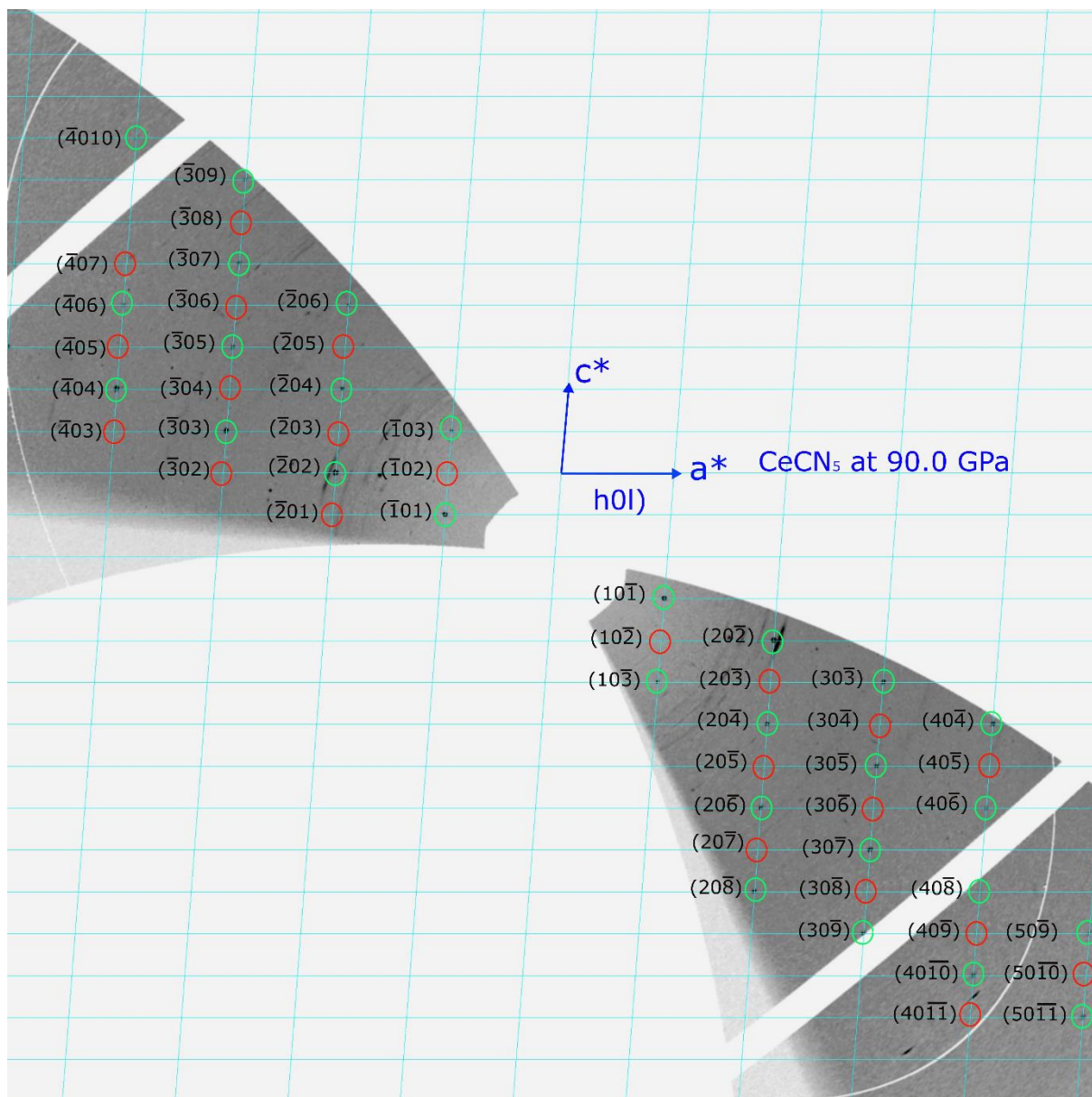


Figure S3. $(h\ 0\ l)$ reciprocal lattice plane of CeCN_5 at 90(2) GPa reconstructed from the experimental SCXRD dataset in CrysAlis^{Pro} software. The reflections circled in green correspond to the crystallite of CeCN_5 whose structure was determined. The red circles illustrate the positions of the $h\ 0\ l$ reflections with $h+l = 2n + 1$, which are systematically absent in the $P2_1/n$ space group. The reflections that are not encircled belong to other crystallites of the same CeCN_5 phase or of other binary Ce-N phases present in the multiphase multigrain sample.

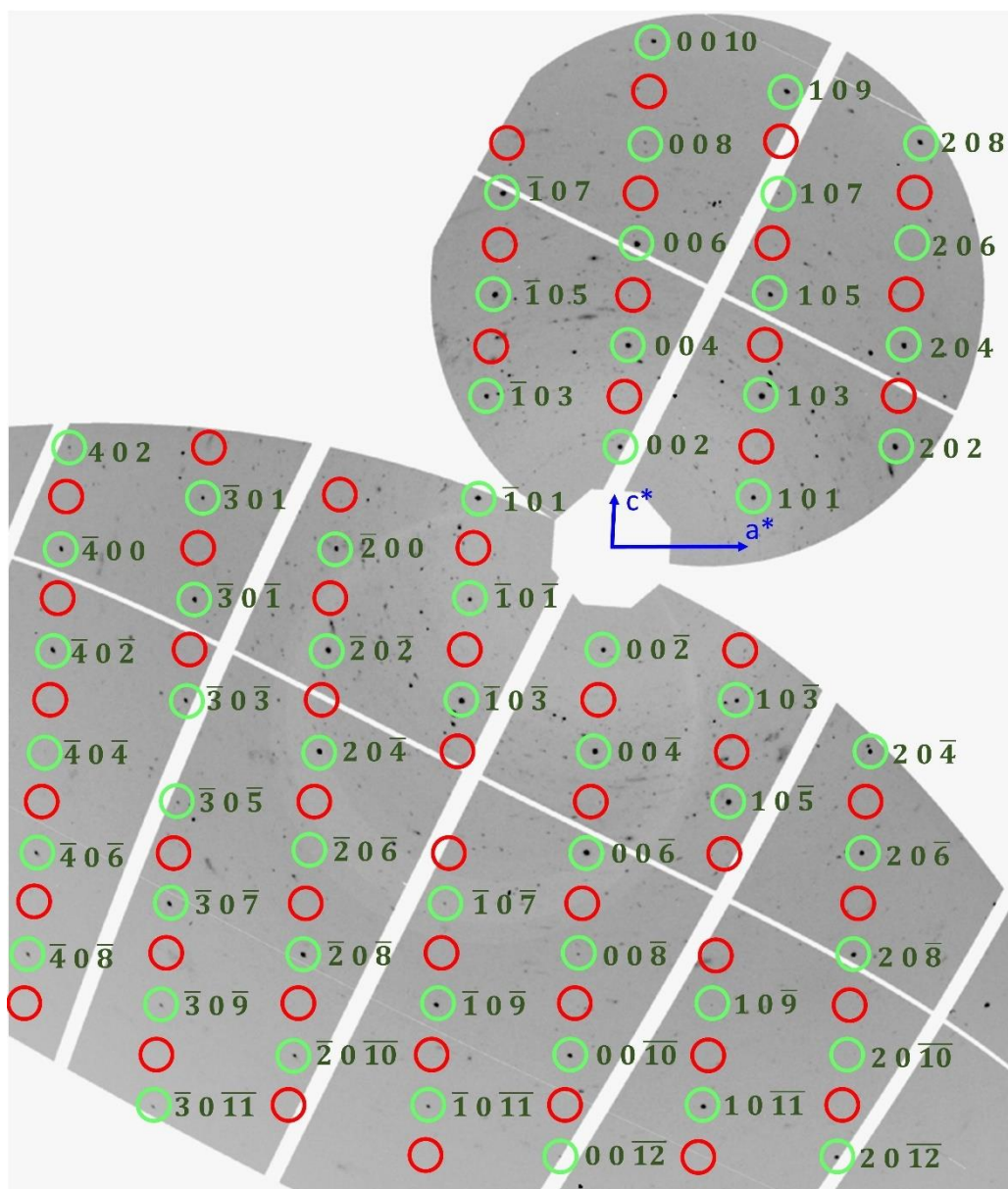


Figure S4. $(h\ 0\ l)$ reciprocal lattice plane of TbCN_5 at 90(2) GPa reconstructed from the experimental SCXRD dataset in CrysAlis^{Pro} software. The reflections circled in green correspond to the crystallite of TbCN_5 whose structure was determined. The red circles illustrate the positions of the $h\ 0\ l$ reflections with $h+l = 2n + 1$, which are systematically absent in the $P2_1/n$ space group. The reflections that are not encircled belong to other crystallites of the same TbCN_5 phase or of other binary Tb-N phases and TbCN_3 present in the multiphase multigrain sample.

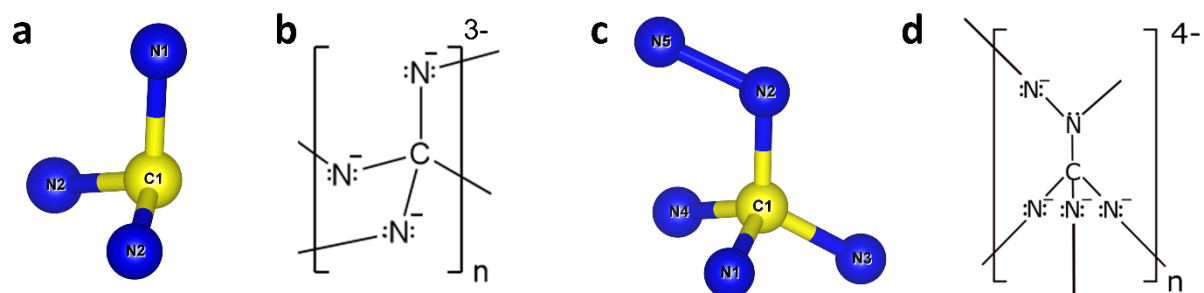
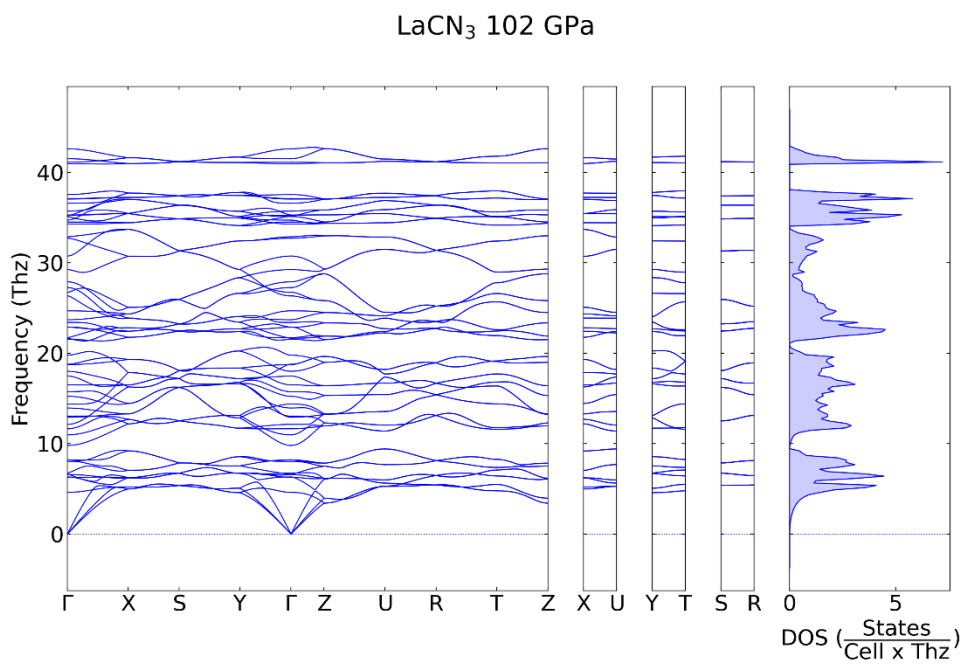
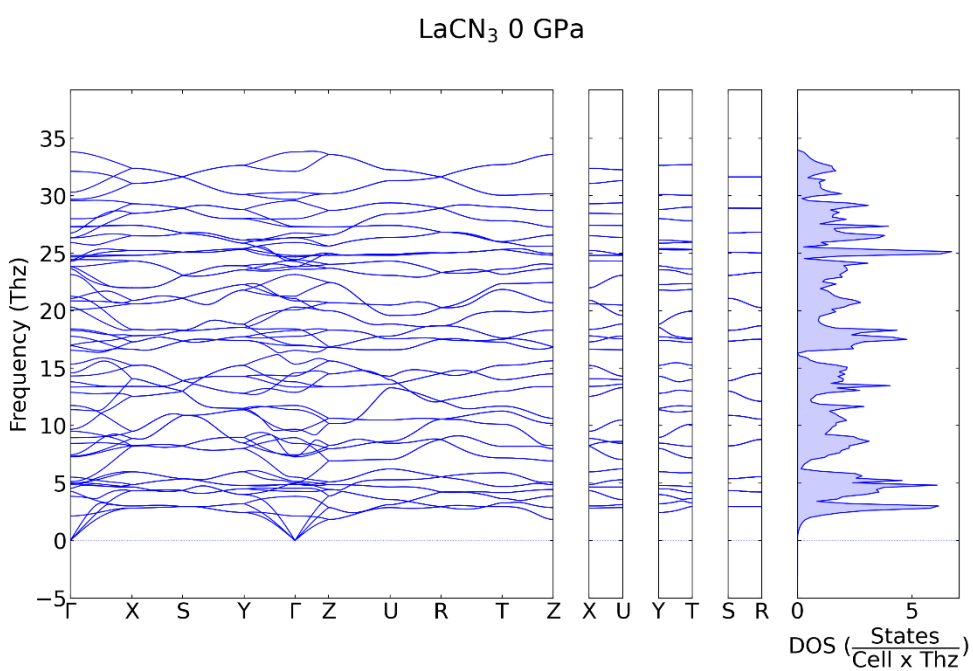


Figure S5. (a) A representation of the repeating CN_3 unit in $\text{LaCN}_3/\text{TbCN}_3$. (b) Lewis formula of the $[\text{CN}_3]_{\infty}^{3-}$ anion in $\text{LaCN}_3/\text{TbCN}_3$. (c) A representation of the repeating CN_5 unit in $\text{CeCN}_5/\text{TbCN}_5$. (d) Lewis formula of the $[\text{CN}_5]_{\infty}^{4-}$ anion in $\text{CeCN}_5/\text{TbCN}_5$.



(a)



(b)

Figure S6. Calculated phonon dispersions of LaCN₃ at (a) 102 GPa and (b) 1 atm.

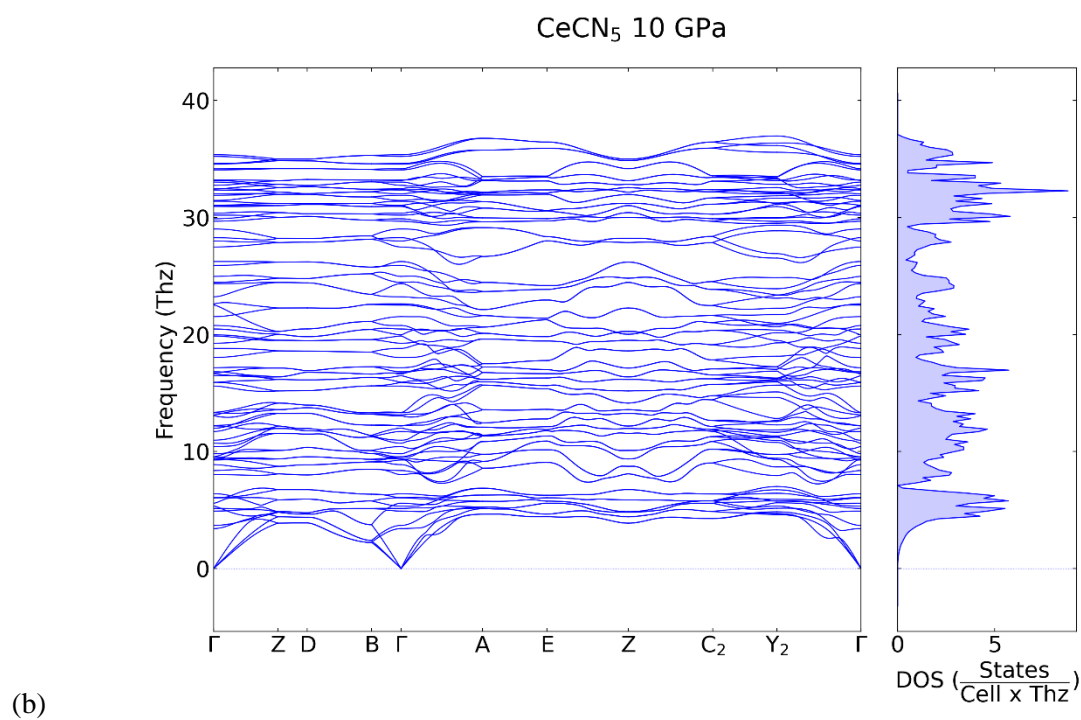
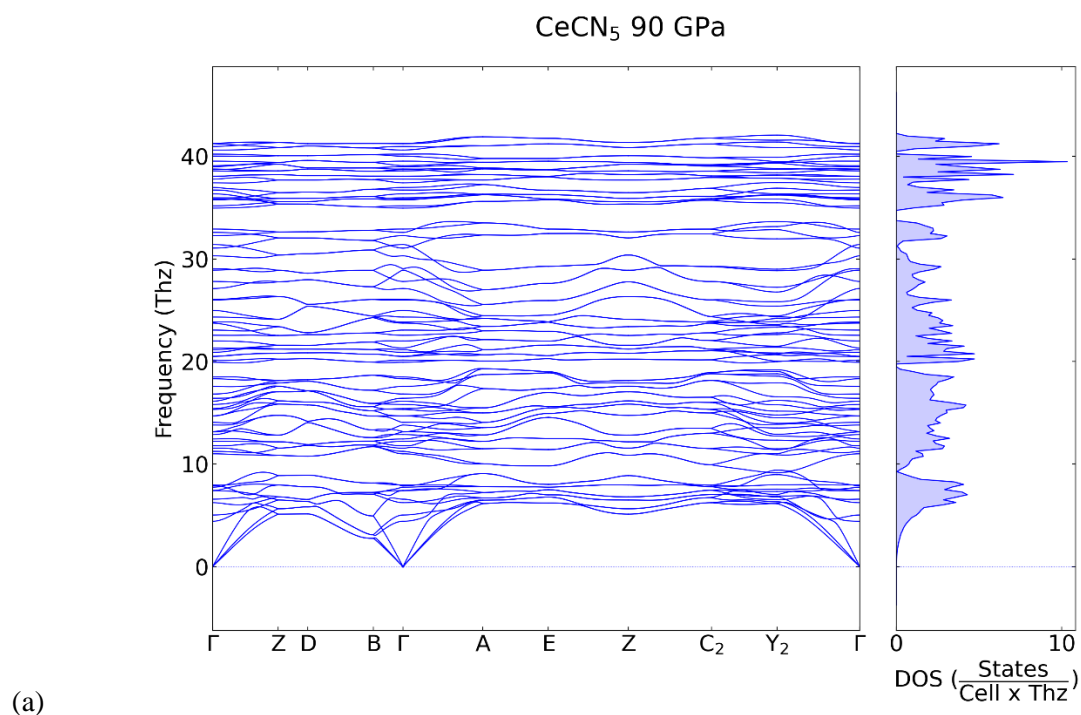


Figure S7. Calculated phonon dispersions of CeCN₅ at (a) 90 GPa and (b) 10 GPa.

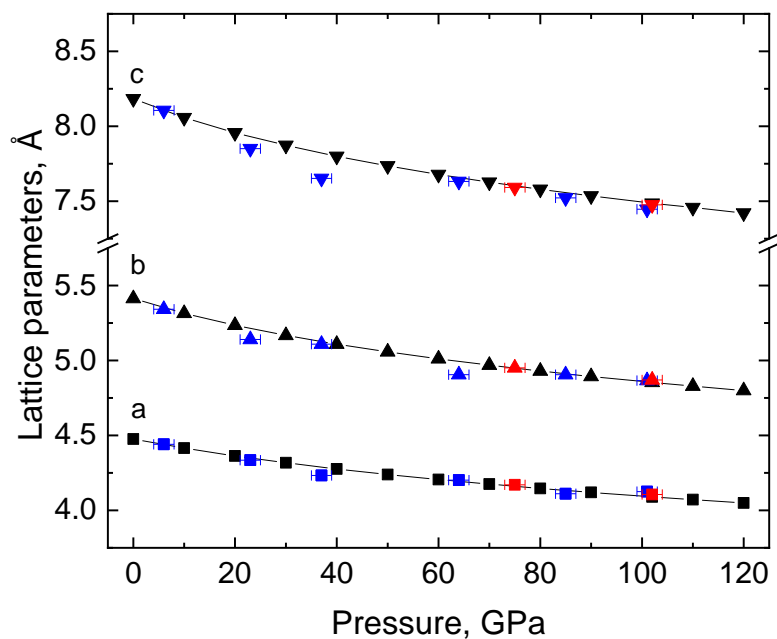


Figure S8. The dependence of the unit cell parameters of LaCN_3 with pressure. The black symbols represent calculated data points obtained from DFT while the red and blue symbols represent experimental data points obtained from SCXRD data collected in DAC#1 and DAC#4, respectively.

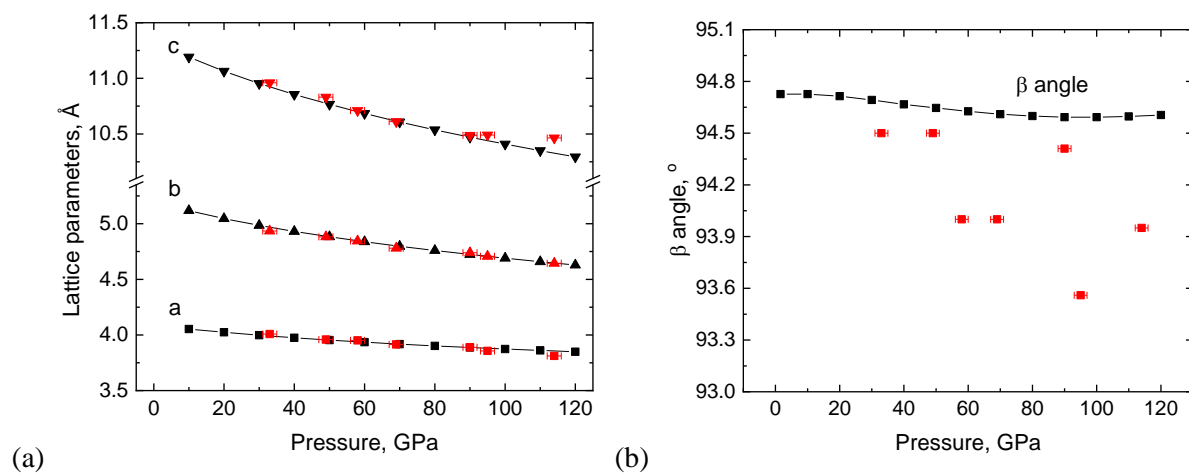


Figure S9. The dependence of the unit cell parameters of CeCN_5 with pressure: (a) a , b , c lattice parameters and (b) β angle. The black symbols represent calculated data points obtained from DFT, the red symbols represent experimental data points obtained from SCXRD data.

Supplementary discussion of CeCN₅ compound with occupied 4*f*-states.

CeCN₅ is a 4*f* electron system, with pure Ce having one 4*f* electron. The cerium oxidation state in the CeCN₅ compound is expected to be +4 (see main paper). The presence of 4*f* electrons requires careful consideration of the many-electron effects, especially when the states are occupied. Previous studies on the rare-earth elements, to which Ce belongs, suggest that local density approximation (LDA) and semi-local generalized gradient approximation (GGA) within DFT may not be sufficient to treat these materials. In this study, the LDA+U method was employed (see Methods, Theoretical Calculations).

At a pressure of 10 GPa and above, all 4*f* states of CeCN₅ are unoccupied according to our calculations. Using LDA+U for CeCN₅, insulating state was obtained in the pressure range from synthesis pressure down to 10 GPa (**Fig. 5b** in the main text). Comparison of structural parameters for CeCN₅ shows that the computed results are in very good agreement with experimental data (**Table S7**). This indicates that LDA+U is likely sufficient to describe the structural properties of this material in the high-pressure phase.

At pressures below 10 GPa, LDA+U simulations result in an electronic transition, upon which one of the *f* electron state becomes occupied (**Fig. SD1**), and CeCN₅ becomes metallic. The material also gains a magnetic moment, specifically originating from the one 4*f* electron. In this level of theory, the transition is accompanied by a rapid change of structural parameters (**Figs. SD2 and SD3**). For an accurate theoretical study of this transition, a higher-level theory is required, such as DFT+DMFT,¹ which can treat many-electron effects in strongly correlated systems, such as CeCN₅ with partly occupied *f*-states.

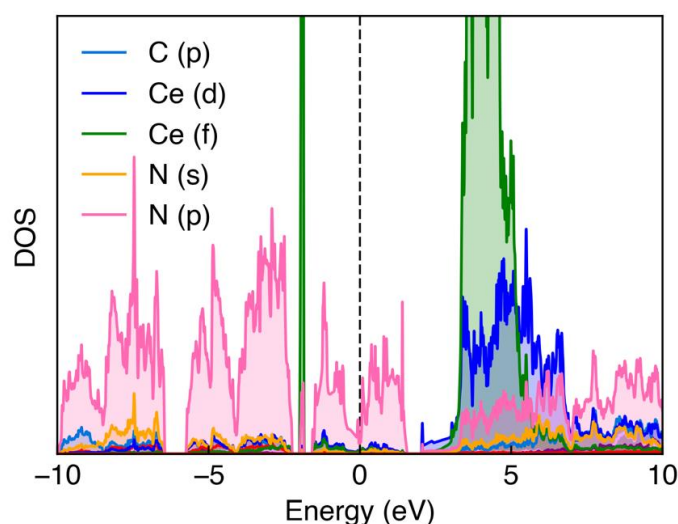


Figure SD1. The electron density of states of CeCN₅ at 1 atm.

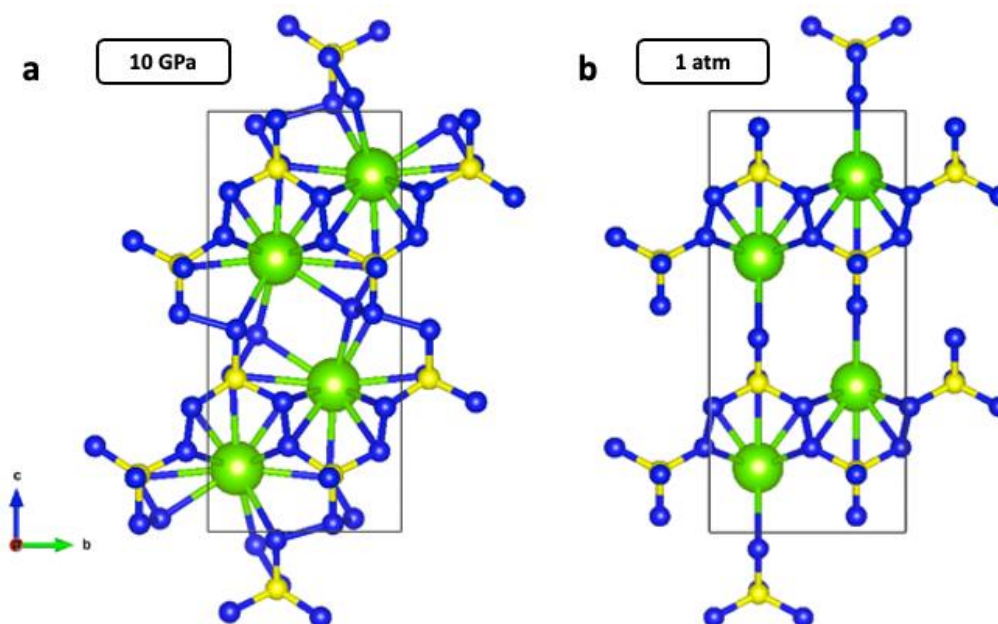


Figure SD2. Crystal structure of CeCN₅ at 10 GPa and at 1 atm, with an electronic and structural transition having occurred in the latter.

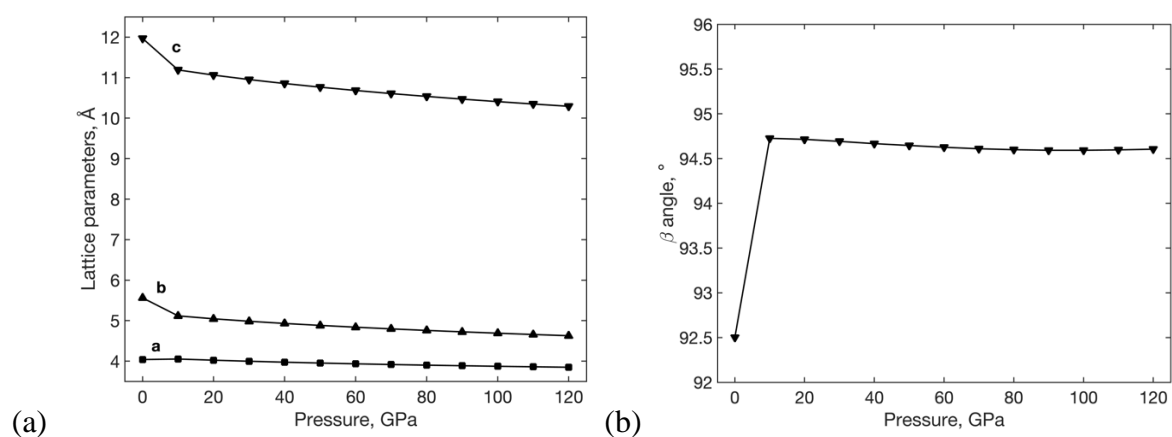


Figure SD3. The dependence of the unit cell parameters of CeCN₅ with pressure: (a) lattice parameters a, b, and c and (b) β-angle.

References

1. Georges, A., Kotliar, G., Krauth, W. & Rozenberg, M. J. Dynamical mean-field theory of strongly correlated fermion systems and the limit of infinite dimensions. *Rev. Mod. Phys.* **68**, 13–125 (1996).

6. List of all author publications

1. A. Aslandukova, **A. Aslandukov**, F.I. Akbar, Y. Yin, F. Trybel, M. Hanfland, A. Pakhomova, S. Chariton, V. Prakapenka, N. Dubrovinskaia, L. Dubrovinsky. (2024) High-Pressure $oC16$ - YBr_3 Polymorph Recoverable to Ambient Conditions: From 3D Framework to Layered Material. *Inorganic Chemistry*, accepted.
DOI: [10.1021/acs.inorgchem.4c00813](https://doi.org/10.1021/acs.inorgchem.4c00813)
2. **A. Aslandukov**, A. Liang, A. Ehn, F. Trybel, Y. Yin, A. Aslandukova, F.I. Akbar, U. Ranieri, J. Spender, R.T. Howie, E.L. Bright, J. Wright, M. Hanfland, G. Garbarino, M. Mezouar, T. Fedotenko, I. A. Abrikosov, N. Dubrovinskaia, L. Dubrovinsky, D. Laniel (2024). Synthesis of $LaCN_3$, $TbCN_3$, $CeCN_5$ and $TbCN_5$ polycarbonitrides at megabar pressures, *Journal of American Chemical Society*, 146(26), 18161–18171.
DOI: [10.1021/jacs.4c06068](https://doi.org/10.1021/jacs.4c06068)
3. F.I. Akbar, A. Aslandukova, Y. Yin, **A. Aslandukov**, D. Laniel, E. Bykova, M. Bykov, E.L. Bright, J. Wright, D. Comboni, M. Hanfland, N. Dubrovinskaia, L. Dubrovinsky. (2024). High-Pressure Dysprosium Carbides Containing Carbon Dimers, Trimers, Chains, and Ribbons. *Carbon*, 119374.
DOI: [10.1016/j.carbon.2024.119374](https://doi.org/10.1016/j.carbon.2024.119374)
4. Y. Yin, L. Dubrovinsky, **A. Aslandukov**, A. Aslandukova, F.I. Akbar, W. Zhou, M. Hanfland, I.A. Abrikosov, N. Dubrovinskaia. (2024). High-Pressure Synthesis of the Iodide Carbonate $Na_5(CO_3)_2I$. *Solids*, 5(2), 333-340.
DOI: [10.3390/solids5020022](https://doi.org/10.3390/solids5020022)
5. A. Liang, I. Osmond, G. Krach, L-T. Shi, L. Brüning, U. Ranieri, J. Spender, F. Tasnadi, B. Massani, C.R. Stevens, R.S. McWilliams, E.L. Bright, N. Giordano, S. Gallego-Parra, Y. Yin, **A. Aslandukov**, F.I. Akbar, E. Gregoryanz, A. Huxley, M. Pena-Alvarez, J-G. Si, W. Schnick, M. Bykov, F. Trybel, D. Laniel. (2024). High-Pressure Synthesis of Ultra-Incompressible, Hard and Superconducting Tungsten Nitrides. *Advanced Functional Materials*, 2313819.
DOI: [10.1002/adfm.202313819](https://doi.org/10.1002/adfm.202313819)
6. S. Khandarkhaeva, T. Fedotenko, A. Aslandukova, F.I. Akbar, M. Bykov, D. Laniel, **A. Aslandukov**, U. Ruschewitz, C. Tobeck, *B. Winkler*, S. Chariton, V. Prakapenka, K. Glazyrin, C. Giacobbe, E.L. Bright, M. Belov, N. Dubrovinskaia, L. Dubrovinsky (2024). Extending carbon chemistry at high-pressure by synthesis of CaC_2 and Ca_3C_7 with deprotonated polyacene-and para-poly (indenoindene)-like nanoribbons. *Nature Communications*, 15(1), 2855.
DOI: [10.1038/s41467-024-47138-2](https://doi.org/10.1038/s41467-024-47138-2)
7. **A. Aslandukov**, A. Aslandukova, D. Laniel, S. Khandarkhaeva, Y. Yin, F. I. Akbar, S. Chariton, V. Prakapenka, E. L. Bright, C. Giacobbe, J. Wright, D. Comboni, M. Hanfland, N. Dubrovinskaia, L. Dubrovinsky (2024). Stabilization of N_6 and N_8 anionic units and 2D polynitrogen layers in high-pressure scandium polynitrides, *Nature Communications*, 15(1), 2244.
DOI: [10.1038/s41467-024-46313-9](https://doi.org/10.1038/s41467-024-46313-9)
8. A. Aslandukova, **A. Aslandukov**, D. Laniel, Y. Yin, F.I. Akbar, M. Bykov, T. Fedotenko, K. Glazyrin, A. Pakhomova, G. Garbarino, E.L. Bright, J. Wright, M. Hanfland, S. Chariton, V. Prakapenka, N. Dubrovinskaia, L. Dubrovinsky (2024). Diverse high-pressure chemistry in $Y-NH_3BH_3$ and Y -paraffin oil systems. *Science Advances*, 10, ead15416
DOI: [10.1126/sciadv.adl5416](https://doi.org/10.1126/sciadv.adl5416)

9. D. Laniel, F. Trybel, **A. Aslandukov**, S. Khandarkhaeva, T. Fedotenko, Y. Yin, F. Tasnádi, A.V. Ponomareva, G. Weck, F.I. Akbar, B. Winkler, A. Néri, S. Chariton, C. Giacobbe, J. Wright, G. Garbarino, B. Wehinger, A. Pakhomova, M. Mezouar, V. Prakapenka, V. Milman, W. Schnick, I.A. Abrikosov, L. Dubrovinsky, N. Dubrovinskaia (2023). Synthesis of Ultra-Incompressible Carbon Nitrides Featuring Three-Dimensional Frameworks of CN₄ Tetrahedra Recoverable at Ambient Conditions. *Advanced Materials*, 36(3), 2308030.
DOI: [10.1002/adma.202308030](https://doi.org/10.1002/adma.202308030)
10. K. Glazyrin, **A. Aslandukov**, A. Aslandukova, T. Fedotenko, S. Khandarkhaeva, D. Laniel, M. Bykov, L. Dubrovinsky. (2023) High-pressure reactions between the pnictogens: the rediscovery of BiN. *Frontiers in Chemistry*, 11, 1257942.
DOI: [10.3389/fchem.2023.1257942](https://doi.org/10.3389/fchem.2023.1257942)
11. D. Laniel, F. Trybel, **A. Aslandukov**, J. Spender, U. Ranieri, T. Fedotenko, K. Glazyrin, E. L. Bright, S. Chariton, V. Prakapenka, I.A. Abrikosov, L. Dubrovinsky, N. Dubrovinskaia. (2023). Structure determination of ζ-N₂ from single-crystal X-ray diffraction and theoretical suggestion for the formation of amorphous nitrogen. *Nature Communications*, 14(1), 6207.
DOI: [10.1038/s41467-023-41968-2](https://doi.org/10.1038/s41467-023-41968-2)
12. F.I. Akbar, A. Aslandukova, **A. Aslandukov**, Y. Yin, F. Trybel, S. Khandarkhaeva, T. Fedotenko, D. Laniel, M. Bykov, E. Bykova, N. Dubrovinskaia, L. Dubrovinsky. (2023). High-pressure synthesis of dysprosium carbides. *Frontiers in Chemistry*, 11, 1210081.
DOI: [10.3389/fchem.2023.1210081](https://doi.org/10.3389/fchem.2023.1210081)
13. **A. Aslandukov**, P.L. Jurzick, M. Bykov, A. Aslandukova, A. Chanyshv, D. Laniel, Y. Yin, F.I. Akbar, S. Khandarkhaeva, T. Fedotenko, K. Glazyrin, S. Chariton, V. Prakapenka, F. Wilhelm, A. Rogalev, D. Comboni, M. Hanfland, N. Dubrovinskaia, L. Dubrovinsky (2023). Stabilization of the CN₃⁵⁻ anion in recoverable high-pressure Ln₃O₂(CN₃) (Ln = La, Eu, Gd, Tb, Ho, Yb) oxoguanidates, *Angewandte Chemie International Edition*, 135(47), e202311516.
DOI: [10.1002/anie.202311516](https://doi.org/10.1002/anie.202311516)
14. Y. Yin, A. Aslandukova, N. Jena, F. Trybel, I.A. Abrikosov, B. Winkler, S. Khandarkhaeva, T. Fedotenko, E. Bykova, D. Laniel, M. Bykov, **A. Aslandukov**, F.I. Akbar, K. Glazyrin, G. Garbarino, C. Giacobbe, E.L. Bright, Z. Jia, L. Dubrovinsky, N. Dubrovinskaia. (2023). Unraveling the Bonding Complexity of Polyhalogen Anions: High-Pressure Synthesis of Unpredicted Sodium Chlorides Na₂Cl₃ and Na₄Cl₅ and Bromide Na₄Br₅. *JACS Au*, 3(6), 1634–1641.
DOI: [10.1021/jacsau.3c00090](https://doi.org/10.1021/jacsau.3c00090)
15. D. Laniel, F. Trybel, Y. Yin, T. Fedotenko, S. Khandarkhaeva, **A. Aslandukov**, A.I. Abrikosov, T.B. Masood, C. Giacobbe, E. L. Bright, K. Glazyrin, M. Hanfland, I. Hotz, I. A. Abrikosov, L. Dubrovinsky, N. Dubrovinskaia. (2023). Aromatic Hexazine [N₆]⁴⁻ Anion Revealed in the Complex Structure of the High-Pressure Potassium Nitride K₉N₅₆. *Nature Chemistry*, 15(5), 641-646.
DOI: [10.1038/s41557-023-01148-7](https://doi.org/10.1038/s41557-023-01148-7)
16. A. Aslandukova, **A. Aslandukov**, D. Laniel, S. Khandarkhaeva, G. Steinle-Neumann, T. Fedotenko, S.V. Ovsyannikov, Y. Yin, F.I. Akbar, K. Glazyrin, M. Hanfland, L. Dubrovinsky, N. Dubrovinskaia. (2023). High-pressure hP3 yttrium allotrope with CaHg₂-type structure as a prototype of the hP3 rare-earth hydride series. *Physical Review B*, 107(1), 014103.
DOI: [10.1103/PhysRevB.107.014103](https://doi.org/10.1103/PhysRevB.107.014103)
17. L. Gorelova, O. Vereshchagin, **A. Aslandukov**, A. Aslandukova, D. Spiridonova, M. Krzhizhanovskaya, A. Kasatkin, L. Dubrovinsky. (2022) Hydroxylherderite

- (Ca₂Be₂P₂O₈(OH)₂) stability under extreme conditions (up to 750°C/100 GPa). *Journal of the American Ceramic Society*, 106(4), 2622-2634.
DOI: [10.1111/jace.18923](https://doi.org/10.1111/jace.18923)
18. S.N. Britvin, N.S. Vlasenko, **A. Aslandukov**, A. Aslandukova, L. Dubrovinsky, L. Gorelova, M.G. Krzhizhanovskaya, O.S. Vereshchagin, V.N. Bocharov, Y.S. Shelukhina, M.S. Lozhkin, A.N. Zaitsev, F. Nestola (2022). Natural cubic perovskite, Ca(Ti,Si,Cr)O_{3-δ}, a versatile potential host for rock-forming and less-common elements up to Earth's mantle pressure. *American Mineralogist*, 107(10), 1936-1945.
DOI: [10.2138/am-2022-8186](https://doi.org/10.2138/am-2022-8186)
 19. Y. Yin, F.I. Akbar, E. Bykova, A. Aslandukova, D. Laniel, **A. Aslandukov**, M. Bykov, M. Hanfland, G. Garbarino, Z. Jia, L. Dubrovinsky, N. Dubrovinskaia. (2022). Synthesis of rare-earth metal compounds through enhanced reactivity of alkali halides at high pressures. *Communications Chemistry*, 5(1), 1-6.
DOI: [10.1038/s42004-022-00736-x](https://doi.org/10.1038/s42004-022-00736-x)
 20. D. Laniel, F. Trybel, A. Néri, Y. Yin, **A. Aslandukov**, T. Fedotenko, S. Khandarkhaeva, F. Tasnádi, S. Chariton, C. Giacobbe, E.L. Bright, M. Hanfland, V. Prakapenka, W. Schnick, I.A. Abrikosov, L. Dubrovinsky, N. Dubrovinskaia. (2022). Revealing Phosphorus Nitrides up to the Megabar Regime: Synthesis of α'-P₃N₅, δ-P₃N₅ and PN₂. *Chemistry—A European Journal*, e202201998.
DOI: [10.1002/chem.202201998](https://doi.org/10.1002/chem.202201998)
 21. **A. Aslandukov**, M. Aslandukov, N. Dubrovinskaia, L. Dubrovinsky. (2022). Domain Auto Finder (DAFi) program: the analysis of single-crystal X-ray diffraction data from polycrystalline samples, *Journal of Applied Crystallography*, 55(5), 1383-1391
DOI: [10.1107/S1600576722008081](https://doi.org/10.1107/S1600576722008081)
 22. **A. Aslandukov**, F. Trybel, A. Aslandukova, D. Laniel, T. Fedotenko, S. Khandarkhaeva, G. Aprilis, C. Giacobbe, E.L. Bright, I.A. Abrikosov, L. Dubrovinsky, N. Dubrovinskaia. (2022). Anionic N₁₈ Macrocycles and a Polynitrogen Double Helix in Novel Yttrium Polynitrides YN₆ and Y₂N₁₁ at 100 GPa. *Angewandte Chemie International Edition*, 61(34), e202207469.
DOI: [10.1002/anie.202207469](https://doi.org/10.1002/anie.202207469)
 23. J. Binck, D. Laniel, L. Bayarjargal, S. Khandarkhaeva, T. Fedotenko, **A. Aslandukov**, K. Glazyrin, V. Milman, S. Chariton, V.B. Prakapenka, N. Dubrovinskaia, L. Dubrovinsky, B. Winkler. (2022). Synthesis of calcium orthocarbonate, Ca₂CO₄-Pnma at PT conditions of Earth's transition zone and lower mantle. *American Mineralogist: Journal of Earth and Planetary Materials*, 107(3), 336-342.
DOI: [10.2138/am-2021-7872](https://doi.org/10.2138/am-2021-7872)
 24. D. Laniel, T. Fedotenko, B. Winkler, A. Aslandukova, **A. Aslandukov**, G. Aprilis, S. Chariton, V. Milman, V. Prakapenka, L. Dubrovinsky, N. Dubrovinskaia. (2022). A reentrant phase transition and a novel polymorph revealed in high-pressure investigations of CF₄ up to 46.5 GPa. *The Journal of Chemical Physics*, 156(4), 044503.
DOI: [10.1063/5.0079402](https://doi.org/10.1063/5.0079402)
 25. D. Laniel, B. Winkler, T. Fedotenko, A. Aslandukova, **A. Aslandukov**, S. Vogel, T. Meier, M. Bykov, S. Chariton, K. Glazyrin, V. Milman, V. Prakapenka, W. Schnick, L. Dubrovinsky, N. Dubrovinskaia. (2022). High-pressure Na₃(N₂)₄, Ca₃(N₂)₄, Sr₃(N₂)₄, and Ba(N₂)₃ featuring nitrogen dimers with noninteger charges and anion-driven metallicity. *Physical Review Materials*, 6(2), 023402.
DOI: [10.1103/PhysRevMaterials.6.023402](https://doi.org/10.1103/PhysRevMaterials.6.023402)

26. A. Aslandukova, **A. Aslandukov**, L. Yuan, D. Laniel, S. Khandarkhaeva, T. Fedotenko, G. Steinle-Neumann, K. Glazyrin, N. Dubrovinskaia, L. Dubrovinsky. (2021). Novel High-Pressure Yttrium Carbide γ -Y₄C₅ Containing [C₂] and Nonlinear [C₃] Units with Unusually Large Formal Charges. *Physical Review Letters*, 127(13), 135501.
DOI: [10.1103/PhysRevLett.127.135501](https://doi.org/10.1103/PhysRevLett.127.135501)
27. D. Laniel, A.A. Aslandukova, **A.N. Aslandukov**, T. Fedotenko, S. Chariton, K. Glazyrin, V.B. Prakapenka, L.S. Dubrovinsky, N. Dubrovinskaia. (2021). High-pressure synthesis of the β -Zn₃N₂ nitride and the α -ZnN₄ and β -ZnN₄ polynitrogen compounds. *Inorganic Chemistry*, 60(19), 14594-14601.
DOI: [10.1021/acs.inorgchem.1c01532](https://doi.org/10.1021/acs.inorgchem.1c01532)
28. **A. Aslandukov**, A. Aslandukova, D. Laniel, I. Koemets, T. Fedotenko, L. Yuan, G. Steinle-Neumann, K. Glazyrin, M. Hanfland, L. Dubrovinsky, N. Dubrovinskaia. (2021). High-pressure yttrium nitride, Y₅N₁₄, featuring three distinct types of nitrogen dimers. *The Journal of Physical Chemistry C*, 125(32), 18077-18084.
DOI: [10.1021/acs.jpcc.1c06210](https://doi.org/10.1021/acs.jpcc.1c06210)
29. S.V. Ovsyannikov, A.A. Aslandukova, **A. Aslandukov**, S. Chariton, A.A. Tsirlin, I.V. Korobeynikov, N.V. Morozova, T. Fedotenko, S. Khandarkhaeva, L. Dubrovinsky. (2021). Structural stability and properties of marokite-type γ -Mn₃O₄. *Inorganic Chemistry*, 60(17), 13440-13452.
DOI: [10.1021/acs.inorgchem.1c01782](https://doi.org/10.1021/acs.inorgchem.1c01782)
30. E. Bykova, M. Bykov, S. Chariton, V.B. Prakapenka, K. Glazyrin, **A. Aslandukov**, A. Aslandukova, G. Criniti, A. Kurnosov, A.F. Goncharov. (2021). Structure and composition of CSH compounds up to 143 GPa. *Physical Review B*, 103(14), L140105.
DOI: [10.1103/PhysRevB.103.L140105](https://doi.org/10.1103/PhysRevB.103.L140105)
31. M. I. Kozlov, **A.N. Aslandukov**, A.A. Vashchenko, A.V. Medved'ko, A.E. Aleksandrov, E.V. Latipov, A.S. Goloveshkin, D.A. Lypenko, A.R. Tameev, V.V. Utochnikova. (2021). Towards efficient terbium-based solution-processed OLEDs: Hole mobility increase by the ligand design. *Journal of Alloys and Compounds*, 887, 161319.
DOI: [10.1016/j.jallcom.2021.161319](https://doi.org/10.1016/j.jallcom.2021.161319)
32. V.V. Utochnikova, **A.N. Aslandukov**, A.A. Vashchenko, A.S. Goloveshkin, A.A. Alexandrov, R. Grzibovskis, J.C.G. Bünzli. (2021). Identifying lifetime as one of the key parameters responsible for the low brightness of lanthanide-based OLEDs. *Dalton Transactions*, 50(37), 12806-12813.
DOI: [10.1039/D1DT02269E](https://doi.org/10.1039/D1DT02269E)
33. K.M. Kuznetsov, M.I. Kozlov, **A.N. Aslandukov**, A.A. Vashchenko, A.V. Medved'ko, E.V. Latipov, A.S. Goloveshkin, D.M. Tsybarenko V.V. Utochnikova. (2021). Eu(tta)₃DPPZ-based organic light-emitting diodes: spin-coating vs. vacuum-deposition. *Dalton Transactions*, 50(28), 9685-9689.
DOI: [10.1039/D1DT01316E](https://doi.org/10.1039/D1DT01316E)
34. M.I. Kozlov, **A.N. Aslandukov**, A.A. Vashchenko, A.V. Medved'ko, A.E. Aleksandrov, R. Grzibovskis, A.S. Goloveshkin, L.S. Lepnev, A.R. Tameev, A. Vembris, V.V. Utochnikova. (2019). On the development of the new approach to the design of lanthanide-based materials for solution-processed OLEDs, *Dalton Transactions*, 48 (46), 17298-17309.
DOI: [10.1039/C9DT03823J](https://doi.org/10.1039/C9DT03823J)

35. I.V. Kolesnik, **A.N. Aslandukov**, A.S. Arkhipin, D.A. Kozlov. (2019). Hydrothermal Synthesis of Layered Titanium Phosphate $\text{Ti}_2\text{O}_2\text{H}(\text{PO}_4)[(\text{NH}_4)_2\text{PO}_4]_2$ and Its Potential Application in Cosmetics, *Crystals*, 9(7), 332.
DOI: [10.3390/cryst9070332](https://doi.org/10.3390/cryst9070332)
36. V.V. Utochnikova, A.S. Kalyakina, N.N. Solodukhin., **A.N. Aslandukov**. (2019). On the structure features of substituted lanthanide benzoates, *European Journal of Inorganic Chemistry*, 2019 (18), 2320-2332.
DOI: [10.1002/ejic.201801561](https://doi.org/10.1002/ejic.201801561)
37. **A.N. Aslandukov**, V.V. Utochnikova, D.O. Goriachiy, A.A. Vashchenko, D.M. Tsymbarenko, M. Hoffmann, M. Pietraszkiewicz, N.P. Kuzmina. (2018). The Development of the New Approach Toward Lanthanide-Based OLED Fabrication: New Host Materials for Tb-Based Emitters, *Dalton Transactions*, 47(45), 16350 – 16357
DOI: [10.1039/C8DT02911C](https://doi.org/10.1039/C8DT02911C)
38. V.V. Utochnikova, N.N. Solodukhin, **A.N. Aslandukov**, M. Lukasz, I.S. Bushmarinov, A.A. Vashchenko, N.P. Kuzmina. (2017). Lanthanide tetrafluorobenzoates as emitters for OLEDs: New approach for host selection, *Organic Electronics*, 44, 85–93.
DOI: [10.1016/j.orgel.2017.01.026](https://doi.org/10.1016/j.orgel.2017.01.026)
39. V.V. Utochnikova, N.N. Solodukhin, **A.N. Aslandukov**, K.V. Zaitsev, A.S. Kalyakina, A.A. Averin, I.V. Ananyev, A.V. Churakov, N.P. Kuzmina. (2017). Highly luminescent, water-soluble lanthanide fluorobenzoates: Syntheses, structures and photophysics. part II: Luminescence enhancement by p-substituent variation, *European Journal of Inorganic Chemistry*, 2017(1), 107–114.
DOI: [10.1002/chem.201501816](https://doi.org/10.1002/chem.201501816)

(Eidesstattliche) Versicherungen und Erklärungen

(§ 9 Satz 2 Nr. 3 PromO BayNAT)

Hiermit versichere ich eidesstattlich, dass ich die Arbeit selbstständig verfasst und keine anderen als die von mir angegebenen Quellen und Hilfsmittel benutzt habe (vgl. Art. 97 Abs. 1 Satz 8 BayHIG).

(§ 9 Satz 2 Nr. 3 PromO BayNAT)

Hiermit erkläre ich, dass ich die Dissertation nicht bereits zur Erlangung eines akademischen Grades eingereicht habe und dass ich nicht bereits diese oder eine gleichartige Doktorprüfung endgültig nicht bestanden habe.

(§ 9 Satz 2 Nr. 4 PromO BayNAT)

Hiermit erkläre ich, dass ich Hilfe von gewerblichen Promotionsberatern bzw. -vermittlern oder ähnlichen Dienstleistern weder bisher in Anspruch genommen habe noch künftig in Anspruch nehmen werde.

(§ 9 Satz 2 Nr. 7 PromO BayNAT)

Hiermit erkläre ich mein Einverständnis, dass die elektronische Fassung meiner Dissertation unter Wahrung meiner Urheberrechte und des Datenschutzes einer gesonderten Überprüfung unterzogen werden kann.

(§ 9 Satz 2 Nr. 8 PromO BayNAT)

Hiermit erkläre ich mein Einverständnis, dass bei Verdacht wissenschaftlichen Fehlverhaltens Ermittlungen durch universitätsinterne Organe der wissenschaftlichen Selbstkontrolle stattfinden können.

.....
Ort, Datum, Unterschrift